8-3-2021 2:30 PM

Development of advanced solid-state electrolytes and interfaces for high-performance sulfide-based all-solid-state lithium batteries

Feipeng Zhao, *The University of Western Ontario*

Supervisor: Sun, Xueliang, *The University of Western Ontario*

A thesis submitted in partial fulfillment of the requirements for the Doctor of Philosophy degree in Mechanical and Materials Engineering

Abstract

All-solid-state lithium batteries (ASSLBs) have become increasingly attractive due to the demand of high-energy-density and high-safety lithium-ion batteries for electric vehicles (EVs). As the core component of ASSLBs, solid-state electrolytes (SSEs) are regarded as essential to determine the electrochemical performance of ASSLBs. The inorganic SSEs is one of the most important categories in all developed SSEs, representing the advance of superionic lithium conductors as well as the cornerstone to construct flexible polymer/inorganic composite SSEs. The sulfide-based inorganic SSE is one of the most promising SSEs that is receiving a lot of attentions, because only sulfide SSEs can show ultrahigh ionic conductivity (up to 10^{-2} S cm^{-1}) at room temperature (RT) that can be comparable to conventional liquid electrolytes. However, sulfide SSEs are suffering interfacial instability at both anode and cathode sides, as well as poor air stability. These drawbacks are hindering the commercialization of ASSLBs using sulfide as the SSE.

In this thesis, first, from the point view of electrolyte synthesis, strategies of element substitution are rationally developed to realize good Li anode compatibility or (and) air stability. It is noted that these strategies are on the premise to achieve decent or improved ionic conductivity for the parent sulfide SSEs. Specifically, replacing Cl partially with F in the *Argyrodite* sulfide Li_6PS_5Cl SSEs can trigger to generate LiF-rich Li anode interface, which can realize ultrastable Li plating and stripping. Additionally, Sn-substituted *Argyrodite* Li_6PS_5I and Li_3PS_4 glass-ceramic sulfide SSEs are developed, respectively. The versatile Sn is verified to improve the air stability, ionic conductivity, and Li anode compatibility, simultaneously. The mechanism of multi-functionality obtained from Sn substitution has been well explored. Overall, these novel sulfide SSEs can be viewed as new choices for developing all-solid-state Li metal batteries with high energy densities. Second, atomic layer deposition is used to design new lithium zirconium oxides (LZO) as the interfacial buffer layer to alleviate the cathode interface problems (slow Li^+ transport and side reaction) between Li_6PS_5Cl sulfide SSEs and $LiCoO_2$ cathode materials. These works focusing on the synthesis of new sulfide SSEs and the interface engineering pave the way to achieve high-performance sulfide-based ASSLBs.

Keywords

All-solid-state lithium batteries, solid-state electrolytes, sulfides, interfaces, Li anode

Summary for Lay Audience

Conventional Li-ion batteries using liquid electrolytes (LEs) are suffering from insufficient energy density and safety issues when used for the flourishing market of electric vehicles (EVs). Replacing LEs with solid-state electrolytes (SSEs) to fabricate all-solid-state lithium batteries (ASSLBs) has been regarded as an essential route to improve energy density and safety. Inorganic SSEs, as one kind of the most popular SSEs, are attracting increasing attention. A quantified SSE requires high ionic conductivity, air/moisture stability, and electrode compatibility to enable high-performance ASSLBs. Currently, sulfide SSEs become attractive due to their high ionic conductivity that can be comparable to the liquid electrolyte. However, sulfide SSEs are suffering poor electrode compatibility (anode and cathode) and air sensitivity, hindering their applications in practical ASSLBs.

In this thesis, first, from the standing point of synthesizing sulfide SSEs, the strategy of element doping (fluorine and tin) is developed to increase the Li metal compatibility and air stability of sulfide SSEs, as well as ionic conductivity for some defective sulfide SSEs. All-solid-state lithium metal batteries (ASSLMBs) using these newly developed sulfide SSEs exhibit promising electrochemical performance at room temperature (RT). These element substitution strategies help to alleviate the problem of existing sulfide SSEs essentially. Second, proceeding from the interface modification, new lithium zirconium oxides (LZO) is developed as cathode coating layers by the advanced nanofabrication technique of atomic layer deposition (ALD). The LZO buffer layer is Li-ion conducting but electron insulating, preventing the direct contact between cathode particles and sulfide SSEs, so that excellent cathode interface is achieved to enable good electrochemical performance at RT. Overall, all findings presented in the thesis would make contributions to the development of qualified superionic conductors and high-performance sulfide-based ASSLBs.

Co-Authorship Statement

1.

Recent Development of Lithium Argyrodite Solid-State Electrolytes for Solid-State Batteries: Synthesis, Structure, Stability and Dynamics

Authors: Chuang Yu+, Feipeng Zhao+, Jing Luo+, Long Zhang, Xueliang Sun

The final version of this review paper has been published in *Nano Energy* 2021, 83, 105858.

C. Yu, F. Zhao, and J. Luo contribute equally to this paper. C. Yu and F. Zhao co drafted the original manuscript. J. Luo commented and edited the manuscript. L. Zhang commented the manuscript. X. Sun gave overall supervision.

2.

Ultrastable anode interface achieved by fluorinating electrolytes for all-solid-state Li metal batteries

The final version of this manuscript has been published in *ACS Energy Lett.* 2020, 5, 4, 1035-1043.

Authors: Feipeng Zhao, Qian Sun, Chuang Yu, Shumin Zhang, Keegan Adair, Sizhe Wang, Yulong Liu, Yang Zhao, Jianwen Liang, Changhong Wang, Xiaona Li, Xia Li, Wei Xia, Ruying Li, Huan Huang, Li Zhang, Shangqian Zhao, Shigang Lu, Xueliang Sun

F.Z. and X.S. conceived the project and designed the experiments. F.Z., C.Y., and S.Z. conducted material synthesis and electrochemical measurements. F.Z., and Q.S. carried out XRD measurement and analysis. Q.S. J.L. and C.W. helped with analyzing XPS data. Q.S. and J.L. helped with the electronic conductivity measurements. S. W. drew the schematic diagram. Y.L., X.L., and R.L. helped with the SEM and EDX analysis. Y.Z. and K.A. participated in the discussion of ToF-SIMS data. J.L. helped to carry out the Raman measurements. Y.Z. W.X. and X.L. helped to analyze the cell performance. H.H., L.Z., S.Z., and S.L. participated in the discussion of data. F.Z. wrote the manuscript. K.A. polished the writing. All authors discussed the results and commented on the manuscript.

3.

A Versatile Sn-Substituted Argyrodite Sulfide Electrolyte for All-Solid-State Li Metal Batteries

The final version of this manuscript has been published in *Adv. Energy Mater.* 2020, 10, 9, 1903422.

Authors: Feipeng Zhao, Jianwen Liang, Chuang Yu, Qian Sun, Xiaona Li, Keegan Adair, Changhong Wang, Yang Zhao, Shumin Zhang, Weihan Li, Sixu Deng, Ruying Li, Yining Huang, Huan Huang, Li Zhang, Shangqian Zhao, Shigang Lu, Xueliang Sun

F.Z. and X.S. conceived the project and designed the experiments. F.Z. and S.Z. conducted material synthesis and electrochemical measurements. J.L. and F.Z. carried out XRD measurement and Rietveld refinement. J.L. conducted the DFT calculation. X.L., J.L., S.Z., and F.Z. performed the air-stability measurement and data analysis. F.Z., C.Y., and Y.H. performed NMR studies and data analysis. C.W., S.D. and R.L. helped with the SEM and EDX studies and analysis. K.A. and W.L helped with the Synchrotron XANES test and analysis. Y.Z. used the ALD method to prepared coating cathode composite. L.Z., S.Z., S.L. and H.H. participated in the discussion of the data. F.Z. wrote the manuscript. K.A. polished the writing. All authors discussed the results and commented on the manuscript.

4.

An Air-Stable and Li-Metal-Compatible Glass-Ceramic Electrolyte enabling High-Performance All-Solid-State Li Metal Batteries

The final version of this manuscript has been published in *Adv. Mater.* 2021, 33, 8, 2006577.

Authors: Feipeng Zhao, Sandamini H Alahakoon, Keegan Adair, Shumin Zhang, Wei Xia, Weihan Li, Chuang Yu, Renfei Feng, Yongfeng Hu, Jianwen Liang, Xiaoting Lin, Yang Zhao, Xiaofei Yang, Tsun-Kong Sham, Huan Huang, Li Zhang, Shangqian Zhao, Shigang Lu, Yining Huang, Xueliang Sun

F.Z., Y.H., and X.S. conceived the project and designed the experiments. F.Z. and S.Z. conducted material synthesis and electrochemical measurements. S.H.A. F.Z., and Y.C.

performed the NMR characterizations and analysis. W.X., J.L. and F.Z. carried out XRD measurement and Rietveld refinement. R.F. helped to collect the Synchrotron XRD data. J.L., S.Z., and F.Z. performed the air-stability measurement and data analysis. X.L. and R.L. helped with the SEM and EDX studies and analysis. K.A., W.L., Y.H., and T.S. helped with the Synchrotron XANES tests and data analysis. Y.Z., X.Y., L.Z., S.Z., S.L. and H.H. participated in the discussion of the data. F.Z. wrote the manuscript. K.A. edited the manuscript. All authors discussed the results and commented on the manuscript.

5.

Tuning bifunctional interface for advanced sulfide-based all-solid-state batteries

The final version of this manuscript has been published in *Energy Storage Mater.* 2020, 33, 139-146.

Authors: Feipeng Zhao, Yang Zhao, Jian Wang, Qian Sun, Keegan Adair, Shumin Zhang, Jing Luo, Junjie Li, Weihan Li, Yipeng Sun, Xiaona Li, Jianwen Liang, Changhong Wang, Ruying Li, Huan Huang, Li Zhang, Shangqian Zhao, Shigang Lu, Xueliang Sun

F. Zhao: Conceptualization, Investigation, Methodology, Data curation, Formal analysis, Writing - original draft. Y. Zhao: Methodology, Data curation, Formal analysis, Writing - review & editing. J. Wang: Methodology, Data curation, Formal analysis, Writing - review & editing. Q. Sun: Data curation, Formal analysis. K. Adair: Formal analysis, Writing - review & editing. S. Zhang: Formal analysis, Writing - review & editing. J. Luo: Formal analysis, Writing - review & editing. J. Li: Data curation, Formal analysis. W. Li: Data curation, Formal analysis. Y. Sun: Data curation, Formal analysis. X. Li: Formal analysis. J. Liang: Formal analysis, Writing - review & editing. C. Wang: Writing - review & editing. R. Li: Resources. H. Huang: Funding acquisition. L. Zhang: Funding acquisition, Writing - review & editing. S. Zhao: Funding acquisition, Writing - review & editing. S. Lu: Funding acquisition, Project administration. X. Sun: Writing - review & editing, Funding acquisition, Project administration, Supervision, Conceptualization.

Acknowledgments

This Ph.D. work was completed in Prof. Xueliang Andy Sun's Advanced Materials for Clean Energy Group at the University of Western Ontario (UWO). I am grateful to acknowledge every individual and funding that support me in the past four years.

First of all, I would like to express my sincerest gratitude to my supervisor, Prof. Xueliang Andy Sun, who is a full professor in the Department of Mechanical and Materials Engineering (MME) at UWO, Canada Research Chair, Fellow of the Canadian Academy of Engineering, and Fellow of the Royal Society of Canada. Prof. Sun provides me a great opportunity and an incredible platform where I can swim and explore the mysteries in the sea of battery science. Knowledgeable and patient Prof. Sun inspires me to solve the practical problems from thinking about the fundamental questions, which makes me gain insights into basic scientific issue behind the phenomenon and develop strategies to alleviate those problems. Prof. Sun teaches me not only how to engage in scientific research, but also how to plan the career and how to get along with others. His prospective vision, careful guidance, as well as the personal charisma have made a profound impact on me. I would like to extend the dearest gratitude to our lab manager Mrs. Ruying Kathy Li for her selfless help and support not only in my research, but also in my life. Without her help, my research could not be carried out smoothly. She cares and cherishes me with her gentle and loving heart and bring me endless warmth these years when I am far away from hometown in China.

I would like to thank my advisory committee members, Prof. Hamidreza Abdolvand and Prof. Aaron Price, who are professors in the department of MME at UWO, for their advices, support, and concerns in every stage during my Ph.D. period. In addition, I deeply appreciate their valuable advices and discussions toward the completion of this Ph.D. thesis.

I am very appreciated that Prof. Yining Huang, the chair of Department of Chemistry at UWO, providing me the opportunity to learn and apply the characterization of solid-state NMR on my research. Also, I deeply thank Dr. Jian Wang, the senior beamline scientist of SM at the Canadian Light Source, for his infinite guidance related to the STXM characterization. Their patient guidance and deep insights broaden my scientific horizon, stimulating my intense interests on exploring the chemistry in the new energy materials. In addition, I would like to

show my gratitude to Dr. Mark Biesinger and Dr. Heng-Yong Nie in the Surface Science Western for the XPS and TOF-SIMS measurements and discussions on the data analysis. I am grateful to Mrs. Sandamini H. Alahakoon, Dr. Mathew Willans, Prof. TK Sham, Dr. Yongfeng Hu, and Dr. Renfei Feng for their help in collecting and analyzing the experimental data. I benefit a lot from their help and powerful characterization techniques.

Undoubtedly, I appreciate all group members in Prof. Sun's lab. I feel much enjoyed working and living with them in Canada. I would like to thank Dr. Qian Sun, Dr. Yang Zhao, Dr. Jianwen Liang, Dr. Yulong Liu, Dr. Chuang Yu, Dr. Wei Xia, Dr. Xiaona Li, Dr. Xia Li, Dr. Changhong Wang, and Dr. Muhammad Iqbal for giving me training when I was new in the lab, as well as constructive suggestions and support when I felt confused in conducting my research. I acknowledge Mr. Keegan Adair for his careful editing and suggestions for all of my manuscripts before submitting. I am grateful to my colleagues and neighbors: Dr. Weihan Li, Mrs. Minsi Li, Dr. Xiaofei Yang, Miss Xuejie Gao, and Mrs. Jing Luo, for their encouragement during working and generous sharing in my daily life. I am also grateful for my early life in Canada that was co-organized by Mr. Yao Yao, Dr. Sizhe Wang, Dr. Fanpeng Kong, and Mr. Junjie Li. The recreation and sport events made me optimistic and energetic to work harder. Last but not least, I extend my appreciation to other members: Dr. Dawei Wang, Dr. Sixu Deng, Dr. Lei Zhang, Dr. Hui Duan, Dr. Jianneng Liang, Dr. Xulei Sui, Mr. Yipeng Sun, Mr. Jiamin Fu, Mr. Matthew Zheng, Mr. Kieran Doyle Davis, Miss Xiaoge Hao, and all former members who studied and worked in the group.

Specially, I deeply thank my family in Canada, which is only established by my wife Shumin Zhang and me. Shumin is also my important work partner in Prof. Sun's lab. She gives me strongest support in my work and life and brings me endless love and happiness. It is no exaggeration to say that any achievement during pursing my Ph.D. cannot be gained without her dedications. I also show my deepest gratitude to my family in China: to my father and mother for their cultivations, unconditional giving, and forever love; to my elder sister for helping take care of my parents.

Last, I am grateful to my financial resource from the Ontario Trillium Scholarship (OTS) program that supports me to live well and complete my Ph.D. studies. Also, I have to acknowledge other funds from Prof. Sun's projects: Nature Sciences and Engineering Research

Council of Canada, Canada Research Chair program, Canada Foundation of Innovation, China Automotive Battery Research Institute Co., Ltd., Glabat Solid-State Battery Inc., and the University of Western Ontario.

Feipeng Zhao

April 16, 2021 at the Forest Hill in London City, ON

Table of Contents

List of Tables

List of Figures

List of Appendices

List of Abbreviations

A

ALD: atomic layer deposition

ASSLB: all-solid-state lithium battery

ASSLMB: all-solid-state lithium metal battery

C

CV: cyclic voltammetry

E

EDS: energy dispersive spectroscopy

EIS: electrochemical impedance spectroscopy

G

GITT: Galvanostatic intermittent titration technique

H

HRTEM: high-resolution transmission electron microscopy

HXMA: hard X-ray micro-analysis

L

LCO: lithium cobalt oxide

LGPS: $Li_{10}GeP_2S_{12}$

LE: liquid electrolyte

LIB: lithium-ion batteries

LNO: $LiNbO_3$

LSV: Linear sweep voltammetry

LZO: lithium zirconium oxide

N

NMC: lithium nickel-manganese-cobalt oxides

S

SSE: solid-state electrolyte

SS-NMR: Solid-state nuclear magnetic resonance

SEI: Solid electrolyte interphase

SEM: secondary electron microscopy

STXM: Scanning transmission X-ray microscopy

T

TEM: transmission electron microscopy

TGA-DSC: Thermogravimetric analysis and differential scanning calorimetry

TOF-SIMS: time-of-flight secondary ion mass spectrometry

X

XAS: X-ray absorption spectroscopy

XANES: X-ray absorption near edge structure

XPS: X-ray photoelectron spectrometer

XRD: X-ray diffraction

Preface

To my family, past, and future.

Chapter 1

1 Introduction to this thesis

1.1 All-solid-state Li batteries

Since the first-generation Lithium ion batteries (LIBs) were commercialized by the Sony Corporation in 1991, they have been developed to be used in every corner to drive our society, ranging from the micro-electromechanical system (MEMS) to the large-scale energy storage grind. Particularly in recent years, advanced LIBs have been widely used for electric vehicles (EVs), aiming in reducing the carbon emission caused by the combustion of fossil fuels. LIBs possess a superior integrated electrochemical performance (high energy density, good cycling durability, decent reusability, and relatively eco-friendly) comparing with other long-standing primary/secondary batteries (e.g., lead acid batteries, alkaline batteries, and redox flow batteries).[1-2] To affirm the significance of LIBs for human beings, as well as the contribution of researchers on developing LIBs, the 2019 Nobel Prize in Chemistry went to three great pioneers (Stanley Whittingham, John Goodenough, and Akira Yoshino) in this field.

Current LIBs launched to the market are still following the first-generation LIBs developed by Sony, using flammable organic liquid electrolytes (LEs), which generally face two challenges to fulfill the requirement of batteries for EVs and other applications in extreme working conditions (e.g., extreme hot/cold environment).[3-4] The first one is the potential safety issue, due to the usage of organic solvents to construct the LEs. The low flash points (FPs, < 80 ^{o}C) and long self-extinguishing time (SET, > 30 s g^{-1}) of most organic solvents used for LEs make them relatively easy to cause the generation of gas, catch fire, or even explode in the circumstance of thermal runaway.[5] The second one the insufficient energy density. The mass energy density of current LE-based LIBs is limited around 300 Wh kg^{-1}, which restricts the mileage below 500 km for EVs powered by conventional LE-based LIBs.[6-7] On the one hand, the insufficient energy density is due to the usage of electrochemically inactive components (e.g., separators, binders, and package materials), which cannot provide any energy storage but occupy specific volumes and weight. On the

other hand, Li metal, the 'Holy Grail' of the anode, which has the potential to deliver the highest energy density coupling with a cathode, cannot be used for LEs-based LIBs.[8-9] The abandon of using Li metal anode is attributed to the instability between Li metal and conventional LEs, as well as the concern of the safety problem because of the possibility of short circuiting by the generating Li dendrites.

To overcome the two challenges, development of all-solid-state Li batteries (ASSLBs) are receiving increasing attention worldwide.[9-11] First, replacing the LEs with solid-state electrolytes (SSEs) can improve the safety, which is viewed as one of the largest motivations to develop ASSLBs. Most SSEs, especially the inorganic SSEs show excellent thermal stability, making the ASSLBs safe to operate even if the thermal runaway occurs. Second, the application of SSEs provides the possibility that using Li metal as the anode to maximize energy density in the form of all-solid-state Li metal batteries (ASSLMBs). Some well-developed SSEs (e.g., $Li_7La_3Zr_2O_{12}$ and Li_3OCl) are chemically stable towards Li metal, and the high Young's modulus of SSEs (at GPa level) is considered hard enough to resist the penetration of Li dendrites.[12-14] Last but not least, the Li-ion conductive but electronically insulated SSEs integrated in ASSLBs can also serve as the separator to prevent the direct contact of positive and negative electrodes. Meanwhile, the bipolar structure and other characteristic engineering technologies (e.g., dry powder mixing, isostatic pressing, etc.) are established to save space and mass of constructing ASSLBs for applications. By this way, high energy density can be achieved.

1.2 Challenges in all-solid-state Li batteries

The development of high-performance ASSLBs is not straightforward, and simply transplanting the mature techniques developed in conventional LE-based LIBs to the ASSLBs is not always effective. The ionic conduction (hoping among active Li sites) in the solid-state counterparts is different from that in the LEs which is associated with solvated ion diffusion.[15] In addition, the solid-to-solid contacts at multiple interfaces of ASSLBs present a lot of incompatible problems, increasing interfacial impedance for Li-ion transport.[16] Therefore, the fundamental studies on ASSLBs are basically focusing on (1) development of promising superionic conductors; (2) mechanism and strategies towards the problematic interfaces of SSEs/active electrode materials.

Generally, there are three kinds of SSEs: inorganic SSEs, polymer SSEs, and inorganic/polymer hybrid SSEs. Among which, inorganic SSEs is a major category and has experienced a long development history. In the past decade, $Li_{10}GeP_2S_{12}$ (LGPS) and its families (e.g., $Li_{9.6}P_3S_{12}$ and $Li_{9.54}Si_{1.74}P_{1.44}S_{11.7}Cl_{0.3}$) have achieved excellent room-temperature (RT) ionic conductivities (> 10^{-2} S cm^{-1}) that can be comparable to LEs, making sulfide-based inorganic SSEs receive extensive attention while disgracing the polymer and inorganic/polymer hybrid SSEs.[17-18] Nevertheless, sulfide-based inorganic SSEs are not stable in the air, and suffering from serious incompatibility with active electrode materials at both anode and cathode interfaces.[19] At the anode side, particularly when using Li metal as the anode, the interfacial side reactions and Li dendrites formation are two major obstacles; at the cathode interface, insufficient interfacial Li^+ transport and incompatibility of sulfide and oxide cathode materials lead to the capacity decay along with battery cycling.

1.3 Thesis objectives

High-performance ASSLBs depend on two aspects: excellent SSEs and outstanding electrode/SSE interfaces. For the SSEs, it is required to possess: (1) high ionic conductivity; and (2) good chemical stability, particularly the moisture stability. For the favorable interface, it is necessary to present: (1) Li dendrite-free and Li-compatible anode interface; (2) ionic conductive and electronic insulating cathode interface; and (3) capability to achieve wide practical electrochemical window. To achieve these, the author has devoted to improve the sulfide-based ASSLBs from the perspectives of electrolyte materials synthesis to the related interface (anode and cathode) designs. The main thesis objectives are list below:

i) To realize Li metal compatibility of Li_6PS_5Cl sulfide SSEs, fluorine element (F) is incorporated to the Li_6PS_5Cl SSEs, which is expected to in-situ generate fluorinated Li metal interface (LiF rich). This highly fluorinated interface will be studied in detail to enable high-performance ASSLMBs. The effects of the F incorporation on ionic conductivity, electronic conductivity, as well as the phase composition of the obtained F-doped Li_6PS_5Cl SSEs will be carefully explored.

ii) To improve the ionic conductivity and moisture stability of argyrodite Li_6PS_5I sulfide SSEs, Sn (+4) is proposed to partially replace P (+5) in the crystal structure. The influence of aliovalent element substitution on the ionic conductivity and air stability will be investigated in detail. On the premise of improved ionic conductivity, the intrinsic potential of achieving Li metal-compatibility (derived from the LiI interfacial products for Li_6PS_5I sulfide SSEs) will be exerted to realize workable ASSLMBs.

iii) To systematically study the effect of Sn (+4) substitution, β-Li_3PS_4 is chosen as the prototype SSEs. Glass-ceramic Sn-substituted Li_3PS_4 will be synthesized and studied in the aspects of ionic conductivity, air stability, as well as the Li metal compatibility in detail. The reason of the versatile Sn substitution will also be investigated deeply by advanced synchrotron X-ray based characterizations and numerical simulations.

iv) To design compatible cathode interface between argyrodite Li_6PS_5Cl sulfide SSEs and $LiCoO_2$ (LCO) cathode materials, ALD technique will be used to fabricate a new lithium zirconium oxides (LZO) coating to alleviate the interface problem. The ALD-LZO process will be tuned in detail to satisfy the general requirement of cathode coating materials. Electrochemical performance of the ASSLBs using LZO coating layer will be studied, and the working mechanism of LZO coating will be studied by combined spectroscopy and microscopy techniques.

1.4 Thesis organization

This thesis is composed of 8 chapters (one introductory chapter, one chapter of literature review, one chapter of experimental and characterization details, four articles, and one conclusion and perspective chapter), which are organized according to the requirements on Integrated-Article form as outlined in the *Thesis Regulation Guide* by the School of Graduate and Postdoctoral Studies (SGPS) of the University of Western Ontario. Specially, it organizes according to the following sequence:

Chapter 1 gives the brief introduction of all-solid-state Li batteries and the challenges to develop sulfide-based ASSLBs. Further, the research objectives and the thesis structure are stated.

Chapter 2 provides a comprehensive literature review on the focused research area, including the classic ionic transport fundamentals, recent research progress of sulfide-based SSEs compared with other two popular inorganic SSEs (halides and oxides), as well as challenges and strategies of developing high-performance sulfide-based ASSLBs.

Chapter 3 outlines the experimental apparatus and characterization techniques. The solid electrolyte synthesis methods and used instruments will be listed. The ALD technique used to develop new coating materials will be included. Characterizations techniques applied to characterize the (electro)chemical/physical properties of materials and batteries will be listed. Specifically, some important physical characterizations, such as solid-state NMR and synchrotron-based X-ray techniques will be introduced.

Chapter 4 reports the incorporation of F into argyrodite Li_6PS_5Cl can obtain a new sulfide SSE with multiple phase compositions. Although the ionic conductivity drops to 10^{-4} S cm^{-1} level due to the strong electronegativity of fluorine, the fluorinated sulfide SSEs can induce to generate dense fluorinated Li metal/sulfide interface that is rich-LiF, which can not only prevent the interface side reactions, but also boost smooth Li plating/stripping. Therefore, high performance of ASSLMBs is achieved at room temperature with the interface-assistant Li anode.

Chapter 5 demonstrates Sn (+4) substitution for P (+5) can significantly improve the ionic conductivity and air stability of argyrodite Li_6PS_5I sulfide SSEs simultaneously. With the decent RT ionic conductivity (10^{-4} S cm^{-1} level, but there is a 125-time increase compared with the pristine Li_6PS_5I), the Sn-substituted Li_6PS_5I SSEs can be used as the interlayer to stabilize the Li metal interface between Li anode and sulfide electrolytes. The LiI-rich interface is considered as the main reason to achieve this.

Chapter 6 further explores the influence of versatile Sn (+4) substitution on the prototypical β-Li_3PS_4 sulfide SSEs. Improved ionic conductivity, excellent air stability, and good Li metal compatibility are presented in the Sn-substituted glass-ceramic Li_3PS_4 SSEs for the first time. The high RT ionic conductivity (10^{-3} S cm^{-1} level) makes the new sulfide electrolyte serve as the single solid-electrolyte layer to enable high-performance ASSLMBs at RT. The Li-Sn alloy is verified embedded in the matrix (Li_2S + Li_3P) as the

interface composition, which can regulate uniform Li flux and promote stable Li plating and stripping.

Chapter 7 develops a new lithium zirconium oxide (LZO) coating material fabricated by the ALD technique. The composition controlled by the ALD process will be explored carefully, which plays an important role to determine the electrochemical performance of sulfide based ASSLBs. The working mechanism of the ALD-LZO film is also revealed by multiple spectroscopy (XPS and XANES) and microscopy characterizations (STXM). Highly conductive and robust LZO coating layer can not only provide sufficient Li^+ flux for electrochemical reactions, but also prevent parasitic interfacial reactions.

Chapter 8 summarizes the results, conclusions, and contributions of the thesis work. In addition, the author provides perspectives for the development of high-performance ASSLBs in the future.

1.5 References

（1）Li, M.; Lu, J.; Chen, Z. W.; Amine, K., *Adv. Mater.* **2018,** *30* (33), 1800561.

（2）Wu, F. X.; Maier, J.; Yu, Y., *Chem. Soc. Rev.* **2020,** *49* (5), 1569-1614.

（3）Zhao, Q.; Stalin, S.; Zhao, C.-Z.; Archer, L. A., *Nat. Rev. Mater.* **2020,** *5* (3), 229-252.

（4）Zhang, Y.; Zuo, T.-T.; Popovic, J.; Lim, K.; Yin, Y.-X.; Maier, J.; Guo, Y.-G., *Mater. Today* **2020,** *33*, 56-74.

（5）Hess, S.; Wohlfahrt-Mehrens, M.; Wachtler, M., *J. Electrochem. Soc.* **2015,** *162* (2), A3084-A3097.

（6）Lee, H.; Oh, P.; Kim, J.; Cha, H.; Chae, S.; Lee, S.; Cho, J., *Adv. Mater.* **2019,** *31* (29), 1900376.

（7）Sun, Y.-K., *ACS Energy Lett.* **2020,** *5* (10), 3221-3223.

（8）Xu, L.; Lu, Y.; Zhao, C. Z.; Yuan, H.; Zhu, G. L.; Hou, L. P.; Zhang, Q.; Huang, J. Q., *Adv. Energy Mater.* **2020,** *11* (4), 2002360.

（9）Cui, G., *Matter* **2020,** *2* (4), 805-815.

（10）Chen, Y.; Wen, K.; Chen, T.; Zhang, X.; Armand, M.; Chen, S., *Energy Storage Mater.* **2020,** *31*, 401-433.

（11）Zhou, Q.; Ma, J.; Dong, S.; Li, X.; Cui, G., *Adv. Mater.* **2019,** *31* (50), 1902029.

（12）Zheng, C.; Li, L.; Wang, K.; Wang, C.; Zhang, J.; Xia, Y.; Huang, H.; Liang, C.; Gan, Y.; He, X.; Tao, X.; Zhang, W., *Batteries & Supercaps* **2020,** *4* (1), 8-38.

（13）Chen, R.; Li, Q.; Yu, X.; Chen, L.; Li, H., *Chem. Rev.* **2019,** *120* (14), 6820–6877.

（14）Zhang, Z.; Shao, Y.; Lotsch, B.; Hu, Y.-S.; Li, H.; Janek, J.; Nazar, L. F.; Nan, C.-W.; Maier, J.; Armand, M.; Chen, L., *Energy Environ. Sci.* **2018,** *11* (8), 1945-1976.

（15）Zou, Z.; Li, Y.; Lu, Z.; Wang, D.; Cui, Y.; Guo, B.; Li, Y.; Liang, X.; Feng, J.; Li, H.; Nan, C. W.; Armand, M.; Chen, L.; Xu, K.; Shi, S., *Chem. Rev.* **2020,** *120* (9), 4169-4221.

（16）Xiao, Y.; Wang, Y.; Bo, S.-H.; Kim, J. C.; Miara, L. J.; Ceder, G., *Nat. Rev. Mater.* **2019,** *5* (2), 105-126.

（17）Kato, Y.; Hori, S.; Saito, T.; Suzuki, K.; Hirayama, M.; Mitsui, A.; Yonemura, M.; Iba, H.; Kanno, R., *Nat. Energy* **2016,** *1* (4), 16030.

（18）Kamaya, N.; Homma, K.; Yamakawa, Y.; Hirayama, M.; Kanno, R.; Yonemura, M.; Kamiyama, T.; Kato, Y.; Hama, S.; Kawamoto, K.; Mitsui, A., *Nat. Mater.* **2011,** *10* (9), 682-686.

（19）Wang, S.; Fang, R.; Li, Y.; Liu, Y.; Xin, C.; Richter, F. H.; Nan, C.-W., *J. Materiomics* **2021,** *7* (2), 209-218.

Chapter 2

2 Literature review

In this chapter the literature review in the field of ASSLBs will be presented, including two parts: the recent research progress of inorganic SSEs (particularly for the sulfide SSEs) and interface related problems and strategies in the sulfide-based ASSLBs.

*Part of the literature review in this chapter has be published as a review paper: *Nano Energy* **2021**, 83, 105858.

2.1 Inorganic solid-state electrolytes (SSEs)

Inorganic SSEs is an essential branch of SSEs for ASSLBs. Compared with relatively emerging polymer and inorganic/polymer hybrid SSEs, inorganic SSEs show high Li-ion transference number and considerable ionic conductivity at RT.[1-2] The synthesis of inorganic SSEs are mostly based on the solid-state reactions (e.g., ball milling method and co-melting method), which avoid using any hazardous solvent-related (e.g., environmentally harmful organic solutions) routes to enhance the complexity and cost.[3] In this section, the history of developing inorganic SSEs will be firstly overviewed. And then, some fundamentals about Li^+ transport in the inorganic SSEs will be introduced. Subsequently, the research progress of three main kinds of inorganic SSEs (sulfides, halides, and oxides) will be reviewed, among which, sulfides is the focus in this thesis.

2.1.1 Development history of inorganic SSEs

The history of developing inorganic SSEs is long and glorious, which is accompanied by the refreshed perception on the fast-ionic conductor. The starting dates of ionic conductor can retrospect to 1830s, when Faraday discovered outstanding properties of ionic conduction in solid Ag_2S and PbF_2 compounds.[3] However, applying superionic SSEs for battery applications occurred in the period of 1960s ~ 1980s, when β-alumina ($Na_2O{\cdot}11Al_2O_3$) was initiatively found to show fast Na-ion transport and enabled high-temperature solid-state Na-S batteries afterwards.[4] Besides, Ag_3SI and $RbAg_4I_5$ ionic conductors were also successfully demonstrated for energy storage.[5-6] It is noted that that these early discovered ionic conductors are all of inorganic feature. After 1980s, the development of inorganic SSEs indicated a spurt trend. Various sulfides, chlorides, and oxides were considerably developed. Oak Ridge National Laboratory discovered a fast ionic conductor: lithium phosphorus oxynitride (LiPON) in 1990s, which was fabricated as a thin film and could be used as the SSE for thin-film Li-ion batteries.[7] Inspired by the LiPON SSEs, increasing efforts have been made towards the development of inorganic Li-ion conductive ceramic materials in the subsequent two decades (before 2018), such as perovskite-type, sodium superionic conductor (NASICON)-type, garnet-type, and sulfide-type materials. During this period, oxides and sulfides attracted more interests compared with halide SSEs. Several representative oxides SSEs show high ionic conductivity of 10^-

^{3} S cm^{-1} level, while sulfides SSEs climbed up to an ultrahigh benchmark of 10^{-2} S cm^{-1} at RT that can be comparable to the LEs.[8-9] However, the application of oxides and sulfides for ASSLBs at ambient environment were still facing huge challenges. Under this circumstance, halide-based SSEs have re-attracted attention since the Panasonic Company reported Li_3YCl_6 and Li_3YBr_6 can be compatible with typical cathode materials ($LiCoO_2$, LCO) in 2018.[10] In addition to the types of inorganic SSEs become increasingly fruitful, understanding the ionic transport mechanism in diverse SSEs also obtained significant progress via conducting advanced characterizations (including computational methods) from the beginning of 21st century.[11]

Overall, after experiencing two centuries, the development of inorganic SSEs has been entered into a flourishing era. Three main types of inorganic SSEs are in the tripartite confrontation. The oxide SSEs seems fall as the last, because of the relatively low ionic conductivity compared with sulfides and halides. Moreover, huge grain boundary and strong rigidity of oxides almost rule out the possibility of using oxide SSEs as the single SSE component to fabricate ASSLBs. The revival of halide SSEs put pressure on the highly conductive sulfide SSEs, since increasing numbers of halides are discovered or re-examined due to the improvement of synthesis approaches. However, the highest ionic conductivity of halides are still under 3×10^{-3} S cm^{-1} at RT,[12] while the catastrophic anode stability of halide SSEs make it impossible to face Li metal directly. Therefore, the author insist that sulfide SSEs are still urgent to be developed, and more efforts should be put on improving the electrode compatibility and air stability of sulfide-based ASSLBs.

2.1.2 Fundamentals about Li^+ transport

Following the classical theory, Li^+ transport in one inorganic SSE generally depends on the concentration and distribution of defects. The ion diffusion mechanisms based on Schottky and Frenkel point defects.[13] There are two sublattices in the superionic conductor: one is anion-based (or polyanion-based) framework involving immobile ions; the other one is Li sublattices. Generally, to achieve fast Li ionic conductivity, three minimum criteria must be fulfilled for the crystal structure of inorganic SSEs: (1) the number of equivalent sites available for the Li ions to occupy should be much more than the number of Li ions; (2) the migration barrier energies between the adjacent available sites should be low

enough for Li^+ hopping; (3) these available sites should be connected to form a continuous ionic transport pathway. Like the transport process in the crystalline inorganic SSEs, Li^+ transport in glassy state SSEs starts with ions at local sites being excited to neighboring sites and then collectively diffusing on a macroscopic scale.[14]

2.1.2.1 Ionic conduction

The ion conduction in solids is described by the ion hopping. Considering the ion hopping is the thermally activated Brownian motion, the probability of successful jumps (p) where a Li ion hops from one stable site to the adjacent site can be given as:

$$p = \exp\left(-\frac{\Delta G}{k_{\mathrm{B}}T}\right) \tag{1}$$

Here, ΔG is the energy barrier ion jump (i.e. difference of Gibbs free energy between a saddle point and a stable position), k_B is the Boltzmann constant, and T is the temperature.

During the ion conduction, ions vibrate within their lattice sites and attempt to overcome the barrier (ΔG) with a frequency of ν. With a probability of p, they can uptake sufficient energy to overcome the barrier and lead to successful jumps. When the bias potential (E_ν) is applied to the SSE, the net velocity of the migrating ions (v_m, e.g., Li^+) along the direction of the electric field is:

$$\mathrm{v_m} = \left(\frac{\nu \mathrm{Zea_0^2 E_\nu}}{k_{\mathrm{B}}T}\right)\exp\left(-\frac{\Delta G}{k_{\mathrm{B}}T}\right) \tag{2}$$

where Z is a charge number of mobile ions, e is an elementary charge, and a_0 is the jump distance. Since drift mobility (μ) and ionic conductivity (σ_{ion}) are defined as $\mu = v_m/E_\nu$ and $\sigma_{ion} = cZe\mu$, respectively. σ_{ion} can be formulated as:

$$\sigma_{\mathrm{ion}} = \left(\frac{\Upsilon c \nu \mathrm{Z}^2\ \mathrm{e}^2\ \mathrm{a}_0^2}{k_{\mathrm{B}}T}\right)\exp\left(-\frac{\Delta G}{k_{\mathrm{B}}T}\right) \tag{3}$$

where c is a carrier density and γ is a geometric factor, which represents the dimensionality of the conduction pathways. The Gibbs free energy (ΔG) of ion migration needs to be

divided as the activation enthalpy (ΔH) and activation entropy (ΔS) ($\Delta G = \Delta H - T\Delta S$). Therefore, question (3) can be expressed as:

$$\sigma_{\mathrm{ion}} = \left(\frac{\Upsilon c v \mathrm{Z}^2\ \mathrm{e}^2\ \mathrm{a}_0^2}{k_{\mathrm{B}}T}\right) \exp\left(-\frac{\Delta \mathrm{S}}{k_{\mathrm{B}}}\right) \exp\left(-\frac{\Delta \mathrm{H}}{k_{\mathrm{B}}T}\right) \tag{4}$$

Since ionic conductivity is usually measured as temperature dependent, an Arrhenius relation gives an activation barrier and a temperature-independent pre-exponential factor σ_0 (or called A) as:

$$\sigma_{\mathrm{ion}}T = \sigma_0 \exp\left(-\frac{\Delta H}{\mathrm{k_B}T}\right) \tag{5}$$

The activation enthalpy (ΔH) is also called the activation energy: E_a. Through mathematic derivation, we can obtain

$$\ln \sigma_{\mathrm{ion}} = \ln\frac{\sigma_0}{T} - \frac{1}{\mathrm{k_B}T}Ea \tag{6}$$

Therefore, we can experimentally measure the T-dependent ionic conductivity (σ_{ion}), and plot the lnσ-1/T (or 'logσ-1/T') liner curve to obtain the $\boldsymbol{E}_a$ according to the slope, which is the major indicator to evaluate the ionic transport in ionic conductors.

2.1.2.2 General requirements for fast ionic conduction

According to the physical meaning of the activation enthalpy ΔH *or* E_a depends on the nature of defects. Intrinsic defects (vacancies and interstitials) are thermally activated. Therefore, the activation energy of ion transport processes that involve such defects is the sum of the defect formation energy and migration energy. Extrinsic defects are usually introduced by alien/domestic doping. In general, the concentration of extrinsic defects far exceeds that of thermally activated intrinsic defects. The activation energy under such conditions can usually be approximated as the migration energy if there is no trapping between the mobile ion and dopants or other defects. Therefore, there are generally some specific requirements for fast ion transport can be derived, which are listed below:

a. High dimensionality of the conduction pathways. Many materials possessing 3D diffusion Pathways exhibit high ionic conductivity.

b. A high carrier density. Increasing carrier density with aliovalent element substitution has been verified as an effective strategy to do so.

c. Low enthalpy and entropy of migration. Structural factors predominate changes of ΔH and ΔS, which is associated with the interaction among sublattices or/and paired anion-Li framework species, lattice polarizability, manner of migration, lattice strains, etc.

2.1.3 Sulfide SSEs

Sulfide SSEs have attracted tremendous attention because of their considerable ionic conductivities at RT, thus the development of sulfide SSEs have received significant progress in recent years.[15] In addition, compared with oxides and the halide SSEs, sulfides are softer and with lower grain boundary resistance. Therefore, excellent contact between sulfide SSEs and electrode materials can be easily realized by simple cold-pressing technology, making the fabrication of bulk solid-state batteries more convenient.[16] Due to these inherent advantages of sulfide SSEs, it is claimed in Toyota's technology roadmap that sulfide SSEs will be loaded on the prototype EVs in 2025. The representative LGPS-type $Li_{9.54}Si_{1.74}P_{1.44}S_{11.7}Cl_{0.3}$ SSE was discovered by Kanno *et al.* in 2016, and is still holding the record of Li^+ ionic conductivity among all existing SSEs for Li^+ conduction, reaching up to 2.5×10^{-2} S cm^{-1} at RT.[8] But early before 2016, various types of sulfide SSEs had already been well developed.[9, 17-20] In general, sulfide SSEs can be divided as the following categories according to the structure of electrolytes: Thio-LISICON, LGPS-tpye, Argyrodite-type, glass-type, and glass-ceramics.

The ultrahigh ionic conductivity of sulfide SSEs is viewed as one of the largest advantages (**Table 2.1**), while there are still several drawbacks for sulfide SSEs, for example, chemical instability, incompatibility with Li metal and high-voltage cathodes, as well as the high fabrication cost. Among which, the most serious problem is the chemical instability (poor air stability), which will be introduced in detail in one of the subsections below.

Table 2.1 Ionic conductivity of representative inorganic SSEs at 25 °C

Inorganic SSE category	Materials	Ionic conductivity at 25°C (S cm^{-1})	Ref.
Sulfide	$Li_{9.54}Si_{1.74}P_{1.44}S_{11.7}Cl_{0.3}$	2.5×10^{-2}	Nat. Energy 2016, 1 (4), 16030.
	$Li_{10}GeP_2S_{12}$	1.2×10^{-2}	Nat. Mater. 2011, 10 (9), 682-686.
	$Li_{6.6}Si_{0.6}Sb_{0.4}S_5I$	1.5×10^{-2}	J. Am. Chem. Soc. 2019, 141 (48), 19002-19013.
	$Li_{6.6}P_{0.4}Ge_{0.6}S_5I$	5.4×10^{-3}	J. Am. Chem. Soc. 2018, 140 (47), 16330-16339
	Li_6PS_5X (X = Cl, Br)	1.0×10^{-3}	Angew. Chem. Int. Ed. 2008, 47 (4), 755-758.
	$Li_{5.5}PS_{4.5}Cl_{1.5}$	9.4×10^{-3}	Angew. Chem. Int. Ed. 2019, 58 (26), 8681-8686
	Glass-ceramic $Li_7P_3S_{11}$	3.2×10^{-3}	Adv. Mater. 2005, 17 (7), 918-921.
Halide	Li_3YCl_6	5.1×10^{-4}	Adv. Mater. 2018, 30 (44), 1803075
	Li_3YBr_6	1.7×10^{-3}	Adv. Mater. 2018, 30 (44), 1803075
	Li_3InCl_6	2.0×10^{-3}	Angew. Chem. Int. Ed. 2019, 58 (46), 16427-16432
	Li_3ScCl_6	3.0×10^{-3}	J. Am. Chem. Soc. 2020, 142 (15), 7012-7022
	$Li_2Sc_{2/3}Cl_4$	1.5×10^{-3}	Energy Environ. Sci. 2020, 13 (7), 2056-2063
Oxide	$Li_{6.55}Ga_{0.15}La_3Zr_2O_{12}$	2.1×10^{-3}	Appl. Phys. Lett. 2018, 112, 113901
	$Li_{6.4}La_3Zr_{1.4}Ta_{0.6}O_{12}$	1.0×10^{-3}	J. Mater. Chem. 2012, 22, 15357–15361
	$Li_{1.3}Al_{0.3}Ti_{1.7}(PO_4)_3$	7.0×10^{-4}	J. Electrochem. Soc. 1990, 137, 1023-1027.
	$Li_{1.5}Al_{0.5}Ge_{1.5}(PO_4)_3$	2.4×10^{-4}	J. Electrochem. Soc. 1993 140 1827
	$Li_{3x}La_{2/3-x}TiO_3$	$\sim 10^{-3}$	Solid State Commun. 1993, 86, 10, 689-693

2.1.3.1 Thio-LISICON

The item 'thio-LISICON' is derived from the oxide lithium superionic conduction (LISICON). Thio-LISICONs can be regarded as the first-generation crystalline sulfide

SSEs and experienced booming development from 1990 to 2010, which was accompany with the exploration of oxide LISICONs. For example, $Li_{14}Zn(GeO_4)_4$ oxide LISICON belonging to the γ-Li_3PO_4. Replacing the oxygen (O) with sulfur (S) can notably increase the ionic conductivity a RT. The reason is related to the weakened interaction between mobile Li ions and anion sublattices that are constructed with large-size and highly polarizable S^{2-} species.[15] The thio-LISICON family contains a wide range of solid solutions with the general formula: $Li_xM_{1-y}N_yS_4$ (M = Si or Ge; N = P, Al, Zn, Ga, or Sb), exhibiting ion conductivities in the range of 10^{-7} ~ 10^{-3} S cm^{-1} at RT.[21] Among which, $Li_{4-x}Ge_{1-x}P_xS_4$ displays the most promising conductivity, and the thio-LISICON $Li_{3.75}Ge_{0.25}P_{0.75}S_4$ shows the highest of 2.2 × 10^{-3} S cm^{-1} at RT.[22] They are derivations of two parent LISICON phases: Li_3PS_4 and Li_4GeS_4, belonging to the Li_3PS_4-Li_4GeS_4 binary solid solutions[23] (see the phase diagram in **Figure 2.1**). It is worth mentioning that the success of discovering superionic LGPS ($Li_{10}GeP_2S_{12}$) SSEs is originated from the precise study of the Li_3PS_4-Li_4GeS_4 pseudo-binary system, which will be discussed in detail in the following 'LGPS-type' part.

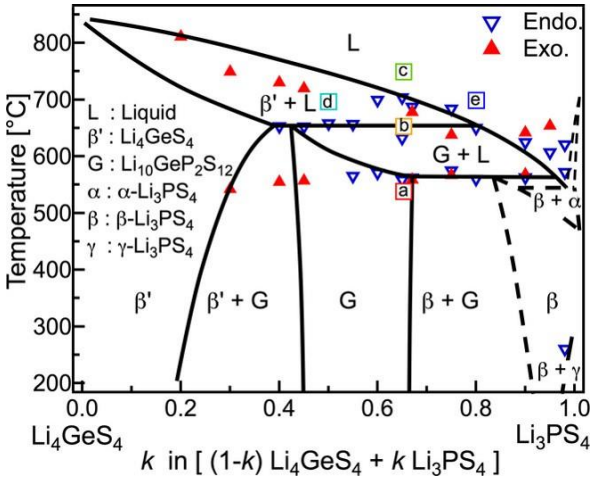

Figure 2.1 Phase diagram for the [(1−*k*) Li_4GeS_4 + *k* Li_3PS_4] system. Empty and solid triangles respectively indicate endo and exothermic reaction temperatures determined from DTA data. Phase boundaries indicated by dotted lines are assumed from experimental results but were not as evident as those shown by solid lines.[23]

Crystalline Li_3PS_4 is the one of the most conventional sulfide SSEs and is considered the archetype of the thio-LISICON. There are three different phases of crystalline Li_3PS_4: α,

β, and γ, showing a reversible phase transformation as a function of temperature. Within a heating process, the low-temperature γ-Li_3PS_4 transformed to the medium-temperature β-Li_3PS_4 at 573 K, which can continue changing to the high-temperature α- Li_3PS_4 at 746 K. Then, in a cooling process, the α-phase directly transformed to the γ-phase between 637 and 543 K without the appearance of the β-Li_3PS_4.[24] The γ-Li_3PS_4 is isostructural with β-Li_3PO_4 (space group: Pmn21) with an orthorhombic unit cell. The β-Li_3PS_4 also presents an orthorhombic cell but shows a different arrangement of PS_4 tetrahedra. The apices of the PS_4 tetrahedron are ordered in the same direction in the γ-phase, while in the β-Li_3PS_4, they are ordered in a zig-zag arrangement (**Figure 2.2a and b**).[24] The PS_4 tetrahedra is α-Li_3PS_4 is isolated with each other, and two layers of disorienting PS_4 are presented to show good arrangement (**Figure 2.2c**).[25] The difference of agreement leads to a higher degree of anion rotation in β-Li_3PS_4 than that in the γ-Li_3PS_4 and α-Li_3PS_4. Also, the zig-zag arrangement in β-Li_3PS_4 SSEs provide the Li with positions both in the octahedral and tetrahedral sites, and these ion partitions easily allow for interstitial migration of Li^+. Therefore, the ionic conductivity in the β-Li_3PS_4 was increased dramatically. Specifically, the γ-Li_3PS_4 SSE shows a RT ionic conductivity of 3.0×10^{-7} S cm^{-1} with an activation energy of 21.3 kJ mol^{-1}, while the β-phase shows an ionic conductivity of 3.0×10^{-2} S cm^{-1} at 500 K with a reduced activation energy of 15.5 kJ mol^{-1}.[24] Although β-Li_3PS_4 is regarded the highly conductive phase, the metastable feature hinders its direct application. Liang *et al*.[19] demonstrated the nanosized β-Li_3PS_4 with numerous nonporous prepared via wet-chemistry (solution) method can still maintain a high ionic conductivity 1.6×10^{-4} S cm^{-1} at RT, which is three orders higher than the β-Li_3PS_4 SSEs obtained by conventional co-melting of solids.

Figures 2.2d shows the crystal structure for Li_4GeS_4 as a basis for other thio-LISICON structures.[26] The material consists of hexagonally close-packed sulfide anions with Ge or P in tetrahedral sites. Li atoms occupies both octahedral and tetrahedral sites creating edge-sharing LiS_6 octahedra chains along the b-axis direction. These tetrahedral sites serve as one-dimensional (1D) conduction pathways for Li^+ transport. Theoretically, when comparing Li_4GeS_4 to Li_3PS_4, the substitution of Ge^{4+} for P^{5+} introduces Li^+ vacancies into the crystal structure, thus the ionic conductivity can increase accordingly. The Li_4GeS_4 phase (β') share the similar crystal with β-Li_3PS_4, and both of them are analogous with the

γ-Li_3PO_4.[26] The ionic conductivity of β'-Li_4GeS_4 at RT is 2.0×10^{-7} S cm^{-1}, which is similar to that of γ-Li_3PS_4, and fall behind β-Li_3PS_4 as we discussed above.

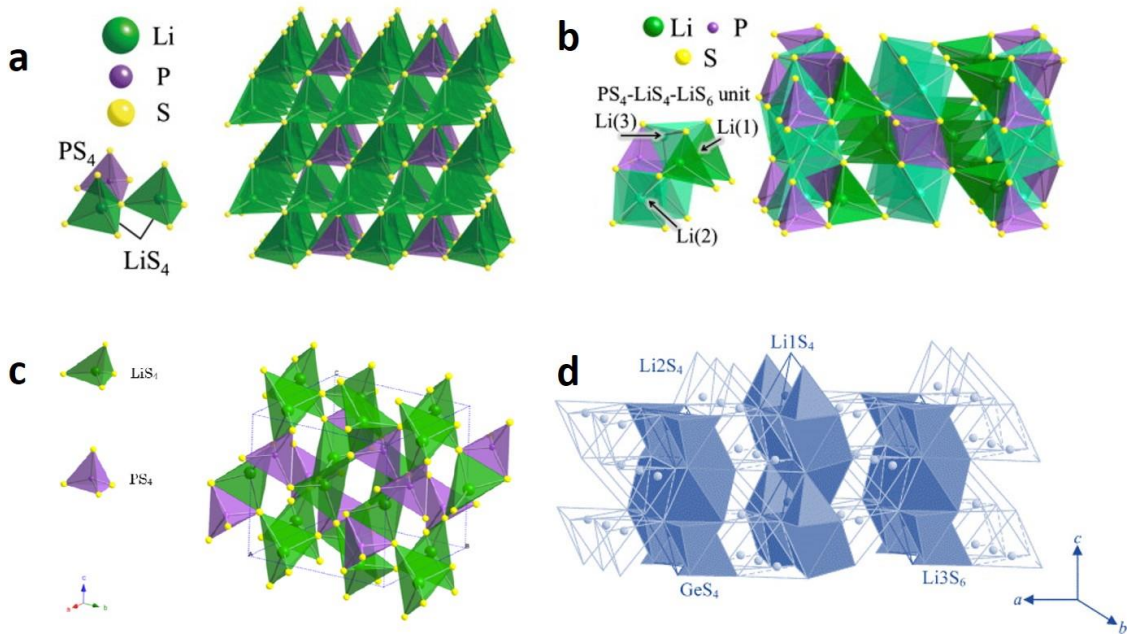

Figure 2.2 (a) Structure of γ-Li_3PS_4;[24] (b) Structure of β-Li_3PS_4;[24] (c) Structure of α-Li_3PS_4;[25] (d) Structure of Li_4GeS_4.[26]

2.1.3.2 LGPS-type

LGPS is short for the chemical formula of a superionic conductor: $Li_{10}GeP_2S_{12}$ that was discovered by Kanno *et al.* in 2011.[9] The RT ionic conductivity of LGPS was reported as 1.2×10^{-2} S cm^{-1}, which was the highest among all the reported inorganic/polymer SSEs at that time. The discovery of LGPS placed the sulfide SSEs in the research boom because it demonstrated for the first time the RT ionic conductivity of Li^+ SSEs can surpass 10^{-2} S cm^{-1} and be comparable with LEs.

As indicated in the 'thio-LISICON' section, the LGPS in a sense is the product of studying the Li_3PS_4-Li_4GeS_4 pseudo-binary system. As shown in the phase diagram (**Figure 2.1**) by Hori *et al.*,[23] β'-Li_4GeS_4 and β-Li_3PS_4 exist as the main crystal phases with the similar crystal structure of γ-Li_3PO_4. The G phase is crystallized as a single phase, and the $Li_{10}GeP_2S_{12}$ composition is the end member in the solid solutions formed in the Li_3PS_4

composition range of 45 ~ 67 mol%. G phase is stable up to around 600 ° C. Specifically, the stabilized temperature presents slightly increase with more amounts of Li_4GeS_4 composition. In a certain composition range, there is a two-phase mixture of G and the liquid phase between 600 and 650 ° C. Above 650 ° C, a two-phase region of β' and the liquid phase exists. Further increasing the temperature results in complete melting. As shown in **Figure 2.3a and b**, LGPS shows a tetragonal unit cell with a space group of $P4_2/nmc$ (group 137). The 3D framework structure is composed of $(Ge_{0.5}P_{0.5})S_4$ tetrahedra, PS_4 tetrahedra, LiS_4 tetrahedra and LiS_6 octahedra. $(Ge_{0.5}P_{0.5})S_4$ tetrahedra and LiS_6 octahedra share a common edge and form a 1D chain along the c axis. These 1D chains are connected to one another through PS_4 tetrahedra, which are connected to LiS_6 octahedra by a common corner. LiS_4 tetrahedra in the 16h and 8f sites share a common edge and form a 1D tetrahedron chain. These chains are connected by common corners of the LiS_4 tetrahedra. Li ions are distributed over 4 crystallographic sites (4c, 4d, 8f, and 16h). There are distinct tunnels hosting Li1 and Li3 along the (0 0 1) direction (c-axis) and it was believed that LGPS is a 1D-pathway superionic conductor. However, later studies (viable-temperature NPD, NMR, and atomistic molecular dynamics simulations) about the Li^+ transport dynamic in the LGPS structure suggested that the Li-ion conduction pathway in the ab-plane and the contribution of Li3-Li2 jumps to the overall conductivity are considerable.[27-29]

Inspired by the LGPS, a lot of crystalline sulfide SSEs were discovered with the similar crystal structure of LGPS, delivering high ionic conductivity at RT. Considering the high cost of Ge, substitutions of Ge^{4+} with Si^{4+}, Sn^{4+}, as well as Al^{3+} were all reported that can be synthesized via ball milling or co-melting method.[30-32] However, their ionic conductivities could not overtake that of the parent LGPS SSEs until Kanno et al. reported halogen doping LGPS: $Li_{9.54}Si_{1.74}P_{1.44}S_{11.7}Cl_{0.3}$ in 2016.[8] A remarkable RT ionic conductivity of 2.5×10^{-2} S cm^{-1} was achieved, which is still the highest value among all existing Li^+ superionic conductor. As displayed in **Figure 2.3c and d**, the anisotropic thermal displacement of lithium and nuclear density distribution indicate the 3D conduction pathways (1D along the c axis and 2D in the ab plane). The Cl-doped LGPS SSE is the first experimental example of widely distributed 3D conduction pathways in the

LGPS structure (only at 25 ^{o}C). This is also believed as the main reason to the further improved ionic conductivity resulting from the small amount of chlorine mainly located in the unique Cl(1)(8g) sites within the P(2b)X_4 tetrahedra.

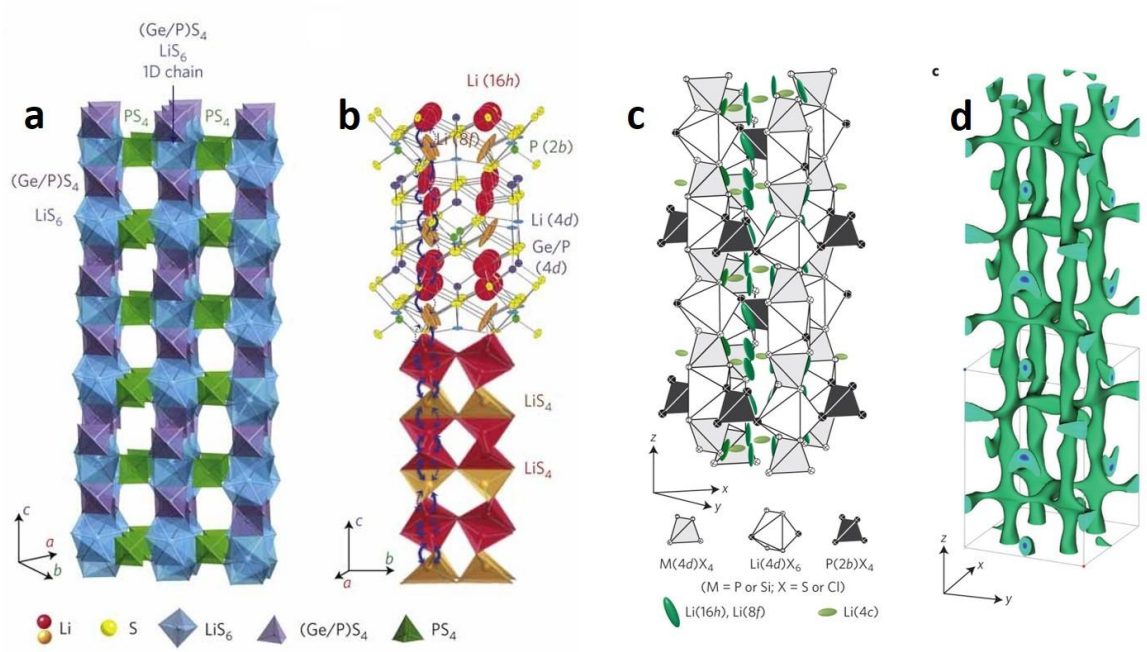

Figure 2.3 (a) Framework structure of $Li_{10}GeP_2S_{12}$;[9] (b) Conduction pathways of Li^+ ions in the $Li_{10}GeP_2S_{12}$;[9] (c) Crystal structure of $Li_{9.54}Si_{1.74}P_{1.44}S_{11.7}Cl_{0.3}$;[8] (d) Nuclear distributions of Li atoms in $Li_{9.54}Si_{1.74}P_{1.44}S_{11.7}Cl_{0.3}$ at 25 °C, calculated using the maximum entropy method at the iso-surface level of −0.06 fm $Å^{-3}$.[8]

2.1.3.3 Argyrodite-type

Argyrodite represents a cubic structure of one class of ion conductor, which was originally found in the mineral Ag_8GeS_6. The Li argyrodites are Li^+ superionic conductors, and they are generally in an ionic formula of $Li^{+}_{12-m-x}(M^{m+}Ch^{2-}_4)N^{2-}_{2-x}X^{-}_x$ (M = P, As, Ge, Si, Sn, Sb; Ch = O, S, Se; X = Cl, Br, I, BH_4, or absent). This kind of sulfide SSE has become popular since the Li_6PS_5X (X = Cl, Br, I) was discovered in 2010, when the Li_6PS_5X (X = Cl, Br) showed high RT ionic conductivity over 1×10^{-3} S cm^{-1}.[18] Very recently, several newly developed Li argyrodites (i.e., $Li_{5.5}PS_{4.5}Cl_{1.5}$,[33] $Li_{6.6}P_{0.4}Ge_{0.6}S_5I$,[34] and $Li_{6.6}Si_{0.6}Sb_{0.4}S_5I$[35]) can perform ionic conductivities close to 10^{-2} S cm^{-1} at RT, which represent the latest breakthroughs for the field of sulfide SSEs. Considering the capability

of achieving high ionic conductivity without involving expensive elements (e.g., Ge), as well as the applicability of synthesis/fabrication routes that are potentially available for commercially potential, the Li argyrodites seem to be the class that is mostly used for sulfide-based ASSLBs.[36]

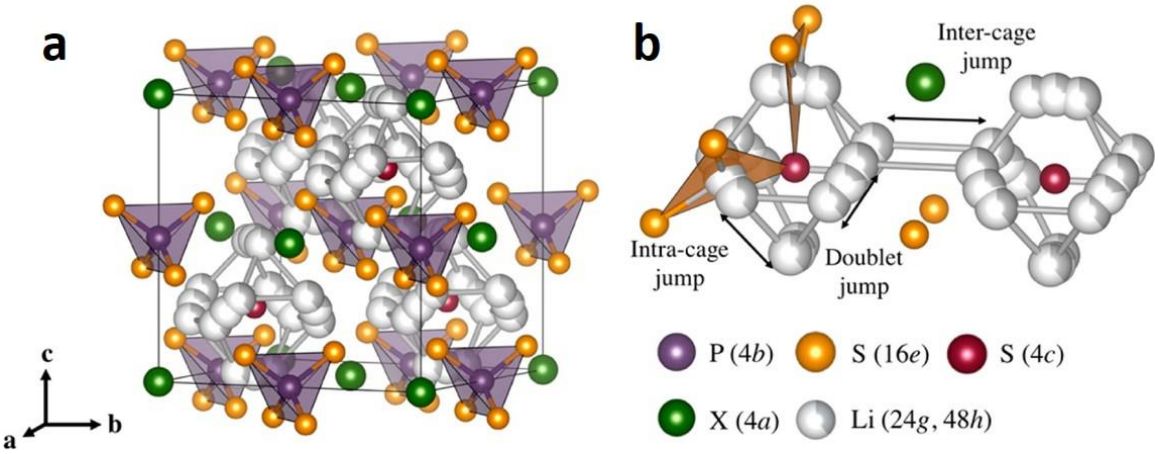

Figure 2.4 (a) Crystal structures of Li_6PS_5X with X = Cl, Br, I;[37] (b) The free S^{2-} anions and the corner of the PS_4^3 tetrahedra derived from Frank–Kasper polyhedral, where shows three Li+ conduction pathways.[37]

Taking the classical Li argyrodite Li_6PS_5X (X = Cl, Br, I) as an example, the crystal structure is suggested in **Figure 2.4a**,[37] which is more straightforward compared with the LGPS structure. Argyrodite Li_6PS_5X has a cubic unit cell (space group: F43m) with a face centered framework constructed by the X^- (Wyckoff position 4a), PS_4^{3-} tetrahedra (P is on Wyckoff 4b), as well as free S^{2-} anions (Wyckoff 4c). PS_4^{3-} tetrahedra occupy the octahedral voids, while half of the tetrahedral voids are filled by X^- anions to form the face centered cubic lattice, and free S^{2-} anions are in the second half of the tetrahedral voids. There is site disorder of X^-/S^{2-} over the 4a and 4c sites, which has been verified to play an essential role to determine the ionic conductivity of the Li argyrodites. The similar ionic radius between I^- and S^{2-} leads to a small side disorder of I^-/S^{2-}, in the structure of Li_6PS_5I, causing the RT ionic conductivity drops to 10^{-6} S cm^{-1} level, which is almost three orders lower compared with the Li_6PS_5X (X = Cl, Br). For the lattice site of Li in these three typical argyrodites, Li^+ ions are distributed over the tetrahedral interstices, and the partially occupied Li positions (24g and 48h) form a cage around the free S^{2-}. Within this cage-like

Li sublattice, isotropic 3D ionic conduction pathways exist consisting of three possible Li^+ jumps as shown in **Figure 2.4b**: (1) the doublet (48h–24g–48h), (2) the intra-cage (48h–48h), and (3) the inter-cage jumps (also 48h–48h).[37] It is obvious that the inter-cage jumps require the longest Li^+ motion pathway and is viewed as the rate-determining step in the Li^+ transport process.

2.1.3.4 Glass-type

Apart from the crystalline sulfide SSEs are well developed, the glass-type (amorphous) sulfide SSEs also have received a lot of attention starting since 1980s.[38-39] Glass sulfides can be obtained in the systems of quasi-binary Li_2S-M_aCh_b, quasi-ternary Li_2S-M_aCh_b-N_cCh_d, and halogen-containing quasi-ternary Li_2S-M_aCh_b-LiX (M, N = P, Ge, Si, B, Al; Ch = O, S, Se; X = Cl, Br, I). In the early years, liquid N_2 quenching is necessary to prepare the glass-state according to the classical glass formation theory, namely the ultrafast cooling can prevent the nucleation from growing crystals. In the recent years, as the development of mechanochemistry, ball milling becomes one of the most common methods to synthesize glass-type sulfide SSEs.[40-41]

The ionic conductivity of glass sulfide SSEs is relatively easy to be tuned by addition of more Li-containing raw materials (increasing the Li^+ concentration), change of the S-M coordination, as well as the incorporation of LiX. The x Li_2S·(100-x) P_2S_5 (x is the mole percentage) system is the mostly maturely developed. RT ionic conductivity increases with the addition of Li_2S raw materials, reaching 2.8×10^{-4} S cm^{-1} when x = 75.[42] Glass with low Li_2S content ($x \leqslant 60$) suggests more di-tetrahedral $P_2S_7^{4-}$ units, which has one bridging S atom and three terminal S atoms in each unit. While glass with more Li_2S ($x \geqslant 70$) has more tetrahedral PS_4^{3-} building blocks, where all the S atoms are terminal.[43] Oxide species with high glass formation ability, such as Li_3MO_3 (M = B, Al, Ga, In)[44] can be incorporated into the Li_2S·SiS_2 glass to increase the RT ionic conductivity over 10^{-3} S cm, which is ascribed to the expanded free volume (benefiting the Li^+ transport) caused by introduced terminal O atoms.[44] Halide-containing LiX (X = Cl, Br, I, mostly are LiI) were also reported to be added to improve the ionic conductivity over 10^{-3} S cm^{-1}, because halogen with large ionic radius can weaken the interaction between the anions and Li^+, thus

reducing the barrier of Li-ion motion.[45-46] However, the detailed mechanism of Li^+ transport in the glassy sulfides are still challenging to study experimentally, because the mode of amorphous materials is difficult to build, which are extremely time and cost consuming if using the modern computational methods (e.g., *Ab initio* molecular dynamics simulations).[1, 47]

Compared with the crystalline sulfide SSEs, glass sulfides show negligible grain boundary, which would be beneficial to prevent the Li dendrites penetrating through the entire electrolyte, because the grain boundary is widely recognized as the nucleation site for growing harmful Li dendrites. In addition, the incorporated Li halides (e.g., LiI) play an important role to construct favorable Li metal interface to benefit the Li plating and stripping, which will be discussed in detail in the 'interface' section.

2.1.3.5 Glass-ceramics

Glass-ceramic sulfide SSEs are one kind of popular superionic conductors mainly developed by Tatsumisago's group based on the glassy precursors. Through post-annealing the glass precursors at around their glass transition (T_g) or crystallization (T_c) temperatures, the partially crystallized sulfide SSEs can be obtained, so called 'glass-ceramics'. Two famous examples of glass-ceramic sulfides are glass-ceramic (gc) Li_3PS_4 [48]and gc $Li_7P_3S_{11}$,[17, 20] which are corresponding to the precipitated products from glassy $75Li_2S{\cdot}25P_2S_5$ and $70Li_2S{\cdot}30P_2S_5$ at ~230 ^oC and ~270 ^oC, respectively. The glassy (amorphous) content in gc sulfides can serve as the stabilizer to restrict the metastable (high-temperature phase) crystalline parts (i.e., β-phase Li_3PS_4 and $Li_7P_3S_{11}$). In this way, significantly improved ionic conductivities are obtained in the gc Li_3PS_4 (~2.0×10^{-4} S cm^{-1}) and gc $Li_7P_3S_{11}$ (3.2×10^{-3} S cm^{-1}) sulfides compared with the glass Li_3PS_4 (~1.0×10^{-4} S cm^{-1}) and glass $Li_7P_3S_{11}$ (5.4×10^{-5} S cm^{-1}) SSEs.[15]

One side effect of participating metastable superionic $Li_7P_3S_{11}$ from the glassy precursor is the introduced grain boundary can bring the increase of interface resistance. Tatsumisago *et al.* [20] referred to the sintering method that was developed to eliminate the grain boundary inside oxide SSEs to improve the ionic conduction at grain boundaries of sulfides. After sintering the gc $Li_7P_3S_{11}$ pellet at the temperature of 280 ^oC, the pellet was densified as

bulk without grain boundary resistance (**Figure 2.5**). The RT ionic conductivity of the heat-treated gc $Li_7P_3S_{11}$ got to 1.7 × 10^{-2} S cm^{-1}, which was the highest value before the discovery of $Li_{9.54}Si_{1.74}P_{1.44}S_{11.7}Cl_{0.3}$.

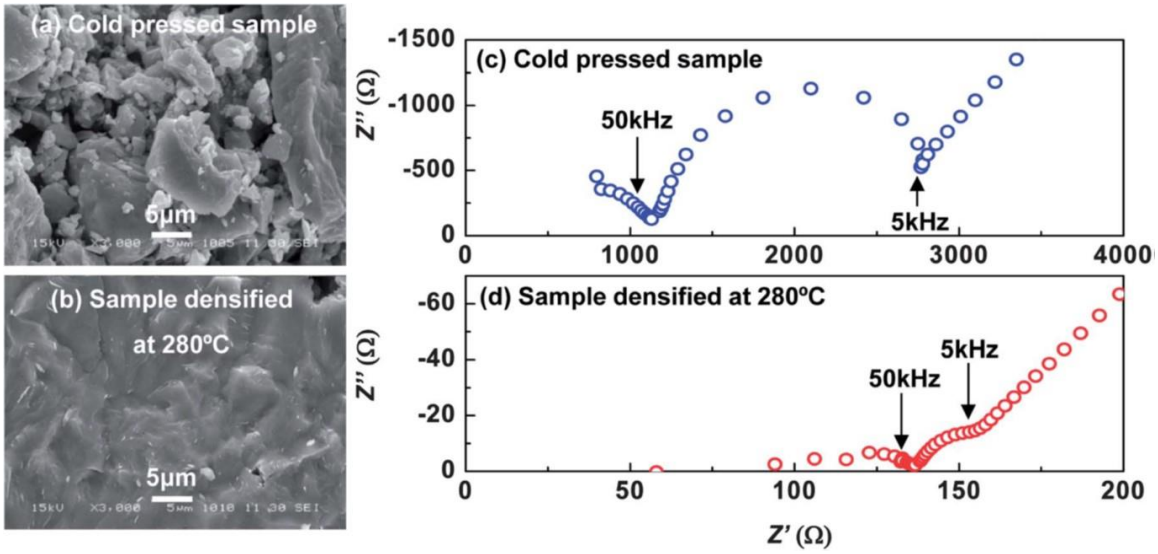

Figure 2.5 SEM images of the glass-ceramic $70Li_2S{\cdot}30P_2S_5$ from a cold-pressed sample (a) and the heat-treated sample at 280 °C (b);[20] Corresponding impedance plots at -35 °C for the glass-ceramic $70Li_2S{\cdot}30P_2S_5$ after cold pressing (c) and heat treatment at 280 °C (d).[20]

2.1.3.6 Air stability of sulfides

One of the biggest issues of using sulfide SSEs for the commercialized ASSLBs is their poor air stability.[15, 49] This is originated from the weak bonding of common S-M coordination (M = P, Ge, Si, B, etc.) in sulfide SSEs. When sulfide SSEs built by these instable S-M units are exposed in the air or even dry-room environment with ~5% humidity, the S-M can be attacked by the O from H_2O and O_2. As a result, the toxic H_2S would generate from the degradation of the structure, thus leading to a sharp decrease in the ionic conductivity.[50] Therefore, sulfide SSEs must be handled in the inert-filled box (e.g., the Ar-filled glovebox) or vacuumed (e.g., the sealed quartz tube) atmosphere. Undisputedly, the requirement for high-standard equipment and cost for applications will increase. Therefore, it is critical to develop facile solutions to increase the air stability or reduce the generation of harmful H_2S.

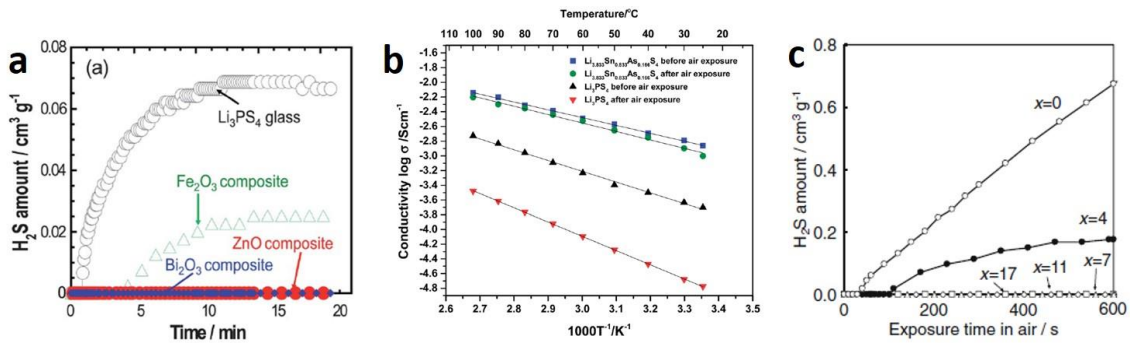

Figure 2.6 Three strategies to improve the air stability of sulfide SSEs: (a) Incorporation of oxide materials. The generation of H_2S is suppressed by adding transition metal oxides;[51] (b) Using HSAB theory to design the stable S-M coordination. Arrhenius plots for $Li_{3.833}Sn_{0.833}As_{0.166}S_4$ and β-Li_3PS_4 before and after air exposure;[54] (c) Incorporation of O, e.g., changing the raw materials from Li_2S to Li_2O in $xLi_2O\cdot(75\text{-}x)Li_2S\cdot 25P_2S_5$ ($x = 0$, 4, 7, 11, and 17).[55]

Generally, there are three kinds of strategies (**Figure 2.6**). First, the most straightforward idea is incorporating H_2S absorbent to the sulfide SSEs with a physical mixing method. Metal oxides, such as Fe_2O_3, ZnO, and Bi_2O_3 can be served as the absorbent and firstly be introduced to the $75Li_2S\cdot 25P_2S_5$ glass, showing good performance to absorb the H_2S gas.[51] However, addition of these alien absorbents sacrifice the ionic conductivity overall. And this method cannot solve the issue of H_2S generation fundamentally. Second, using the element substitution for the problematic coordinating elements (e.g., P). Li-Sn-S sulfide SSEs (e.g., Li_4SnS_4 [52] and Li_2SnS_3 [53]) is the only reported sulfide system that is stable against the air, because based on the hard and soft acids and bases (HSAB) theory, the Sn (soft acid) prefers to bond with S (soft base) rather than interact with O (hard base).[54] However, the limited RT ionic conductivity (10^{-5} S cm^{-1} level) hinders their applications. Liang *et al.* [54] reported Arsenic (As) -substituted Li_4SnS_4 SSEs can increase the RT ionic conductivity to 1.39×10^{-3} S cm^{-1} and show good resistance to air exposure, but the hyper toxic As-based compounds prevent their commercialization. The third method is the extend for the second one, that is partial replacement of lattice S with O. Using Li_2O and P_2O_5 as the partial raw materials instead of complexly using Li_2S and P_2S_5 was reported can enhance the resistance of oxidation, but this solution is still at the cost of decreased ionic conductivity. For example, the ionic conductivities of the x $Li_2O\cdot$ (75-x) $Li_2S\cdot$ 25 P_2S_5

glasses decrease monotonously with increased Li_2O content,[55] and the similar trend can be seen in the 75 Li_2S· (25-x) P_2S_5· x P_2O_5 glass system.[56] Overall, it is still very challenging to have an all-rounded strategy that can solve the air-sensitive problem of sulfide SSEs without losing the ionic conductivity either other advantages (e.g., environmentally friendly and low cost).

2.1.4 Halide SSEs

Halides, one type of a reviving SSE, are attracting increasing attention due to the requirement of developing highly stable SSEs that can operate against high-voltage cathode materials or/and Li metal anode.[57-58] The coordination in Li^+ conductive halide SSEs can be constructed with halogen X (X = F, Cl, Br, and I) as the center atom, and transition metal elements, rare earth elements, or even chalcogen (O, S, Se) as the ligating atoms. Therefore, the abundant choice of elements makes the family of halide SSEs intricate in the classification. From the point view of physicochemical property, halide SSEs are placed roughly between sulfide and oxide SSEs (**Figure 2.7**).[58] For example, the ionic conductivity of halides has be developed onto 10^{-3} S cm^{-1} level in recent two years, which is superior to oxide SSEs because of the less grain boundary, but still falls far behind the softer sulfide SSEs. (**Table 2.1**) The halide SSEs are always deliquescent, so their chemical stabilities (e.g., air stability) cannot compare with oxide SSEs. However, the water absorption of halides have not resulted in the spontaneous generation of corrosive HX acids.[59] This situation is better than sulfides whose degradation can cause the release of hyper toxic H_2S.

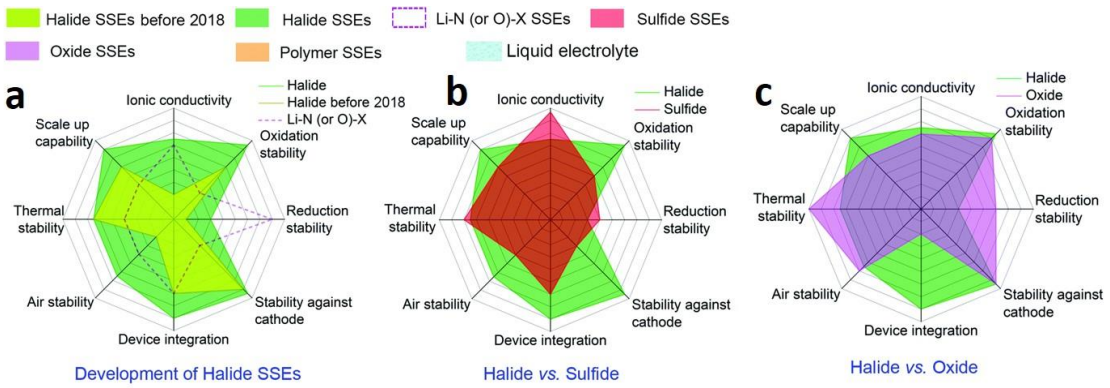

Figure 2.7 Radar plots of the various properties of different types of SSEs.[58] (a) Properties of halide SSEs, including new developed halide, non-metal halides, and previously reported halides; (b) comparison between halides and sulfides; (c) comparison between halides and sulfides.

In the section of 'halide SSEs', the revival process of halides will be first introduced, which indicates the essential requirement for developing halide SSEs as well as for the practical ASSLBs. The main research progress of Li-M-Cl (M: metal elements) will be overviewed subsequently. The reason of focusing on the Li-M-Cl is from the comprehensive consideration of ionic conductivity and electrode compatibility: decent RT ionic conductivity (10^{-3} S cm^{-1} level) and good high-voltage stability.

2.1.4.1 Revival of halide SSEs

In the 1930s, simplest Li halides, LiX (X = F, Cl, Br, I) were found to be Li^+ conductive. Among which, LiI shows the highest RT ionic conductivity of 10^{-7} S cm^{-1}, whose applications were demonstrated in the film-type primary ASSLBs, such as Li/LiI/AgI in the 1970s.[60-62] Li-Al-Cl halides ($LiAlCl_4$ and molten LiCl-$AlCl_3$) were the earliest developed Li-M-Cl halides. $LiAlCl_4$ was reported to exhibit a RT ionic conductivity of 10^{-6} S cm^{-1} in 1976,[63] and applied to a thin-film Li_xTiS_2/$LiAlCl_4$/$Li_{1-x}CoO_2$ ASSLB in 1992.[64] In the 1980s and 1990s, there was a blowout-type development toward Li-M-X halides. The divalent/trivalent metal elements in groups 3, 13 and La-Lu were reported, but most of them showed low ionic conductivity from 10^{-7} to 10^{-6} at RT.[58] High-temperature-phase (HT) Li_3InBr_6 possessed high ionic conductivity of 10^{-3} S cm^{-1} at RT, but the metastable structure could collapse and led to the fast drop of ionic conductivity when used practically.[65] In the same period, oxides and sulfides were frequently reported as superionic conductors, which could show an obviously advantage in the RT ionic conductivity (10^{-5} ~ 10^{-3}). Therefore, the development of halides were laggard till to 2018, when Tetsuya Asano *et al.* from the Panasonic Company reported superionic Li_3YCl_6 and Li_3YBr_6.[10] These two SSEs can display high ionic conductivity of 0.03 ~ 1.7 × 10^{-3} S cm^{-1} at RT. Importantly, their wide electrochemical windows enable ASSLBs to operate with coating-free cathode materials. In the next two years (2018 ~ 2020), several new halides were discovered. Our group developed Li_3InCl_6 with both solid-state and water-mediated

methods, showing RT ionic conductivity of 0.84 ~ 2.04 × 10^{-3} S cm^{-1}.[66-67] Li-Sc-Cl system was also discovered with high ionic conductivity (up to 3.0 × 10^{-3} S cm^{-1}) by our group and Nazar's group almost at the same time.[12, 68] $Li_{3-x}M_{1-x}Zr_xCl_6$ (M = Y, Er)[69-70] and Li-Er-X (X = Cl, I)[70] with ionic conductivity of 10^{-4} ~ 10^{-3} S cm^{-1} were developed as well. In addition, fundamental studies (e.g., factors that can determine ionic conductivity, theoretical/experimental air stability of halides) were frequently reported toward the halide SSEs.[57, 59, 71] Overall, more and more researches are focusing on the new Li-M-Cl halides, which show high ionic conductivity over 10^{-3} S cm^{-1} at RT and potential to be used for fabricating coating-free cathode composites for practical ASSLBs. However, the insufficient ionic conductivity (compared with the well-developed sulfide SSEs) is still one of the main weaknesses of halide SSEs.

2.1.4.2 Li-M-Cl

As indicated above, the revival of Li-M-Cl started from the discovery of high ionic conductivity in Li_3YCl_6 and Li_3YBr_6 by Tetsuya Asano *et al.* in 2018.[10] Ball milling and subsequent annealing procedures were used to prepare the electrolytes with good crystallinity. For Li_3YBr_6, the annealing process benefits to increase the RT ionic conductivity from 0.72 to 1.7 × 10^{-3} S cm^{-1}, while the annealing treatment reduce the ionic conductivity of Li_3YCl_6 SSEs from 0.51 to 0.03 × 10^{-3} S cm^{-1} (**Figure 2.8a**). The Li_3YCl_6 and Li_3YBr_6 SSEs possess a trigonal (space group of P-3m1) with structure with an hcp anion sublattice and a monoclinic structure (space group of C2/m) with a ccp anion sublattice, respectively, as shown in **Figure 2.8b** and **c**. These two SSEs can combine with coating-free LCO cathode materials to serve as the cathode composites to enable ASSLBs. The initial Coulombic efficiency of the Li_3YCl_6-cell and Li_3YBr_6-cell was as high as 94.8 % and 94.2 %, respectively, compared to that of 84 % using Li_3PS_4 sulfides as the SSE (**Figure 2.8d**). Furthermore, the interfacial resistance between the SSE and LCO after the first charging was 6.6 ~ 16.8 Ω cm^{-2} when using Li_3YCl_6 and Li_3YBr_6 as SSEs compared to that of 128.4 Ω cm^{-2} in the Li_3PS_4 case (**Figure 2.8e**). The excellent (electro)chemical stability of Li_3YCl_6/Li_3YBr_6 toward LCO cathode materials endow the ASSLBs with good cycling and rate performance. It is worth noting that this work was the first demonstrating

good ASSLBs performance can be obtained without any interface modification (e.g., cathode coating).

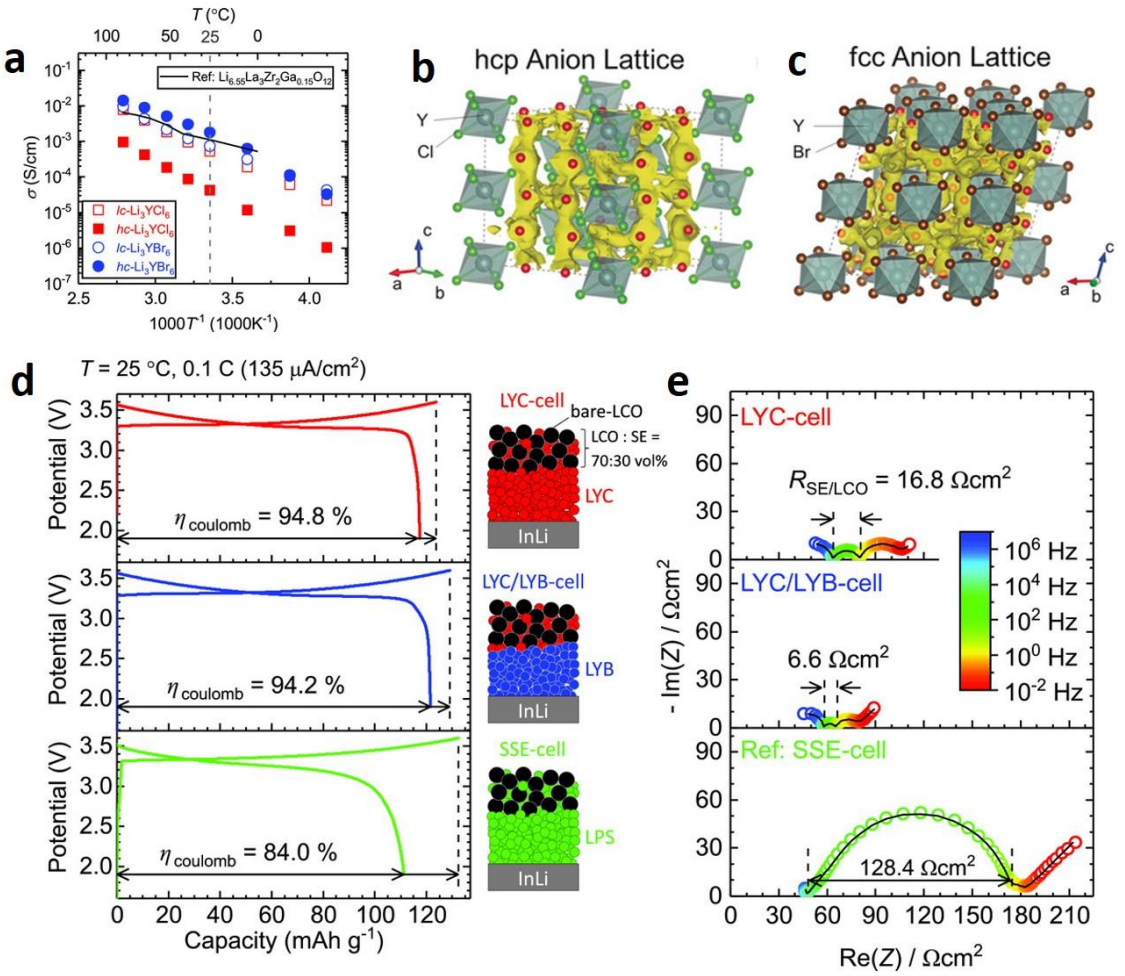

Figure 2.8 (a) Arrhenius plots of Li_3YCl_6 and Li_3YBr_6, with and without heating treatments;[10] (b) Crystal structure of Li_3YCl_6;[58] (c) Crystal structure of Li_3YBr_6;[58] (d) Initial charge/discharge curves of bulk-type ASSB cells at 25 °C at 0.1 C;[10] (e) Nyquist plots of the EIS spectra of ASSLBs after the first charging cycle.[10]

Our group developed Li_3InCl_6 SSEs through ball-milling and followed by further annealing at relatively low temperature of 260 °C.[67] Like the feature presented in preparing highly ion conductive Li_3YBr_3, Li_3InCl_6 obtained by post heating exhibited higher RT ionic conductivity (1.49×10^{-3} S cm^{-1}) compared with the ball-milled Li_3InCl_6 (0.84×10^{-3} S cm^{-1}). Importantly, we found the Li_3InCl_6 SSEs can also be synthesized through a H_2O-

mediated solution method.[66] Simply dissolving LiCl and $InCl_3$ raw materials into H_2O can obtain a white $Li_3InCl_6 \cdot 2H_2O$ intermediate complex precursor. Followed by heating at 200 °C in vacuum, the precursor can completely convert to crystalline Li_3InCl_6. Although the prepared via H_2O-mediated method displays a similar monoclinic unit cell, slightly higher ionic conductivity (2.04×10^{-3} S cm^{-1}) was reported compared to the Li_3InCl_6 fabricated by solid reactions (1.49×10^{-3} S cm^{-1}), which is believed to be related to the different atomic occupation with different synthesis routes. Another successful Li-M-Cl system is the Li-Sc-Cl, which was reported by our group and Nazar's group in 2020.[12, 68] Our group discovered a series of Li_xScCl_{3+x} SSEs (x = 2.5, 3, 3.5, and 4) based on the cubic close-packed (CCP) anion sublattice with high RT ionic conductivities up to 3×10^{-3} S cm^{-1} (Li_3ScCl_6). With increasing x value, the concentration of Li^+ and vacancy, as well as the blocking effect from Sc^{3+} can be tuned, which are verified to determine the barrier for Li^+ migration. Nazar's group reported the first spinel-type superionic halide: $Li_2Sc_{2/3}Cl_4$, which exhibits an ionic conductivity of 1.5×10^{-3} S cm^{-1}. They used powder neutron diffraction to reveal a significantly disordered Li^+ ion distribution over available tetrahedral and octahedral sites within the lattice, thus forming an infinitely 3D connected Li^+ ion diffusion pathway comprised of face-sharing $LiCl_6$ octahedra and $LiCl_4$ tetrahedra. Both Li_3ScCl_6 and $Li_2Sc_{2/3}Cl_4$ were reported to be stable with coating-free cathode materials (e.g., LCO, $LiNi_{0.6}Mn_{0.2}Co_{0.2}O_2$, and high-Ni $LiNi_{0.85}Mn_{0.1}Co_{0.05}O_2$).

2.1.5 Oxide SSEs

Oxide SSEs is one important category, but is not the focus in the thesis. In general, oxides SSEs are ceramic materials that prepared by high-temperature (> 700 ºC) calcination in the air, and show ion conductivity up to 10^{-3} S cm^{-1} level. There are mainly three types of oxide SSEs with high crystallinity: NASICON like, Perovskite type, and Garnet type.[16] As shown in **Table 2.2**, the advantages of oxide SSEs are their high (electro)chemical stability, high mechanical strength, and high anodic stability. Meanwhile, the disadvantages are the high-grain-boundary resistance resulted from the high crystallinity, non-flexible, and expensive large-scale productions where (ultra)high-temperature sintering is always required.

Table 2.2 General comparison among three main kinds of inorganic SSEs

Type of SSEs	Advantages	Disadvantages	Representatives
Sulfide	Ultrahigh ionic conductivity (10^{-2} S cm^{-1}); Good physical contact; Low grain boundary resistance.	Moisture sensitivity; Narrow electrochemical window; Incompatibility with anode/cathode.	LGPS; Li Argyrodites; Glass; Glass-ceramics.
Halide (Li-M-Cl)	Multiple synthesis route; Excellent cathode compatibility; Middle mechanical property.	Highly reactive with Li metal; Moisture sensitivity; High hardness.	Li-In-Cl; Li-Y-Cl; Li-Sc-Cl.
Oxide	High chemical and electrochemical stability; High mechanical property; High oxidation potential.	Significant grain boundary resistance; High-temperature processing; Non-flexibility.	NASICON; Perovskite; Garnet.

NASICON (Na Super Ion CONductors) type electrolytes with the general formula $Na_{1+x}Zr_2Si_{2-x}P_xO_{12}$ ($0 \leq x \leq 3$) were first reported in 1976 by Goodenough and Hong.[72-73] They are derived from $NaZr_2(PO_4)_3$ by partial substitution of Si for P with excess Na to balance the negative charge. Their Li analogues are presented as $LiM_2(PO_4)_3$ (M = Zr, Ti, Hf, Ge, or Sn). $LiTi_2(PO_4)_3$ is one of the mostly studied cases, offering the most suitable lattice size for Li ion conduction.[74] However, $LiTi_2(PO_4)_3$ pellets obtained by a conventional sintering process showed very high porosity (34%), resulting a low ionic conductivity at RT is 2×10^{-7} S cm^{-1}. The partial substitution of Ti^{4+} by trivalent cations (e.e., Al^{3+}, Sc^{3+}, Ga^{3+}, Fe^{3+}, In^{3+}, and Cr^{3+}) in $Li_{1+x}R_xTi_{2-x}(PO_4)_3$ materials can improve the ion conductivity. In particular, a high RT ionic of 7×10^{-4} S cm^{-1} was reported in the varietal composition of $Li_{1.3}Al_{0.3}Ti_{l.7}(PO_4)_3$ (LATP).[75] Similar effects caused by trivalent cation doping at M sites are also observed in the $LiGe_2(PO_4)_3$ phase, and a high ionic conductivity of 2.4×10^{-4} S cm^{-1} can be achieved in well-known $Li_{1+x}Al_xGe_{2-x}(PO_4)_3$ (LAGP).[76] LAGP system has also been widely investigated because of its relatively wide electrochemical stability window. Therefore, they are considered as one kind of suitable SSEs for high-voltage cathode materials in ASSLBs.

Perovskite-type oxide SSEs refer to the electrolytes with the formula of $Li_{3x}La_{2/3-x1/3-2x}TiO_3$ (LLTO, $0.04 \leq x \leq 0.17$) and their variants, which can show high RT ion conductivities of

~ 10^{-3} S cm^{-1}.[77] LLTO has a perovskite (ABO_3) structure as reported elsewhere, with the A-sites partially occupied by Li or La. The A-site cations are not randomly distributed but are ordered to form alternately stacked La-rich and La-poor layers along the c axis. The Li-ion conducting behavior in the grain interior is highly dependent on the crystal structure, composition (e.g., A-site vacancy concentration, the degree of A site cation ordering, and dopants) and structural distortions.[78-79] Although this material created much interest among researchers, it has been deemed unsuitable against Li metal because of the reduction of Ti^{4+} upon contacting each other.[80]

Garnet-type materials share the general formula of $A_3B_2M_3O_{12}$, in which the A and B cations have eightfold and six-fold coordination, respectively. Since it was first discovered in 1969 ($Li_3M_2Ln_3O_{12}$ (M = W or Te).[81] Within the garnet family, cubic $Li_7La_3Zr_2O_{12}$ (LLZO), first reported by Murugan *et al*.[82] is considered as one of the most attractive candidate for ASSLBs, owing to its high RT ionic conductivity (> 10^{-4} S cm^{-1}), a wide electrochemical potential window, and particularly high chemical stability towards the Li metal.[83] Among all reported LLZO-related SSEs, the highest RT ionic conductivity was reported as 2.06 × 10^{-3} S cm^{-1}, which was realized in the composition of $Li_{6.55}Ga_{0.15}La_3Zr_2O_{12}$.[84] However, the preparation of LLZO-family oxide SSEs requires an ultrahigh crystallization temperature in the range of 900 ~ 1230 ^{o}C, depending on the composition.[16] This would increase the requirement of synthesis equipment and the difficulty of coupling with various thermally instable cathode materials (< 700 ^{o}C). In addition, the LLZO family was reported sensitive to the air, particularly for the CO_2 and H_2O. The degradation of LLZO exposing to air leads to the generation of Li_2CO_3-containing passivation layer, which can decrease the Li mobility through the LLZO/electrode interface.[83, 85]

2.2 Interfaces in sulfide-based ASSLBs

Since sulfide SSEs are the focus in this thesis, the interface issues that are discussed in this section are within the sulfide-based ASSLBs. In the section of '2.1', several classes of sulfide SSEs showing comparable ionic conductivity (10^{-2} S cm^{-1}) to the commercialized LEs were overviewed (**Table 2.1**). Nevertheless, it is pity that only high ionic conductivity cannot guarantee excellent electrochemical performance of ASSLBs. There are variety of

interfaces in one ASSLBs, and any one shortcoming (e.g., contact loss, incompatibility, and reactivity) can determine the delivered performance.[86-87] All in all, a superior interface is an essential requirement for pursuing high-performance ASSLBs besides the ionic conductivity. Generally, a perfect interface should be an integrate product of close contact, chemical inertness, and electrochemical compatibility. In this section, interface issues in sulfide-based ASSLBs will be unfolded under the sub-titles of anode interface, cathode interface, and electrochemical window.[88]

2.2.1 Anode interface

One of the biggest motivations that stimulates the development of ASSLBs is the potential of using Li metal as the anode materials, because it was early accepted that the high Young's modulus of SSEs (> 18 MPa) can resist the penetration of Li dendrites.[89-90] However, recent studies suggested that the short circuits caused by Li dendrites still exist as the one of the main failure mechanisms in the solid-state system.[90] In addition, the chemical/electrochemical compatibility at the interface of inorganic SSEs/Li metal are mostly not stable against what we expected before.[87, 90] In this section, two aspects of Li anode interface problems and corresponding strategies will be discussed: one is the high reactivity of Li metal towards sulfide SSEs; the other one is the issue of Li dendrites generated at the anode interface.

2.2.1.1 High reactivity of Li metal anode

Due to the strong reducing capability of Li metal, almost every reported sulfide-based SSEs can be reduced by Li metal upon electrochemical cycling or even upon contact. Early in 2015, Zhu *et al*.[91] used computational simulation to determine the reduction potential of various sulfide SSEs is in the range of 1.62 ~ 2.28 V. Several common sulfides, such as Li_3PS_4, LGPS, and argyrodite LPSCl all show the reduction potential of 1.71 V, while $Li_7P_3S_{11}$ even indicates higher reduction potential of 2.28 V. The calculation also suggested that reduction products of sulfides are always including P, Li_2S, metal alloys (e.g. Li-Ge) and Li halides (e.g., LiCl and LiI). Practical interfacial products of Li/sulfide SSEs have been experimentally verified. For example, Wenzel *et al*.[92-93] used in-situ X-ray photoelectron spectroscopy (XPS) combining with Li metal deposition and time-resolved

electrochemical impedance spectroscopy (EIS) to investigate the interfacial composition formed in-situ between Li metal and LGPS as well as the argyrodite Li_6PS_5X (LPSX, X = Cl, Br, I) SSEs. As shown in **Figure 2.9a** and **b**, the decomposition of LGPS at the Li metal interface leads to the formation of an interphase composed of Li_3P, Li_2S, and Li-Ge alloy, while the decomposed interphase of Li/LPSCl mainly consists of Li_3P, Li_2S and LiCl compounds. These results are in perfect agreement with theoretical predictions.[91] In addition, the increase of interfacial resistance at both Li/LGPS (**Figure 2.9c**) and Li/LPSX interfaces could be observed in the contacting time-resolved EIS measurements which is attributed to the degradation of sulfide SSEs contacting with Li metal. The interfacial reactions can also lead to the continuously increased overpotential during Li plating and stripping, which were particularly observed in cases of LGPS-type SSEs.

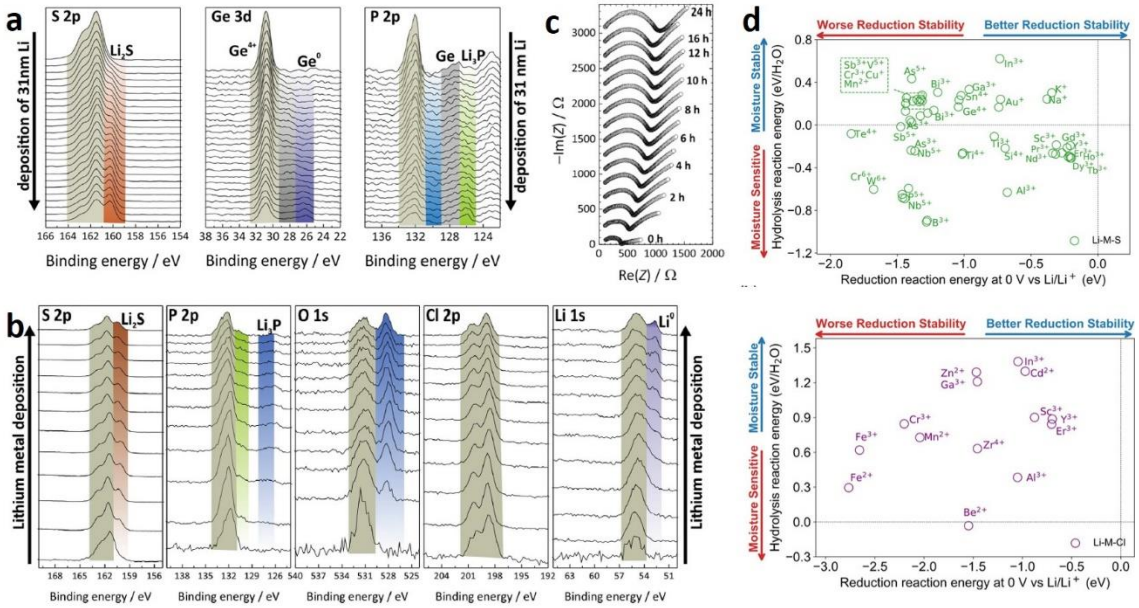

Figure 2.9 X-ray photoelectron (XPS) spectra recorded during deposition of Li metal on $Li_{10}GeP_2S_{12}$ (LGPS) (a)[92] and Li_6PS_5Cl (LPSCl) (b)[93]; (c) Nyquist plots of the Li/LGPS/Li symmetric cell during 24 h rest time;[92] (d) Calculated reduction stability of Li-M-S and Li-M-Cl.[59]

The reactivity between Li metal and Li-M-X halide SSEs is catastrophic, although the oxidation stability of halides is better than that of sulfides. As indicated in the calculated reduction stability of the Li-M-Cl system (**Figure 2.9d**), the reduction reaction energy of

all the studied cases, including the recently founded superionic halides based on In, Sc, Y, Er, and Zr, suggests a value under 0 V (vs. Li/Li^+). This means all these Li-M-Cl halide SSEs can be reduced by Li metal spontaneously. Indeed, according to all published results, halide SSEs were never be used to face Li metal (or even In metal) directly in the full-cell configurations, where highly conductive and relatively stable sulfide SSEs were always needed to serve as the interlayer to separate the Li (or In) metal and halide SSEs. Therefore, Mo *et al.* insists that the reduction stability is a critical issue for developing Li-M-Cl halide SSEs for applications.[59] And this huge drawback of halide SSEs make our research focus (in this thesis) on sulfide SSEs, rather than halides.

2.2.1.2 Li dendrites

Growth of Li dendrites is another problem at the interface between Li metal anode and SSEs. The rough electrolyte surface promotes the formation of uneven Li deposition at the interface of Li/SSEs, which causes that the Li dendrites penetrate through the grain boundary or the voids among the bulk electrolytes.[94] The penetration of Li dendrites would reduce the efficiency of SSEs in conducting Li ions, and further cause the short circuiting eventually. In practical, the Li dendrite rather than the interfacial reaction is the main issue of the Li/argyrodite LPSCl interface, so the dendrite problem at the interface of Li/sulfide SSEs were always analyzed in the case of argyrodite LPSCl.

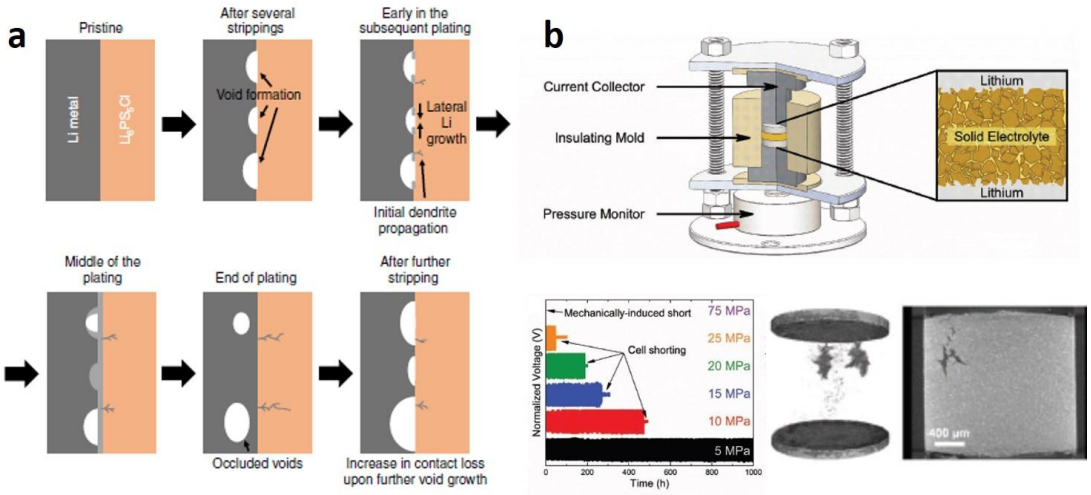

Figure 2.10 (a) Schematic diagram of the formation of voids and Li dendrites at the interface of Li/ Li_6PS_5Cl;[95] (b) Pressure effect on the interface performance of Li/ Li_6PS_5Cl

SSEs, including the cell design and the tested performance, as well as using X-ray tomography to observe the Li dendrite under the applied pressure of 25 MPa.[96]

Kasemchainan *et al*.[95] demonstrated that the critical current density is crucial for the Li plating and stripping behaviors using argyrodite LPSCl SSEs. As illustrated in **Figure 2.10a**, once the Li is removed from the interface at a current density faster than it can be replenished, voids are generated in the Li bulk near the interface with the SSE layer and accumulate upon following cycles. The edges of these voids localize a higher current density than elsewhere and ultimately leads to Li dendrites formation. The stack pressure is another important factor that can determine the formation of Li dendrites. As shown in **Figure 2.10b**, Doux *et al*. [96] designed a special cell with the feature of adjustable pressure and emphasized the importance of a reasonable pressure for long-life cycling of Li/Li_6PS_5Cl/Li symmetric cells. A suitable pressure can ensure a good contact between the Li metal and the argyrodite LPSCl in spite of the volume fluctuations of the Li metal electrodes during long-term cycling. Nevertheless, excess pressure (≥ 25 MPa) showed inverse effect because the Li can creep into the pores of Li_6PS_5Cl SSEs under high pressure and accelerated the growth of Li dendrites.

2.2.1.3 Strategies to increase the anode interface stability

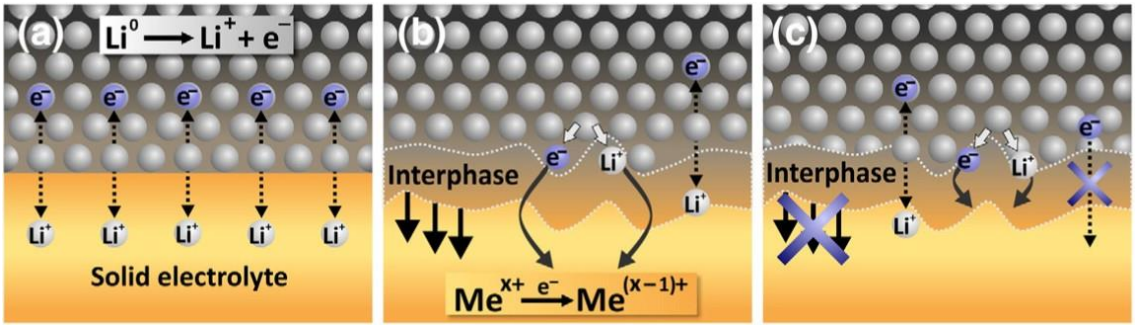

Figure 2.11 Types of interfaces between Li metal and a SSE. (a) Non-reactive and thermodynamically stable interface; (b) reactive and mixed conducting interphase (MCI); (c) reactive and metastable solid-electrolyte interphase (SEI).

As illustrated in **Figure 2.11**, it is generally accepted that one perfect Li/SSEs anode interface is Li-ion conductive but electron insulating, and the formed interface requires

smooth and robust features to withdraw the growth of Li dendrites. The developed strategies always follow this tenet, which are mainly divided into three categories: (1) inserting interlayers via chemical or electrochemical methods; (2) designing advanced SSEs to promote the generation of excellent interface; (3) using Li-Metal alloys to stabilize the Li plating/stripping.

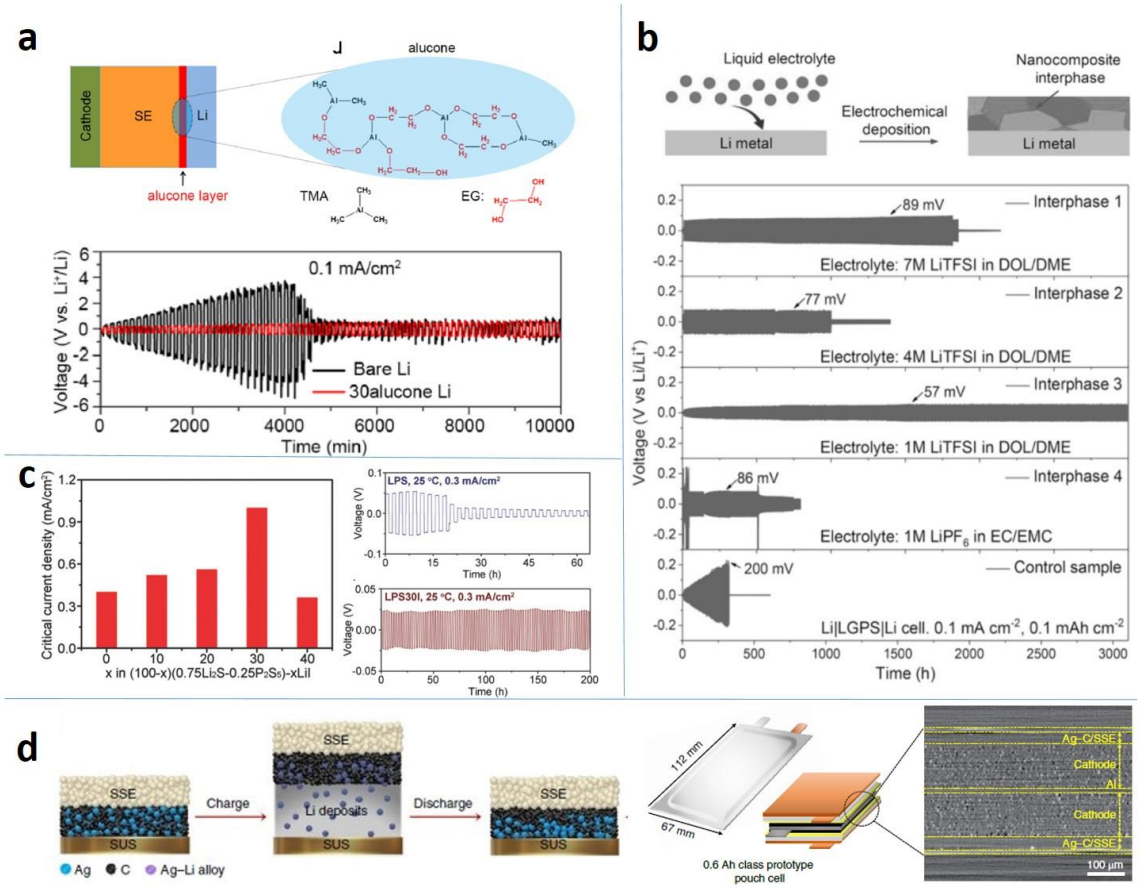

Figure 2.12 Strategies to solve the Li/SSEs interfacial issues. (a) interface engineering MLD-Alucone coating to prevent the side reaction and Li dendrites formation between Li metal and $Li_{10}SnP_2S_{12}$;[97] (b) using electrochemically derived interphase to improve the interfacial stability between Li metal and LGPS;[99] (c) Incorporation of LiI in LPS glass SSEs to increase the CCD and cycling stability;[104] (d) using Li-free anode design (Ag-C anode) to construct ultrahigh performance of pouch-type sulfide-based (Li_6PS_5Cl) ASSLBs.[107]

The first strategy is the most commonly used. As show in **Figure 2.12a**, our group, for the first time, employed molecular layer deposition (MLD) to coat the Li metal with an organic alucone layer.[97] The nanosized (9 ~ 15 nm) interlayer can suppress the side reactions between Li metal and $Li_{10}SnP_2S_{12}$ (LSPS) sulfide SSE, while the thin interlayer cannot block the Li^+ transport through the interface. In addition, the flexible organic interlayer can accumulate the volume change of Li metal during cycling and prevent the dendrite formation. Following this idea, various functional interlayers (polymer, inorganic, inorganic/organic composites) were reported to alleviate the interfacial problems at Li/Sulfide SSEs.[98] However, the strategy of inserting interlayer is time consuming and of high cost. For example, those interlayer achieved by in-situ electrochemical deposition within a LE-based battery (**Figure 2.12b**).[99] The complex process hinders this method to be practically used for large-scale applications.

The second strategy is the most straightforward but is full of challenges. The interface composition is adjusted by the modified SSEs, and the resultant interfacial products determine the feasibility. Therefore, no extra modification towards the interface is required, and the interface can be maintained well with the self-healing feature during the long-term cycling without considering the risk of broken interlayers. In general, LiX (X = F, Cl, Br, I) compounds are viewed as functional interfacial products to improve the Li plating and stripping, due to the high interface energy of highly electronegative halogens.[100] LiF is frequently reported as an essential interfacial composition to improve the Li metal interface stability in the LE-based LIBs,[101-103] while LiI was firstly discovered by Han *et al*.[104] that can constitute a favorable interface together with Li_2S and Li_3P between Li metal and LiI-incorporated Li_3PS_4 glass SSEs. The existence of LiI at the interface was regarded to reduce the electronic conductivity and increase the ionic conductivity, thus suppressing the formation of Li dendrites. As shown in **Figure 2.12c**, the critical current density (CCD) of the Li symmetric cell using the 30 mol% LiI incorporated LPS glass can increase to 1 mA cm^{-2}. The cycling life of the symmetric cell is also extended dramatically compared with the bare LPS glass SSEs.

The third strategy is based on changing the Li metal to other alternatives, which can alloy with Li to show stable Li plating/stripping behavior. This anode can be Li-M alloy or M

metal (M = In, Al, Ag, *etc.*).[105-108] Using this strategy, the reactivity of the anode/SSEs interface is reduced comparing to the direct usage of pure Li metal. The smooth Li (de)alloying can also be presented to avoid the tough (requiring high energy barrier) Li deposition. One obvious drawback of using this kind of anode materials is the decreased working voltage/energy density of constructed full cells, supposing using the same cathode materials as in the case of using Li metal anode, because the reduction potential of all other metals is higher than that of Li metal. Li-In alloy is the mostly used alternative anode material to Li metal, which is demonstrated as stable facing sulfide SSEs and some Li-M-Cl halide SSEs (e.g., Li_3YCl_6, Li_3YBr_6, and Li_3ScCl_6).[10, 12, 67] Only using metal M as the anode is also feasible, but it would loss the benefit of using Li-M alloy that can produce some excessive Li for compensating Li loss during electrochemical cycling. Therefore, development of Li-free anode is still very challenging, which requires more in aspects of the fast ion/electro kinetic of the metal electrode. Very recently, Lee *et al*.[107] presented a milestone performance of pouch cells using Li_6PS_5Cl as the SSE, and in-house designed Ag-C as the anode and a Li_2O-ZrO (LZO) coated high-Ni NMC cathode. The ultrathin Ag-C anode can effectively regulate Li deposition and avoid growth of Li dendrites (**Figure 2.12d**). This Li-free strategy eliminates the pre-loading of Li metal and solved problematic interface between fresh Li metal and argyrodite LPSCl. As a result, the fabricated pouch-type ASSLBs realized a high areal capacity of 6.8 mAh cm^{-2} and high energy density of more than 900 Wh L^{-1} with an impressive electrochemical cycling ability over 1000 cycles at 60 ^{o}C.

2.2.2 Cathode interface

The reason of the poor cathode interface stability in sulfide based ASSLBs is originated form the low oxidation potential of common sulfide SSEs. This brings big chemical-potential gap between sulfides and oxide cathode materials, which would cause the formation of space-charge layer and increase the interfacial impedance.[109-110] Additionally, the low oxidation limit of sulfides leads to severe decomposition of SSEs at the cathode interface, thus affecting the interfacial transport of Li ions.[91] In this section, these two aspects of interfacial issues will be introduced and the most used coating strategy will be also overviewed.

2.2.2.1 Space-charge layer (SCL) effect

In ASSLBs, the SCL is formed thermodynamically when electrode materials and SSEs with different chemical potential are brought in contact with each other.[111] Atoms or electrons are unable to migrate to establish local charge neutrality, but charged species (e.g., Li^+ from the electrodes or the SSE, electrons from mix-conducting electrodes) are able to migrate to compensate the potential difference gap between two bulk materials. This would generate a region where charges establish.[112] The formation of SCL can cause the Li depletion in either electrode or SSE layer near the interface, whose thickness can be from sub-nanometers to several microns depending on the involving material systems. In general, the SCL in large scale of can dramatically increase the difficulty of Li-ion migration across the interface and cause the growth spurt of interfacial impedance, therefore is regarded as a one of main detrimental effects on the electrochemical performance.[109-110, 113]

The SCL effect has been frequently reported in the sulfide-based ASSLBs, which is fundamentally because of the big potential difference between sulfide SSEs and common-used oxide cathode materials ($\mu_{oxides} > \mu_{sulfides}$). Taking the representative β-Li_3PS_4 (LPS) sulfide SSEs and $LiCoO_2$ cathode materials as the example, the movable Li^+ can transfer from the LPS side to the LCO once these two materials contact with each other.[110] Due to the mix-conducting feature of LCO cathode materials, the electron (e^-) would generate to balance the concentration gradient of Li^+. In this way, the SCL at the oxide side vanished. However, the Li^+ in LPS would further transfer to reach an equilibrium state, which can extend the region of SCL at the LPS side and increase the interfacial resistance. The problem of SCL effect can be well alleviated by incorporating one ion-conducting and electron-insulating oxide buffer layer.[109] The ionic conductivity of the oxide buffer layer is generally several-order lower than that of the sulfide SSE, so the buffer layer should be nanosized to maintain a favorable interfacial impedance. Typically, this buffer layer is obtained by the fabrication of coating layer on various cathode materials, such as, Lithium niobium oxides (LNO), Lithium tantalum oxides (LTaO), Lithium titanium oxides (LTiO), Lithium zirconium oxides (LZO), Lithium phosphorus oxides (LPO), etc.[114] Ohta *et al.* suggested two interfaces could form when using the buffer layer. One interface is between

the mixing cathode oxide material and ion-conducting buffer layer, and the other one is between ion-conducting buffer layer and the sulfide SSEs.[113] The formation of thick SCL is largely suppressed, because (1) there is a similar chemical potential for two oxide layers of the first interface; (2) electronically insulated features of the buffer layer and sulfide SSEs.

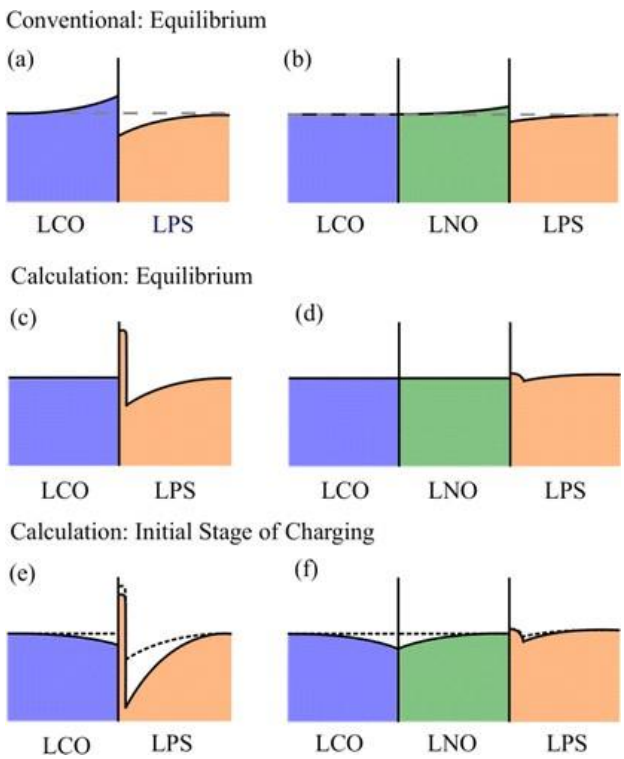

Figure 2.13 Schematic illustrations of the interfacial Li potential (concentration) at various states: LCO/LPS and LCO/LNO/LPS interfaces at the conventional equilibrium state (a and b); at the calculated equilibrium state (c and d); and at the initial stage of charging (e and f).[110]

Since the characterization of SCL is at atomic level, it is still very challenging to study the SCL with experimental approaches. Haruyama *et al.*[110] firstly used density functional theory (DFT) and U framework to elucidate the effect of the interposition of LNO buffer layer on the SCL formed at the LCO/LPS interface in both rest and charging states. In the conventional equilibrium, the LCO/LNO/LPS distribution is shown in **Figure 2.13b**. Compared with LCO/LPS interface (**Figure 2.13a**), the amount of Li redistribution is much smaller, because of the insulating properties of the interposed LNO buffer. During the

calculation, slightly modified distributions are indicated. The interfacial Li atoms in the LPS side heavily are attractive to the LCO surface. In sharp contrast, the attractive sites on the LCO surface disappear by incorporating of the LNO layers, and the SCL at this interface is significantly suppressed. In addition, the distribution on the LNO/LPS becomes much flatter due to the rather inactive essence of LNO and LPS (**Figure 2.13c** and **d**). In the initial charging state, Li ions at the LCO/LPS interface could transfer into the bulk LPS with releasing the electron to the LCO cathode. This can enhance the SCL in the sulfide side (**Figure 2.13e**), which was also visualized in the initial charging profile reported elsewhere. With the LNO buffer, **Figure 2.13f** indicates that the slope in the voltage profile, corresponding to the SCL growth, is fully suppressed.

2.2.2.2 Interfacial side reactions

The side reactions at the interface of oxide/sulfide SSEs is one of the most concerns in developing sulfide based ASSLBs. Zhu *et al.*[91] used DFT theoretical calculations to determine that all sulfide SSEs show a low oxidation potential below 2.5 V (vs. Li/Li^+). For example, the famous LGPS is limited at 2.14 V; the promising argyrodite LPSCl indicates even lower at 2.01 V; the highest oxidation limit occurs to Li_3PS_4, but is still as low as 2.31 V. Theoretically (without consideration of the kinetics of interphase), these upper limits cannot support any common oxide cathode materials which show redox reaction at the potential over 3 V. Therefore, the interfacial side reactions at the cathode side become critical to influence the battery performance. Taking the argyrodite LPSCl as the example, the interfacial side reactions between LPSCl and various cathode materials have been studied over the past decade. Early in 2012, Boulineau *et al.*[115] experimentally demonstrated that LPSX (X = Cl, Br) SSEs can support reversible Li intercalation/deintercalation for LCO cathode materials (redox potential ~3.9 V, theoretical capacity ~140 mAh g^{-1}). However, the ASSLB delivered limited reversible capacity of 46 mAh g^{-1} even at a low current density of 64 μA cm^{-2}.

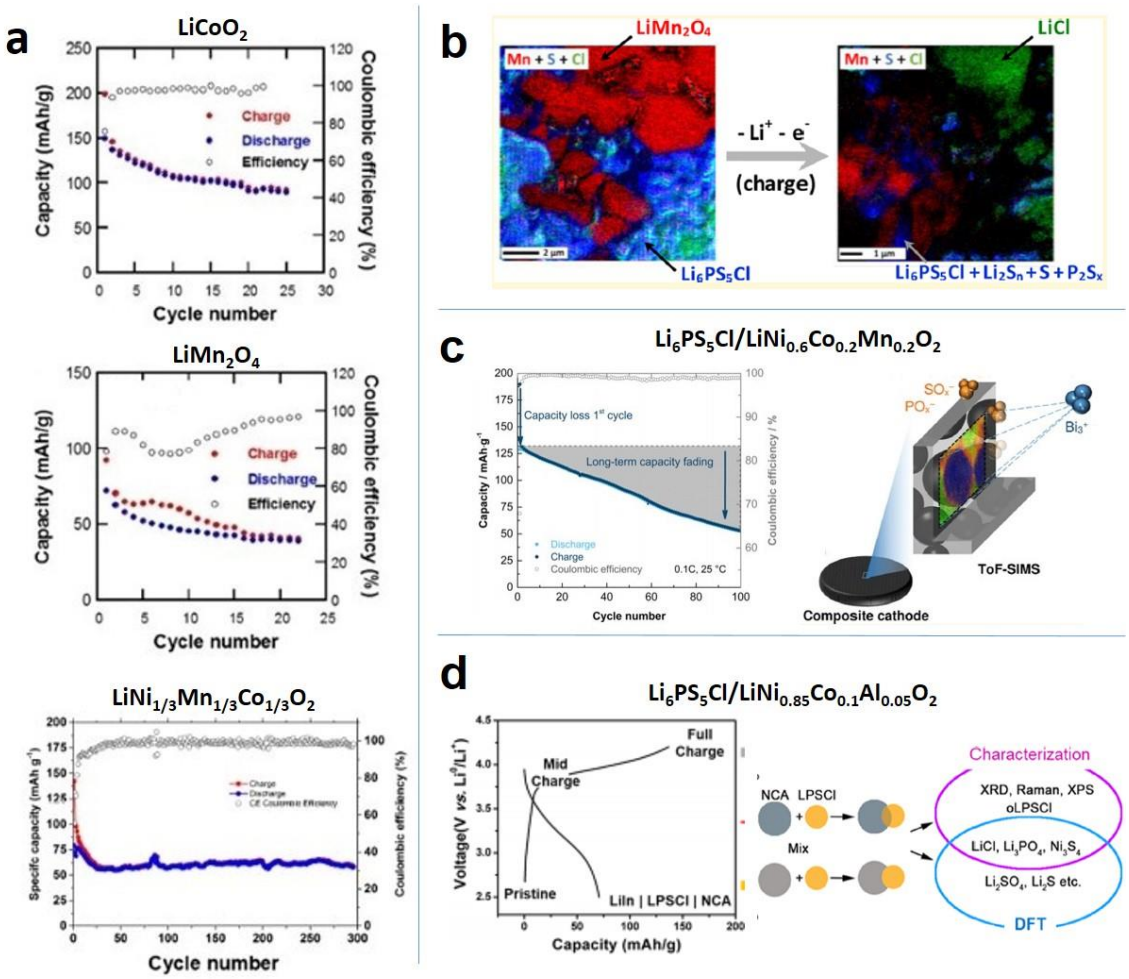

Figure 2.14 Problematic cathode/ Argyrodites interface. (a) Cycling performance of using Li Argyrodites as the electrolyte for different popular cathode materials.[116] (b) Using SAM to map the distribution of interfacial reaction products between Li_6PS_5Cl SSEs and LMO cathode materials.[116] (c) Using ToF-SIMS to know the interface component between Li_6PS_5Cl and NCM622 cathode materials.[117] (d) Experimental routes of studying the interface problem between Li_6PS_5Cl and NCA cathode materials.[118]

Auvergniot *et al*.[116] first systematically studied the interfacial compatibility of argyrodite LPSCl toward three kinds of popular cathode materials: LCO, $LiNi_{1/3}Co_{1/3}Mn_{1/3}O_2$ (NCM) and $LiMn_2O_4$ (LMO). As shown in **Figure 2.14a** rapid capacity decay was observed in all three cases. The XPS analyses to identify the side reaction products (such as S, polysulfide, P_2S_x, LiCl, Li_2S_x and even phosphate) from LPSCl and the cathode active materials at the

interface. Scanning auger microscopy (SAM) was employed to map the distribution of these products (**Figure 2.14b**). After charging, the distribution of LPSCl was overwhelmed by its decomposition products.[116] Furthermore, Walther *et al*.[117] utilized time-of-flight secondary ion mass spectrometry (TOF-SIMS) to observe the interfacial composition between LPSCl and $LiNi_{0.6}Co_{0.2}Mn_{0.2}O_2$ (NCM622) cathode materials (**Figure 2.14c**). The interested interface was mainly composed of sulfates and phosphates, while transition-metal chlorides, phosphides, and sulfides can be neglected. Moreover, Banerjee *et al*.[118] segregated the effects of spontaneous reaction of LPSCl SSEs and $LiNi_{0.85}Co_{0.1}Al_{0.05}O_2$ (NCA) cathode materials at the interface. By using various synchrotron-based characterization tools and first-principles calculations, the intrinsic electrochemical decomposition was studied (**Figure 2.14d**). The interfacial products were Ni_3S_4, LiCl, Li_3PO_4 and oxidized Li_6PS_5Cl from the spontaneous chemical reaction between NCA and LPSCl. Similar side reactions could also be found in other sulfide systems (LGPS, LPS, etc.).[119-122] There are three main direct consequences of these interfacial reactions: (1) retarding interfacial Li^+ transport; (2) decomposing active cathode materials and sulfide SSEs; (3) increasing the interfacial impedance. All these results lead to the decay of capacity and deteriorate the battery performance.

2.2.2.3 Coating strategies

Designing coating materials for cathode particles is the mostly common strategy to alleviate the cathode interface problems.[114] There are several primary requirements for the coating layer: (1) (electro)chemical compatibility with cathode and SSEs; (2) high ionic conductivity; (3) low electronic conductivity; (4) high oxidation limit. Obviously, the (electro)chemical compatibility of coating layers is most basic requirement. High ionic conductivity can maintain sufficient interfacial Li^+ transport. Low electronic conductivity and high oxidation limit are required to avoid occurring interfacial reactions.

A large number of binary oxide coatings (e.g., ZrO_2, Al_2O_3, TiO_2, SiO_2, etc.) have been developed as cathode coating layer to improve the lifespan of conventional LE-based LIBs, but limited binary oxides (except for Al_2O_3, SiO_2, ZrO_2) can be used for the solid-state counterparts.[114] The reason is due to the Li-deficient oxide coating cannot provide the necessary Li^+ ionic conductivity at the interface, while the LE can diffuse to small pores of

the oxide coating layer to supply sufficient ion transport. Therefore, Li-containing ternary oxide coating layers are always required to alleviate the cathode interface problem in the field of ASSLBs. Li-Ti-O, Li-Nb-O, Li-Ta-O, Li-Zr-O, Li-P-O, Li-Si-O, and Li-Ti-O have been all reported to improve the cathode interface by decreasing the interfacial impedance and prevent the inter-reaction between cathode materials and sulfide SSEs.[114] Among all the ternary oxide coating materials, $LiNbO_3$ (LNO) is the most well-known coating materials, because the amorphous LNO shows a high ionic conductivity (10^{-5} S cm^{-1} level) at RT and a low electronic conductivity of 10^{-11} S cm^{-1}.[123] Both theoretical and experimental studies suggest the LNO coating can solve the interfacial problem and enhance the performance of ASSLBs.[110, 113] Sol-gel method is one of the most common methods to fabricate these cathode coating layers, because this method is the most straightforward and can be relatively conducted for large-scale applications without using complicated or expensive instruments. However, one potential drawback is that the thickness, morphology, and homogeneity of the coating layer is quite difficult to control.[114]

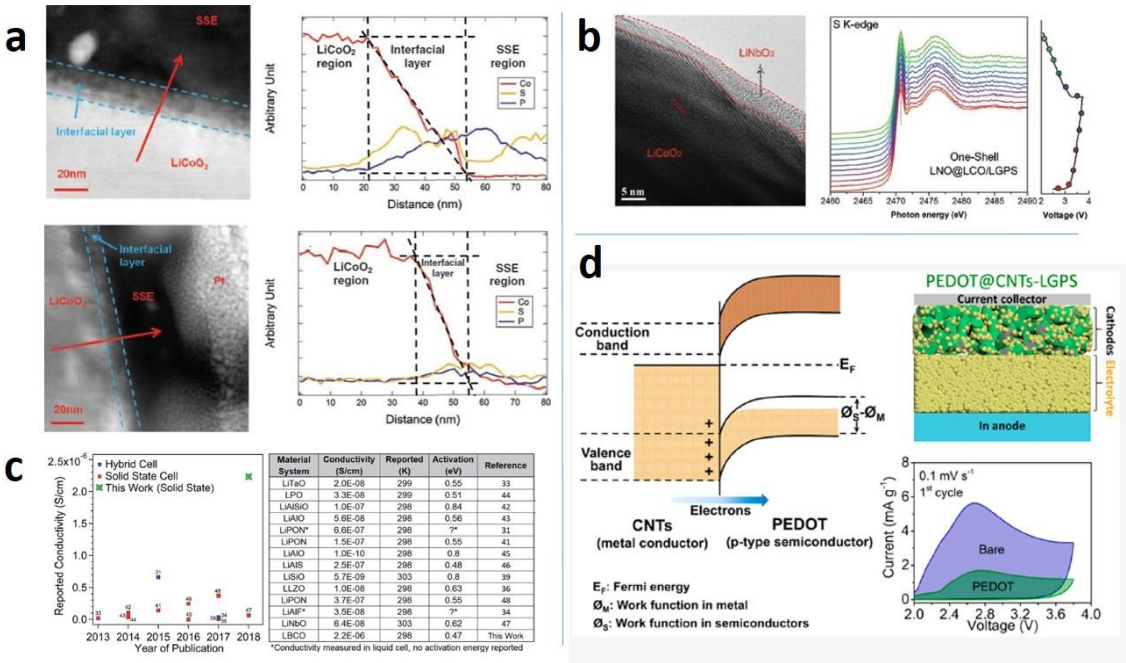

Figure 2.15 (a) ALD-Al2O3 for the interface of LiCoO2/$Li_{3.15}Ge_{0.15}P_{0.85}S_4$;[125] (b) ALD-LiNbO3 for improving the interface of LiCoO2/LGPS;[120] (c) ALD deposited lithium borate-carbonate shows the highest ionic conductivity among all ALD coating materials;[127]

(d) using the ALD-derived MLD technique to design PEDOT coating layer to improve the three-phase interface in the cathode composite.[128]

Atomic layer deposition (ALD) is an advanced film fabricating technique, capable of tuning the interface property with atomic-level thickness control at relatively low temperature (< 400 ^{o}C). Compared with the conventional wet chemical method (e.g., sol-gel method), the ALD method can not only show the ability of developing Li-containing ternary oxides coating with uniform and conformal features, but also completely avoid the negative effects of using solvents and high-temperature treatment.[124] Lee's group firstly demonstrated that ALD-Al_2O_3 layers coated on LCO cathode materials can effectively prolong the cycle life of the ASSLBs.[125] High-resolution TEM and EELS aided in observing that the ALD-Al_2O_3 layer can reduce the thickness of the formed interface. The inter-diffusion of each element from LCO cathode materials and $Li_{3.15}Ge_{0.15}P_{0.85}S_4$ SSEs are also inhibited (**Figure 2.15a).** Our group further demonstrated the ALD deposited amorphous and Li-ion conductive $LiNbO_x$ (LNO) and $LiPO_x$ (LPO) coating layers on the LCO particles and NMC cathode materials, respectively.[120, 126] In-situ XANES results imply that the LNO shell can suppress the interfacial reactions between LCO and $Li_{10}GeP_2S_{12}$ during charging and discharging processes (**Figure 2.15b**).[120] In addition to the binary and ternary coating materials, the amorphous ALD-LBCO (including Li, B, C, and O element) layer was verified to work well in the thin film battery, which shows a very promising ionic conductivity of 2.2×10^{-6} S cm^{-1} at 25 ^{o}C (**Figure 2.15c**).[127] Therefore, ALD-LBCO protection layer is anticipated to be able to perform excellent performance when applied to the cathode materials for ASSLBs. Besides the ionic conductivity, electronic conductivity is another important interfacial factor that can determine interfacial reactions. Our group recently developed poly(3,4-ethylenedioxythiophene) (PEDOT) by ALD-derived molecular layer deposition (MLD) as a semiconducting additive for cathode composites in the sulfide-based ASSLBs (**Figure 2.15d**). The MLD-PEDOT modification on the conductive additive-CNTs can not only significantly suppresses the side reactions but also realizes effective electron transfer at the cathode/SSE/carbon three-phase interface.[128]

2.2.3 Practical electrochemical window

According to theoretical calculations of thermodynamics for representative SSEs the stable electrochemical window is very limited.[91, 129] As shown in **Figure 2.16a**, sulfide-based SSEs shows the narrowest window, while chlorides are much better and fluorides are the best. However, in practical, many publications reported that the developed sulfide SSEs can present a much wider electrochemical window liner scanning voltammetry (LSV) measurement. This outstanding stability is be regarded as a result of the kinetic stabilization with interphases.[91] The sluggish kinetics of the decomposition reactions cause a high overpotential at both anode and cathode sides, which can extend the electrochemical window via increasing the oxidation limit and reduction limit, respectively (**Figure 2.16b**).[91] Therefore, the practical electrochemical window is based on consideration of the formed interphase due to initial decomposition of SSEs, and this 'real' electrochemical window is important for applications. But determination of the practical electrochemical window is not easy. It is always dependent on the cell configuration and test conditions (e.g., applied pressure, temperature). Recently, Schwietert et al.[130] studied the relationship between redox activity (interphase) and electrochemical stability (electrochemical window) of argyrodite LPSCl SSEs. As displayed in **Figure 2.16c**, The electrochemical stability window is determined by the oxidation and reduction potentials of Li_4PS_5Cl (S/S^{2-} redox, at 2.24 V) and $Li_{11}PS_5Cl$ (through the P/P^{5+} redox, at 1.08 V), respectively, showing a considerable improvement compared with the theoretical window (1.71 ~ 2.01 V). In the oxidation, unstable argyrodite phases rapidly decompose into the expected stable Li_3PS_4, S and LiCl species in the first step, and then oxidized to $P_2S_7^{-4}$ at 2.9 V. In the reduction, the first decomposition is going to P, Li_2S, and LiCl species, and further to final Li_3P at 0.8 V. It is suggested that the kinetically most favorable decomposition route via the redox activity of argyrodite LPSCl SSEs, thereby determining the electrochemical stability window. Therefore, the interfacial products play an important role to determine the practical electrochemical window, which would be different when using various electrode materials. Based on this mechanism, the design of stable solid electrolytes and their interfaces should focus on maximizing the (de)lithiation redox potentials of the solid electrolytes, as well as on designing outstanding interphase with coating layers.

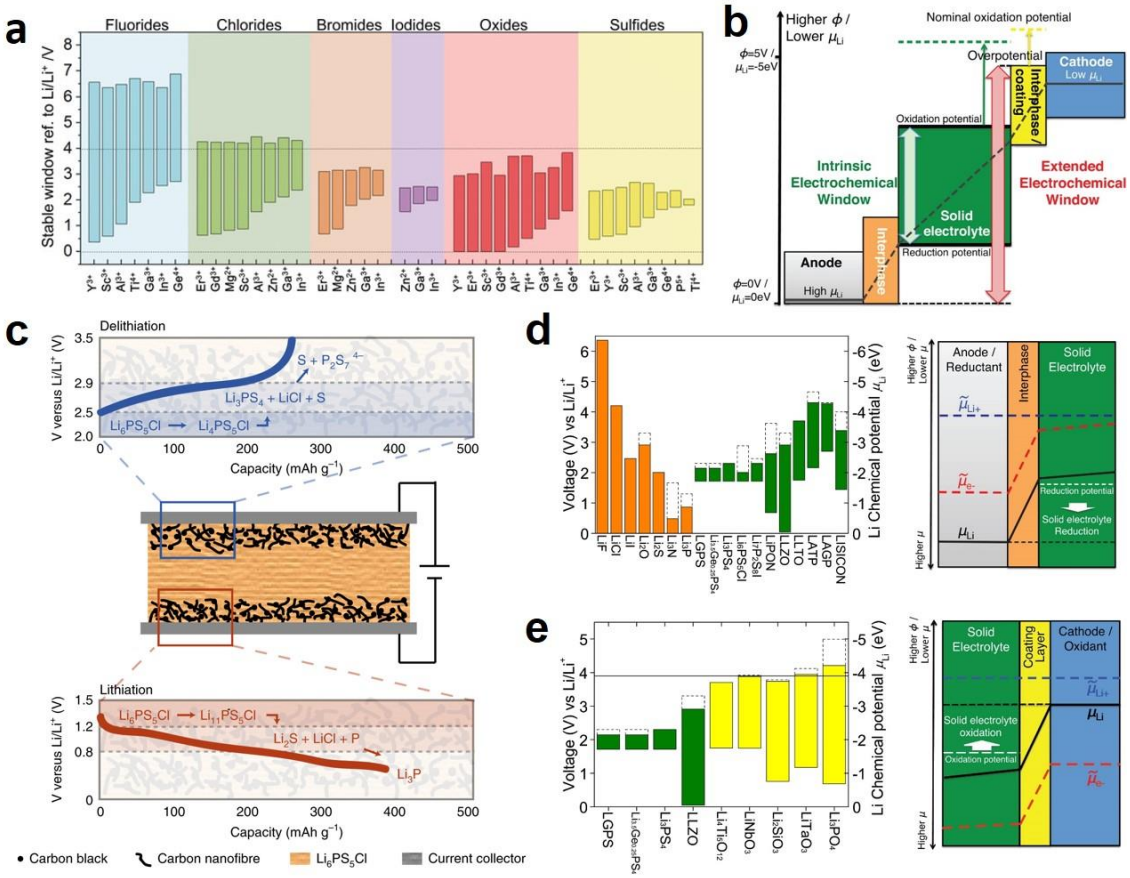

Figure 2.16 (a) Calculated thermodynamics intrinsic electrochemical windows of Li–M–X ternary fluorides, chlorides, bromides, iodides, oxides, and sulfides;[129] (b) Schematic diagram of the extended electrochemical window achieved by the anode/cathode interphases;[91] (c) Electrochemical activity of argyrodite LPSCl on oxidation and reduction;[130] (d and e) Illustrations of the reduced (or increased) reduction (or oxidation) potential by anode (or cathode) interface design.[91]

At the anode side (**Figure 2.16d**),[91] the interphase consisting of LiX (X = F, Cl, Br, I), Li_2O, Li_2S, Li_3N, or Li_3P products is stable against the Li metal, which is beyond the reduction limit of most SSEs (except for LLZO). At the equilibrium, the redistribution of Li^+ and other charged carriers (such as e^-) are formed at the interface to account for the space-charge layer. The electrochemical potential of the highly mobile Li^+ ($\tilde{\mu}_{Li+}$), suggesting the electrostatic potential energy, is constant across the interface. The electrochemical potential of the electrons ($\tilde{\mu}e^-$) decreases significantly in the interphase

from the anode to the solid electrolyte supposing the qualified interphase is electron insulating. Therefore, the Li chemical potential (μ_{Li}), which equals to the sum of $\tilde{\mu}_{Li+}$ and $\tilde{\mu}e^-$, decreases in the interphase from anode to electrolyte. As a result, the decomposition of the electrolyte has no thermodynamic driving force to continue into the bulk, and the electrolyte is stabilized by the decomposition interphases (or called 'solid electrolyte interphase', SEI). At the cathode side (**Figure 2.16e**),[91] the coating materials (e.g., $LiNbO_3$, $LiNbO_3$, Li_3PO_4) always show high oxidation potential of 3.7 ~ 4.2 V, which are stable in the usual voltage range for practical usage. Since the qualified coating layer materials have poor electronic conductivity and can serve as artificial CEI (cathode electrolyte interphase) to passivate the solid electrolyte through the similar mechanisms, where the oxidation limit can be increased. Utilizing these interphases, the practical electrochemical window can be well extended.

2.3 References

（1）Bachman, J. C.; Muy, S.; Grimaud, A.; Chang, H. H.; Pour, N.; Lux, S. F.; Paschos, O.; Maglia, F.; Lupart, S.; Lamp, P.; Giordano, L.; Shao-Horn, Y., *Chem. Rev.* **2016,** *116* (1), 140-62.

（2）Li, M.; Wang, C.; Chen, Z.; Xu, K.; Lu, J., *Chem. Rev.* **2020**, 6783–6819.

（3）Manthiram, A.; Yu, X.; Wang, S., *Nat. Rev. Mater.* **2017,** *2* (4), 16103.

（4）Oshima, T.; Kajita, M.; Okuno, A., *Int. J. Appl. Ceram. Tec.* **2004,** *1* (3), 269-276.

（5）Chandra, S.; Lal, H. B.; Shahi, K., *J. Phys. D: Appl. Phys.* **1974,** *7* (1), 194-198.

（6）Chandra, S.; MoFhabey, V. K., *J. Phys. D: Appl. Phys.* **1975,** *8* (5), 576-580.

（7）Dudney, N. J.; Bates, J. B.; Zuhr, R. A.; Luck, C. F.; Robertson, J. D., *Solid State Ionics* **1992,** *53*, 655-661.

（8）Kato, Y.; Hori, S.; Saito, T.; Suzuki, K.; Hirayama, M.; Mitsui, A.; Yonemura, M.; Iba, H.; Kanno, R., *Nat. Energy* **2016,** *1* (4), 16030.

（9）Kamaya, N.; Homma, K.; Yamakawa, Y.; Hirayama, M.; Kanno, R.; Yonemura, M.; Kamiyama, T.; Kato, Y.; Hama, S.; Kawamoto, K.; Mitsui, A., *Nat. Mater.* **2011,** *10* (9), 682-686.

（10）Asano, T.; Sakai, A.; Ouchi, S.; Sakaida, M.; Miyazaki, A.; Hasegawa, S., *Adv. Mater.* **2018,** *30* (44).

（11）Zou, Z.; Li, Y.; Lu, Z.; Wang, D.; Cui, Y.; Guo, B.; Li, Y.; Liang, X.; Feng, J.; Li, H.; Nan, C. W.; Armand, M.; Chen, L.; Xu, K.; Shi, S., *Chem. Rev.* **2020,** *120* (9), 4169-4221.

（12）Liang, J. W.; Li, X. N.; Wang, S.; Adair, K. R.; Li, W. H.; Zhao, Y.; Wang, C. H.; Hu, Y. F.; Zhang, L.; Zhao, S. Q.; Lu, S. G.; Huang, H.; Li, R. Y.; Mo, Y. F.; Sun, X. L., *J. Am. Chem. Soc.* **2020,** *142* (15), 7012-7022.

（13）Abakumov, A. M.; Fedotov, S. S.; Antipov, E. V.; Tarascon, J. M., *Nat. Commun.* **2020,** *11* (1), 4976.

（14）Angell, C. A., *Annu. Rev. Phys. Chem.* **1992,** *43*, 693-717.

（15）Zhang, Q.; Cao, D.; Ma, Y.; Natan, A.; Aurora, P.; Zhu, H., *Adv. Mater.* **2019,** *31*, 1901131.

（16）Zhang, Z.; Shao, Y.; Lotsch, B.; Hu, Y.-S.; Li, H.; Janek, J.; Nazar, L. F.; Nan, C.-W.; Maier, J.; Armand, M.; Chen, L., *Energy Environ. Sci.* **2018,** *11* (8), 1945-1976.

（17）Mizuno, F.; Hayashi, A.; Tadanaga, K.; Tatsumisago, M., *Adv. Mater.* **2005,** *17* (7), 918-921.

（18）Deiseroth, H. J.; Kong, S. T.; Eckert, H.; Vannahme, J.; Reiner, C.; Zaiss, T.; Schlosser, M., *Angew. Chem. Int. Ed.* **2008,** *47* (4), 755-758.

（19）Liu, Z. C.; Fu, W. J.; Payzant, E. A.; Yu, X.; Wu, Z. L.; Dudney, N. J.; Kiggans, J.; Hong, K. L.; Rondinone, A. J.; Liang, C. D., *J. Am. Chem. Soc.* **2013,** *135* (3), 975-978.

（20）Seino, Y.; Ota, T.; Takada, K.; Hayashi, A.; Tatsumisago, M., *Energy Environ. Sci.* **2014,** *7* (2), 627-631.

（21）Murayama, M.; Sonoyama, N.; Yamada, A.; Kanno, R., *Solid State Ionics* **2004,** *170* (3-4), 173-180.

（22）Kanno, R.; Maruyama, M., *J. Electrochem. Soc.* **2001,** *148* (7), A742-A746.

（23）Hori, S.; Kato, M.; Suzuki, K.; Hirayama, M.; Kato, Y.; Kanno, R., *J. Am. Ceram. Soc.* **2015,** *98* (10), 3352-3360.

（24）Homma, K.; Yonemura, M.; Kobayashi, T.; Nagao, M.; Hirayama, M.; Kanno, R., *Solid State Ionics* **2011,** *182* (1), 53-58.

（25）Homma, K.; Yonemura, M.; Nagao, M.; Hirayama, M.; Kanno, R., *J. Phys. Soc. Jpn.* **2010,** *79*, 90-93.

（26）Murayama, M.; Kanno, R.; Kawamoto, Y.; Kamiyama, T., *Solid State Ionics* **2002,** *154-155*, 789-794.

（27）Liang, X. M.; Wang, L. Y.; Jiang, Y. M.; Wang, J.; Luo, H.; Liu, C. Y.; Feng, J. W., *Chem. Mater.* **2015,** *27* (16), 5503-5510.

（28）Weber, D. A.; Senyshyn, A.; Weldert, K. S.; Wenzel, S.; Zhang, W. B.; Kaiser, R.; Berendts, S.; Janek, J.; Zeier, W. G., *Chem. Mater.* **2016,** *28* (16), 5905-5915.

（29）Adams, S.; Rao, R. P., *J. Mater. Chem.* **2012,** *22* (16), 7687-7691.

（30）Zhou, P. F.; Wang, J. B.; Cheng, F. Y.; Li, F. J.; Chen, J., *Chem. Commun.* **2016,** *52* (36), 6091-6094.

（31）Hori, S.; Suzuki, K.; Hirayama, M.; Kato, Y.; Saito, T.; Yonemura, M.; Kanno, R., *Faraday Discuss* **2014,** *176*, 83-94.

（32）Bron, P.; Johansson, S.; Zick, K.; auf der Gunne, J. S.; Dehnen, S.; Roling, B., *J. Am. Chem. Soc.* **2013,** *135* (42), 15694-15697.

（33）Adeli, P.; Bazak, J. D.; Park, K. H.; Kochetkov, I.; Huq, A.; Goward, G. R.; Nazar, L. F., *Angew Chem. Int. Edit.* **2019,** *58* (26), 8681-8686.

（34）Kraft, M. A.; Ohno, S.; Zinkevich, T.; Koerver, R.; Culver, S. P.; Fuchs, T.; Senyshyn, A.; Indris, S.; Morgan, B. J.; Zeier, W. G., *J. Am. Chem. Soc.* **2018,** *140* (47), 16330-16339.

（35）Zhou, L. D.; Assoud, A.; Zhang, Q.; Wu, X. H.; Nazar, L. F., *J. Am. Chem. Soc.* **2019,** *141* (48), 19002-19013.

（36）Yu, C.; Zhao, F.; Luo, J.; Zhang, L.; Sun, X., *Nano Energy* **2021,** *83*, 105858.

（37）Kraft, M. A.; Culver, S. P.; Calderon, M.; Bocher, F.; Krauskopf, T.; Senyshyn, A.; Dietrich, C.; Zevalkink, A.; Janek, J.; Zeier, W. G., *J. Am. Chem. Soc.* **2017,** *139* (31), 10909-10918.

（38）Hayashi, A.; Minami, K.; Tatsumisago, M., *J. Solid State Electrochem.* **2010,** *14* (10), 1761-1767.

（39）Tatsumisago, M.; Mizuno, F.; Hayashi, A., *J. Power Sources* **2006,** *159* (1), 193-199.

（40）Hayashi, A.; Tatsumisago, M., *Electron. Mater. Lett.* **2012,** *8* (2), 199-207.

（41）Minami, T.; Hayashi, A.; Tatsumisago, M., *Solid State Ionics* **2006,** *177* (26-32), 2715-2720.

（42）Hayashi, A.; Hama, S.; Morimoto, H.; Tatsumisago, M.; Minami, T., *J. Am. Ceram. Soc.* **2001,** *84* (2), 477-479.

（43）Dietrich, C.; Weber, D. A.; Sedlmaier, S. J.; Indris, S.; Culver, S. P.; Walter, D.; Janek, J.; Zeier, W. G., *J. Mater. Chem. A* **2017,** *5* (34), 18111-18119.

（44）Hayashi, A.; Komiya, R.; Tatsumisago, M.; Minami, T., *Solid State Ionics* **2002,** *152*, 285-290.

（45）Mercier, R.; Malugani, J. P.; Fahys, B.; Robert, G., *Solid State Ionics* **1981,** *5*, 663-666.

（46）Kennedy, J. H.; Zhang, Z. M., *J. Electrochem. Soc.* **1988,** *135* (4), 859-862.

（47）Kulkarni, A. R.; Maiti, H. S.; Paul, A., *Bull. Mater. Sci.* **1984,** *6* (2), 201-221.

（48）Mizuno, F.; Hayashi, A.; Tadanaga, K.; Tatsumisago, M., *Solid State Ionics* **2006,** *177* (26-32), 2721-2725.

（49）Lee, H.; Oh, P.; Kim, J.; Cha, H.; Chae, S.; Lee, S.; Cho, J., *Adv. Mater.* **2019,** *31* (29), 1900376.

（50）Muramatsu, H.; Hayashi, A.; Ohtomo, T.; Hama, S.; Tatsumisago, M., *Solid State Ionics* **2011,** *182* (1), 116-119.

（51）Hayashi, A.; Muramatsu, H.; Ohtomo, T.; Hama, S.; Tatsumisago, M., *J. Mater. Chem. A* **2013,** *1* (21), 6320-6326.

（52）Kaib, T.; Haddadpour, S.; Kapitein, M.; Bron, P.; Schröder, C.; Eckert, H.; Roling, B.; Dehnen, S., *Chem. Mater.* **2012,** *24* (11), 2211-2219.

（53）Brant, J. A.; Massi, D. M.; Holzwarth, N. A. W.; MacNeil, J. H.; Douvalis, A. P.; Bakas, T.; Martin, S. W.; Gross, M. D.; Aitken, J. A., *Chem. Mater.* **2014,** *27* (1), 189-196.

（54）Sahu, G.; Lin, Z.; Li, J.; Liu, Z.; Dudney, N.; Liang, C., *Energy Environ. Sci.* **2014,** *7* (3), 1053-1058.

（55）Ohtomo, T.; Hayashi, A.; Tatsumisago, M.; Kawamoto, K., *J. Solid State Electrochem.* **2013,** *17* (10), 2551-2557.

（56）Hayashi, A.; Muramatsu, H.; Ohtomo, T.; Hama, S.; Tatsumisago, M., *J. Alloys Compd.* **2014,** *591*, 247-250.

（57）Liang, J. W.; Li, X. N.; Adair, K. R.; Sun, X. L., *Acc. Chem. Res.* **2021,** *54* (4), 1023-1033.

（58）Li, X. N.; Liang, J. W.; Yang, X. F.; Adair, K. R.; Wang, C. H.; Zhao, F. P.; Sun, X. L., *Energy Environ. Sci.* **2020,** *13* (5), 1429-1461.

（59）Zhu, Y. Z.; Mo, Y. F., *Angew Chem. Int. Edit.* **2020,** *59* (40), 17472-17476.

（60）Jackson, B. J. H.; Young, D. A., *J. Phys. Chem. Solids* **1969,** *30* (8), 1973-1976.

（61）Haven, Y., *Recl. Trav. Chim. Pay. B* **1950,** *69* (9), 1471-1489.

（62）Liang, C. C.; Epstein, J.; Boyle, G. H., *J. Electrochem. Soc.* **1969,** *116* (10), 1452-&.

（63）Weppner, W.; Huggins, R. A., *Phys. Lett. A* **1976,** *58* (4), 245-248.

（64）Plichta, E. J.; Behl, W. K.; Vujic, D.; Chang, W. H. S.; Schleich, D. M., *J. Electrochem. Soc.* **1992,** *139* (6), 1509-1513.

（65）Tomita, Y.; Fuji-i, A.; Ohki, H.; Yamada, K.; Okuda, T., *Chem. Lett.* **1998,** (3), 223-224.

（66）Li, X. N.; Liang, J. W.; Chen, N.; Luo, J.; Adair, K. R.; Wang, C. H.; Banis, M. N.; Sham, T. K.; Zhang, L.; Zhao, S. Q.; Lu, S. G.; Huang, H.; Li, R. Y.; Sun, X. L., *Angew Chem. Int. Edit.* **2019,** *58* (46), 16427-16432.

（67）Li, X. N.; Liang, J. W.; Luo, J.; Banis, M. N.; Wang, C. H.; Li, W. H.; Deng, S. X.; Yu, C.; Zhao, F. P.; Hu, Y. F.; Sham, T. K.; Zhang, L.; Zhao, S. Q.; Lu, S. G.; Huang, H.; Li, R. Y.; Adair, K. R.; Sun, X. L., *Energy Environ. Sci.* **2019,** *12* (9), 2665-2671.

（68）Zhou, L. D.; Kwok, C. Y.; Shyamsunder, A.; Zhang, Q.; Wu, X. H.; Nazar, L. F., *Energy Environ. Sci.* **2020,** *13* (7), 2056-2063.

（69）Park, K. H.; Kaup, K.; Assoud, A.; Zhang, Q.; Wu, X. H.; Nazar, L. F., *ACS Energy Lett.* **2020,** *5* (2), 533-539.

（70）Schlem, R.; Bernges, T.; Li, C.; Kraft, M. A.; Minafra, N.; Zeier, W. G., *ACS Appl. Energ Mater.* **2020,** *3* (4), 3684-3691.

（71）Li, X. N.; Liang, J. W.; Adair, K. R.; Li, J. J.; Li, W. H.; Zhao, F. P.; Hu, Y. F.; Sham, T. K.; Zhang, L.; Zhao, S. Q.; Lu, S. G.; Huang, H.; Li, R. Y.; Chen, N.; Sun, X. L., *Nano Lett.* **2020,** *20* (6), 4384-4392.

（72）Goodenough, J. B.; Hong, H. Y. P.; Kafalas, J. A., *Mater. Res, Bull* **1976,** *11* (2), 203-220.

（73）Hong, H. Y. P., *Mater. Res. Bull* **1976,** *11* (2), 173-182.

（74）Aono, H.; Sugimoto, E.; Sadaoka, Y.; Imanaka, N.; Adachi, G., *J. Electrochem. Soc.* **1993,** *140* (7), 1827-1833.

（75）Aono, H.; Sugimoto, E.; Sadaoka, Y.; Imanaka, N.; Adachi, G., *J. Electrochem. Soc.* **1990,** *137* (4), 1023-1027.

（76）Aono, H.; Sugimoto, E.; Sadaoka, Y.; Imanaka, N.; Adachi, G. Y., *B Chem. Soc. Jpn.* **1992,** *65* (8), 2200-2204.

（77）Inaguma, Y.; Chen, L. Q.; Itoh, M.; Nakamura, T.; Uchida, T.; Ikuta, H.; Wakihara, M., *Solid State Commun.* **1993,** *86* (10), 689-693.

（78）Inaguma, Y.; Katsumata, T.; Itoh, M.; Morii, Y., *J. Solid State Chem.* **2002,** *166* (1), 67-72.

（79）Yashima, M.; Itoh, M.; Inaguma, Y.; Morii, Y., *J. Am. Chem. Soc.* **2005,** *127* (10), 3491-3495.

（80）Wang, M. J.; Wolfenstine, J. B.; Sakamoto, J., *Adv. Funct. Mater.* **2020,** *30* (10), 1909140.

（81）Kasper, H. M., *Inorg. Chem.* **1969,** *8* (4), 1000-1002.

（82）Murugan, R.; Thangadurai, V.; Weppner, W., *Angew Chem. Int. Edit.* **2007,** *46* (41), 7778-7781.

（83）Wang, C. W.; Fu, K.; Kammampata, S. P.; Mcowen, D. W.; Samson, A. J.; Zhang, L.; Hitz, G. T.; Nolan, A. M.; Wachsman, E. D.; Mo, Y. F.; Thangadurai, V.; Hu, L. B., *Chem. Rev.* **2020,** *120* (10), 4257-4300.

（84）Qin, S. Y.; Zhu, X. H.; Jiang, Y.; Ling, M. E.; Hu, Z. W.; Zhu, J. L., *Appl. Phys. Lett.* **2018,** *112* (11).

（85）Huo, H. Y.; Luo, J.; Thangadurai, V.; Guo, X. X.; Nan, C. W.; Sun, X. L., *ACS Energy Lett.* **2020,** *5* (1), 252-262.

（86）Xiao, Y.; Wang, Y.; Bo, S.-H.; Kim, J. C.; Miara, L. J.; Ceder, G., *Nat. Rev. Mater.* **2019,** *5* (2), 105-126.

（87）Chen, R.; Li, Q.; Yu, X.; Chen, L.; Li, H., *Chem. Rev.* **2019,** *120* (14), 6820–6877.

（88）Weiss, M.; Simon, F. J.; Busche, M. R.; Nakamura, T.; Schröder, D.; Richter, F. H.; Janek, J., *Electrochem. Energy Rev.* **2020,** *3*, 221–238.

（89）Zhang, Y.; Zuo, T.-T.; Popovic, J.; Lim, K.; Yin, Y.-X.; Maier, J.; Guo, Y.-G., *Mater. Today* **2020,** *33*, 56-74.

（90）Cui, G., *Matter* **2020,** *2* (4), 805-815.

（91）Zhu, Y.; He, X.; Mo, Y., *ACS Appl. Mater. Interfaces* **2015,** *7* (42), 23685-23693.

（92）Wenzel, S.; Randau, S.; Leichtweiß, T.; Weber, D. A.; Sann, J.; Zeier, W. G.; Janek, J., *Chem. Mater.* **2016,** *28* (7), 2400-2407.

（93）Wenzel, S.; Sedlmaier, S. J.; Dietrich, C.; Zeier, W. G.; Janek, J., *Solid State Ionics* **2018,** *318*, 102-112.

（94）Cao, D.; Sun, X.; Li, Q.; Natan, A.; Xiang, P.; Zhu, H., *Matter* **2020,** *3* (1), 57-94.

（95）Kasemchainan, J.; Zekoll, S.; Jolly, D. S.; Ning, Z. Y.; Hartley, G. O.; Marrow, J.; Bruce, P. G., *Nat. Mater.* **2019,** *18* (10), 1105-1111.

（96）Doux, J. M.; Nguyen, H.; Tan, D. H. S.; Banerjee, A.; Wang, X. F.; Wu, E. A.; Jo, C.; Yang, H. D.; Meng, Y. S., *Adv. Energy Mater.* **2020,** *10* (1), 1903253.

（97）Wang, C.; Zhao, Y.; Sun, Q.; Li, X.; Liu, Y.; Liang, J.; Li, X.; Lin, X.; Li, R.; Adair, K. R.; Zhang, L.; Yang, R.; Lu, S.; Sun, X., *Nano Energy* **2018,** *53*, 168-174.

（98）Cao, D.; Zhao, Y.; Sun, X.; Natan, A.; Wang, Y.; Xiang, P.; Wang, W.; Zhu, H., *ACS Energy Lett.* **2020,** *5* (11), 3468-3489.

（99）Gao, Y.; Wang, D. W.; Li, Y. G. C.; Yu, Z. X.; Mallouk, T. E.; Wang, D. H., *Angew. Chem. Int. Ed.* **2018,** *57* (41), 13608-13612.

（100）Yang, Q. F.; Li, C. L., *Energy Storage Mater.* **2018,** *14*, 100-117.

（101）Lu, Y. Y.; Tu, Z. Y.; Archer, L. A., *Nat.Mater.* **2014,** *13* (10), 961-969.

（102）Ko, J.; Yoon, Y. S., *Ceram. Int.* **2019,** *45* (1), 30-49.

（103）Zhang, Q., *Nat. Nanotechnol.* **2018,** *13* (8), 623-624.

（104）Han, F.; Yue, J.; Zhu, X.; Wang, C., *Adv. Energy Mater.* **2018,** *8* (18), 1703644.

（105）Takada, K.; Aotani, N.; Iwamoto, K.; Kondo, S., *Solid State Ionics* **1996,** *86-8*, 877-882.

（106）Kanno, R.; Murayama, M.; Inada, T.; Kobayashi, T.; Sakamoto, K.; Sonoyama, N.; Yamada, A.; Kondo, S., *Electrochem. Solid St.* **2004,** *7* (12), A455-A458.

（107）Lee, Y. G.; Fujiki, S.; Jung, C. H.; Suzuki, N.; Yashiro, N.; Omoda, R.; Ko, D. S.; Shiratsuchi, T.; Sugimoto, T.; Ryu, S.; Ku, J. H.; Watanabe, T.; Park, Y.; Aihara, Y.; Im, D.; Han, I. T., *Nat. Energy* **2020,** *5* (4), 348-348.

（108）Sakuma, M.; Suzuki, K.; Hirayama, M.; Kanno, R., *Solid State Ionics* **2016,** *285*, 101-105.

（109）Takada, K.; Ohta, N.; Zhang, L. Q.; Fukuda, K.; Sakaguchi, I.; Ma, R.; Osada, M.; Sasaki, T., *Solid State Ionics* **2008,** *179* (27-32), 1333-1337.

（110）Haruyama, J.; Sodeyama, K.; Han, L. Y.; Takada, K.; Tateyama, Y., *Chem. Mater.* **2014,** *26* (14), 4248-4255.

（111）Swift, M. W.; Qi, Y., *Phys. Rev. Lett.* **2019,** *122* (16).

（112）de Klerk, N. J. J.; Wagemaker, M., *ACS Appl. Energ. Mater.* **2018,** *1* (10), 5609-5618.

（113）Ohta, N.; Takada, K.; Zhang, L. Q.; Ma, R. Z.; Osada, M.; Sasaki, T., *Adv. Mater.* **2006,** *18* (17), 2226-2229.

（114）Culver, S. P.; Koerver, R.; Zeier, W. G.; Janek, J., *Adv. Energy Mater.* **2019,** *9* (24), 1900626.

（115）Boulineau, S.; Courty, M.; Tarascon, J. M.; Viallet, V., *Solid State Ionics* **2012,** *221*, 1-5.

（116）Auvergniot, J.; Cassel, A.; Ledeuil, J. B.; Viallet, V.; Seznec, V.; Dedryvere, R., *Chem. Mater.* **2017,** *29* (9), 3883-3890.

（117）Walther, F.; Koerver, R.; Fuchs, T.; Ohno, S.; Sann, J.; Rohnke, M.; Zeier, W. G.; Janek, J., *Chem. Mater.* **2019,** *31* (10), 3745-3755.

（118）Banerjee, A.; Tang, H. M.; Wang, X. F.; Cheng, J. H.; Nguyen, H.; Zhang, M. H.; Tang, D. H. S.; Wynn, T. A.; Wu, E. A.; Doux, J. M.; Wu, T. P.; Ma, L.; Sterbinsky, G. E.; D'Souza, M. S.; Ong, S. P.; Meng, Y. S., *ACS Appl. Mater. Interfaces* **2019,** *11* (46), 43138-43145.

（119）Zhang, W. B.; Richter, F. H.; Culver, S. P.; Leichtweiss, T.; Lozano, J. G.; Dietrich, C.; Bruce, P. G.; Zeier, W. G.; Janek, J., *ACS Appl. Mater. Interfaces* **2018,** *10* (26), 22226-22236.

（120）Wang, C. H.; Li, X.; Zhao, Y.; Banis, M. N.; Liang, J. W.; Li, X. N.; Sun, Y. P.; Adair, K. R.; Sun, Q.; Liu, Y. L.; Zhao, F. P.; Deng, S. X.; Lin, X. T.; Li, R. Y.; Hu, Y. F.; Sham, T. K.; Huang, H.; Zhang, L.; Yang, R.; Lu, S. G.; Sun, X. L., *Small Methods* **2019,** *3* (10), 1900261.

（121）Sakuda, A.; Hayashi, A.; Tatsumisago, M., *Chem. Mater.* **2010,** *22* (3), 949-956.

（122）Kitaura, H.; Hayashi, A.; Ohtomo, T.; Hama, S.; Tatsumisago, M., *J. Mater. Chem.* **2011,** *21* (1), 118-124.

（123）Glass, A. M.; Nassau, K.; Negran, T. J., *J. Appl. Phys.* **1978,** *49* (9), 4808-4811.

（124）Zhao, Y.; Zhang, L.; Liu, J.; Adair, K.; Zhao, F.; Sun, Y.; Wu, T.; Bi, X.; Amine, K.; Lu, J.; Sun, X., *Chem. Soc.Rev.* **2021,** *50* (6), 3889-3956.

（125）Woo, J. H.; Trevey, J. E.; Cavanagh, A. S.; Choi, Y. S.; Kim, S. C.; George, S. M.; Oh, K. H.; Lee, S. H., *J. Electrochem. Soc.* **2012,** *159* (7), A1120-A1124.

（126）Deng, S. X.; Li, X.; Ren, Z. H.; Li, W. H.; Luo, J.; Liang, J. W.; Liang, J. N.; Banis, M. N.; Li, M. S.; Zhao, Y.; Li, X. N.; Wang, C. H.; Sun, Y. P.; Sun, Q.; Li, R. Y.; Hu, Y. F.; Huang, H.; Zhang, L.; Lu, S. G.; Luo, J.; Sun, X. L., *Energy Storage Mater.* **2020,** *27*, 117-123.

（127）Kazyak, E.; Chen, K.-H.; Davis, A. L.; Yu, S.; Sanchez, A. J.; Lasso, J.; Bielinski, A. R.; Thompson, T.; Sakamoto, J.; Siegel, D. J.; Dasgupta, N. P., *J. Mater. Chem. A* **2018,** *6* (40), 19425-19437.

（128）Deng, S. X.; Sun, Y. P.; Li, X.; Ren, Z. H.; Liang, J. W.; Doyle-Davis, K.; Liang, J. N.; Li, W. H.; Banis, M. N.; Sun, Q.; Li, R. Y.; Hu, Y. F.; Huang, H.; Zhang, L.; Lu, S. G.; Luo, J.; Sun, X. L., *ACS Energy Lett.* **2020,** *5* (4), 1243-1251.

（129）Wang, S.; Bai, Q.; Nolan, A. M.; Liu, Y. S.; Gong, S.; Sun, Q.; Mo, Y. F., *Angew Chem. Int. Ed.* **2019,** *58* (24), 8039-8043.

（130）Schwietert, T. K.; Arszelewska, V. A.; Wang, C.; Yu, C.; Vasileiadis, A.; de Klerk, N. J. J.; Hageman, J.; Hupfer, T.; Kerkamm, I.; Xu, Y. L.; van der Maas, E.; Kelder, E. M.; Ganapathy, S.; Wagemaker, M., *Nat. Mater.* **2020,** *19* (4), 428-435.

Chapter 3

3 Experimental apparatus and characterization techniques

In this chapter, the experimental apparatus and main characterization methods are listed with brief introductions.

3.1 Experimental apparatus

Experimental apparatus used to synthesize SSEs and cathode coating layers are introduced in this sub-section.

3.1.1 Ball mill

The ball milling process is the first step to synthesize SSEs, in this thesis two kinds of ball mills are used to synthesize the sulfide SSEs. One is four-station planetary ball mill (**Figure 3.1a**). It is produced by Micro-Nano Tools Company in Canada. The other one is two-station PM200 (**Figure 3.1b**) produced by Retsch Company in Germany. The former one can support four ball milling jars working simultaneously, which can improve the synthesis efficiency. The latter one shows higher powder, which makes it easier to prepare glassy precursor of sulfide SSEs.

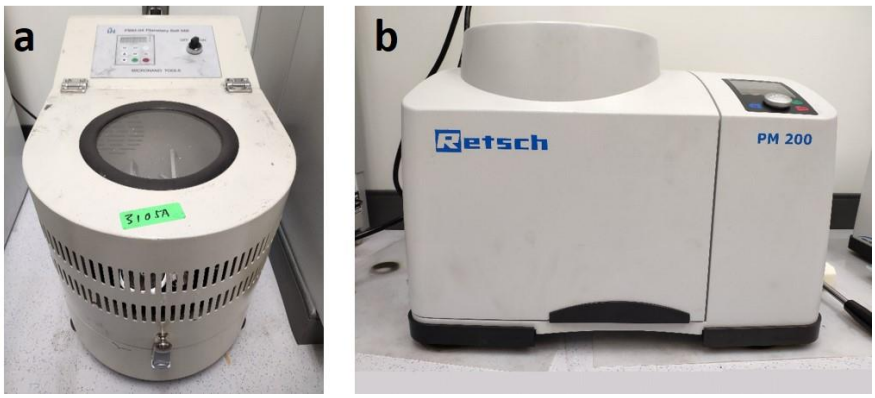

Figure 3.1 (a) A four-station planetary ball mill produced by Micronano Tools Company; (b) A PM200 two-station planetary ball mill produced by Retsch.

3.1.2 Quartz tube encapsulation

To prevent the exposure of air, quartz tube is used to encapsulate the SSEs under vacuum for heating treatments afterwards. **Figure 3.2a** shows the real picture of the quartz tube sealing equipment, which mainly consists of methane fuel gas and oxygen combustion accelerator, as well as the vacuum pump. Strict training and protective measures are need prior to operating this apparatus.

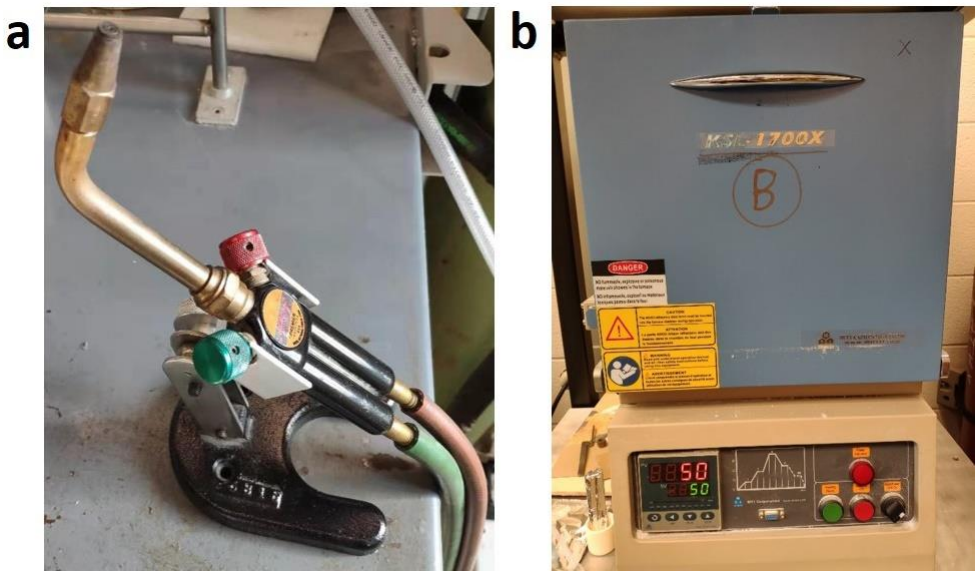

Figure 3.2 (a) The equipment for quartz tube encapsulation. (b) Muffle furnace used to synthesis inorganic SSEs

3.1.3 Muffle furnace

The muffle furnace is always used to provide heating treatments as the last step during synthesizing the inorganic SSEs in this thesis. As shown in **Figure 3.2b**, the muffle furnace can provide temperature-programmed heating from RT to 1700 ^{o}C.

3.1.4 Atomic layer deposition (ALD)

In this thesis, ALD is used to develop new Li zirconium oxides (LZO) and Li niobium oxides (LNO) coating layers on cathode materials to solve the cathode interface problem in ASSLBs. As shown in **Figure 3.3**, it is a real picture of the Savannah 200 ALD system,

which is produced by Veeco Instruments Inc. Details about using this ALD technique can be found in the experimental part of Chapter 6.

Figure 3.3 The Savannah 200 ALD system produced by Veeco Instruments Inc. in the USA.

3.2 Characterization techniques

In this section, normal physical characterizations (such as XRD, XPS, Raman, SEM, etc.) and electrochemical measurements are listed. In addition, large-scale experimental facilities, namely solid-state NMR and synchrotron-based X-ray characterizations are also introduced.

3.2.1 Physical characterizations

3.2.1.1 Solid-state nuclear magnetic resonance (ss-NMR)

The ss-NMR spectroscopy is powerful for probing the chemical environments of various magnetically active elements. It is ideal to investigate the subtle changes in local structure that occur upon alien elements participating or interaction generating.[1] In this thesis, on the one hand, magic angle spinning (MAS) ss-NMR is used analyze the chemical environment

of ^{31}P and ^{119}Sn in the glass and glass-ceramic sulfide SSEs. On the other hand, ss-NMR is used to precisely analyze the dynamic feature of Li^+ in SSEs via designing variable-temperature (VT) experiments. Specifically, the motional narrowing effect of NMR lineshapes for nuclei reflects the Li-ion dynamics in different crystal structures, while the spin-lattice relaxation time (T_1) indicates the rate of energy transfers from an excited state to equilibrium under the influence of neighboring environment (coordination, vacancy, etc.).[2]

The NMR-related work in this thesis was collaborated with Prof. Yining Huang's group in the department of chemistry of Western University. The ss-NMR facility is shown in **Figure 3.4**. It is a Varian Infinity Plus 400 (I+400), which can support variable-temperature NMR experiments from -140 °C to 250 °C.

Figure 3.4 The Infinity Plus 400 MAS Unit, Magnet, Console, and Computer.

3.2.1.2 Synchrotron-based X-ray characterizations

Synchrotron-based X-ray characterizations are completed at Canadian Light Source (CLS). The advanced synchrotron analytical techniques are capable of probing in various length and time scales in/ex-situ to study the structure and morphology of studying objects.

Compared with laboratory X-ray sources, one of the advantages of synchrotron radiation is the continuously tunable photon energy across a wide range (tens eV to tens keV) with pertained high brightness and flux.[3] X-ray near-edge absorption spectra (XANES) can be measured to analyze the oxidation state of interested elements in the targeted samples. X-ray diffraction can be used to analyze the crystal structure of materials. Soft X-ray (tens eV to ~2 keV) imaging helps to observe the morphology of the sample combining with the obtained spectra.

In this thesis, the author in-person operated the experiments at the VESPERS beamline (07B2-1) (**Figure 3.5a**) to gain the high-energy diffraction patterns to analyze the crystal structure of synthesized SSEs. STXM (**Figure 3.5b**) measurements was also conducted by the author at the SM beamline (10ID-1) to observe the cathode interface with and without ALD coating layers after cycling in ASSLBs. In addition, SXRMB, HXMA beamlines were used to collect XANES data to investigate the fine structure of elements in the SSEs and interfaces.

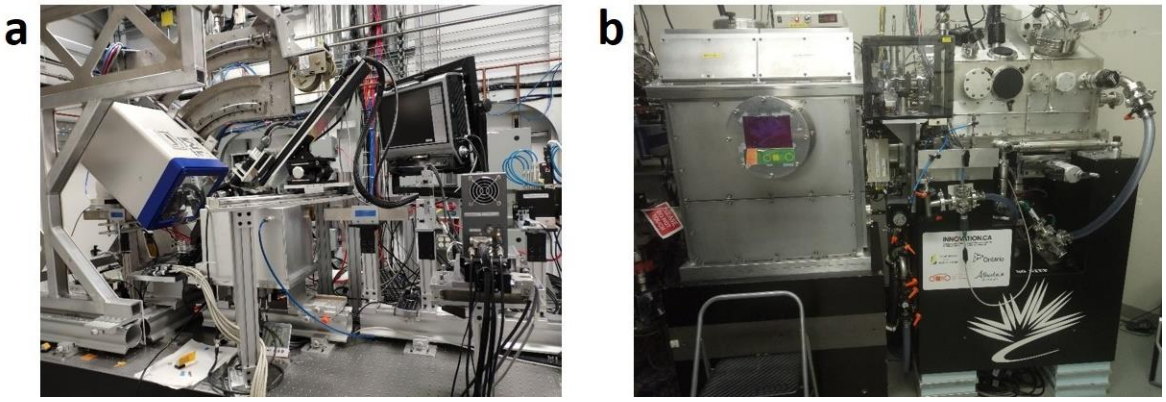

Figure 3.5 (a) CCD detector and working platform at the VESPERS beamline (07B2-1) of CLS; (b) Chamber and instrumentation group of STXM at the SM beamline (10ID-1) of CLS.

3.2.1.3 Lab X-ray diffraction (XRD)

Lab XRD was used to analyze the crystal structure generally. As shown in **Figure 3.6**, X-ray wavelength provided by the Bruker D8 Advance Diffractometer is 1.5406 Å (Cu Kα). The inset shows the XRD sample holder for protecting air-sensitive measurements. In XRD

patterns of this thesis, the broad diffraction peak at ~ 20º is due to the signal from the lid of the XRD holder.

Figure 3.6 The Bruker D8 Advance Diffractometer XRD system. The inset show the holder that prevent the air-sensitive samples (e.g., SSEs, electrode) from air exposure.

3.2.1.4 Raman

Raman spectroscopy is a technique to understand the vibration of chemical bonds through detecting the inelastic scattering of incident monochromatic light. In this thesis, the Raman spectra were collected on a HORIBA Scientific LabRAM Raman spectrometer equipped with a 532 nm laser (**Figure 3.7**). The Raman spectra were used frequently to analyze the coordination of polyhedral in sulfide SSEs in this thesis.

Figure 3.7 The HORIBA Scientific LabRAM HR Raman spectrometer system.

3.2.1.5 Thermo gravimetric analysis and differential scanning calorimetry (TGA-DSC)

As suggested in **Figure 3.8**, TGA-DSC measurements for the SSEs can examine the thermal stability according to the mass change, as well as monitor the heating flow of the SSEs to know the temperature of glass formation (T_g), crystallization (T_c), melting points (T_m), etc. In this thesis, the measurement was carried on SDT Q600 by TA Company to know the T_c of sulfide SSEs. Importantly, TGA-DSC test was used to record the mass change during the sulfide SSEs exposing to the O_2 or dry air to evaluate the air-stability of studied sulfide SSEs.

Figure 3.8 The SDT Q600 by TA Company to carry out the TGA-DSC measurements

3.2.1.6 Scanning electron microscope (SEM) and transmission electron microscope (TEM)

The morphologies of the SSEs and the Li metal surface were characterized by a Hitachi S-4800 SEM equipped with energy dispersive spectroscopy (EDS), as shown in **Figure 3.9**. In this thesis, the SEM imaging operates at an acceleration voltage of 5 kV, while the EDS mapping is conducted at 20 kV. TEM measurements were completed at the Canadian Centre for Electron Microscopy (CEEM). The JEOL 2010F field emission TEM (acceleration voltage 200 kV) was used to observe the nanostructure of LZO coating prepared by ALD method. The element mapping was analyzed by the equipped EDS.

Figure 3.9 The Hitachi S-4800 SEM, equid with EDS.

3.2.1.7 X-ray photoelectron spectroscopy (XPS)

XPS is used to analyze the chemical composition and bonding by detecting the amount of the escaped electrons from the surface of the samples at a certain excitation energy. In this thesis, the XPS measurements were carried out in Western Surface Science using an Ar glovebox connected XPS (Kratos AXIS Ultra Spectrometer) system for air sensitive samples.

3.2.1.8 Humidity-controlled chamber

The humidity-controlled chamber is customized as shown in **Figure 3.10** to study the air stability of modified sulfide SSEs.[4] Desiccating agents ($CaCl_2$, silica gel, etc.) were placed in the chamber to keep the humidity as low as possible in everyday situations. When SSE powder samples were placed in the chamber, high vacuum was applied to make the humidity dropped to < 1% immediately. Then, the vacuum valve was closed, while slowly

opening the air valve would flow into moist air. Once the hygrometer inside the chamber suggested a specific humidity value, the air valve would be closed as well. In this way, the SSE powder could be exposed to moist environment with designed humidity values for further studies.

Figure 3.10 The customized humidity-control chamber based on a vacuum oven. A hygrometer is placed in the chamber to indicate the real-time humidity value.

3.2.2 Electrochemical characterizations

3.2.2.1 Mold cell

The mold cell is custom-made as shown in **Figure 3.11**, consisting of two parts. The internal cell is used to fabricate the battery or testing cell via pressing layer-by-layer. The outer shell is used to seal the internal cell in the Ar-filled glovebox to prevent the air exposure. In this thesis, mold cells were used for various electrochemical characterizations, including electrochemical impedance spectroscopy (EIS) measurements, cyclic voltammetry (CV) tests, galvanstatic charge and discharge, linear scanning voltammetry (LSV) tests, galvanostatic intermittent titration technique (GITT) tests, etc.

Figure 3.11 A real photo showing the mold cell with the internal parts and the shell.

3.2.2.2 Electrochemical working station

EIS measurements, LSV tests and CV tests were completed on a multichannel potentiostation 3/Z (German VMP3). As shown in **Figure 3.12a**, the VMP3 was connected with a programmable thermal test chamber (-75 ^{o}C ~ 80 ^{o}C), so that VT-EIS could be realized.

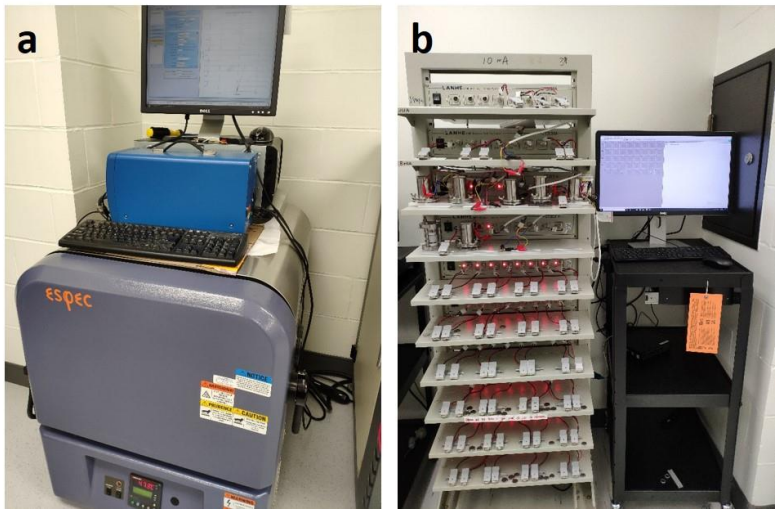

Figure 3.11 (a) The electrochemical working station of German VMP3, connected with a programmable thermal test chamber (-75 ^{o}C ~ 80 ^{o}C). **(b)** The Land 2001A Battery Test System.

3.2.2.3 Battery testing system

The battery performance is measured on the Land 2001A Battery Test System (**Figure 3.12b**). In this thesis, galvanstatic charge and discharge tests carried out on the system were used to examine the cycling stability and rater capability. GITT tests were carried on this system to study the Li^+ diffusion coefficient. The test system could be connected with low-temperature freezers and thermal ovens to study the battery performance at low and high temperatures, respectively.

3.3 References

（1）Morales, D. J.; Greenbaum, S., *Int. J. Mol. Sci.* **2020,** *21* (9), 3402.

（2）Yu, C.; Ganapathy, S.; de Klerk, N. J. J.; Roslon, I.; van Eck, E. R. H.; Kentgens, A. P. M.; Wagemaker, M., *J. Am. Chem. Soc.* **2016,** *138* (35), 11192-11201.

（3）Lin, F.; Liu, Y. J.; Yu, X. Q.; Cheng, L.; Singer, A.; Shpyrko, O. G.; Xing, H. L. L.; Tamura, N.; Tian, C. X.; Weng, T. C.; Yang, X. Q.; Meng, Y. S.; Nordlund, D.; Yang, W. L.; Doeff, M. M., *Chem. Rev.* **2017,** *117* (21), 13123-13186.

（4）Liang, J.; Chen, N.; Li, X.; Li, X.; Adair, K. R.; Li, J.; Wang, C.; Yu, C.; Norouzi Banis, M.; Zhang, L.; Zhao, S.; Lu, S.; Huang, H.; Li, R.; Huang, Y.; Sun, X., *Chem. Mater.* **2020,** *32* (6), 2664-2672.

Chapter 4

4 Fluorinated argyrodite sulfide solid-state electrolytes for excellent Li metal/SSE interface

All-solid-state Li metal batteries (ASSLMBs) have aroused significant attention because of their high energy density and improved safety. However, the poor stability at the Li anode/solid-state electrolyte (SSE) interface is the long-standing problem that limits the current density and capacity, thus hindering the practical application of ASSLMBs. In this chapter, fluorination of an Argyrodite Li_6PS_5Cl (LPSCl) sulfide electrolyte is proposed to enhance the interfacial stability towards the Li metal anode. Thanks to the condensed and highly fluorinated interface that forms in-situ with self-healing essence, the Li metal symmetric cell employing the fluorinated LPSCl SSE enables an ultra-stable Li plating/stripping over 250 hours at a super-high current density of 6.37 mA cm^{-2} and cut-off capacity of 5 mAh cm^{-2}. Furthermore, the Li metal treated by the fluorinated LPSCl SSE is demonstrated to deliver good durability and rate capability in full cells. Fluorinating sulfide electrolytes provides a new strategy to realize high-performance ASSLMBs.

*A version of this chapter has been published in *ACS Energy Letters* 2020, 5 (4), 1035-1043.

4.1 Introduction

All-solid-state Li-metal batteries (ASSLMBs) have been attracting increasing interest due to their high specific energy density and improved safety compared to conventional liquid-based Li-ion batteries (LIBs).[1-3] As one of the most important components of ASSLMBs, the solid-state electrolyte (SSE) plays a crucial role for the performance of ASSLMBs.[3-5] Over the past decades, a large amount of research has been reported in improving the ionic conductivity of SSEs. Sulfide-based SSEs exhibit a very competitive ionic conductivity compared with the oxide and polymer-based counterparts. In addition, sulfide-based SSEs can show a medium mechanical stiffness, intimate contact with electrode materials, as well as negligible grain boundary resistance.[6-9] Therefore, sulfide-based SSEs are viewed as one of the most promising SSEs candidates for the commercialization of high-performance ASSLMBs.[10-11]

However, the poor compatibility at the Li anode and sulfide SSE interface is one of the major problems in sulfide-based ASSLMBs.[11-12] The following issues need to be addressed at the Li metal/SSE interface: (1) The high reactivity between Li and sulfide SSEs:[13-14] sulfide SSEs can be easily reduced by Li metal and decompose to form a passivation layer. The uncontrollable growth of the passivated layer can increase the interface impedance with continued cycling, eventually leading to performance degradation. (2) Li dendrite formation through the grain boundary or voids in sulfide SSEs:[15-16] electrons are inclined to accumulate on the grain boundary, which facilitates dendrite growth and propagation. Consequently, Li dendrites grow along the grain boundaries or voids of the SSE resulting from the inherent loose tap-density. This would eventually lead to internal short circuits and battery failure.

Surface modification of the Li anode can effectively prevent the interfacial side reactions and the Li dendrite growth to some extent.[17-20] Both F and I-containing Li surfaces obtained by pretreating Li metal with various chemicals have been reported to be effective in reducing the interface impedance and hindering the formation of Li dendrites. However, the relatively low plating/stripping current density and capacity at room temperature (RT) (less than 0.5 mA cm^{-2}/ 0.5 mAh cm^{-2}) limit their applications in high-rate ASSLMBs. On

the other hand, LPS-based (Li_3PS_4) SSEs incorporated with LiI additives can show significantly improved capabilities (1 mA cm^{-2}/ 1 mAh cm^{-2} at RT) in suppressing Li dendrite at the Li/LPS-LiI interface.[21] The LiI-containing solid-electrolyte interphase (SEI) layer can provide a favorable Li^+ ion conductivity and enable a homogeneous Li deposition. Nevertheless, considering the requirement for the practical application of ASSLBs, these previous reported strategies are still insufficient to meet the high current densities and cut-off capacities required to compete with state-of-the-art LIBs based on liquid electrolytes.[22]

LiF is a very popular compound that is widely employed as an essential component in stabilizing the SEI layer.[23-26] Additionally, it is reported that comparing with the strategy that is developed on the surface treatment of Li metal, the other one based on modifying SSEs exhibits a better protection for the Li metal. This is attributed to the self-healing feature of the SEI layer that forms in-situ between the electrolyte and Li metal during cycling.[27-28] However, to the best of our knowledge, it is hardly reported that using F-containing SSEs to derive the formation of functional SEI layers with high concentration of LiF. Herein, the concept that fluorinating the sulfide-based SSEs can induce the formation of highly fluorinated Li anode interface is proposed. We take Argyrodite Li_6PS_5Cl (LPSCl) SSE as the host material, and successfully incorporate F by replacing LiCl with various contents of LiF in the precursors to synthesize fluorinated $LPSCl_{1-x}F_x$ sulfide SSEs (x = 0.05, 0.3, 0.5, 0.7, 0.8, and 1). The Li symmetric cell using the optimized '$LPSCl_{0.3}F_{0.7}$' SSE can deliver an ultra-stable Li plating and stripping for over 250 h at a rarely reported current density of 6.37 mA cm^{-2} and specific capacity of 5 mAh cm^{-2} at RT. This performance can be even comparable to the best performances in the liquid-electrolyte counterparts. The in-situ formed interface between the Li metal and $LPSCl_{0.3}F_{0.7}$ SSEs possesses a dense morphology and shows high concentration of LiF, playing a crucial role in achieving the high performance. In addition, when the high-quality Li anode interface is applied to the full cell, very promising cycling stability and rate performance are achieved at RT.

4.2 Experimental section

4.2.1 Preparation of materials

$LPSCl_{1-x}F_x$ (x = 0, 0.05, 0.3, 0.5, 0.7, 0.8, 1) sulfide-based SSEs: The starting materials are Li_2S (Alfa Aesar, 99.9%), P_2S_5 (Sigma Aldrich, >99%), LiCl (Alfa Aesar, 99.9%, ultra-dry), and LiF (Sigma Aldrich, 99.98%). Firstly, they were weighed in appropriate molar ratio and mixed by hand with an agate mortar. The 1 g of this mixture was then placed in a zirconia pot containing ~40 g of zirconia balls, and the mixture was mechanically milled by using the planetary ball milling apparatus at 510 rpm for 13 h. All operations were conducted in an Ar-filled glovebox. Then, the resulting ball-milled product was pressed into pellets, sealed in a quartz tube, and heated at a reaction temperature of 550 ^oC for 5 h in a muffle furnace. The temperature was raised at a rate of 20 ^oC/min. After the reaction was completed, the quartz tube was slowly cooled to room temperature. LCO@LNO cathode materials and LCO@LNO/LPSCl cathode composites: As reported elsewhere, commercial LCO (Sigma Aldrich, 99.8%) was coated with LNO layer on the surface via a sol-gel method. The LCO@LNO/LPSCl cathode composite was prepared by milling LCO@LNO powder and LPSCl electrolyte in a ratio of 7:3 with a roll mixer.

4.2.2 Ionic conductivity measurements

Ionic conductivity of various $LPSCl_{1-x}F_x$ electrolytes were measured by the a.c. impedance method. This was completed on a versatile multichannel potentiostation 3/Z (VMP3). The applied frequency range is 1 Hz to 7 MHz and the amplitude is 10 mV. The temperature related ionic conductivities were obtained at various temperature between -25 ^oC to 25 ^oC with an elevated step of 10 ^oC. The cell was fabricated as follows: 100 mg of $LPSCl_{l-x}F_x$ electrolyte powder was pressed into a pellet (diameter 1 cm; thickness 0.7 mm) with a pressure of ~ 240 MPa. Two pieces of indium (In) foil were used as the current collectors pressed successively on both sides of the pressed electrolyte pellet in a model cell.

4.2.3 Cell assembly and electrochemical measurements

All-solid-state Li//$LPSCl_{0.3}F_{0.7}$//Li symmetric cells were assembled to evaluate the electrochemical performance of the electrolytes towards Li metal. Typically, 80 mg of $LPSCl_{0.3}F_{0.7}$ electrolytes was pressed successively under 240 MPa to form solid electrolyte layer. Two pieces of Li metal (purchased from *China Energy Lithium Co. LTD*) were subsequently pressed onto both sides of the $LPSCl_{1-x}F_x$ electrolyte layer under 50 MPa. Li

plating/stripping measurement was conducted on LAND battery test systems (CT-2001A, Wuhan Rambo Testing Equipment Co., Ltd.). Specific current densities and cut-off capacities were set firstly for cell testing. For all-solid-state Li@LPSCl$_{0.3}$F$_{0.7}$//LPSCl//LCO@LNO/LPSCl batteries, Li@LPSCl-70F anode is the Li metal electrode that was obtained after Li plating/stripping in Li//LPSCl$_{0.3}$F$_{0.7}$//Li symmetric cells. The used current and capacity are 0.127 mA cm^{-2} and 0.1 mAh cm^{-2}, respectively. The plating/stripping time is ~200 h (127 cycles). Pure Li_6PS_5Cl (LPSCl) electrolytes was used as the electrolyte, and the cathode composite is LCO@LNO/LPSCl. Typically, 80 mg of the LPSCl electrolyte was pressed successively under 240 MPa to form a solid electrolyte layer. The cathode composite powder was uniformly spread onto the surface of the electrolyte layer and pressed under 360 MPa. Li metal anode was subsequently pressed onto the other side of the electrolyte layer under 50 MPa. The three-layered pellet was sandwiched between two stainless-steel rods as current collectors. Galvanostatic charge-discharge was conducted on the LAND battery test system. The voltage window was 2.8~4.2 V (vs. Li/Li$^+$). Rate performance was obtained by elevating the discharge current densities from 0.05 C to 0.1, 0.2, 0.5, 0.8, and 1 C (1 C corresponds to 1.3 mA cm^{-2}), while maintaining the charge current density at 0.05 C. All processes of assembling solid-state cells were performed in an Ar-filled glove box. Liquid electrolyte-based coin cells were assembled by employing Li metal as the reference electrode and polypropylene separator (Celgard 2400) as the separator. Cathode is prepared by casting LCO sllurry on Al foil. N, N-Dimethylformamide (NMP) was used as the solvent to dissolve the mixture of LCO/ Super P/ poly (vinylidene difluoride) (PVDF) (8:1:1) to form the slurry. The electrode was vacuum-dried at 120 ^{o}C overnight prior to use. The active material loading is ~ 1 mg cm^{-2}. Charge and discharge profiles were obtained in LAND battery test system within the voltage window of 2.8~4.2 V (vs. Li/Li$^+$) at the current density of 0.05 C.

4.2.4 Characterization methods

SEM images and element dispersion were obtained by using a Hitachi S-4800 field-emission scanning electron microscope (FE-SEM, acceleration voltage 5 kV) equipped with energy dispersive spectroscopy (EDS). Lab X-ray diffraction (XRD) measurements

were performed on Bruker AXS D8 Advance with Cu Kα radiation (λ = 1.54178 Å). Raman spectra were measured with a HORIBA Scientific LabRAM HR Raman spectrometer operated under an incident laser beam at 532 nm. X-ray photoelectron spectroscopy (XPS) spectra were obtain by using Krotos AXIS Ultra Spectrometer system using a monochromatic Al K(alpha) source (25mA, 15kV). The Kratos charge neutralizer system was used for all analyses. High resolution analyses were carried out with an analysis area of 110 microns and a pass energy of 40 eV. For depth profiling, a gas cluster ion source beam of 20 KeV Ar500+ with a sputter area of 1.4 × 1.4 mm was used. Multiple signal collections (50 times in total) were conducted after sputtering for 30 min at intervals. For post-analysis of the Li metal and the interface after Li plating/stripping measurements, the cycled all-solid-state cells were disassembled in the Ar-filled glovebox. Li metal specimen were sealed in centrifuge tubes with parafilm for transportation and testing. All cross-sections of the specimen were prepared by cutting the cell with a blade. Residual electrolytes powder were blew away before the characterization. ToF-SIMS measurements were conducted using an ION-TOF (GmbH, Germany) ToF-SIMS IV with a bismuth liquid metal ion source in the Surface Science Western (SSW). The base pressure of the analysis chamber was ~10^{-8} mbar. The action of the primary ion beam bombardment on the sample surface induces the emission of negative secondary ions. Sputtering with a Cs^+ ion beam (3 keV) was used for depth profiling analysis.

4.3 Results and discussion

Using the conventional solid-state reaction method, various amounts of LiF were employed as one of the Li-halogen starting materials in replacement of LiCl to prepare a series of fluorinated $LPSCl_{1-x}F_x$ sulfide-based SSEs with different contents of incorporated F (see the detail in Experimental Procedures). X-ray diffraction (XRD) measurements were conducted in an air-sensitive sample holder for the prepared SSEs. The evolution of the phase composition in the final products with different amount of incorporated F is displayed in **Figure 4.1**a. It is noted that the broad diffraction peak at around 19° is caused by the background from the Kapton film used on the holder, and the additional diffraction peak at ~27.0 is assigned to the trace of Li_2S raw materials (PDF# 00-026-1188). When x = 0, the product is pure Argyrodite Li_6PS_5Cl electrolyte, and the corresponding diffraction

peaks are consistent with the standard LPSCl pattern indexed as PDF# 04-018-1429.[29] With the fluorination degree of LPSCl-based electrolytes increasing, the phase transformation from LPSCl to β-Li_3PS_4 is observed. The intensity of characteristic diffraction peaks belonging to the Li_6PS_5Cl phase reduces continuously, while the characteristic peaks of β-Li_3PS_4 phase (PDF# 04-010-1784) become apparent gradually. Diffraction peaks belonging to LiF can be observed after x = 0.5, which can be attributed to the excessive LiF precursor existing after completely incorporating F to the LPSCl structure. The excessive LiF can fill in the boundary/pore of the SSEs, which is able to reduce the electronic conductivity and enhance the rigidity of the SSEs to suppress the penetration of Li dendrites.[30] X-ray photoelectron spectroscopy (XPS) was then employed to analyze the element chemical environment of the introduced F in the fluorinated $LPSCl_{1-x}F_x$ sulfide SSEs. As shown in **Figure 4.1b**, once the x reaches 30, an obvious peak at 686.7 eV can be observed. This is ascribed to the interaction between F and PS_4^{3-} molecules, which can be expressed as '$F^{\delta-}$-$Li^{\delta+}$-$PS_4^{\delta-}$'.[31] The existing peaks at 684.9 eV suggest that existence of Li-F bonds in the prepared $LPSCl_{1-x}F_x$ sulfide SSEs.[18] The corresponding change for S 2p and P 2p spectra can be observed in **Figure S4.1** in the supporting information. The characteristic peaks shift to higher binding energy, confirming the electron cloud around S and P becomes weak after F incorporation. Raman spectra of the series of fluorinated $LPSCl_{1-x}F_x$ (x = 0, 0.5, 0.7, 0.8, 1) sulfide-based SSEs (**Figure S4.2**) also verify that the F incorporation can cause a red shift of the P-S symmetric stretching of PS_4^{3-} fingerprint ions (at ~ 425 cm^{-1}),[32-33] indicating a strong electronegativity effect of F elements towards the PS_4^{3-} molecules. However, the acquisition of further detailed structure information is still needed in future studies.

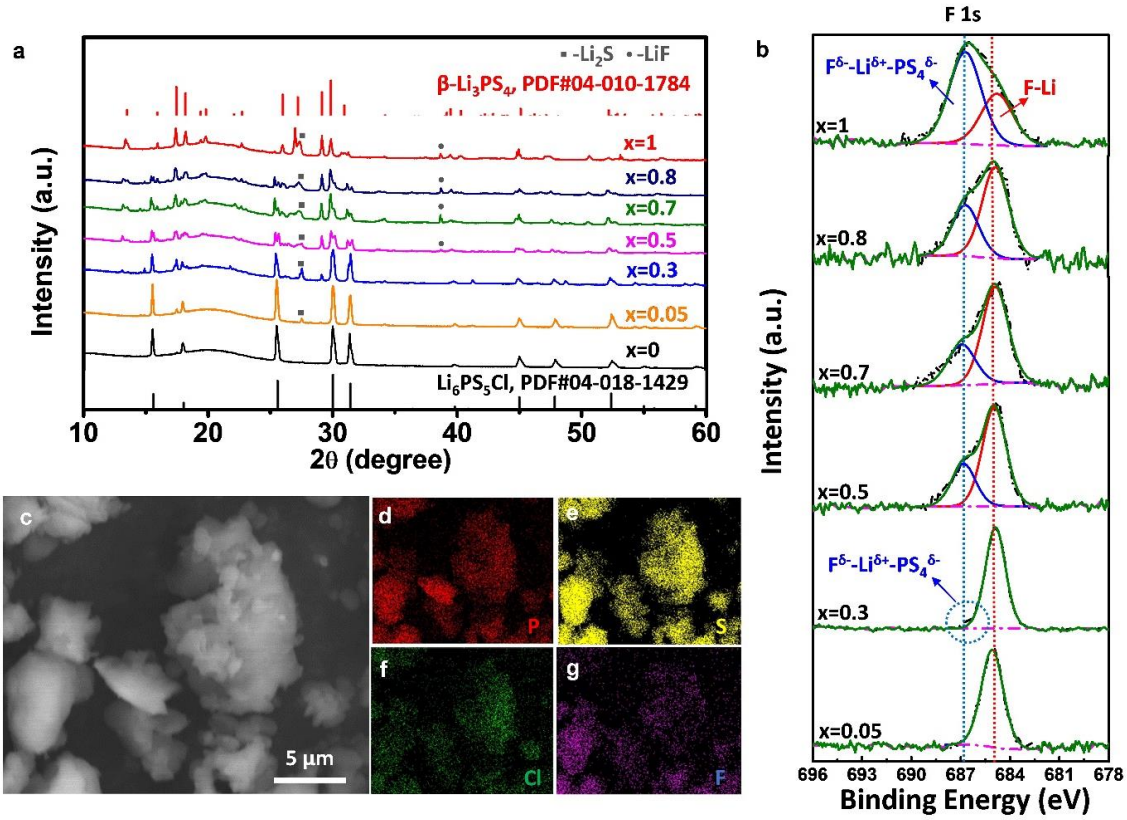

Figure 4.1 Characterizations of fluorinated sulfide-based SSEs. (a) XRD patterns of the prepared $LPSCl_{1-x}F_x$ sulfide-based electrolytes (x = 0, 0.05, 0.3, 0.5, 0.7, 0.8, 1). (b) XPS spectra of F 1s in $LPSCl_{1-x}F_x$ sulfide-based electrolytes (x = 0.05, 0.3, 0.5, 0.7, 0.8, 1). (c) A SEM image of the $LPSCl_{0.3}F_{0.7}$ electrolyte. (d-g) EDX element mapping of the observed area of (c).

Morphology of the prepared $LPSCl_{0.3}F_{0.7}$ electrolyte was studied via using scanning electron microscopy (SEM). Similar to other reported Lithium Argyrodite SSEs,[29, 34] the $LPSCl_{0.3}F_{0.7}$ electrolyte shows irregular particles with micro-level size (**Figure 4.1c**). Energy disperse spectroscopy (EDS) element mapping (**Figure 4.1d-g**) for the selected area demonstrates that elements P, S, Cl, and F are homogeneously distributed. Electrochemical impedance spectroscopy (EIS) was employed to derive the ionic conductivity of prepared $LPSCl_{1-x}F_x$ electrolytes. As shown in **Figure S4.3**, the ionic conductivity decreases with an increase of F content at RT. The ionic conductivity of pure LPSCl electrolytes at RT reaches 3.1×10^{-3} S cm^{-1}, which agrees well with the published results.[35] When fully introducing F (x = 1) in the electrolyte, the ionic conductivity drops

to 5.2 × 10^{-4} S cm^{-1}. This ionic conductivity falls right at the level of LPS-based (β-Li_3PS_4) electrolytes. This evolution trend reflects that incorporated F in Argyrodite LPSCl phase can induce the gradual formation of a β-Li_3PS_4 conductive phase. Direct current (DC) polarization measurements (**Figure S4.4**) were conducted to determine that the electronic conductivity of one representative composition: $LPSCl_{0.3}F_{0.7}$ SSEs is approximately 9.85 × 10^{-10} S cm^{-1}, which is lower than that of the LPSCl SSEs (6.81 × 10^{-9} S cm^{-1}). The lower electronic conductivity is favorable and can restrict the formation of Li dendrite at Li/SSE interface, as demonstrated recently by Han et al.[36]

The interface stability between Li metal and fluorinated $LPSCl_{1-x}F_x$ sulfide SSEs was then carefully evaluated through cycling Li-Li symmetrical cells under various current densities and cut-off capacities. As demonstrated in **Figure S4.5**, due to the Li dendrite grows arbitrarily through the SSE, short circuits quickly occur in the symmetric cells with pure LPSCl and pure β-Li_3PS_4 electrolytes.[16, 37] $LPSCl_{1-x}F_x$ electrolytes with low degree of fluorination (x = 0.05, 0.3, and 0.5) cannot effectively prevent the short circuit caused by dendrite growth, while high degree of fluorination (x = 0.8 and 1) can cause large overpotentials because of the lower ionic conductivity of the SSEs and thicker fluorinated interphase formed during plating/stripping. By contrast, x = 70 is found to be the optimized condition to guarantee a stable Li/$LPSCl_{0.3}F_{0.7}$ interface, with a limited overpotential and long cycling durability. As shown in **Figure 4.2**a, under a moderate plating/stripping condition of 0.127 mA cm^{-2} and 0.1 mAh cm^{-2}, the initial overpotential is around 15 mV (**Figure 4.2a-1**). This value is approximately three times larger than that for plating/stripping of Li in pure LPSCl electrolyte-based Li-Li symmetric cells, which is ascribed to the lower ionic conductivity of $LPSCl_{0.3}F_{0.7}$ electrolytes (7.1 × 10^{-4} S cm^{-1} at RT). With the initial activation process, a stable Li/$LPSCl_{0.3}F_{0.7}$ interface starts to form, and the overpotential reaches a maximum of 40 mV (**Figure 4.2a-2**). This in-situ formed Li/$LPSCl_{0.3}F_{0.7}$ interphase is robust and can prevent further side reactions and Li dendrite formation. Even after 1000 hours, the Li// $LPSCl_{0.3}F_{0.7}$//Li symmetric cell remains stable, and shows a very stable overpotential that recovers to the initial state at around 17 mV (**Figure 4.2a-3**). Time-resolved EIS profiles (**Figure S4.6**) are recorded for the Li/$LPSCl_{0.3}F_{0.7}$ interfacial impendence evolution at different stages during the plating/stripping process. The results agree well with the changes in cell overpotential,

suggesting that electrochemically derived interface evolution enables the formation of a robust and stable Li/$LPSCl_{0.3}F_{0.7}$ interface.

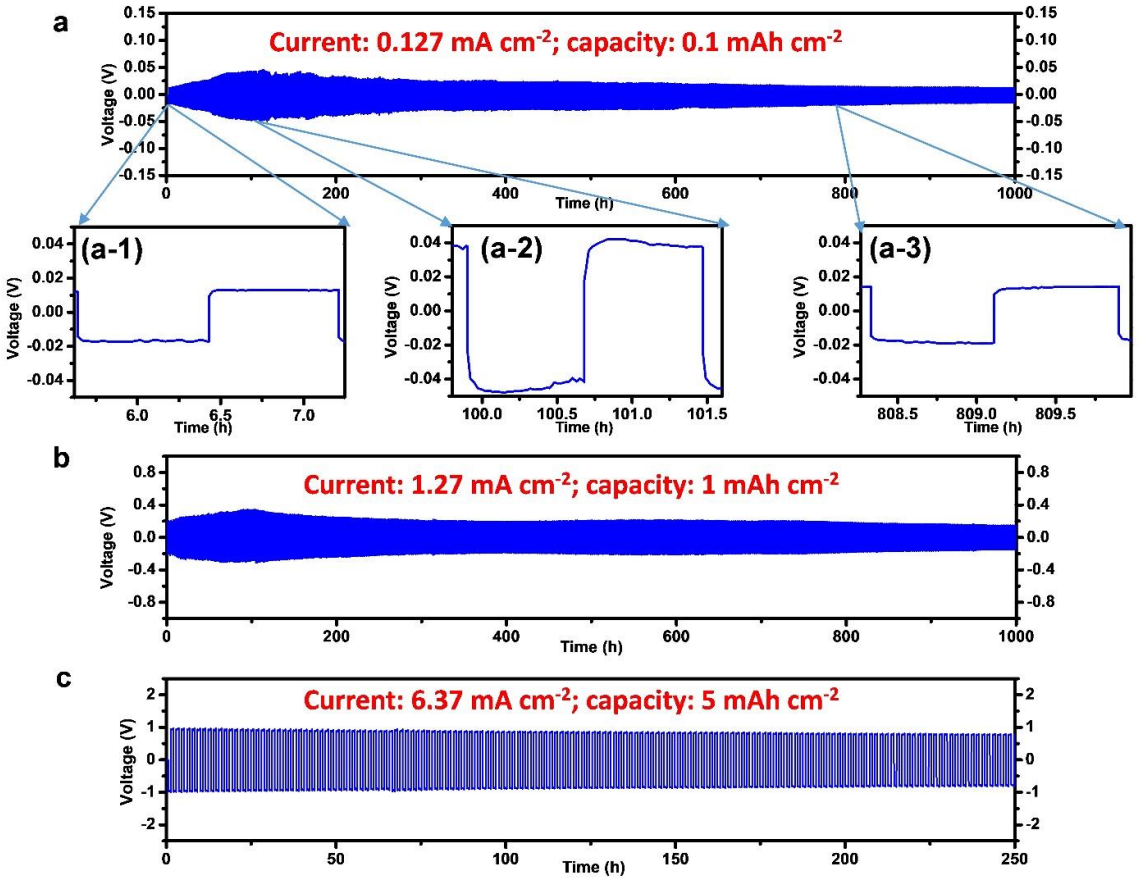

Figure 4.2 Li plating and stripping in Li//$LPSCl_{0.3}F_{0.7}$//Li symmetric cells. (a) The current density: 0.127 mA cm^{-2}, and the cut-off capacity: 0.1 mAh cm^{-2}. (a-1, 2, and 3) are the magnified areas in (a). (b) The current density: 1.27 mA cm^{-2}, and the cut-off capacity: 1 mAh cm^{-2}. (c) The current density: 6.37 mA cm^{-2}, and the cut-off capacity: 5 mAh cm^{-2}.

The Li plating/stripping behavior at 1.27 mA cm^{-2} and 1 mAh cm^{-2} is displayed in **Figure 4.2b**. The symmetric cell undergoes a similar initial activation process as the cells cycled at 0.127 mA cm^{-2}: the overpotential raises from ~220 mV to ~350 mV in the initial 100 hours, followed by a stable overpotential which is maintained at ~150 mV after 1000 hours. More remarkably, when we elevated the current density and cut-off capacity to 6.37 mA cm^{-2} and 5 mAh cm^{-2} respectively for the cycled symmetric cell, the cell can continue performing an ultra-stable Li plating and stripping for another 250 hours (**Figure 4.2c**).

The magnified polarization curves of Li plating/stripping are shown in **Figure S4.7**, suggesting a typically featured Li nucleation and growth process at such high current density and cut-off capacity. To the best of our knowledge, the presented Li//$LPSCl_{0.3}F_{0.7}$//Li symmetric cell performance has surpassed any other reported performance with various sulfide SSEs at RT, and can be comparable to the best performance in liquid electrolyte systems without using complicatedly designed Li metals (see the performance comparison in **Table S4.1**).

To understand the reason behind the high performance in Li//$LPSCl_{0.3}F_{0.7}$//Li symmetric cells, several characterizations were carried out. Firstly, rest time-resolved EIS of the fabricated Li//$LPSCl_{0.3}F_{0.7}$//Li symmetric cell (**Figure S4.8**) verifies that the Li/$LPSCl_{0.3}F_{0.7}$ interface is chemically stable, due to the negligible change of the interface impedance during 24 hours. Then, SEM was used to examine the morphology difference between LPSCl and $LPSCl_{0.3}F_{0.7}$ electrolytes pellets made through cold pressing before electrochemical cycling. **Figure S4.9a** suggests that there is large area of cracks on the surface of the LPSCl pellet. These gaps would provide space for the Li dendrite growth, and thus easily cause short circuits.[38] By contrast, the surface of $LPSCl_{0.3}F_{0.7}$ pellet (**Figure S4.9b**) is much denser and relatively smoother, resulting from the good densification ability of $LPSCl_{0.3}F_{0.7}$ electrolyte derived from the effective fluorination. For the $LPSCl_{0.3}F_{0.7}$ SSE with F incorporated, the bonding energy of P-S is reduced, while the free volume of the SSE would increase to reduce the Young's modulus.[39] The lower bonding energy and Young's modulus can result in an increase of relative density for enhanced densification ability of the electrolyte.[39] In addition to the potentially improved mechanical property of the fluorinated $LPSCl_{0.3}F_{0.7}$ sulfide SSE, the in-situ formed functional Li/$LPSCl_{0.3}F_{0.7}$ interface is confirmed by using various characterizations. Ex-situ SEM measurements were conducted to study the morphology of the Li metal surface after Li plating/stripping for ~200 h (0.127 mA cm^{-2}/ 0.1 mAh cm^{-2}) in the Li//$LPSCl_{0.3}F_{0.7}$//Li symmetric cell (namely underwent activation process). As suggested in **Figure 4.3**a-1, the Li surface after the Li plating/stripping is very smooth. Close observation (**Figure 4.3a-2**) suggests that numerous nanosheets are present on the consecutive and homogeneous surface. The side-view SEM images of the Li metal layer **(Figure S4.10**) also suggest the formation of sheet like coating on the Li metal surface. However, obvious corrosion

reactions happen to the Li/LPSCl interface (Li plating/stripping for ~20 h) as suggested in Figure **S4.11a**. The black spots in **Figure S4.10b** indicate the lithium dendrite growth from these sites. Side-view SEM images of the Li metal surface (obtained after the short circuit happens to the Li//LPSCl//Li symmetric cell) can also witness the formation of Li dendrites (**Figure S4.11c** and **d**).

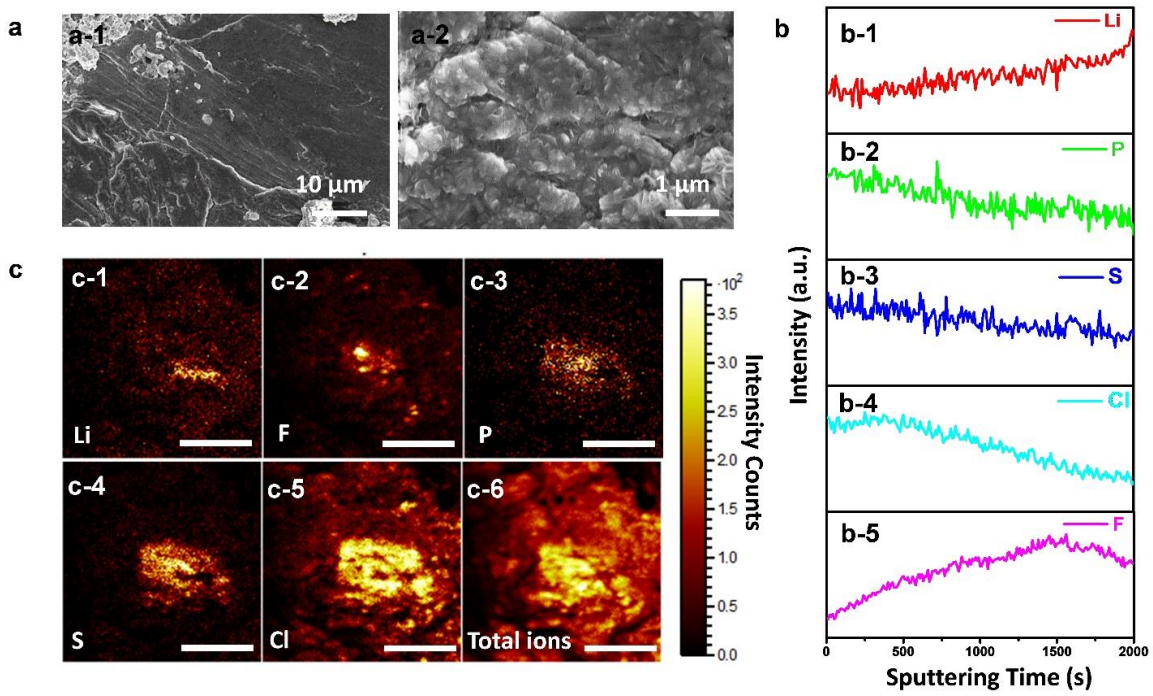

Figure 4.3 Characterizations of Li metal after cycling in the symmetric cells. (a) SEM images of the Li metal surface morphology. (b) ToF-SIMS depth profiles of each element on the Li metal. (c) Chemical species images on the Li metal after sputtering with Cs^+ ion beam during the ToF-SIMS measurement. Scar bar: 200 um.

Time-of-flight secondary ion mass spectrometry (ToF-SIMS) was used to analyze the surface chemical species on the cycled Li metal electrode with ion milling depth profiling. For an analysis area of 500 um × 500 um, before Cs^+ ions sputtering, the obtained chemical species mapping suggest Li, F, P, S, Cl species disperse uniformly on the Li metal surface (**Figure S4.12**). Along with Cs^+ ions sputtering, ToF-SIMS depth profiles are performed in **Figure 4.3b**. Increasing count intensity of Li suggests detection depth is gradually approaching the Li metal surface. Obviously, the intensity of P, S, and Cl species decrease

with this increased probing depth. It is interesting to note that the maximum F intensity was observed before reaching to the Li metal surface, which suggests the F species have a gradient dispersed in the direction perpendicular to the Li metal surface. After Cs^+ ions sputtering, the series of chemical species images are indicated in **Figure 4.3c**. The spatially different disperse of Li, F, P, S, Cl containing species derived from gradient differences can also be observed directly.

XPS depth profiling analysis was further conducted to study the chemical composition of the Li/$LPSCl_{0.3}F_{0.7}$ interface (after ~200 h pre-cycling in the Li//$LPSCl_{0.3}F_{0.7}$//Li symmetric cell at 0.127 mA cm^{-2}/ 0.1 mAh cm^{-2}). Multiple signal collections (50 times in total) were conducted after sputtering with the Ar500+ cluster ion source for 30 min at intervals. The overall spectra evolution of P 2p, S 2p, and Cl 2p from the Li@$LPSCl_{0.3}F_{0.7}$ surface to the Li metal is present in **Figure S4.13**. Along with the sputtering depth increasing, signal intensities gradually reduce and nearly reach zero towards the end of the testing period, suggesting the depth profiling successfully penetrated through the interface layer to the Li metal layer. The spectra evolution of Li 1s and F 1s are studied in detail as displayed in **Figure 4.4a** and **b**, respectively. Representative spectra of Li 1s and F 1s in different layers of interest are extracted and summarized as **Figure 4.4c**. The spectra of 1# ~ 3# are assigned to the SSE layer. The intensity of both Li 1s and F 1s in this layer tend to decrease when progressing towards the interface. No binding energy shift is observed in the characteristic peaks of each element, indicating the peripheral $LPSCl_{0.3}F_{0.7}$ SSE is stable against Li metal. In the interface layer (4# ~ 8#), for Li 1s spectra, peaks at ~55.9 eV assigned to the Li 1s in the $LPSCl_{0.3}F_{0.7}$ electrolyte reduce along with increasing sputtering depth, which accompanies with the rise of elemental Li (Li^0) peak at ~53.9 eV.[17, 40] One small peak at ~55.1 eV starts to occur at the place that is very close to the Li metal and even in the Li metal layer, which is related to the strong electronegativity of F towards Li in LiF compounds. F 1s spectra at the interface show a different evolution trend compared with Li 1s. The dominant F species at the interface is from Li-F bonds (indexed at ~684.8 eV).[19] The intensity of Li-F (from $LPSCl_{0.3}F_{0.7}$ SSEs) reduces in the initial of reaching the interface layer because of the vanishing $LPSCl_{0.3}F_{0.7}$ SSEs, while increase in the deeper interface closing to the Li metal resulting from the gradual formation of LiF compounds. This result agrees well with the ToF-SIMS result as shown in **Figure 4.3b** and **c**. In short,

effective LiF-containing interface was formed through the interface and the closed Li metal layer, serving as the robust protection layer for the observed ultra-stable Li plating/stripping.

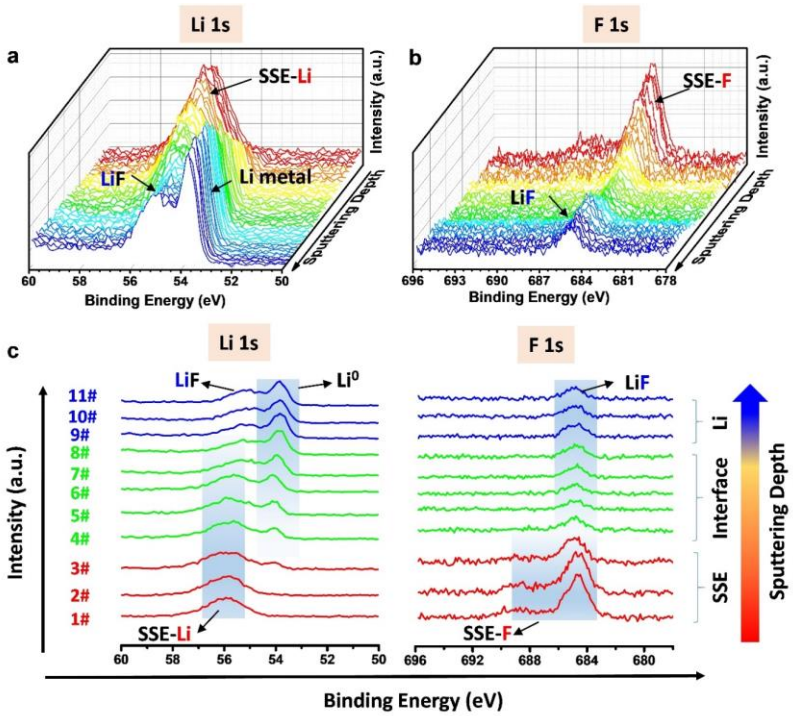

Figure 4.4 XPS depth profiling analysis of the Li metal/SSE interface. (a and b) Overall spectra evolution of Li 1s and F 1s along with the sputtering depth at the Li/$LPSCl_{0.3}F_{0.7}$ interface. (c) Representative XPS spectra of Li 1s and F 1s extracted from Figure 4.4a and b.

Overall, the smooth interphase of Li/$LPSCl_{0.3}F_{0.7}$ with dense and sheet-like morphology is formed in-situ after the initial activation process. Moreover, the fluorinated $LPSCl_{0.3}F_{0.7}$ electrolyte can support the formation of robust fluorinated interface (rich-LiF). Also, the self-healing feature of this interface layer guarantees a long-term protection. All these morphology and physicochemical properties have been demonstrated to play very important roles in preventing Li dendrite formation and stabilize the interface between Li metal and sulfide electrolytes.

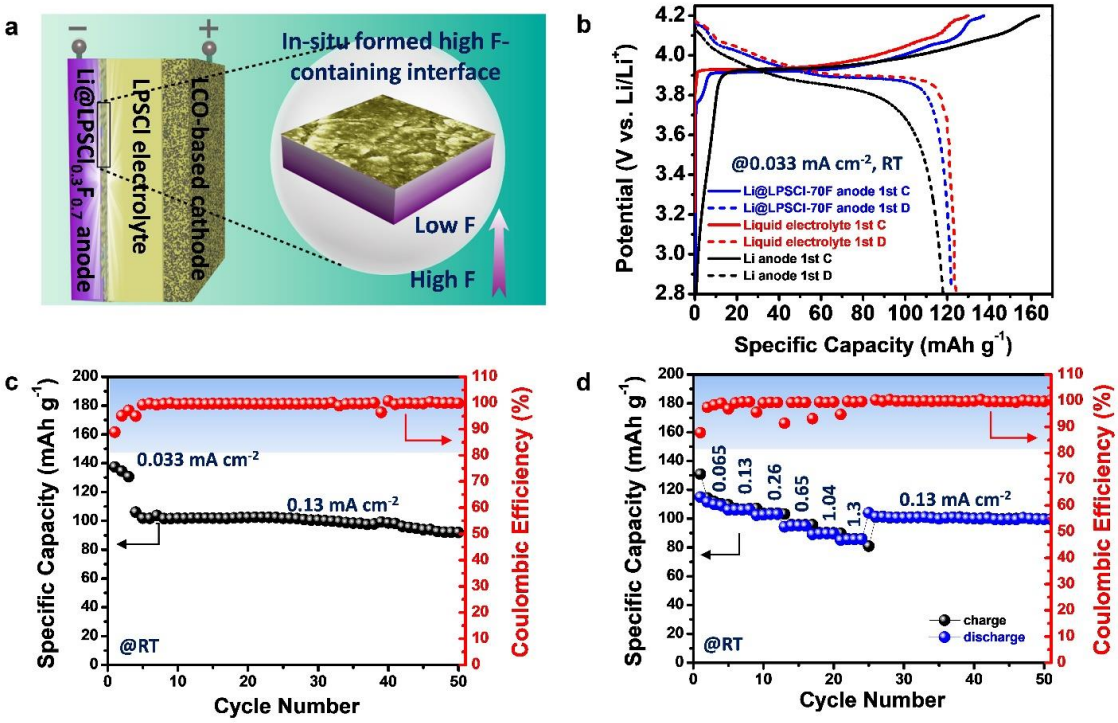

Figure 4.5 Electrochemical performance of ASSLMBs. (a) Schematic diagram of the Li@LPSCl$_{0.3}$F$_{0.7}$//LPSCl//LCO@LNO/LPSCl ASSLMBs with the highlighted fluorinated interface layer. (b) Charge-discharge profiles of the fabricated ASSLMBs. (c) Cycling stability of the Li@LPSCl$_{0.3}$F$_{0.7}$//LPSCl//LCO@LNO/LPSCl ASSLBs at RT. (d) Rate capability of the Li@LPSCl$_{0.3}$F$_{0.7}$//LPSCl//LCO@LNO/LPSCl ASSLBs at RT.

To demonstrate the application potential of the stabilized Li metal interface with high degree of fluorination, sulfide-based ASSLMBs are constructed by using LPSCl$_{0.3}$F$_{0.7}$ pretreated Li metal (~200 h plating/stripping at 0.127 mA cm^{-2}/ 0.1 mAh cm^{-2}) as the anode (Li@ LPSCl$_{0.3}$F$_{0.7}$), LiCoO$_2$ (LCO) with a LiNbO$_x$ (LNO) protection coating layer combining with LPSCl as the cathode composite (LCO@LNO/LPSCl), and LPSCl as the electrolyte (**Figure 4.5**a). The loading mass of the LCO cathode is ~8.92 mg cm^{-2}. SEM images and EDX elements mapping of the cross section of this full battery are presented in **Figure S4.14**, indicating good contacts between the LPSCl$_{0.3}$F$_{0.7}$ anode and LPSCl SSEs as well as within the cathode layer. Room temperature (RT) galvanostatic charge and discharge experiments were conducted in the voltage range of 2.8 ~ 4.2 V (vs. Li/Li$^+$). The charge and discharge curve obtained at a low current density of 0.033 mA cm^{-2} (1 C

corresponds to 1.3 mA cm^{-2}) is shown as the blue curve in **Figure 4.5b**, which is extremely similar with the red curve that was obtained in the liquid electrolyte-based coin cell (Li//liquid electrolyte//LCO). This indicates a smooth electrochemical reaction takes place in the solid-state. In addition, no obvious voltage plateau/slope corresponding to the side reaction on cathode or anode is found in the charge and discharge process of Li@$LPSCl_{0.3}F_{0.7}$//LPSCl//LCO@LNO/LPSCl ASSLMBs, with the exception of the somewhat inevitable space charge effect indicated by a small slope before reaching to the charging plateau of 3.9 V.[41] Similar to the capacity and high reversibility delivered in the Li//liquid electrolyte//LCO battery, the first discharge specific capacity is up to 122 mAh g^{-1} and a high coulombic efficiency of 89 % can be achieved in the Li@$LPSCl_{0.3}F_{0.7}$//LPSCl//LCO@LNO/LPSCl battery. By contrast, if using the Li metal without $LPSCl_{0.3}F_{0.7}$ pretreatment as the anode, the Li//LPSCl//LCO@LNO/LPSCl ASSLMBs present very poor electrochemical performance (black charge and discharge curves in **Figure 4.5b**). Side reactions take place severely at the Li/LPSCl interface leading to a large irreversible capacity. RT cycling stability of the Li@$LPSCl_{0.3}F_{0.7}$//LPSCl//LCO@LNO/LPSCl battery is performed in **Figure 4.5c**, after initial cycling at a low current density of 0.033 mA cm^{-2}, the battery operates smoothly at 0.13 mA cm^{-2}. The specific discharge capacity remains stable in the first 40 cycles with an ultra-high coulombic efficiency (> 99.5 %), and the capacity retention stands at 95 % after 50 cycles. The problems associated with the Li anode/sulfide electrolyte interface (interfacial side reactions and the Li dendrite formation) would be much more serious under high current densities,[42] while the Li/$LPSCl_{0.3}F_{0.7}$//LPSCl//LCO@LNO/LPSCl battery can show an excellent rate capability at RT. As suggested in **Figure 4.5d**, the specific capacity stands at 118 mAh g^{-1} under a low current density of 0.065 mA cm^{-2}, while the specific capacity can reach as high as 115, 103, 95, 89, and 86 mAh g^{-1} at the elevated current densities of 0.13, 0.26, 0.65, 1.04, and 1.3 mA cm^{-2}, respectively. Furthermore, the specific capacity can recover to 101 mAh g^{-1} and keep stable, when the current density declines to 0.13 mA cm^{-2}. These results prove the performance of our full cells is one of the best in the reported sulfide-based ASSLMBs (see the performance comparison in **Table S4.2**). In stark contrast to the excellent electrochemical performance of the sulfide-based ASSLMBs employing Li@$LPSCl_{0.3}F_{0.7}$ as the anode, Li//LPSCl//LCO@LNO/LPSCl full batteries

that use bare Li as the anode cannot even operate under the current density of 0.13 mA cm^{-2} when extending the cycling number (**Figure S4.15**). The battery has difficulty in charging and delivers a very large but false specific charge capacity, which is ascribed to the unstable Li/LPSCl interface and the resultant degradation of LPSCl electrolytes.

4.4 Conclusion

In conclusion, F is incorporated into the popular Argyrodite Li_6LP_5Cl sulfide-based electrolytes ('LPSCl-xF') for the first time via conventional solid-state synthesis routes. It is verified that the fluorinated $LPSCl_{0.3}F_{0.7}$ electrolyte exhibits an outstanding stability towards Li metal during Li plating/stripping. In the Li//$LPSCl_{0.3}F_{0.7}$//Li symmetric cell, a stable Li plating/stripping for over 1000 hours can be achieved at the current density of 1.27 mA cm^{-2} and capacity of 1 mAh cm^{-2}. Even under a rarely reported current density of 6.37 mA cm^{-2} and capacity of 5 mAh cm^{-2}, the Li//$LPSCl_{0.3}F_{0.7}$//Li symmetric cell can still display a stable Li plating/stripping for over 250 hours. Furthermore, the excellent Li metal interface is applicable to realize high performance in Li@$LPSCl_{0.3}F_{0.7}$//LPSCl//LCO@LNO/LPSCl full batteries. The superior in-situ formed interface between Li metal and $LPSCl_{0.3}F_{0.7}$ is demonstrated to be endowed with highly dense and sheet-like surface morphology, as well as high concentration of LiF compounds. The fluorinated sulfide SSE can induce the formation of an ultra-stable Li metal interface and is expected to make significant steps towards the development of high-performance ASSLMBs.

4.5 Acknowledgments

This research was supported by the Natural Sciences and Engineering Research Council of Canada (NSERC), the Canada Research Chair Program (CRC), the Canada Foundation for Innovation (CFI), Ontario Research Foundation (ORF), China Automotive Battery Research Institute Co., Ltd., Glabat Solid-State Battery Inc., and the University of Western Ontario (UWO). We gratefully acknowledge Dr. Mark Biesinger and Dr. Heng-Yong Nie for their kind help on the test and analysis of XPS and TOF-SIMS at Surface Science Western (Western University).

4.6 References

（1）Manthiram, A.; Yu, X.; Wang, S., Lithium battery chemistries enabled by solid-state electrolytes. *Nat. Rev. Mater.* **2017**, *2*, 16103.

（2）Xin, S.; You, Y.; Wang, S.; Gao, H.-C.; Yin, Y.-X.; Guo, Y.-G., Solid-State Lithium Metal Batteries Promoted by Nanotechnology: Progress and Prospects. *ACS Energy Lett.* **2017**, *2*, 1385-1394.

（3）Chen, R.; Li, Q.; Yu, X.; Chen, L.; Li, H., Approaching Practically Accessible Solid-State Batteries: Stability Issues Related to Solid Electrolytes and Interfaces. *Chem. Rev.* **2019**, DOI: 10.1021/acs.chemrev.9b00268.

（4）Quartarone, E.; Mustarelli, P., Electrolytes for solid-state lithium rechargeable batteries: recent advances and perspectives. *Chem. Soc. Rev.* **2011**, *40*, 2525-2540.

（5）Zhang, Z.; Shao, Y.; Lotsch, B.; Hu, Y.-S.; Li, H.; Janek, J.; Nazar, L. F.; Nan, C.-W.; Maier, J.; Armand, M.; Chen, L., New horizons for inorganic solid state ion conductors. *Energy Environ. Sci.* **2018**, *11*, 1945-1976.

（6）Fan, L.; Wei, S.; Li, S.; Li, Q.; Lu, Y., Recent Progress of the Solid-State Electrolytes for High-Energy Metal-Based Batteries. *Adv. Energy Mater.* **2018**, *8*, 1702657.

（7）Gao, Z.; Sun, H.; Fu, L.; Ye, F.; Zhang, Y.; Luo, W.; Huang, Y., Promises, Challenges, and Recent Progress of Inorganic Solid-State Electrolytes for All-Solid-State Lithium Batteries. *Adv. Mater.* **2018**, *30*, 1705702.

（8）Kato, Y.; Hori, S.; Saito, T.; Suzuki, K.; Hirayama, M.; Mitsui, A.; Yonemura, M.; Iba, H.; Kanno, R., High-power all-solid-state batteries using sulfide superionic conductors. *Nat. Energy* **2016**, *1*, 16030.

（9）Kamaya, N.; Homma, K.; Yamakawa, Y.; Hirayama, M.; Kanno, R.; Yonemura, M.; Kamiyama, T.; Kato, Y.; Hama, S.; Kawamoto, K.; Mitsui, A., A lithium superionic conductor. *Nat. Mater.* **2011**, *10*, 682-686.

（10）Lee, H.; Oh, P.; Kim, J.; Cha, H.; Chae, S.; Lee, S.; Cho, J., Advances and Prospects of Sulfide All-Solid-State Lithium Batteries via One-to-One Comparison with Conventional Liquid Lithium Ion Batteries. *Adv. Mater.* **2019**, *31*, 1900376.

（11）Zhang, Q.; Cao, D.; Ma, Y.; Natan, A.; Aurora, P.; Zhu, H., Sulfide-Based Solid-State Electrolytes: Synthesis, Stability, and Potential for All-Solid-State Batteries. *Adv. Mater.* **2019**, *31*, 1901131.

（12）Xu, L.; Tang, S.; Cheng, Y.; Wang, K. Y.; Liang, J. Y.; Liu, C.; Cao, Y. C.; Wei, F.; Mai, L. Q., Interfaces in Solid-State Lithium Batteries. *Joule* **2018**, *2*, 1991-2015.

（13）Wenzel, S.; Leichtweiss, T.; Krüger, D.; Sann, J.; Janek, J., Interphase formation on lithium solid electrolytes—An in situ approach to study interfacial reactions by photoelectron spectroscopy. *Solid State Ionics* **2015**, *278*, 98-105.

（14）Zhu, Y.; He, X.; Mo, Y., First principles study on electrochemical and chemical stability of solid electrolyte–electrode interfaces in all-solid-state Li-ion batteries. *J. Mater. Chem. A* **2016**, *4*, 3253-3266.

（15）Kobayashi, T.; Yamada, A.; Kanno, R., Interfacial reactions at electrode/electrolyte boundary in all solid-state lithium battery using inorganic solid electrolyte, thio-LISICON. *Electrochim. Acta* **2008**, *53*, 5045-5050.

（16）Kato, A.; Kowada, H.; Deguchi, M.; Hotehama, C.; Hayashi, A.; Tatsumisago, M., XPS and SEM analysis between Li/Li 3 PS 4 interface with Au thin film for all-solid-state lithium batteries. *Solid State Ionics* **2018**, *322*, 1-4.

（17）Gao, Y.; Wang, D. W.; Li, Y. G. C.; Yu, Z. X.; Mallouk, T. E.; Wang, D. H., Salt-Based Organic-Inorganic Nanocomposites: Towards A Stable Lithium Metal/Li10GeP2S12 Solid Electrolyte Interface. *Angew. Chem. Int. Ed.* **2018**, *57*, 13608-13612.

（18）Xu, R.; Han, F.; Ji, X.; Fan, X.; Tu, J.; Wang, C., Interface engineering of sulfide electrolytes for all-solid-state lithium batteries. *Nano Energy* **2018**, *53*, 958-966.

（19）Fan, X.; Ji, X.; Han, F.; Yue, J.; Chen, J.; Chen, L.; Deng, T.; Jiang, J.; Wang, C., Fluorinated solid electrolyte interphase enables highly reversible solid-state Li metal battery. *Sci. Adv.* **2018**, *4*, 12.

（20）Wen, J. Y.; Huang, Y.; Duan, J.; Wu, Y. M.; Luo, W.; Zhou, L. H.; Hu, C. C.; Huang, L. Q.; Zheng, X. Y.; Yang, W. J.; Wen, Z. Y.; Huang, Y. H., Highly Adhesive Li-BN Nanosheet Composite Anode with Excellent Interfacial Compatibility for Solid-State Li Metal Batteries. *ACS Nano* **2019**, *13*, 14549-14556.

（21）Han, F.; Yue, J.; Zhu, X.; Wang, C., Suppressing Li Dendrite Formation in Li2S-P2S5 Solid Electrolyte by LiI Incorporation. *Adv. Energy Mater.* **2018**, *8*, 1703644.

（22）Albertus, P.; Babinec, S.; Litzelman, S.; Newman, A., Status and challenges in enabling the lithium metal electrode for high-energy and low-cost rechargeable batteries. *Nat. Energy* **2018**, *3*, 16-21.

（23）Zhang, Q., Fluorinated interphases. *Nat. Nanotechnol.* **2018**, *13*, 623-624.

（24）Wang, C.; Meng, Y. S.; Xu, K., Perspective—Fluorinating Interphases. *J. Electrochem. Soc.* **2018**, *166*, A5184-A5186.

（25）Aspern, N.; Roschenthaler, G. V.; Winter, M.; Cekic-Laskovic, I., Fluorine and Lithium: Ideal Partners for High-Performance Rechargeable Battery Electrolytes. *Angew. Chem. Int. Ed.* **2019**, *58*, 15978-16000.

（26）Li, T.; Zhang, X.-Q.; Shi, P.; Zhang, Q., Fluorinated Solid-Electrolyte Interphase in High-Voltage Lithium Metal Batteries. *Joule* **2019**, *3*, 2647-2661.

（27）He, M.; Guo, R.; Hobold, G. M.; Gao, H.; Gallant, B. M., The intrinsic behavior of lithium fluoride in solid electrolyte interphases on lithium. *PNAS* **2020**, *117*, 73-79.

（28）Xu, R.; Cheng, X.-B.; Yan, C.; Zhang, X.-Q.; Xiao, Y.; Zhao, C.-Z.; Huang, J.-Q.; Zhang, Q., Artificial Interphases for Highly Stable Lithium Metal Anode. *Matter* **2019**, *1*, 317-344.

（29）Yu, C.; van Eijck, L.; Ganapathy, S.; Wagemaker, M., Synthesis, structure and electrochemical performance of the argyrodite Li 6 PS 5 Cl solid electrolyte for Li-ion solid state batteries. *Electrochim. Acta* **2016**, *215*, 93-99.

（30）Mo, F.; Ruan, J.; Sun, S.; Lian, Z.; Yang, S.; Yue, X.; Song, Y.; Zhou, Y.; Fang, F.; Sun, G.; Peng, S.; Sun, D., Inside or Outside: Origin of Lithium Dendrite Formation of All Solid-State Electrolytes. *Adv. Energy Mater.* **2019**, *9*, 1902123.

（31）Dietrich, C.; Koerver, R.; Gaultois, M. W.; Kieslich, G.; Cibin, G.; Janek, J.; Zeier, W. G., Spectroscopic characterization of lithium thiophosphates by XPS and XAS - a model to help monitor interfacial reactions in all-solid-state batteries. *Phys. Chem. Chem. Phys.* **2018**, *20*, 20088-20095.

（32）Deiseroth, H. J.; Kong, S. T.; Eckert, H.; Vannahme, J.; Reiner, C.; Zaiss, T.; Schlosser, M., Li6PS5X: a class of crystalline Li-rich solids with an unusually high Li+ mobility. *Angew. Chem. Int. Ed.* **2008**, *47*, 755-758.

（33）Yubuchi, S.; Teragawa, S.; Aso, K.; Tadanaga, K.; Hayashi, A.; Tatsumisago, M., Preparation of high lithium-ion conducting Li6PS5Cl solid electrolyte from ethanol solution for all-solid-state lithium batteries. *J. Power Sources* **2015**, *293*, 941-945.

（34）Zhang, Z.; Zhang, L.; Liu, Y.; Yu, C.; Yan, X.; Xu, B.; Wang, L.-m., Synthesis and characterization of argyrodite solid electrolytes for all-solid-state Li-ion batteries. *J. Alloys Compd.* **2018**, *747*, 227-235.

（35）Wang, S.; Zhang, Y.; Zhang, X.; Liu, T.; Lin, Y.-H.; Shen, Y.; Li, L.; Nan, C.-W., High-Conductivity Argyrodite Li6PS5Cl Solid Electrolytes Prepared via Optimized Sintering Processes for All-Solid-State Lithium–Sulfur Batteries. *ACS Appl. Mater. Interfaces* **2018**, *10*, 42279-42285.

（36）Han, F.; Westover, A.; Yue, J.; Fan, X.; Wang, F.; Chi, M.; Leonard, D.; Dudney, N.; Wang, H.; Wang, C., High electronic conductivity as the origin of lithium dendrite formation within solid electrolytes. *Nat. Energy* **2019**, *4*, 187-196.

（37）Wenzel, S.; Sedlmaier, S. J.; Dietrich, C.; Zeier, W. G.; Janek, J., Interfacial reactivity and interphase growth of argyrodite solid electrolytes at lithium metal electrodes. *Solid State Ionics* **2018**, *318*, 102-112.

（38）Nagao, M.; Hayashi, A.; Tatsumisago, M.; Kanetsuku, T.; Tsuda, T.; Kuwabata, S., In situ SEM study of a lithium deposition and dissolution mechanism in a bulk-type solid-state cell with a Li2S-P2S5 solid electrolyte. *Phys. Chem. Chem. Phys.* **2013**, *15*, 18600-18606.

（39）Kato, A.; Yamamoto, M.; Sakuda, A.; Hayashi, A.; Tatsumisago, M., Mechanical Properties of Li2S-P2S5 Glasses with Lithium Halides and Application in All-Solid-State Batteries. *ACS Appl. Energy Mater.* **2018**, *1*, 1002-1007.

（40）Huang, Y.; Chen, B.; Duan, J.; Yang, F.; Wang, T. R.; Wang, Z. F.; Yang, W. J.; Hu, C. C.; Luo, W.; Huang, Y. H., Graphitic Carbon Nitride (g-C3N4): An Interface Enabler for Solid-State Lithium Metal Batteries. *Angew. Chem. Int. Ed.* **2020**, *59*, 3699-3704.

（41）Haruyama, J.; Sodeyama, K.; Han, L. Y.; Takada, K.; Tateyama, Y., Space-Charge Layer Effect at Interface between Oxide Cathode and Sulfide Electrolyte in All-Solid-State Lithium-Ion Battery. *Chem. Mater.* **2014**, *26*, 4248-4255.

（42）Garcia-Mendez, R.; Mizuno, F.; Zhang, R.; Arthur, T. S.; Sakamoto, J., Effect of Processing Conditions of 75Li2S-25P2S5 Solid Electrolyte on its DC Electrochemical Behavior. *Electrochim. Acta* **2017**, *237*, 144-151.

4.7 Supporting information

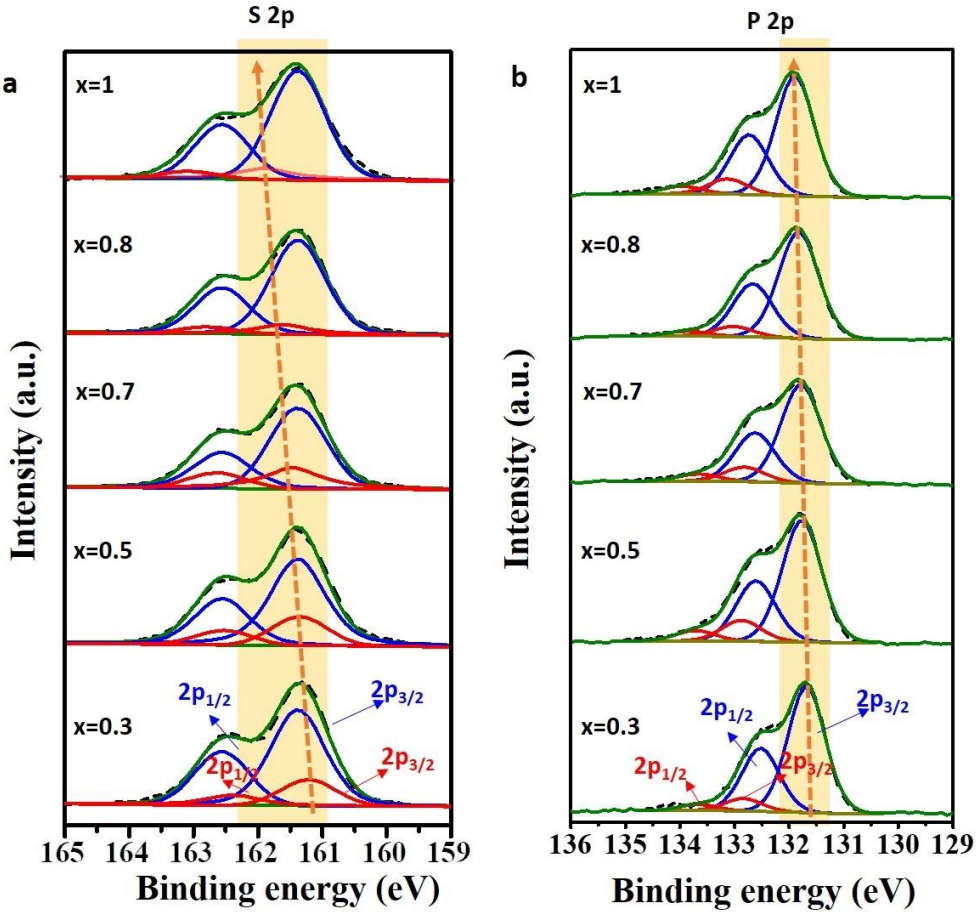

Figure S4.1 XPS spectra of S 2p (a) and P 2p (b) in the prepared $LPSCl_{1-x}F_x$ sulfide-based electrolytes (x = 0.3, 0.5, 0.7, 0.8, 1).

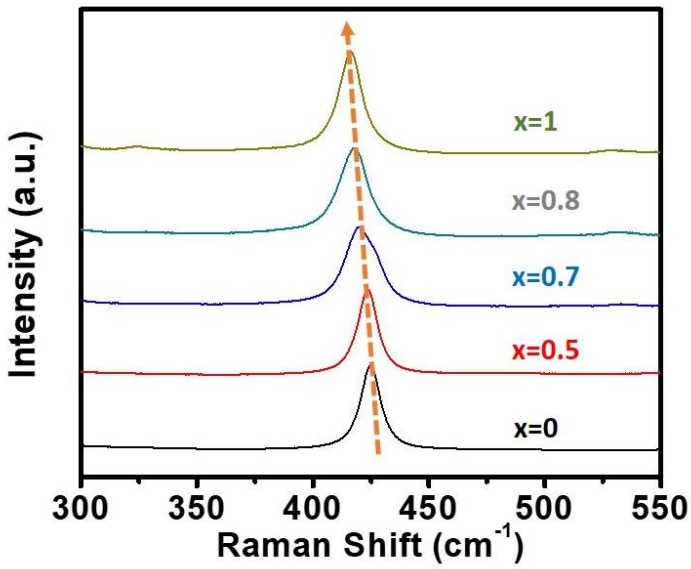

Figure S4.2 Raman spectra of the prepared $LPSCl_{1-x}F_x$ sulfide-based electrolytes (x = 0, 0.5, 0.7, 0.8, 1).

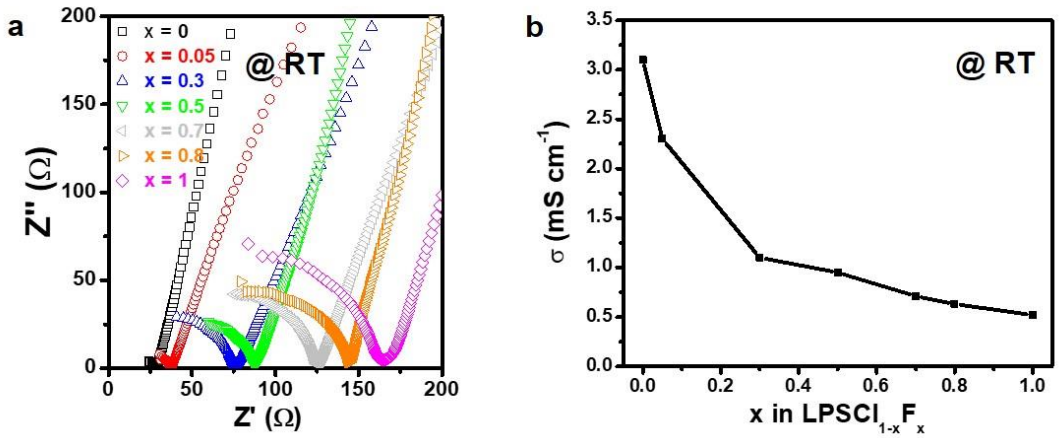

Figure S4.3 (a) Impedance plots of $LPSCl_{1-x}F_x$ sulfide-based electrolytes at RT. (b) F-content dependent ionic conductivity at RT of the $LPSCl_{1-x}F_x$ electrolyte (x = 0, 0.05, 0.3, 0.5, 0.7, 0.8, 1).

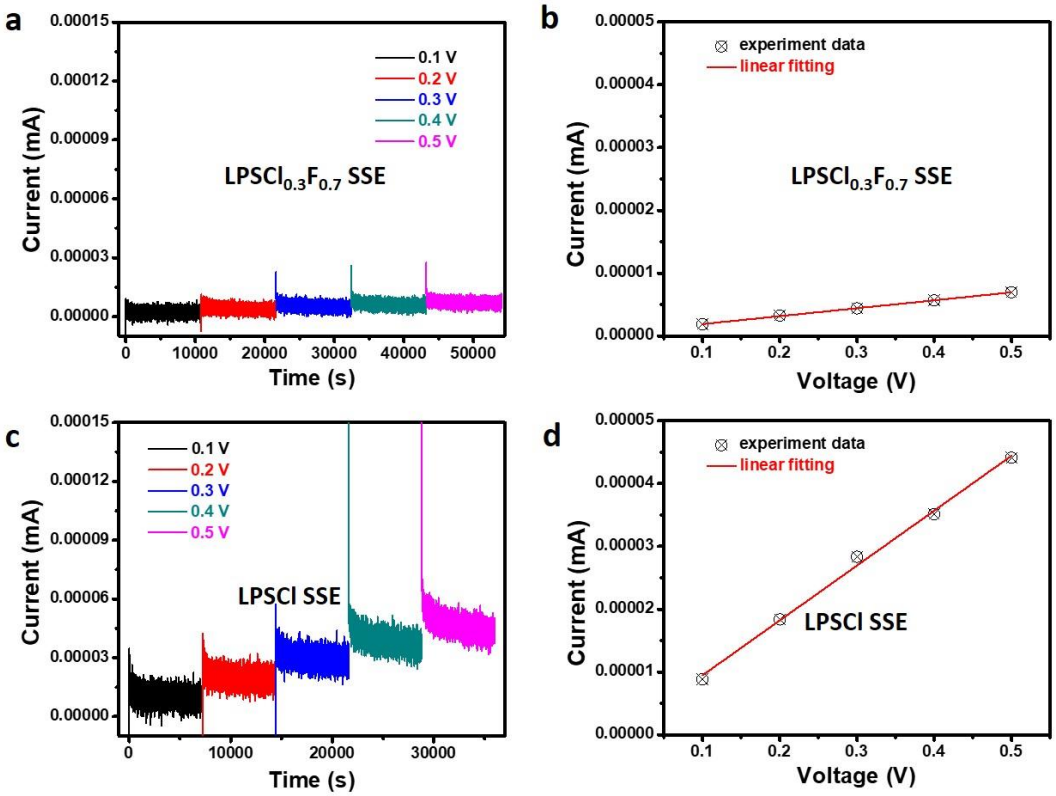

Figure S4.4 DC polarization curves of $LPSCl_{0.3}F_{0.7}$ (a) and LPSCl (c) using symmetric cells at different voltages. Stable current response of $LPSCl_{0.3}F_{0.7}$ (b) and LPSCl (d) symmetric cells at different voltages.

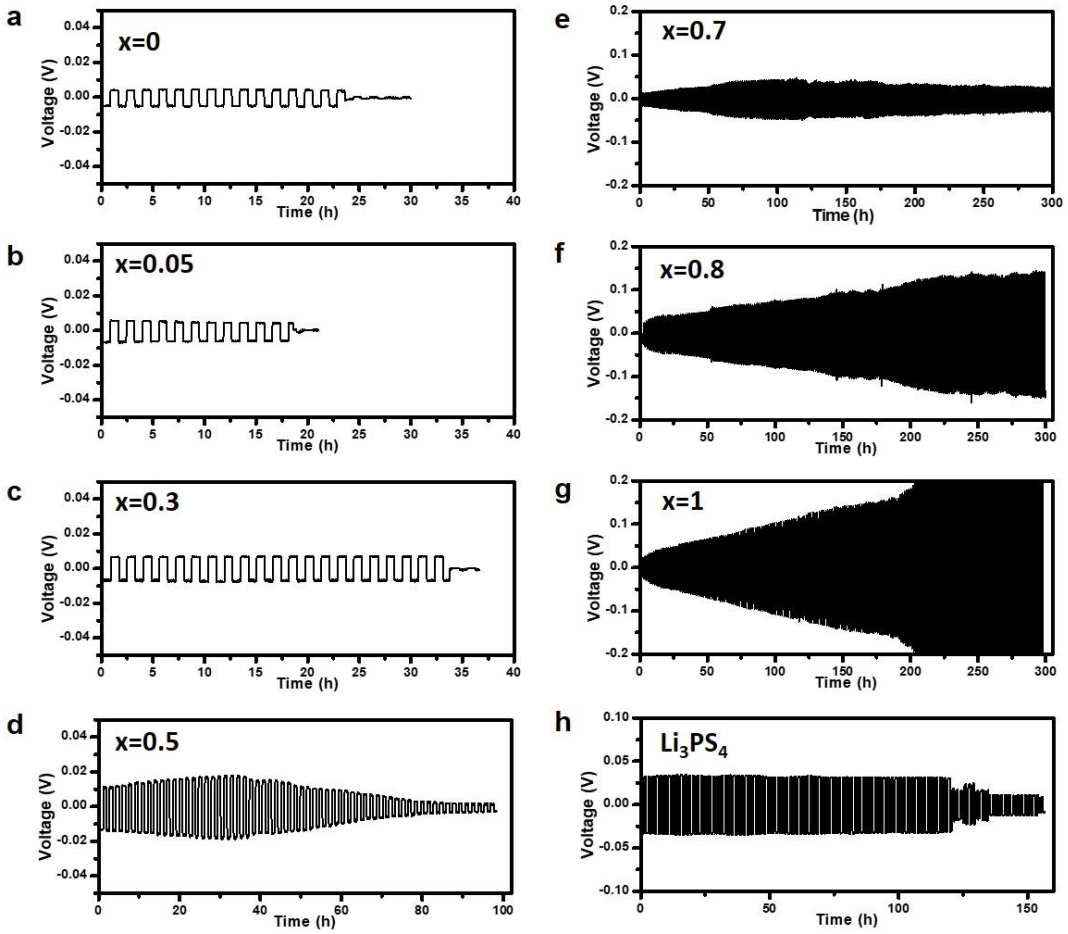

Figure S4.5 Li//Li symmetric cell plating and stripping behavior when employing $LPSCl_{1-x}F_x$ (x = 0.05, 0.3, 0.5, 0.7, 0.8, 1).as the electrolytes compared with that using LPSCl and LPS electrolytes. The current density is 0.127 mA cm^{-2} and capacity is 0.1 mAh cm^{-2}.

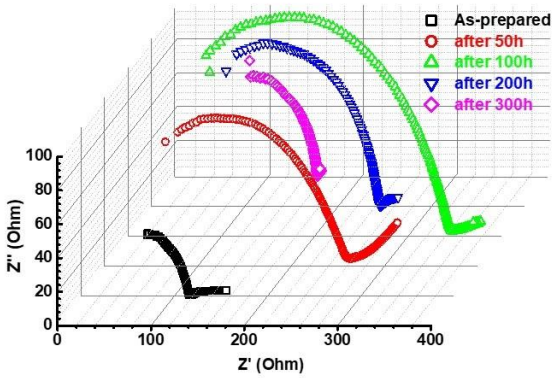

Figure S4.6 Time-resolved EIS profiles of a Li//$LPSCl_{0.3}F_{0.7}$//Li symmetric cell at different stages of cycling.

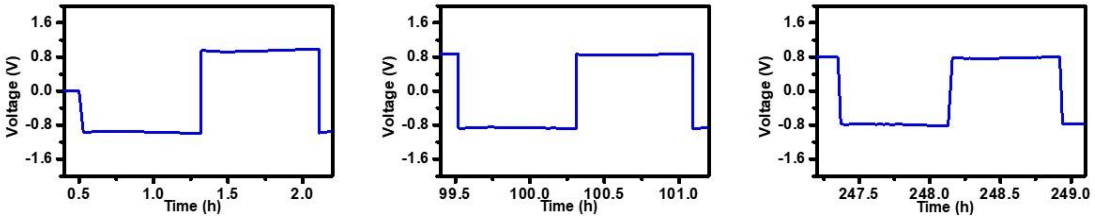

Figure S4.7 Magnified areas of Li plating/stripping curves of the Li//$LPSCl_{0.3}F_{0.7}$//Li symmetric cell tested at 6.37 mA cm^{-2} and 5 mAh cm^{-2}.

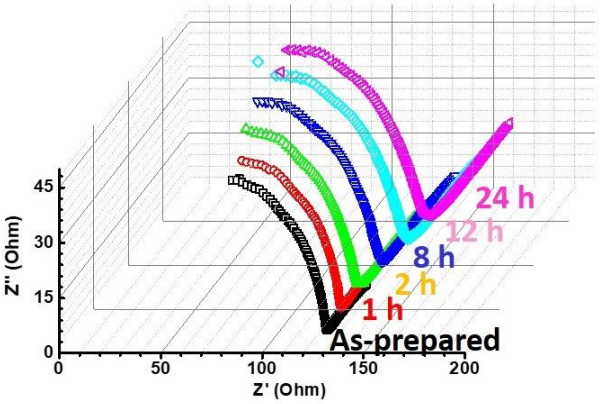

Figure S4.8 Rest time-resolved EIS profiles of a Li//$LPSCl_{0.3}F_{0.7}$//Li symmetric cell.

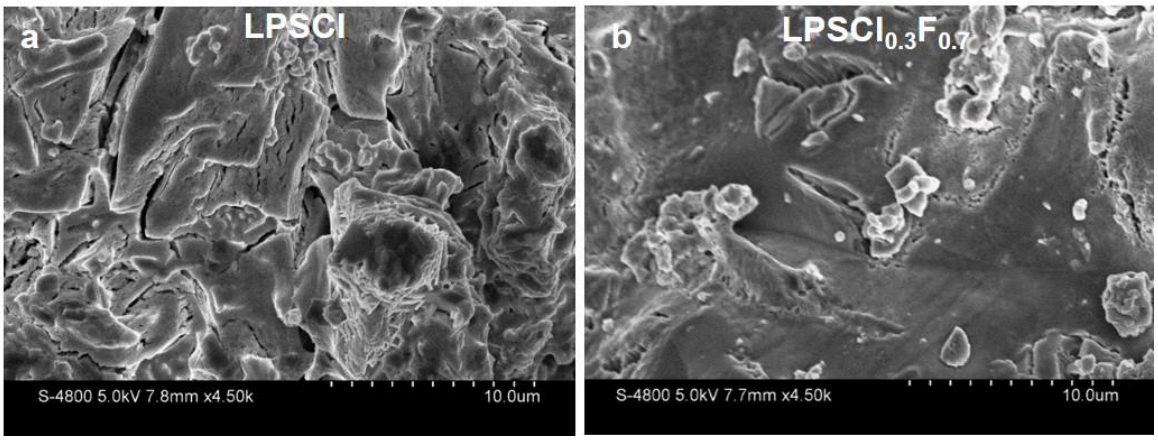

Figure S4.9 SEM images of the surface morphologies of (a) LPSCl and (b) $LPSCl_{0.3}F_{0.7}$ pellets prepared by cold pressing.

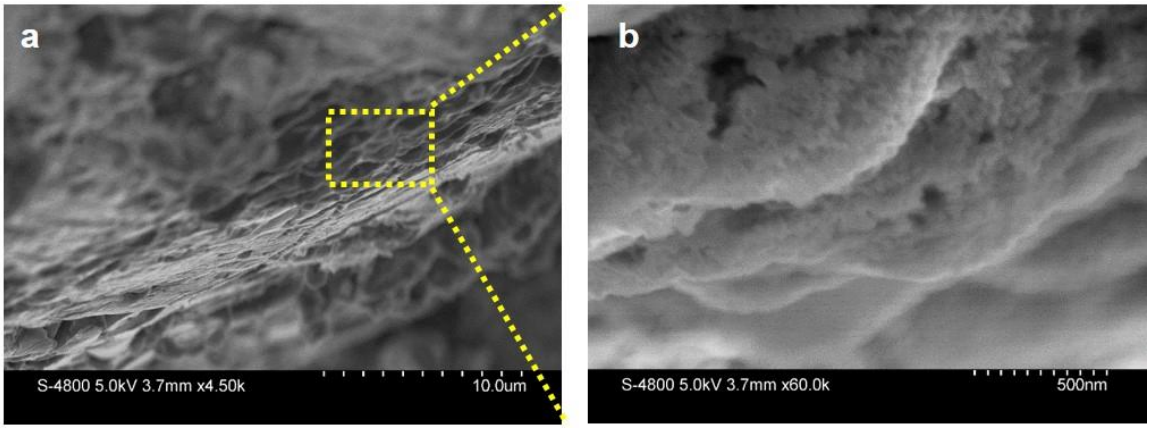

Figure S4.10 SEM images of the side views of Li surface (Li/ $LPSCl_{0.3}F_{0.7}$ interface) after ~200 h cycling.

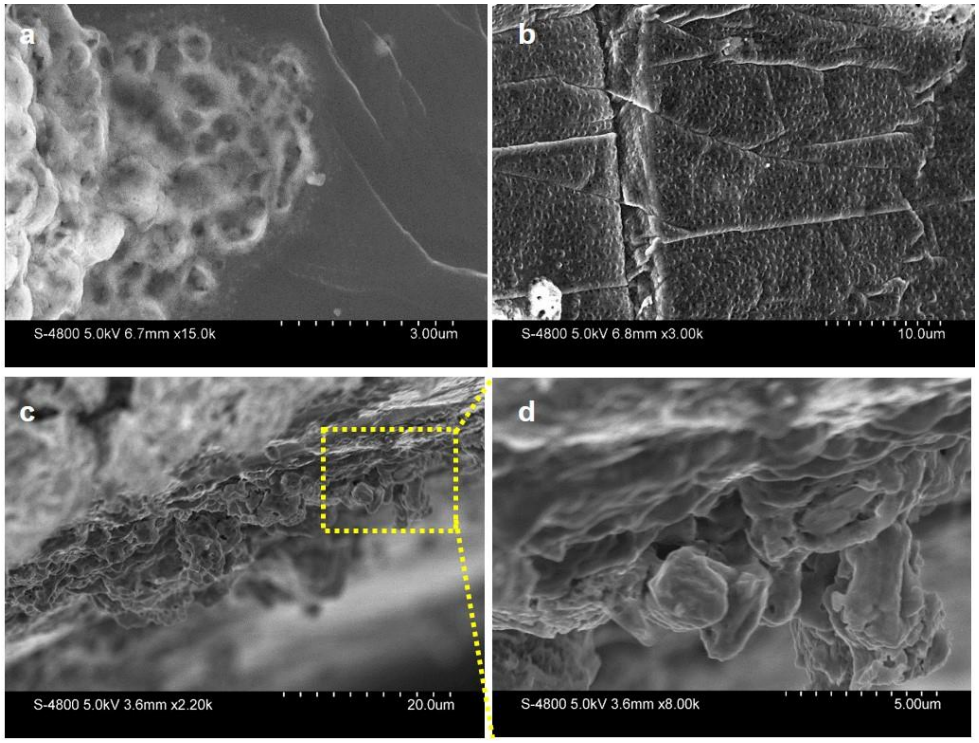

Figure S4.11 (a and b) SEM images of the Li metal surface after Li plating/stripping for 20 h in Li//LPSCl//Li symmetric cells. (c and d) Side-view SEM images of Li surface after cell failure.

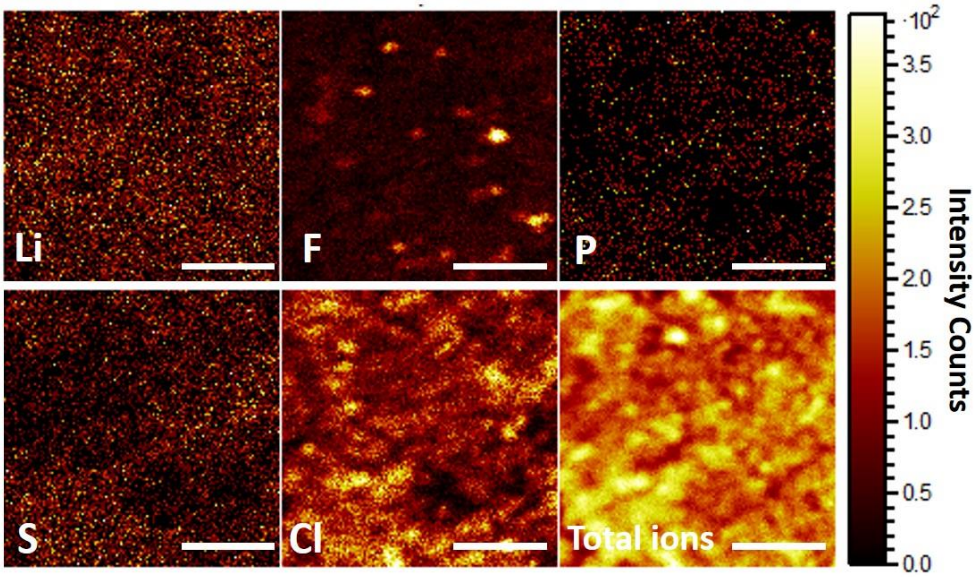

Figure S4.12 ToF-SIMS chemical species images on Li metal (after Li-Li symmetric cell tests) surface before Cs^+ ion sputtering. Scale bar: 100 um.

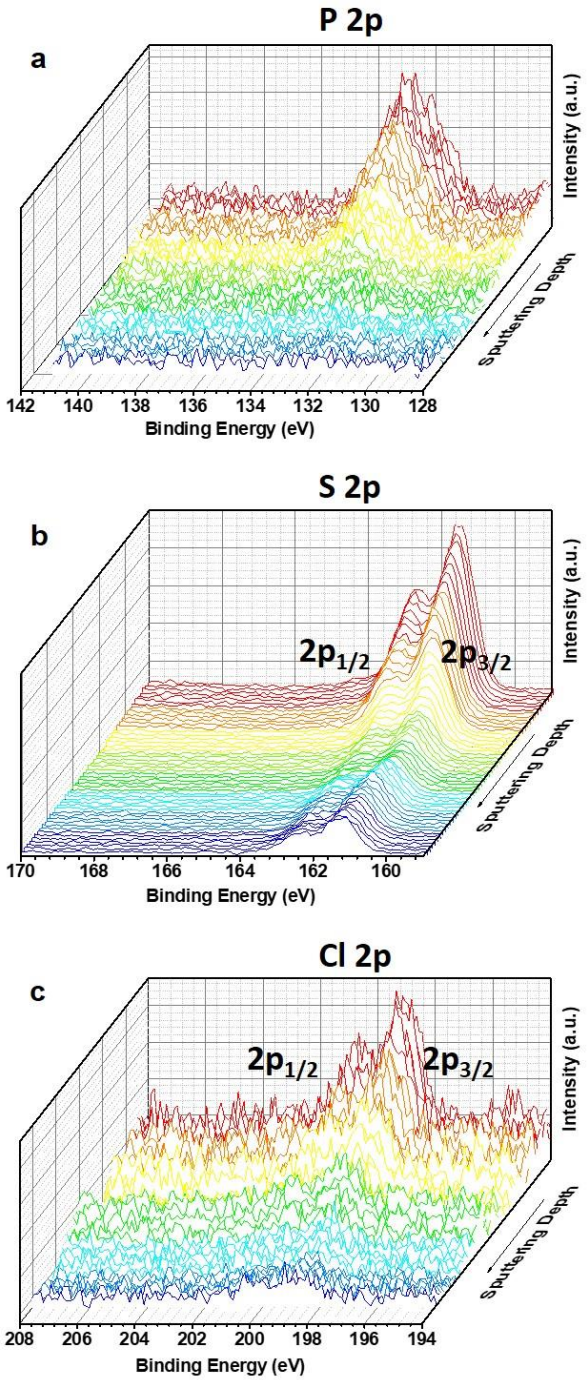

Figure S4.13 Obtained by XPS depth profiling analysis, overall evolution of three elements along with the sputtering depth at the Li/LPS$Cl_{0.3}F_{0.7}$ interface: (a) Li 1s; (b) S 2p; (c) Cl 2p.

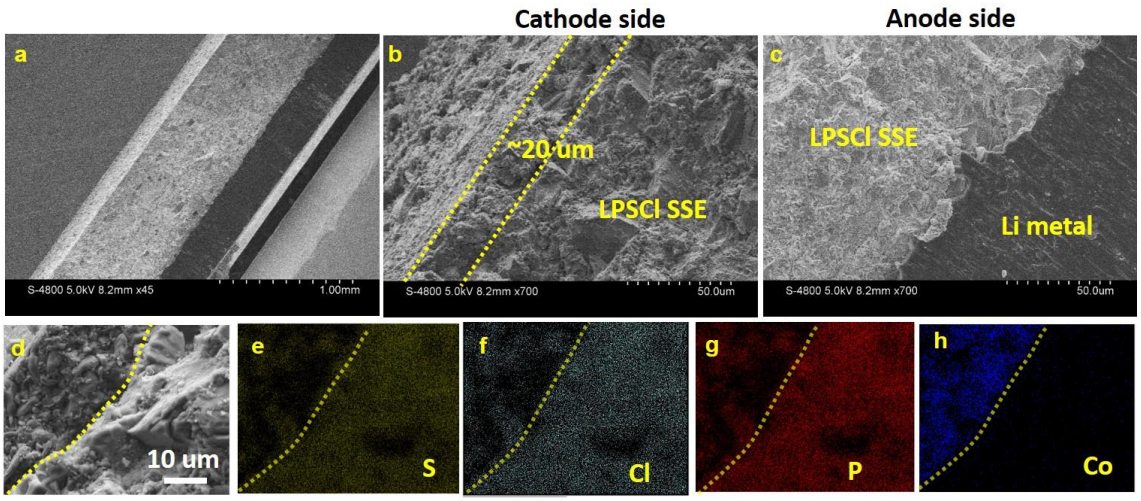

Figure S4.14 SEM images of cross sections of (a) a Li@LPSCl$_{0.3}$F$_{0.7}$//LPSCl//LCO@LNO/LPSCl full battery, (b) cathode side: LPSCl//LCO@LNO/LPSCl, and (c) anode side: Li@LPSCl$_{0.3}$F$_{0.7}$//LPSCl. Selected area at cathode side (d) and corresponding elements mapping (e-h).

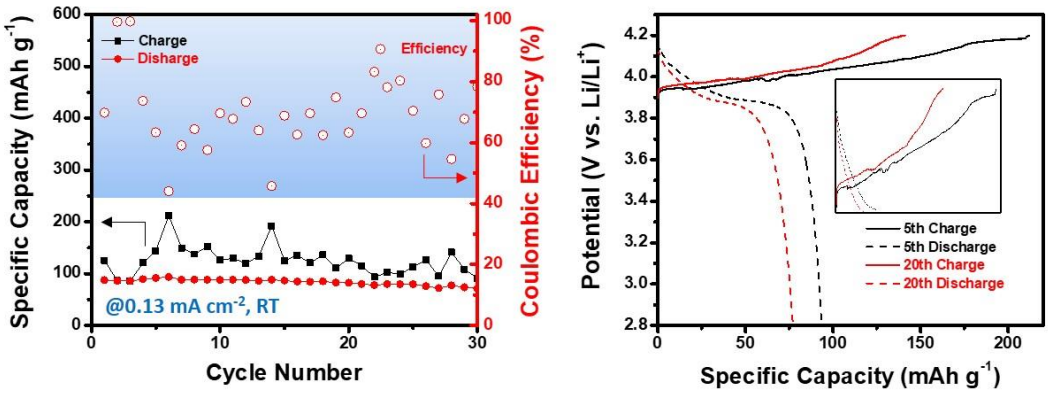

Figure S4.15 Poor electrochemical performance of the Li//LPSCl//LCO@LNO/LPSCl ASSLBs.

Table S4.1 Summary of the sulfide electrolyte-based Li-Li symmetric cells performance

Electrolyte type	**Cell type**	**Plating current density, mA cm^{-2}**	**Plating specific capacity, mAh cm^{-2}**	**Number of cycle**	**Test temperature**	**Ref.**
Sulfide SSEs	Li// $LPSCl_{0.3}F_{0.7}$//Li	1.27	1	636	RT	This work
		6.37	5	159	RT	This work
	Li/G–LGPS–G/Li (given high pressure)	10	0.25	10	RT	1
	LE pretreated Li//LGPS// LE pretreated Li	0.1	0.1	1500	RT	2
	Li/LiF//LPS//LiF/Li	0.5	0.1	100	RT	3
	Li/LiI//LPS//LiI/Li	0.5	0.1	60	RT	
	Li//LPS30I//Li	0.3	0.3	100	RT	4
		0.6	0.6	100	60 ºC	
		1.5	1.5	100	100 ºC	
	Li/Cu film//Li_3PS_4//Li/Cu film	1.3	6.5	5	100 ºC	5
	Li//$Li_7P_2S_8I$//Li	0.2	0.2	800	RT	6
	Li|LiFSI@LPS|Li	0.3	0.6	90	RT	7
	Li//MOF-modified electrolyte//Li	10	10	800	RT	8
	PNIPAM-2@Cu@Li//1 M LiTFSI in	20	5	2000	RT	9

	DOL/DME/$LiNO_3$// Li@PNIPAM-2@Cu					
	Li/Cu@Au//1M LiTFSI in DOL/DME//Li/Cu@Au	10	3	500	RT	10
	Li//4M LiTFSI in DME//Li	10	0.5	6000	RT	11
LEs	Li/$Li_{13}In_3$//1M LiTFSI in DOL/DME//Li/$Li_{13}In_3$	2	2	600	RT	12
	LiZn/Li //1M LiTFSI in DOL/DME//LiZn/Li	2	2	500	RT	
	Li/PI@ZnO//1M LiTFSI in DOL/DME//Li/PI@ZnO	5	1	100	RT	13
	Li/LiF//1M Li_6PF_6 in carbonate//Li/LiF	5	1	300	RT	14
	10 M LiFSI-EC/DMC	1	2	500	RT	15

Table S4.2 Summary of the sulfide electrolyte-based all-solid-state Li metal batteries performance (LCO cathode material)

Battery configuration (anode/electrolyte/ cathode)	**Cycling stability (current density/ cycle number/ capacity retention)**	**Rate capability (current density/ capacity)**	**1st CE**	**Active material loading**	**Test temperature**	**Ref.**
Li@$LPSCl_{0.3}F_{0.7}$//LPSCl//LCO@LNO	0.1 C/ 50 cycles/ 95% (1 C corresponds to 1.3 mA cm^{-2})	0.05 C / 115 mAh g^{-1} 1 C/ 85.7 mAh g^{-1}	89%	8.92 mg cm^{-2}	RT	This work
Li@LiF/$Li_7P_3S_{11}$(HFE)/LCO	0.1 mA cm^{-2}/ 50 cycles/ ~90% 0.1 mA cm^{-2}/ 100 cycles/ 81.4%	0.1 mA cm^{-2}/ 117.8 mAh g^{-1} 1 mA cm^{-2}/ 59.2 mAh g^{-1}	NA (~80 %)	3.6 mg cm^{-2}	RT	3
Li//LPS_{30}I/LCO@LNO	0.2 C/ 40 cycles/ 82%	NA (0.2 C/ 120 mAh g^{-1})	NA	10 mg cm^{-2}	RT	4
Li//LiFSI@LPS//LCO	0.3 mA/cm^2/ 50 cycles/ >90%	NA (0.3 mA cm^{-2}/ 120 mAh g^{-1})	65%	~7 mg cm^{-2}	RT	7
Li@alucone//LSnPS//LCO	0.1 C/ 150 cycles/ 50%	NA (0.1 C/ 120 mAh g^{-1})	75 %	~8 mg cm^{-2}	55 ºC	16
Li@LiH_2PO_4//LGPS//LCO@LNO	0.1 C/ 50 cycles/ 91.9% 0.1 C/ 500 cycles/ 86.7%	0.1 C/ 131.1 mAh g^{-1} 1 C/ 44.5 mAh g^{-1}	85.9 %	~5.5 mg cm^{-2}	RT	17

References for the supporting information of Chapter 4

（1）Su, Y.; Ye, L.; Fitzhugh, W.; Wang, Y.; Gil-González, E.; Kim, I.; Li, X., *Energy Environ. Sci.* **2020**, DOI: 10.1039/C9EE04007B.

（2）Gao, Y.; Wang, D. W.; Li, Y. G. C.; Yu, Z. X.; Mallouk, T. E.; Wang, D. H., *Angew. Chem. Int. Ed.* **2018**, *57*, 13608-13612.

（3）Xu, R.; Han, F.; Ji, X.; Fan, X.; Tu, J.; Wang, C., *Nano Energy* **2018**, *53*, 958-966.

（4）Han, F.; Yue, J.; Zhu, X.; Wang, C., *Adv. Energy Mater.* **2018**, *8*, 1703644.

（5）Kato, A.; Suyama, M.; Hotehama, C.; Kowada, H.; Sakuda, A.; Hayashi, A.; Tatsumisago, M., *J. Electrochem. Soc.* **2018**, *165*, A1950-A1954.

（6）Rangasamy, E.; Liu, Z. C.; Gobet, M.; Pilar, K.; Sahu, G.; Zhou, W.; Wu, H.; Greenbaum, S.; Liang, C. D., *J. Am. Chem. Soc.* **2015**, *137*, 1384-1387.

（7）Fan, X.; Ji, X.; Han, F.; Yue, J.; Chen, J.; Chen, L.; Deng, T.; Jiang, J.; Wang, C., *Sci. Adv.* **2018**, *4*, 12.

（8）Bai, S.; Sun, Y.; Yi, J.; He, Y.; Qiao, Y.; Zhou, H., *Joule* **2018**, *2*, 2117-2132.

（9）Li, N.; Ye, Q.; Zhang, K.; Yan, H.; Shen, C.; Wei, B.; Xie, K., *Angew. Chem. Int. Ed.* **2019**, *131*, 18414-18419.

（10）Gu, Y.; Wang, W. W.; Li, Y. J.; Wu, Q. H.; Tang, S.; Yan, J. W.; Zheng, M. S.; Wu, D. Y.; Fan, C. H.; Hu, W. Q.; Chen, Z. B.; Fang, Y.; Zhang, Q. H.; Dong, Q. F.; Mao, B. W., *Nat. Commun.* **2018**, *9*, 1339.

（11）Qian, J.; Henderson, W. A.; Xu, W.; Bhattacharya, P.; Engelhard, M.; Borodin, O.; Zhang, J. G., *Nat. Commun.* **2015**, *6*, 6362.

（12）Liang, X.; Pang, Q.; Kochetkov, I. R.; Sempere, M. S.; Huang, H.; Sun, X. Q.; Nazar, L. F., *Nat. Energy* **2017**, *2*, 17119.

（13）Liu, Y.; Lin, D.; Liang, Z.; Zhao, J.; Yan, K.; Cui, Y., *Nat. Commun.* **2016**, *7*, 10992.

（14）Zhao, J.; Liao, L.; Shi, F. F.; Lei, T.; Chen, G. X.; Pei, A.; Sun, J.; Yan, K.; Zhou, G. M.; Xie, J.; Liu, C.; Li, Y. Z.; Liang, Z.; Bao, Z. N.; Cui, Y., *J. Am. Chem. Soc.* **2017**, *139*, 11550-11558.

（15）Fan, X.; Chen, L.; Ji, X.; Deng, T.; Hou, S.; Chen, J.; Zheng, J.; Wang, F.; Jiang, J.; Xu, K.; Wang, C., *Chem* **2018**, *4*, 174-185.

（16）Wang, C.; Zhao, Y.; Sun, Q.; Li, X.; Liu, Y.; Liang, J.; Li, X.; Lin, X.; Li, R.; Adair, K. R.; Zhang, L.; Yang, R.; Lu, S.; Sun, X., *Nano Energy* **2018**, *53*, 168-174.

（17）Zhang, Z.; Chen, S.; Yang, J.; Wang, J.; Yao, L.; Yao, X.; Cui, P.; Xu, X., *ACS Appl. Mater. Interfaces* **2018**, *10*, 2556-2565.

Chapter 5

5 Sn-substituted argyrodite sulfide solid-state electrolytes

In the chapter 4, fluorinating sulfide sulfides has been demonstrated to improve the Li anode stability. Thus, is there any other modification strategy can show multi-functionality in enhancing ionic conductivity, Li metal compatibility, as well as air stability? .In this chapter, the Sn (IV) substitution for P (V) in Argyrodite sulfide Li_6PS_5I (LPSI) SSEs is reported to prepare novel LPSI-xSn SSEs (where x is the Sn substitution percentage). Appropriate aliovalent element substitutions with larger atomic radius ($R_{<Sn>} > R_{<P>}$) provides the optimized LPSI-20Sn electrolyte with a 125-times higher ionic conductivity compared to that of the LPSI electrolyte. The decent ionic conductivity of LPSI-20Sn enables the rich I-containing electrolyte to serve as a stabilized interlayer against Li metal in sulfide-based ASSLMBs with outstanding cycling stability and rate capability. Most importantly, benefiting from the strong Sn-S bonding in Sn-substituted electrolytes, the LPSI-20Sn electrolyte shows excellent structural stability and improved air stability after exposure to O_2 and moisture. The versatile Sn substitution in Argyrodite LPSI electrolytes is believed to provide a new and effective strategy to achieve Li metal-compatible and air-stable sulfide-based SSEs for large-scale applications.

*A version of this chapter has been published in *Advanced Energy Materials*, 2020, 10, 9, 1903422.

5.1 Introduction

All-solid-state Li metal batteries (ASSLMBs) have been proposed to eliminate the safety problems and limited energy density (< 500 Wh/kg) in current lithium-ion batteries (LIBs).[1-3] The solid-state electrolyte (SSE) is a critical component in ASSLMBs and has received extensive attention.[1, 4-5] Among the various types of SSEs, sulfide-based SSEs are considered as one of the most promising candidates, because of their high ionic conductivity, inherent softness for intimate contact between electrodes and electrolytes, as well as good mechanical strength for large-scale practical applications.[6-7]

However, two major detrimental factors have plagued the development of sulfide SSEs. Firstly, the poor electrode material/sulfide SSEs interface deteriorates the battery performance.[5, 8-9] Since the compatibility issue between cathode materials and sulfide SSEs has prevented sulfide SSEs from achieving stable cycling performance, considerable efforts have been made to develop strategies to alleviate those problems.[2-3, 7] In contrast, catastrophic Li metal anode interface makes the use of Li metal as an anode directly against sulfide electrolyte extremely challenging,[10-12] because of its strong reducing capabilities towards almost all kinds of sulfide SSEs, such as β-Li_3PS_4,[13] $Li_7P_3S_{11}$,[14] Argyrodite-type,[15] and thio-LISICON-type electrolytes.[16] Moreover, the uneven Li deposition can cause Li dendrites formation, which can penetrate through the soft electrolyte to vitiate batteries.[17-18] Secondly, the air-sensitive nature of sulfide SSEs increases the difficulty for manufacturing and practical applications.[19-20] Due to the high oxygen affinity of P^{5+}, the sulfide SSEs that contain PS_4^{3-} structure blocks are extremely prone to reacting with H_2O to generate toxic H_2S gas. Thus, vacuum or inert gas atmosphere is required to handle sulfide SSEs, which would complicate the manufacturing and preparation processes with increased fabrication cost.

To alleviate the poor Li metal anode/sulfide SSEs interface problem, rich I or F-containing Li metal anode/sulfide SSEs interfaces have been reported.[21-24] The functional interface can exhibit very stable electrochemical behaviors against sulfide SSEs in fabricated symmetric or full cells. LiI or LiF compositions in the solid-electrolyte-interphase (SEI) formed between Li metal and sulfide SSEs play crucial roles in preventing side reactions

and Li dendrites formation. Especially when I or F-based sulfide SSEs are used, high current density and reversible cut-off capacities can be achieved to meet the requirement of high-energy-density ASSLMBs.[24-25] Nevertheless, it is still very challenging to realize air-stable sulfide SSEs with decent room temperature (RT) ionic conductivity (> 10^{-4} S cm^{-1}). Li-Sn-S electrolytes (Li_4SnS_4 and Li_2SnS_3) were demonstrated to possess excellent air-stability, benefiting from the hard-softs-acid-bases (HSAB) theory.[26-28] Sn is classified as a soft acid, which prefers to bond with soft base S rather than bond with hard base O. However, the low ionic conductivity of pristine Li-Sn-S electrolytes limited at 10^{-5} S cm^{-1} level restrains their development. Although As substitution in Li_4SnS_4 can improve the RT ionic conductivity to reach 1.0×10^{-3} S cm^{-1}, the highly toxic As element brings additional safety and environmental concerns.[29] Nevertheless, the air stability of the sulfide electrolytes is predicted to be improved after Sn substitution in the PS_4^{3-} structure. Furthermore, the aliovalent element (Sn) substitution with larger atomic radius and lower valence compared with phosphorus (P) can expand the cell volume and increase the Li solubility in the unit cells, which can synergistically increase the corresponding ionic conductivity.[30-31]

Argyrodite electrolytes Li_6PS_5X (LPSX, X = Cl, Br, and I) represent one type of popular sulfide electrolytes, due to the low cost of raw materials and high ionic conductivity.[32-34] Both LPSCl and LPSBr with a high ionic conductivity of > 1×10^{-3} S cm^{-1} still suffer from the problems that are mentioned above.[15, 35] Li_6PS_5I (LPSI) has received less attention, because the low S^-/ I^- exchange disorder leads to a low conductivity in the order of 10^{-6} S cm^{-1}.[36] However, the high I concentration in the electrolyte itself is highly anticipated to stabilize the Li metal/LPSI-based electrolyte interface in ASSLMBs if decent ionic conductivity can be obtained. Recent studies show that the ionic conductivity of LPSI SSE can be significantly improved by aliovalent element substitutions. [30, 37] Different from previous work that is fundamentally dedicated to improve the ionic conductivity fundamentally, we aim in using a versatile strategy to achieve an excellent sulfide SSE with good Li metal compatibility, improved air stability and decent ionic conductivity, simultaneously. Herein, we originally propose to partially substitute Sn for P in LPSI Argyrodite electrolytes to prepare new Argyrodite-type electrolytes: LPSI-xSn or $Li_{6+y}P_{1-y}Sn_yS_5I$ (x is the Sn substitution percentage, y = x %). The optimized ionic conductivity of

LPSI-20Sn reaches a value as high as 3.5 × 10^{-4} S cm^{-1}, which is 125 times higher that of the LPSI electrolyte without Sn substitution. More importantly, LPSI-20Sn electrolyte is stable without any degradation in pure O_2, and even shows negligible decrease in ionic conductivity after being exposed to 10 % humidity atmosphere and post-heating treatment. Additionally, the robust Li/LPSI-20Sn interface enables ultra-stable Li plating/stripping for over 200 hours at a high current density (1.26 mA cm^{-2}) and cut-off capacity (1 mAh cm^{-2}) in Li//LPSI-20Sn//Li symmetric cells. The application of this electrolyte is also demonstrated in ASSLMBs by using LPSI-20Sn as the Li anode interlayer in full cells that exhibits excellent cycling stability and rate capability.

5.2 Experimental section

5.2.1 Synthesis of SSEs

All materials were used directly without any purification. P_2S_5 (> 99 %), LiI (99.99 %, anhydrous), LiCl (> 99.98 %, anhydrous), LiBr (99.9 %, anhydrous), and LCO (99.8%) particles were purchased from Sigma Aldrich. Li_2S (99.9%) was purchase from Alfa Aesar. SnS_2 (99.999 %) was purchased from American Elements.

Preparation of LPSI-xSn sulfide SSEs (x, the Sn substitution percentage, equals to 0, 10, 15, 17.5, 20, 22.5, 25, 30, 50, 80, and 100): Stoichiometric raw materials (Li_2S, P_2S_5, LiI, and SnS_2 were weighed (total 1 g) and sealed in zirconia ball milling pots. The mass ratio between the mixture and the zirconia ball is 1: 40. Low-speed ball milling (180 rpm for 2 h) was used at first to fully mix the starting materials. After that, high-speed of 510 rpm for 13 h was conducted on the mixture. All ball milling processes was protected under Ar gas atmosphere by using planetary ball milling apparatus. Then, the ball-milled product was pressed into pellets, and sealed in quartz tubes for post annealing treatment. The annealing condition was 450 ^{o}C/ 8 h in the muffle furnace. The rate of increasing temperature was fixed at 5 ^{o}C/ min. After the annealing was completed, the sample naturally cooled down to room temperature (RT). It is noted that S vacancy can be produced if partly replacing P_2S_5 with SnS_2 in the starting raw materials, which can be represented by the following defect equation using Kröger-Vink notation: $2SnS_2 \xrightarrow{P_2S_5} 2Sn_P^{'} + 4S_S^{\times} + V_S^{\bullet\bullet}$. Through reacting with other reactants, the S vacancy is

occupied, while more Li atoms are introduced to keep charge balance, increasing the solubility of Li^+ ions in the crystal structure.

Preparation of LPSBr-xSn SSEs (substitution percentage x = 1, 2.5, 5, 10, 12.5, 15, 20, 30) and LPSCl-xSn SSEs (substitution percentage x = 0 and 30): Li_2S, P_2S_5, SnS_2, and LiBr were used for LPSBr-xSn SSEs preparation, while Li_2S, P_2S_5, SnS_2, and LiCl raw materials for LPSCl-xSn. Similar to the preparation process of synthesizing LPSI-xSn SSEs, same ball milling condition and annealing process were used to prepare LPSBr-xSn and LPSCl-xSn SSEs.

Preparation of LCO@LNO cathode materials and LCO@LNO/LGPS cathode composites: According to the previously reported method from our group[45], ALD process was used to prepare a $LiNbO_x$ coating layer on the commercial LCO particles to form LCO@LNO composites. The LCO@LNO/LGPS cathode composite was prepared by milling LCO@LNO powder and LGPS electrolyte (mass ratio 7:3) with a roll mixer.

5.2.2 Ionic conductivity measurements

Ionic conductivity of prepared SSEs was measured by the EIS measurements and corresponding simulation method. EIS measurements were completed on a multichannel potentiostation 3/Z (German VMP3). The applied frequency range is 0.1 Hz ~ 7 MHz and the amplitude is 20 mV. The test cell was fabricated as follows: 80 mg of the SSEs were pressed into a pellet (diameter 1 cm, thickness 0.7 mm) with a pressure of ~ 300 MPa. Subsequently, two pieces of indium (In) foil serving as the current collector were pressed on both sides of the electrolyte pellet in a model cell. To gain the Arrhenius plot, variable-temperature EIS was measured from -5 ^oC to 45 ^oC with an interval of 10 ^oC.

5.2.3 Cell assembly and electrochemical measurements

For Li//LPSI-20Sn//Li symmetric cells, typically, 80 mg of LPSI-20Sn electrolyte was pressed by ~300 MPa to form solid pellet. Two pieces of Li metal (China Energy Lithium Co. LTD) were placed onto both sides of the LPSI-20Sn pellet and then pressed by ~120 MPa for 3 minutes. Li plating/stripping experiments were carried out on LAND battery testing stations (CT-2001A, Wuhan Rambo Testing Equipment Co., Ltd.). Current density and cut-off capacity were set at 0.1 mA cm^{-2} and 0.1 mAh cm^{-2}. For Li/LPSI-20Sn//LGPS//LCO@LNO//LGPS ASSLMBs were fabricated using LGPS as the electrolyte, prepared LCO@LNO/LGPS as the cathode composite, LPSI-20Sn as the Li

metal anode interlayer, and Li metal as the anode. Typically, 80 mg of the LGPS electrolyte (purchased from MSE supplies LLC) was pressed under ~300 MPa to form a solid LGPS layer (diameter: 10 mm, thickness: 0.65 mm). 20 mg of LPSI-20Sn electrolyte was spread on one side of the LGPS layer, and pressed under ~300 MPa to form an interlayer (diameter: 10 mm, thickness: 0.17 mm) to separate Li metal and LGPS layer. 10 mg of LCO@LNO/LGPS powder was uniformly spread onto the surface of the other side of LGPS layer and pressed under ~360 MPa for 5 minutes. Finally, Li metal was placed on the LPSI-20Sn layer and pressed by ~120 MPa for 3 minutes. The four-layered pellet cell was sandwiched between two stainless-steel rods as current collectors and sealed in the model cell. Galvanostatic charge-discharge was conducted on the LAND battery test system. The voltage window was set as 2.8~4.2 V (vs. Li/Li^+), and various constant current densities were applied to evaluate the cycling stability and the rate performance. All cell fabrication processes were conducted in an Ar-filled glove box.

5.2.4 Air stability measurements

The electrolyte stability against dry O_2 was measured in the thermogravimetric analysis (TGA) instrument. Powder electrolytes were placed in the atmosphere of continuous flow of dry O_2 with the weight recorded by the built-in micro balance. The stability toward moisture was evaluated as the follows: electrolytes were placed in an airtight chamber with humidity and gas (O_2, N_2, air, and vacuum) controlling. After exposure of 10% humidity overnight, XRD and the EIS measurements were conducted for the electrolyte samples. Reheating process was processed in a vacuum oven (180 ^oC) overnight.

5.2.5 Characterization

SEM images and element mapping were obtained by using a Hitachi S-4800 field-emission scanning electron microscope (FE-SEM, acceleration voltage 5 kV) equipped with energy dispersive spectroscopy (EDS). X-ray diffraction (XRD) measurements were performed on Bruker AXS D8 Advance with Cu Kα radiation (λ = 1.54178 Å). Capton tape was covered on the XRD holder to prevent from the air exposure. Low-speed-scan XRD pattern of LPSI-20Sn electrolyte was obtained by scanning at the speed of 5s/step (1 step = 0.02 °) from 10 to 90° (2θ). XRD Rietveld refinement was performed by using Materials Studio software. Raman spectra were measured with a HORIBA Scientific LabRAM HR Raman spectrometer operated under an incident laser beam at 532 nm. Electrolyte samples were

sealed and sandwiched in two pieces of transparent glasses for Raman testing. X-ray photoelectron spectroscopy (XPS) spectra were obtain by using Krotos AXIS Ultra Spectrometer system using a monochromatic Al K(alpha) source (25 mA, 15 kV). Solid-state ^{7}Li NMR measurements were carried out on a Varian Infinity Plus 400 (I+400) NMR spectrometer (B_o = 9.4 T), operating at a ^{7}Li resonance frequency of 155.248 MHz. The $\pi/2$ pulse length was determined to be 2.3 μs. Chemical shifts were referenced with respect to a 1.0 M LiCl solution. The electrolyte sample was sealed in custom-made Teflon tubes (ϕ = 4.7 mm) in an argon-filled glovebox. Variable temperature (-40 ^{o}C to 130 ^{o}C with an interval of 5 ^{o}C or 10 ^{o}C) measurements were performed by using a 5 mm static probe. T_1 relaxation (spin-lattice) time at various temperature were determined by using the saturation recovery method.

Density functional theory (DFT) calculation: It was conducted to both static computation and geometry optimization of LPSI and LPSI-20Sn crystal, using the CASTEP DFT code of Accelrys Material Studio 8.0 with the exchange-correlation functional of Perdew-Burke-Ernzerh (PBE) based on generalized gradient approximation (GGA).[46-47] The cut-off energy for the plane-wave basis is set as 380.0 eV. The k-point mesh of 2×2×2 is adopted and the SCF tolerance is set as 5.0×10^{-7} eV/Å. The FFT grid density is set as 90×90×90. The crystal structure of LPSI-20Sn crystal was employed by using different occupation ratio of Sn and P in the same site position. The oxygen replacement reaction energy (ΔE) of LPSI-20Sn and LPSI electrolytes were simulated based on the differential energy by changing one of the S atom to O atom in the model structure. One 2×2×2 supercell of LPSI or LPSI-20Sn was use as the model structure by changing one of the S atom. The oxygen replacment reaction energy (ΔE) can be calculate as $\Delta E = U_{(S\ atom)} + U_{(PS3O\ tetrahedron)} - U_{(O\ atom)} - U_{(PS4\ tetrahedron)}$, which can be defined as one of the indicator to reveal the resistance capability of sulfide electrolyte (containing PS_4 tetrahedron) to O_2.

5.3 Results and Discussion

5.3.1 Synthesis and Structure of LPSI-xSn SSEs

Conventional solid-state-reaction methods were employed to synthesize a series of Sn-substituted Argyrodite Li_6PS_5I (LPSI) -based electrolytes with various Sn substitution percentages: LPSI-xSn (x = 0, 10, 20, 30, 50, 80, and 100, where x = 0 is the pristine LPSI

electrolyte, and x = 100 means complete substitution of P with Sn in the LPSI electrolyte). The corresponding chemical reaction equation can be written as: (5+y) Li_2S + (1-y) P_2S_5 + (2y) SnS_2 + 2 LiI = 2 $Li_{6+y}P_{1-y}Sn_yS_5I$, where y is the substitution content of Sn ($0 \leq y \leq 1$). X-ray diffraction (XRD) measurements were first carried out to study the phase composition of the prepared LPSI-xSn electrolytes. As shown in **Figure 5.1a**, pure LPSI phase can be obtained without any Sn substitution, which is highly consistent with the referenced LPSI (PDF# 04-018-1431). The border diffraction peak at around 18° is assigned to the Kapton tape, which is used to seal the XRD sample and prevent air exposure. With the Sn substitution percentage increasing, the characteristic diffraction peaks of LPSI vanish, while some peaks belonging to the Li_4SnS_4 and LiI phases raise gradually. Close inspection on the XRD pattern in the 2θ range of 24.5^o ~ 25° (**Figure 5.1b**) suggests that the strongest diffraction peak in LPSI patterns at 24.8^o shifts continually to lower diffraction angle along with increased Sn substitution amount. **Figure 5.1c** presents a low-speed-scan XRD with Rietveld refinement of the representative LPSI-20Sn electrolyte. One predominant phase is a Argyrodite structure with cubic symmetry (space group F-43m) with unit cell parameters: a = b = c = 10.21760 Å, α = β = γ = 90.00° and V = 1066.71 Å^3 (**Table S5.1**, Supporting Information). The small amount of impurity (2.7%) is identified as LiI. The distorted Argyrodite structure (as shown in **Figure 5.1d**) exhibits a non-stoichiometric composition of $Li_{6.24}P_{0.823}Sn_{0.177}S_{4.58}I_{0.9}$ with Li-rich and vacancy in the structure (**Table S5.2,** Supporting Information). The substituted Sn atom in the 4b site is shared with P and the occupation is around 17.8%, which is closed to the designed substitution content (20%). It is found that the Li-rich environment and vacancy distribution within the synthesized of $Li_{6.24}P_{0.823}Sn_{0.177}S_{4.58}I_{0.9}$ is quite different from that of the Li_6PS_5I structure (**Table S5.3,** Supporting Information), indicating different Li^+ conduction and migration pathways in the electrolytes. The enlarged crystal unit cell is derived from the replacement of P with Sn, which has a larger atomic radius ($R_{<Sn>}$ 1.40 Å > $R_{<P>}$ 1.10 Å), and the increased Li^+ ion concentration in the specific unit cell. The characteristic unit cell is expected to benefit the Li^+ ion conduction and to increase the ionic conductivity.[30-31] A similar phenomenon is observed in the LPSBr-xSn (x = 0, 1, 5, 10, 12.5, 15, 20, 30) system (**Figure S5.1**, Supporting Information), but cannot occur in the LPSCl-xSn (x = 0 and 30) system (**Figure S5.2**, Supporting Information). The reason is

related to the atomic radius of X in the Argyrodite structure (X = Cl, Br, and I), where the larger size of the I atom endows the LPSX structure with more possibilities of various aliovalent elemental substitutions.[30]

Furthermore, Raman spectral measurements were conducted to verify Sn substitution in the position of P in LPSI-xSn electrolytes. As shown in **Figure S5.3**, the Raman shift at 416.3 cm^{-1} is the fingerprint position that reflects the PS_4 blocks (P only exists in tetrahedral PS_4 in LPSI electrolyte) in LPSI electrolyte.[38] After Sn substitution, the intensity of PS_4 peak reduces, and an additional peak in the 337.7 ~ 342.9 cm^{-1} region appears and increases in intensity with increased Sn substitution percentage. Co-existence of the two peaks implies the formation of $(P/Sn)S_4$ structure. In the fully Sn-substituted sample LPSI-100Sn, the only characteristic peak at 342.9 cm^{-1} agrees well with the previously reported position that indicates the formation of SnS_4 structure.[28] Scanning electron microscopy (SEM) was used to examine the morphology and the element distribution in LPSI-20Sn electrolyte (**Figure S5.4**, Supporting Information). Micro-sized irregular LPSI-20Sn secondary particle is composed of nano-sized primary particles (~100 nm). Energy disperse spectroscopy (EDS) element mapping for the selected area demonstrates that P, S, Sn, and I are homogeneously dispersed in granular LPSI-20Sn electrolytes. In other words, the Sn precursors can fully mix and react with other raw materials for substitution. The results of the above mentioned structural and compositional analyses confirm that successful Sn substitution for P in LPSI-xSn structure is achieved. The expanded unit cells and small electrolyte particle sizes are desirable for high ionic conductivity and applicable LPSI-based electrolytes. The derived I chemistry at Li/electrolyte interface is favorable towards achieving a stable Li metal anode. In addition, the formation of the Sn-S bonds is also beneficial for enhanced air stability.

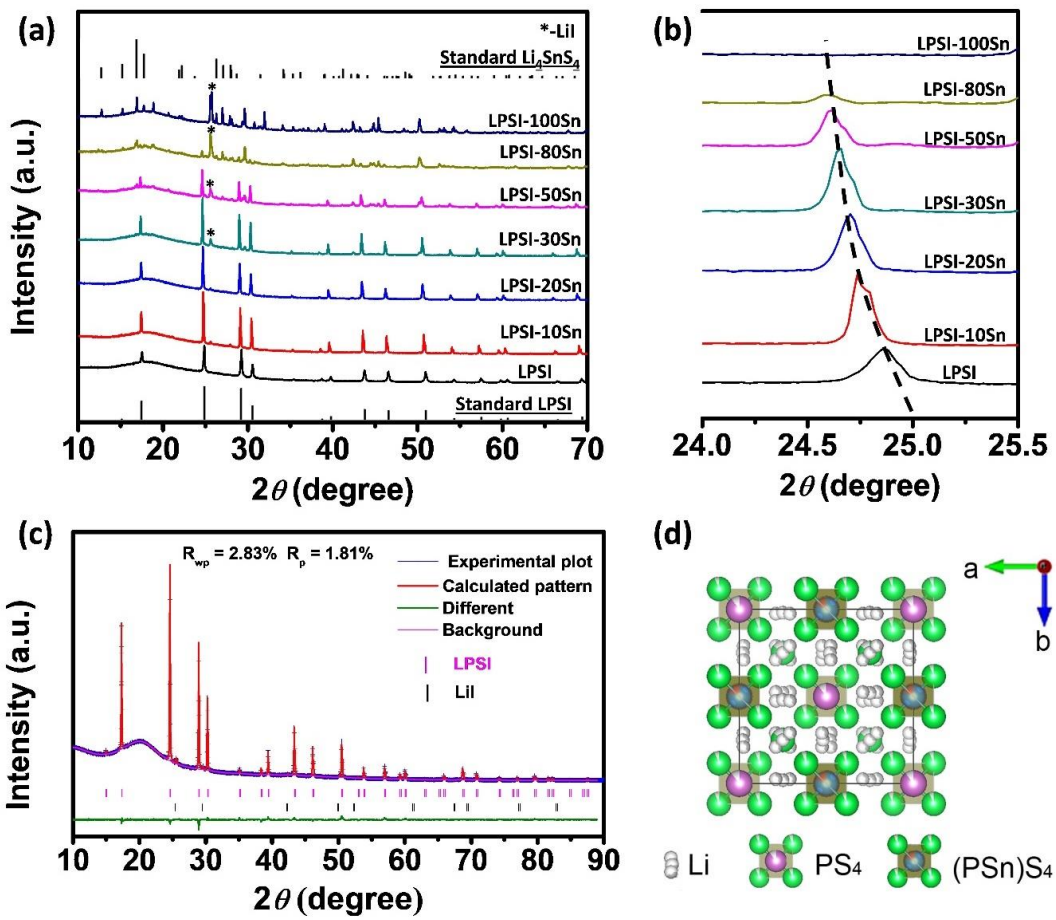

Figure 5.1 (a) XRD patterns of the prepared LPSI-xSn sulfide-based electrolytes (x = 0, 10, 20, 30, 50, 80, 100); (b) magnified region of the XRD patterns in the 2θ range: 24° < 2θ < 25.5°; (c) Low-speed-scan XRD pattern of representative LPSI-20Sn electrolyte and the corresponding Rietveld refinements; (d) Structure of prepaed LPSI-20Sn ($Li_{6.24}P_{0.823}Sn_{0.177}S_{4.58}I_{0.9}$) from the view of perpendicular to c-axis.

5.3.2. Ionic Conductivity and Li^+ Ion Dynamics of LPSI-xSn SSEs

Electrochemical impedance spectroscopy (EIS) was measured to deduce the ionic conductivity (σ) of the prepared LPSI-xSn electrolytes. The plot of σ value as a function of Sn content at room temperature (RT) is shown in **Figure 5.2a**. The LPSI electrolyte without any Sn substitution shows a very low σ of 2.8×10^{-6} S cm^{-1}, which is in agreement with previously reported literatures.[36] After partly replacing P with Sn in the tetrahedral PS_4 of LPSI-based electrolyte, dramatic change of σ takes place. 10% Sn substitution can

significantly increase the σ to 4.2×10^{-5} S cm^{-1}, showing a 15-times increase. The optimized σ can reach 3.5×10^{-4} S cm^{-1} when the Sn substitution percentage is 20%. Compared with the σ of the pristine LPSI electrolyte, the σ of LPSI-20Sn exhibits an increase of 125 times. This makes LPSI-20Sn comparable to some common sulfide SSEs in terms of ionic conductivity.[4] Nevertheless, too much Sn substitution can lead to decrease in σ as a result of the formation of impurity phases. **Figure 5.2b** compares the Arrhenius plots of LPSI and LPSI-20Sn electrolytes derived from a series of ionic conductivities in a temperature range from -5 to 45 ^{o}C (interval 10 ^{o}C for each point). The σ value of the LPSI-20Sn electrolyte at any given temperature is about two orders of magnitude higher than that of LPSI electrolyte without Sn substitution. Furthermore, the activation energy of Li^{+} ion transport in LPSI-20Sn structure (E_a-LPSI-20Sn) calculated from the slop of Arrhenius plot is 0.299 eV, which is much lower than that in LPSI structure (E_a-LPSI = 0.424 eV). Arrhenius plots of other Sn-substituted LPSI-xSn electrolytes (x = 10, 15, 17.5, 22.5, 25, 30, 50, 80) are also present in **Figure S5.5**, and the derived activation energy of each composition is displayed in **Figure 5.2c**. The trend for change in E_a against Sn substitution amount is inverse compared with the trend in **Figure 5.2a**. Li^{+} ion movement becomes much easier after Sn substituting in the LPSI structure. The lowest point appears with a substitution percentage of 20%, which is corresponding to the fastest Li^{+} ion motion and the largest ionic conductivity in this structure. The activation energy shows an increasing trend after the Sn substitution percentage is over 20%. This is ascribed to the gradually increasing amount of impurity phases (mainly LiI and Li_4SnS_4). σ of another Sn-substituted system, LPSBr-xSn (substitution percentage x = 1, 2.5, 5, 10, 12.5, 15, 20, 30), was also investigated to further understand the Sn substitution effect on the ionic conductivity. The results are shown in **Figure S5.6**. The optimized σ value of 2.1×10^{-3} S cm^{-1} is achieved when the degree of Sn substitution is at 12.5 % in the LPSBr structure. This σ value of LPSBr-12.5Sn is twice larger than that of LPSBr electrolyte (σ-LPSBr = 1.0×10^{-3} S cm^{-1}). Meanwhile, the activation energy of LPSBr-12.5Sn (0.30 eV) is lower than that of LPSBr (0.33 eV).

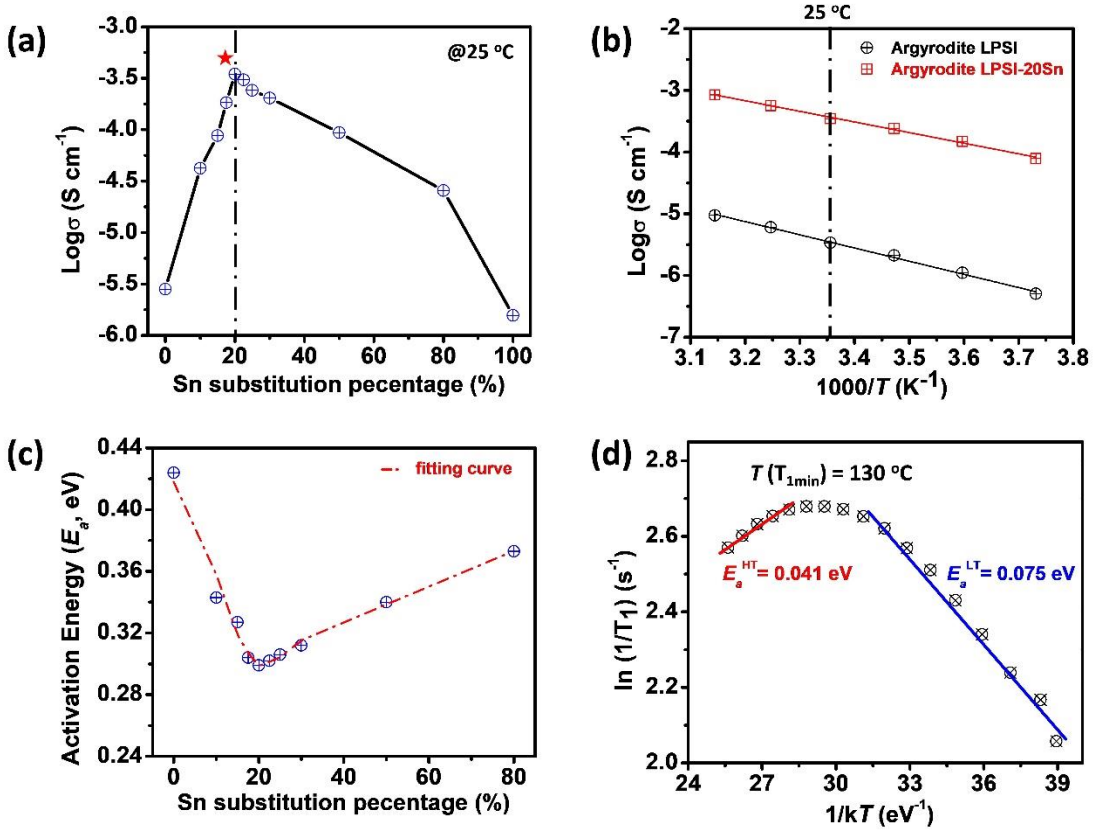

Figure 5.2 (a) The room temperature (RT, 25 °C) ionic conductivity of LPSI-xSn sulfide-based electrolytes with different amounts of Sn substitution (x = 0, 10, 15, 17.5, 20, 22.5, 25, 30, 50, 80, 100); (b) Arrhenius plots of the LPSI-20Sn electrolyte and LPSI electrolyte without Sn substitution; (c) change trend of the activation energy against different substitution percentages; (d) Temperature-dependent ^{7}Li spin−lattice relaxation (SLR) NMR rates measured in the laboratory frame for LPSI-20Sn electrolytes.

^{7}Li solid-state nuclear magnetic resonance (^{7}Li-NMR) was employed to probe the Li^{+} ion dynamics in LPSI-20Sn at an atomic level. It can provide information on bulk ionic conductivity of the electrolyte without the contribution from grain boundaries in SSEs. First, the line-shapes of ^{7}Li static NMR resonance of LPSI-20Sn at different temperatures are presented as **Figure S5.7**. The line-shape of ^{7}Li resonance becomes narrower with increasing temperature, a phenomenon reported elsewhere.[39] The observed line narrowing is due to the increased Li-ion mobility that averages out the dipolar interaction at higher test temperatures. Then, ^{7}Li spin-lattice relaxation (SLR) rates ($1/T_1$) were measured as a

function of temperature (*T*). As shown in **Figure 5.2d**, a minimum T_1 (T_{1min}) is observed when T reaches 130 ^{o}C. The slopes of the linear portions of the curves on both low temperature (LT) and high temperature sides of the T_{1min} are used to calculate the activation energy of short-range (E_a^{LT}) and long-range (E_a^{HT}) Li^+ ion mobility, respectively.[40] They are 0.041 eV and 0.075 eV for E_a^{HT} and E_a^{LT}, respectively. These results are reasonable as they are much lower than the values derived from the EIS measurements, because the negative effect of boundary has been excluded.[39-40] In contrast, for the LPSI electrolyte without Sn substitution, the ^{7}Li SLR results (**Figure S5.8**, Supporting Information) show a larger activation energy in both HT and LT regions (0.076 and 0.082 eV, respectively). All above Li^+ ion motion analyses (both EIS and ^{7}Li-NMR results) confirm that replacing P with appropriate amounts of Sn can promote Li^+ ion transport in the favorable Sn-substituted Argyrodite LPSI structures. The Sn substitution results in significantly improved ionic conductivity and reduced Li^+ ion motional activation energy.

5.3.3. Air Stability of LPSI-20Sn SSEs

After optimizing ionic conductivity and probing Li^+ ion mobility in the LPSI-xSn electrolyte system, the air-stability of the LPSI-20Sn electrolyte was examined. The reactivity towards O_2 was investigated by monitoring the weight change of the electrolyte in a micro-balance of a thermogravimetric analysis (TGA) instrument when the electrolyte is exposed to pure O_2 (99.999 %) flow. **Figure 5.3a** illustrates the change in mass percentage of the electrolytes as a function of the exposure time in pure O_2 atmosphere. Compared with pure LPSI electrolyte (specific surface area: 1.50 cm^3 g^{-1}) whose weight increases by 1.12% after being exposed to O_2 for 10h, LPSI-20Sn electrolyte (specific surface area: 1.41 cm^3 g^{-1}) shows significantly improved resistance toward O_2. The mass percentage increase is as low as 0.28 % after exposure to pure O_2 for 10 h and only 0.35 % after 20 h, which indicates that the LPSI-20Sn electrolyte maintains its structure in pure O_2 after initial minor decomposition. In addition to the good resistance to O_2, LPSI-20Sn electrolyte also exhibits excellent stability towards moisture. As shown in **Figure 5.3b**, the XRD patterns exhibit little difference between LPSI-20Sn electrolytes before and after exposure to 10% humidity overnight except for some small unknown impurity peaks (**Figure S5.9**, Supporting Information). X-ray absorption near-edge spectra (XANES) of P

K-edge (**Figure 5.3c**) cannot also witness the chemical environment change of P after exposing to 10% humidity overnight, but the ionic conductivity of LPSI-20Sn drops slightly to 2.2 × 10^{-4} S cm^{-1} at RT (**Figure 5.3d**). This might be ascribed to the decomposition of some PS_4 blocks which are not effectively Sn substituted. However, the ionic conductivity of LPSI-20Sn can recover to 3.1 × 10^{-4} S cm^{-1} at RT after a post-heating process (180 ^{o}C in vacuum oven) is conducted. The XRD pattern of the post-heated sample in **Figure 5.3b** confirms that the impurity phases vanish and all featured diffraction peaks agree well with the pristine LPSI-20Sn electrolyte. In contrast, a larger amount of impurity diffraction peaks can be observed after exposing LPSI electrolytes to 10% humidity (**Figure S5.10**, Supporting Information). Even after the same post-heating treatment, the diffraction peaks from impurities still exist.

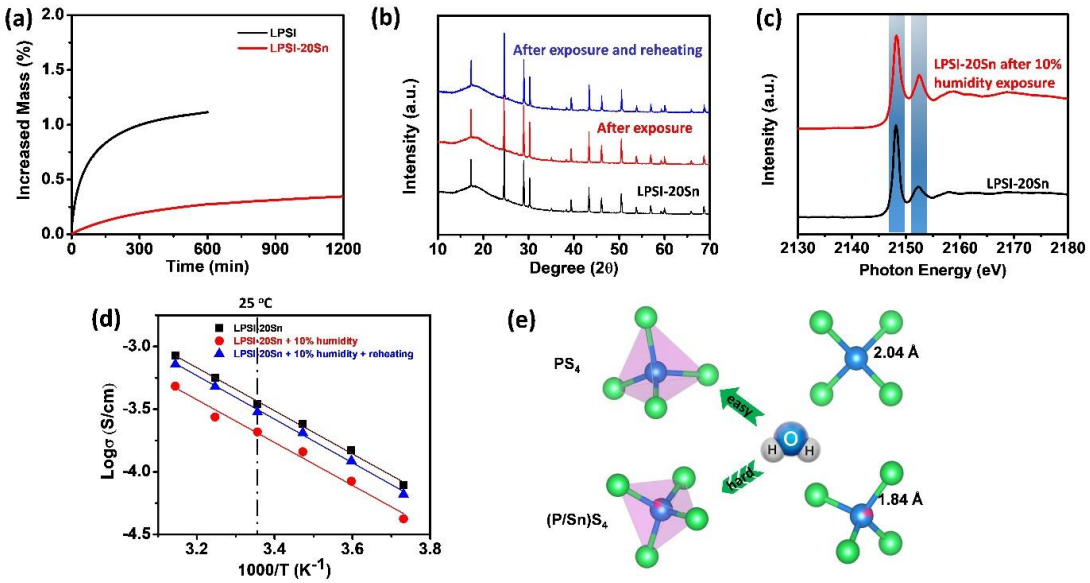

Figure 5.3 (a) Time-resolved mass change of LPSI and LPSI-20Sn electrolytes in pure O_2; XRD patterns (b) and Arrhenius plots (d) of the LPSI-20Sn electrolyte before and after exposure to air with 10% humidity, as well as after post-heating process; (c) XANES of P K-edge in LPSI-20Sn and the sample after exposing to 10% humidity; (e) Schematic diagram of the difficult degree of being oxidized by H_2O of PS_4 and $(P/Sn)S_4$ tetrahedrons based on the DFT calculation.

Density functional theory (DFT) calculations of the oxygen replacment reaction energy (ΔE) was conducted to reveal the improved air-stability of LPSI-20Sn electrolytes. Generally, the first-step degradation of the sulfide electrolyte containing PS_4 tetrahedron towards O_2 or H_2O is related to the replacment reaction of S with O atom.[19-20] The oxygen replacment reaction energy of LPSI-20Sn and LPSI electrolytes were simulated based on the differential energy by changing one of the S atom to O atom in the model structure. When changing one of the PS_4 tetrahedron to PS_3O tetrahedron in the whole crystal structure, the reaction can be simulated as PS_4 tetrahedron + O atom = PS_3O tetrahedron + S atom. Therefore, the oxygen replacment reaction energy (ΔE) can be calculate as $\Delta E = U_{(S\ atom)} + U_{(PS3O\ tetrahedron)} - U_{(O\ atom)} - U_{(PS4\ tetrahedron)}$. The oxygen replacment reaction energy (ΔE) can be defined as one of the indicators to evaluate the reaction capabilities between sulfide electrolytes and O_2 or H_2O. As a result of the DFT calculation, the ΔE of LPSI and LPSI-20Sn electrolyte is 2.667 eV and 9.298 eV, respectively. The results indicate a much stronger bonding energy of (P/Sn)-S in the $(P/Sn)S_4$ tetrahedron than that of P-S in the PS_4 tetrahedron when replacing S with O. In other words, a better resistance capability of LPSI-based electrolytes can be obtained after Sn substitution (see the schematic diagram in **Figure 5.3e**). The Sn substituted in the lattice prefers to bond to S rather than O, endowing the LPSI-20Sn electrolyte to have a stable crystal structure.

5.3.4. Li Metal Compatibility of LPSI-20Sn SSEs

The Li anode interface stability of Li/LPSI-20Sn compared to that of Li/LPSI with was evaluated by the Li-Li symmetric cells cycling. The results are shown in **Figure 5.4**. Under a current density of 0.1 mA cm^{-2} and a cut-off capacity of 0.1 mAh cm^{-2}, Li//LPSI-20Sn//Li symmetric cell can perform an ultra-stable Li plating/stripping for over 700 hours (350 cycles) at RT (**Figure 5.4a**). Even under a high current density of 1.26 mA cm^{-2} and cut-off capacity of 1 mAh cm^{-2}, our Li//LPSI-20Sn//Li symmetric cell can still display a very stable Li plating and stripping behaviour for ~200 h (125 cycles) at RT (**Figure 5.4c**). The durability can be comparable to the best performances in the previous reported symmetric cells using sulfide-based electrolytes (**Table S5.4**, Supporting Information). Detailed plating/stripping voltage profiles under low current density of 0.1 mA cm^{-2} can be seen in the magnified regions at different cycling time points in **Figure 5.4a-1, a-2, and a-3**. Flat

and axisymmetric polarization curves exhibit ultra-stable and highly reversible Li plating and stripping behaviours at the Li/LPSI-20Sn interface. The initial overpotential is 30 mV, which is comparable to that of the LiI-doped LPS electrolytes.[24] After 700 h of stable Li plating and stripping process, the overpotential increase to 56 mV, which is due to the in-situ formed SEI layer slightly increasing the interfacial impedance. In sharp contrast, the Li-Li symmetric cell using LPSI as the electrolyte even cannot plate and strip regularly for one cycle. The ultra-low ionic conductivity of LPSI leads to a high overpotential of more than 3V. The violent fluctuation and gradually reduced overpotential indicate poor Li plating/stripping kinetics at the Li/LPSI interface (**Figure 5.4b**). Time-resolved EIS of the Li//LPSI-20Sn//Li symmetric cell was also used to enclose the stable Li/LPSI-20Sn interface before symmetric cell cycling (**Figure S5.11**, Supporting Information). During the 24 hours after assembling, negligible impedance change can be found in the Li//LPSI-20Sn//Li symmetric cell. This reveals that there is no side reaction happening to the Li/LPSI-20Sn interface. The robust Li anode interface benefits from the rich I-containing electrolytes (7.7 % mole ratio), which has also been demonstrated in LiI-doped LPS electrolytes. SEM measurements for the Li metal surface were conducted after Li plating/stripping in the Li//LPSI-20Sn//Li symmetric cell at 0.1 mA cm^{-2}/ 0.1mAh cm^{-2} for ~60 h (**Figure S5.12**, supporting information). A relatively smooth and dense Li surface is formed in-situ, which shows a uniform distribution of I-containing species. X-ray photoelectron spectroscopy (XPS) measurements for the surface further confirm the I species is LiI compounds (**Figure S5.13**). The binding energy of $3d_{2/3}$ (630.6 eV) and $3d_{5/3}$ (619.1 eV) agree well with the previous literature.[41] The LiI formed at the Li anode interface can serve as a vital component for stabilizing SEI to create uniform electron and ion distribution as well as suppress the formation of Li dendrites.[22, 42]

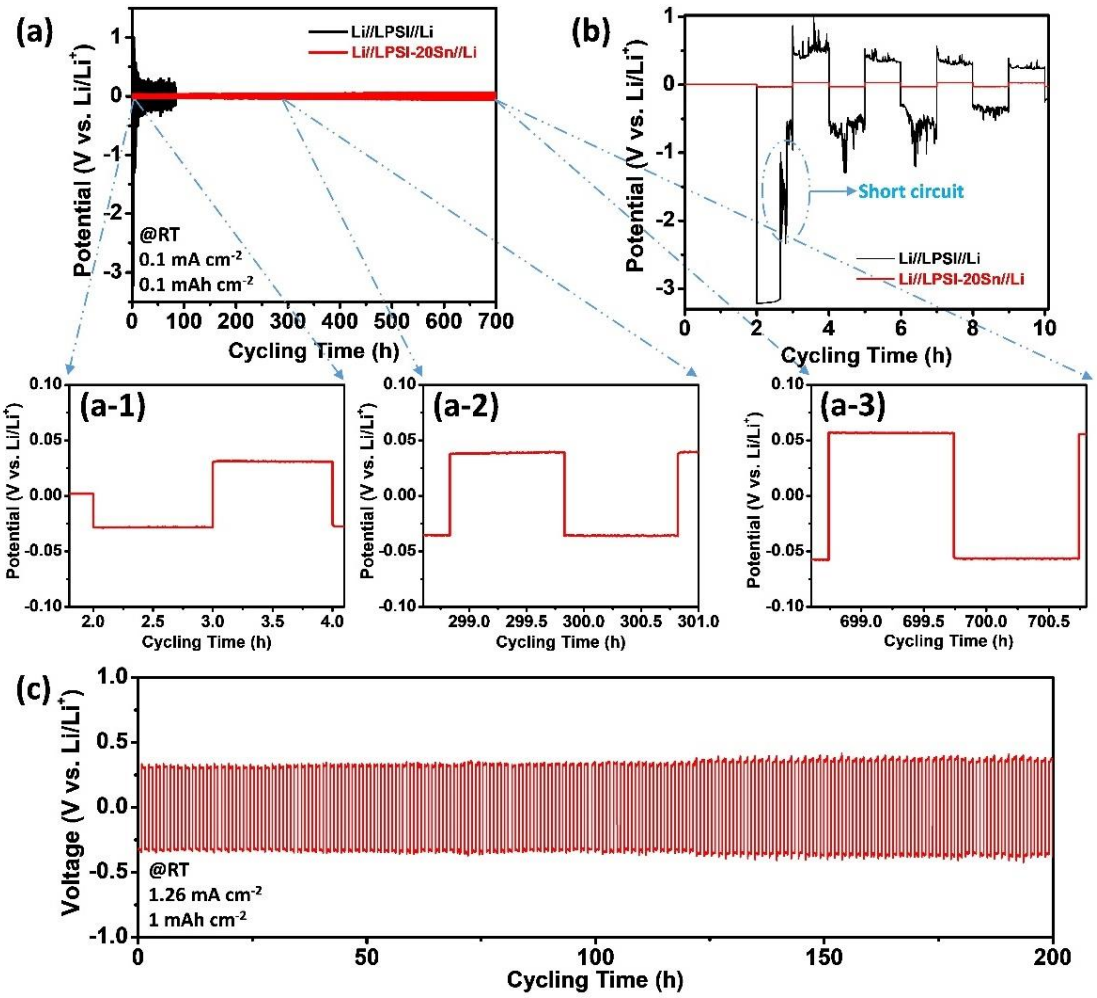

Figure 5.4 Li-Li symmetric cells performance: (a) comparison of using LPSI and LPSI-20Sn electrolytes; (b) magnified region of 0~10 h in Figure 5.4a; (a-1), (a-2), and (a-3) are the magnified regions of the voltage profile at different time from Figure 5.4a. (c) Li plating/stripping polarization of the Li//LPSI-20Sn//Li symmetric cell tested under 1.26 mA cm^{-2}/ 1 mAh cm^{-2}.

5.3.5. Full Battery Performance

To demonstrate the applicability of the LPSI-20Sn electrolyte in ASSLMBs, we further employed the LPSI-20Sn electrolyte as the interlayer separating the Li metal and $Li_{10}GeP_2S_{12}$ (LGPS) electrolyte, with the use of a $LiNbO_x$ coated $LiCoO_2$ (LCO@LNO) cathode (as shown in the schematic diagram **Figure 5.5a).** RT galvanostatic charge-discharge tests were conducted on full batteries in a voltage window of 2.8~4.2 V (Li/Li^+

,the same below) and under various current densities at RT. **Figure 5.5b** shows the first three charging and discharging curves under a low current density of 0.05 C (1 C = 140 mA g_{LCO}^{-1}). The charge and discharge curves with a plateau at ~ 3.9 V are extremely similar to those in the liquid electrolyte systems, suggesting highly reversible Li^+ ion de-intercalation and intercalation behavior towards the LCO cathode materials.[43] The first-cycle reversible specific capacity is 123.7 mAh g^{-1}, and the corresponding Coulombic efficiency can reach as high as 91%. The first cycle efficiency is one of the highest reported for ASSLMBs using Li metal as the anode directly. The high efficiency is attributed to the excellent stability of Li/LPSI-20Sn interface. Because Li^+ ions can smoothly shutter through this LiI-assistant robust Li anode interface, no waste of Li source accounts for consumption of irreversible reactions and the Li dendrites. After three initial cycles at 0.05 C, the cycling stability of this full battery at 0.1 C at RT is displayed in **Figure 5.5c**. The reversible specific capacity maintains steady at ~113.0 mAh g^{-1}, and negligible capacity decay is observed in the first 20 cycles. After 50 cycles, a capacity retention of 88.5% can be achieved. Remarkably, the average coulombic efficiency reaches 99.8 % during the long cycling process, suggesting highly reversible Li^+ ion intercalation/de-intercalation. In sharp contrast, the full battery without the LPSI-20Sn functional interlayer (Li//LGPS//LCO@LNO//LGPS) shows large voltage polarization at 0.05 C and even cannot deliver reversible capacity at 0.1 C (**Figure S5.14**, Supporting Information). Apart from the cycling stability, the rate capability was also evaluated as shown in **Figure 5.5d**. The rate performance was obtained by elevating the discharge current densities, while keeping the charge current density at 0.05 C. This method enables the complete uptake of Li source from the cathode and an estimate of the influence of sluggish Li^+ ion transport problem in cathode composites.[44] In this way, reversible specific capacities can hold to as high as 98.1 and 93.8 mAh g^{-1} at high current densities of 0.8 C and 1 C, respectively. Moreover, when the current density is reduced to 0.1 C afterward, the specific capacity can recover to 111.0 mAh g^{-1} and remains stable in the following cycling. Unlike the reported results that indicate Li dendrites are prone to form under high current densities, our full batteries have been proved to possess very promising performance, particularly, the rate capability for the practical applications (**Table S5.5**, Supporting Information).

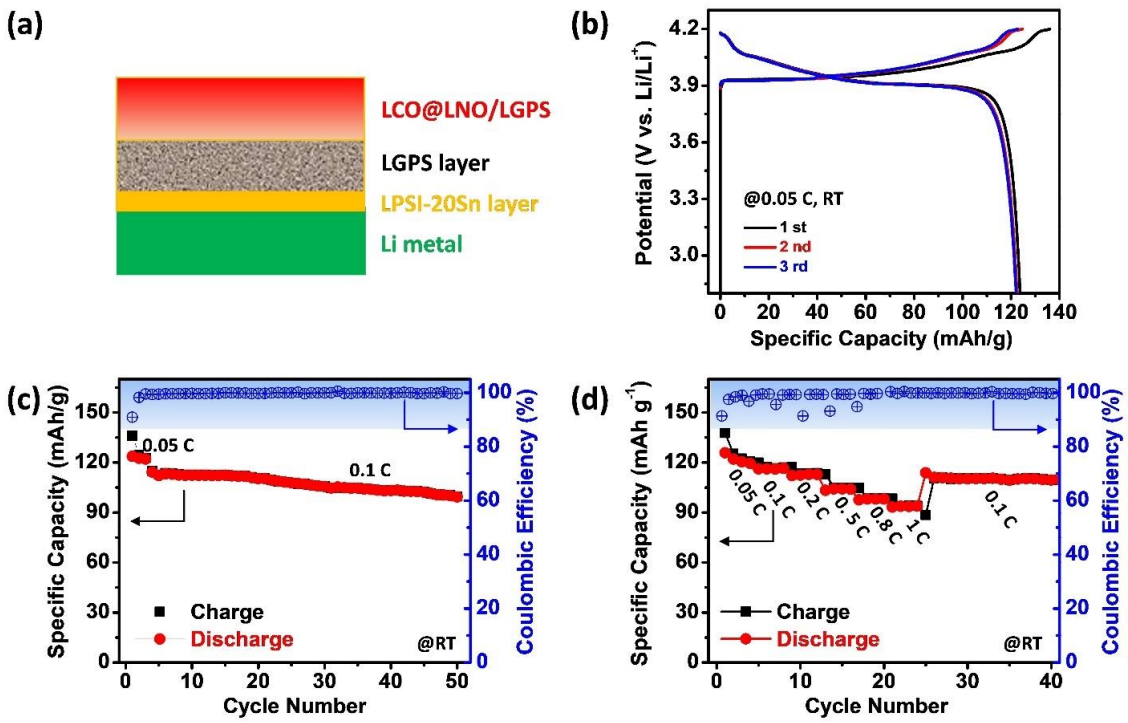

Figure 5.5 ASSLMBs electrochemical performance: (a) schematic diagram of the Li/LPSI-20Sn//LGPS//LCO@LNO//LGPS ASSLMBs with the highlighted anode interlayer; (b) the first three charge-discharge profiles of the fabricated ASSLMBs; cycling stability (c) and rate capability (d) of the Li/LPSI-20Sn//LGPS//LCO@LNO//LGPS at RT.

5.4 Conclusion

To conclude, P (V) in Argyrodite LPSI electrolyte was partially replaced by Sn (IV) to form a series of new LPSI-xSn electrolytes. The larger cell volume and increased Li^+ solubility resulting from Sn substitution for P in the PS_4 tetrahedral structure endow the optimized LPSI-20Sn electrolyte with two orders of magnitudes higher (125 times) ionic conductivity (3.5×10^{-4} S cm^{-1}) compared with LPSI electrolyte (2.8×10^{-6} S cm^{-1}). More remarkably, the optimized LPSI-20Sn electrolyte is also proved to process excellent air stability (O_2 and moisture) derived from the strong Sn-S bonding energy in $(P/Sn)S_4$ structure. The mass and ionic conductivity of LPSI-20Sn exhibit negligible changes after O_2 and 10%-humidity exposure (after reheating), respectively. In addition, benefiting from the I-based chemistry in stabilizing the Li metal anode interface against sulfide electrolytes, Li-Li symmetric cells using LPSI-20Sn as the electrolyte can exhibit outstanding plating

and stripping for over 200 hours at a high current density (1.26 mA cm^{-2}) and cut-off capacity (1 mAh cm^{-2}) in the Li//LPSI-20Sn//Li symmetric cell. LPSI-20Sn electrolyte was further employed as the Li metal anode interlayer in ASSLMBs to provide a stabilized Li metal anode interface for achieving excellent cycling stability and rate capability. All these results suggest that the reasonable aliovalent element substitution for the problematic element in promising sulfide electrolytes can exhibit multi-functions capabilities and making them more suitable for application in sulfide-based ASSLMBs.

5.5 Acknowledgements

F. Zhao and J. Liang contributed equally to this work. This research was supported by the Natural Science and Engineering Research Council of Canada (NSERC), the Canada Research Chair Program (CRC), the Canada Foundation for Innovation (CFI), Ontario Research Foundation (ORF), China Automotive Battery Research Institute Co., Ltd., Glabat Solid-State Battery Inc., and the University of Western Ontario (UWO).

5.6 References

（1）Manthiram, A.; Yu, X.; Wang, S., *Nat. Rev. Mater*. **2017,** *2* (4), 16103.

（2）Kato, Y.; Hori, S.; Saito, T.; Suzuki, K.; Hirayama, M.; Mitsui, A.; Yonemura, M.; Iba, H.; Kanno, R., *Nat. Energy* **2016,** *1* (4), 16030.

（3）Kamaya, N.; Homma, K.; Yamakawa, Y.; Hirayama, M.; Kanno, R.; Yonemura, M.; Kamiyama, T.; Kato, Y.; Hama, S.; Kawamoto, K.; Mitsui, A., *Nat. Mater.* **2011,** *10* (9), 682-686.

（4）Zhang, Z.; Shao, Y.; Lotsch, B.; Hu, Y.-S.; Li, H.; Janek, J.; Nazar, L. F.; Nan, C.-W.; Maier, J.; Armand, M.; Chen, L., *Energy Environ. Sci.* **2018,** *11* (8), 1945-1976.

（5）Gao, Z.; Sun, H.; Fu, L.; Ye, F.; Zhang, Y.; Luo, W.; Huang, Y., *Adv. Mater.* **2018,** *30* (17), 1705702.

（6）Chen, S.; Xie, D.; Liu, G.; Mwizerwa, J. P.; Zhang, Q.; Zhao, Y.; Xu, X.; Yao, X., *Energy Storage Mater.* **2018,** *14*, 58-74.

（7）Lau, J.; DeBlock, R. H.; Butts, D. M.; Ashby, D. S.; Choi, C. S.; Dunn, B. S., *Adv. Energy Mater.* **2018,** *8* (27), 1800933.

（8）Culver, S. P.; Koerver, R.; Krauskopf, T.; Zeier, W. G., *Chem. Mater.* **2018,** *30* (13), 4179-4192.

（9）Xu, R.; Xia, X.; Zhang, S.; Xie, D.; Wang, X.; Tu, J., *Electrochim. Acta* **2018,** *284*, 177-187.

（10）Fan, L.; Wei, S.; Li, S.; Li, Q.; Lu, Y., *Adv. Energy Mater.* **2018,** *8* (11), 1702657.

（11）Albertus, P.; Babinec, S.; Litzelman, S.; Newman, A., *Nat. Energy* **2018,** *3* (1), 16-21.

（12）Zhu, Y.; He, X.; Mo, Y., *ACS Appl. Mater. Interfaces* **2015,** *7* (42), 23685-23693.

（13）Kato, A.; Kowada, H.; Deguchi, M.; Hotehama, C.; Hayashi, A.; Tatsumisago, M., *Solid State Ionics* **2018,** *322*, 1-4.

（14）Wenzel, S.; Weber, D. A.; Leichtweiss, T.; Busche, M. R.; Sann, J.; Janek, J., *Solid State Ionics* **2016,** *286*, 24-33.

（15）Wenzel, S.; Sedlmaier, S. J.; Dietrich, C.; Zeier, W. G.; Janek, J., *Solid State Ionics* **2018,** *318*, 102-112.

（16）Wenzel, S.; Randau, S.; Leichtweiß, T.; Weber, D. A.; Sann, J.; Zeier, W. G.; Janek, J., *Chem. Mater.* **2016,** *28* (7), 2400-2407.

（17）Nagao, M.; Hayashi, A.; Tatsumisago, M.; Kanetsuku, T.; Tsuda, T.; Kuwabata, S., *Phys. Chem. Chem. Phys.* **2013,** *15* (42), 18600-18606.

（18）Cheng, X. B.; Zhang, R.; Zhao, C. Z.; Zhang, Q., *Chem. Rev.* **2017,** *117* (15), 10403-10473.

（19）Muramatsu, H.; Hayashi, A.; Ohtomo, T.; Hama, S.; Tatsumisago, M., *Solid State Ionics* **2011,** *182* (1), 116-119.

（20）Luther, G. W.; Findlay, A. J.; Macdonald, D. J.; Owings, S. M.; Hanson, T. E.; Beinart, R. A.; Girguis, P. R., *Front. Microbiol.* **2011,** *2*, 62.

（21）Gao, Y.; Wang, D. W.; Li, Y. G. C.; Yu, Z. X.; Mallouk, T. E.; Wang, D. H., *Angew. Chem. Int. Ed.* **2018,** *57* (41), 13608-13612.

（22）Xu, R.; Han, F.; Ji, X.; Fan, X.; Tu, J.; Wang, C., *Nano Energy* **2018,** *53*, 958-966.

（23）Fan, X.; Ji, X.; Han, F.; Yue, J.; Chen, J.; Chen, L.; Deng, T.; Jiang, J.; Wang, C., *Sci. Adv.* **2018,** *4* (12), 12.

（24）Han, F.; Yue, J.; Zhu, X.; Wang, C., *Adv. Energy Mater.* **2018,** *8* (18), 1703644.

（25）Suyama, M.; Kato, A.; Sakuda, A.; Hayashi, A.; Tatsumisago, M., *Electrochim. Acta* **2018,** *286*, 158-162.

（26）Brant, J. A.; Massi, D. M.; Holzwarth, N. A. W.; MacNeil, J. H.; Douvalis, A. P.; Bakas, T.; Martin, S. W.; Gross, M. D.; Aitken, J. A., *Chem. Mater.* **2014,** *27* (1), 189-196.

（27）Kaib, T.; Haddadpour, S.; Kapitein, M.; Bron, P.; Schröder, C.; Eckert, H.; Roling, B.; Dehnen, S., *Chem. Mater.* **2012,** *24* (11), 2211-2219.

（28）Kanazawa, K.; Yubuchi, S.; Hotehama, C.; Otoyama, M.; Shimono, S.; Ishibashi, H.; Kubota, Y.; Sakuda, A.; Hayashi, A.; Tatsumisago, M., *Inorg. Chem.* **2018,** *57* (16), 9925-9930.

（29）Sahu, G.; Lin, Z.; Li, J.; Liu, Z.; Dudney, N.; Liang, C., *Energy Environ. Sci.* **2014,** *7* (3), 1053-1058.

（30）Kraft, M. A.; Ohno, S.; Zinkevich, T.; Koerver, R.; Culver, S. P.; Fuchs, T.; Senyshyn, A.; Indris, S.; Morgan, B. J.; Zeier, W. G., *J. Am. Chem. Soc.* **2018,** *140* (47), 16330-16339.

（31）Minafra, N.; Culver, S. P.; Krauskopf, T.; Senyshyn, A.; Zeier, W. G., *J. Mater. Chem. A* **2018,** *6* (2), 645-651.

（32）Deiseroth, H. J.; Kong, S. T.; Eckert, H.; Vannahme, J.; Reiner, C.; Zaiss, T.; Schlosser, M., *Angew. Chem. Int. Ed.* **2008,** *47* (4), 755-758.

（33）Yu, C.; van Eijck, L.; Ganapathy, S.; Wagemaker, M., *Electrochim. Acta* **2016,** *215*, 93-99.

（34）Yu, C.; Ganapathy, S.; Hageman, J.; van Eijck, L.; van Eck, E. R. H.; Zhang, L.; Schwietert, T.; Basak, S.; Kelder, E. M.; Wagemaker, M., *ACS Appl. Mater. Interfaces* **2018,** *10* (39), 33296-33306.

（35）Zhang, Z.; Zhang, L.; Yan, X.; Wang, H.; Liu, Y.; Yu, C.; Cao, X.; van Eijck, L.; Wen, B., *J. Power Sources* **2019,** *410-411*, 162-170.

（36）Kraft, M. A.; Culver, S. P.; Calderon, M.; Bocher, F.; Krauskopf, T.; Senyshyn, A.; Dietrich, C.; Zevalkink, A.; Janek, J.; Zeier, W. G., *J. Am. Chem. Soc.* **2017,** *139* (31), 10909-10918.

（37）Ohno, S.; Helm, B.; Fuchs, T.; Dewald, G.; Kraft, M. A.; Culver, S. P.; Senyshyn, A.; Zeier, W. G., *Chem. Mater.* **2019,** *31* (13), 4936-4944.

（38）Yubuchi, S.; Teragawa, S.; Aso, K.; Tadanaga, K.; Hayashi, A.; Tatsumisago, M., *J. Power Sources* **2015,** *293*, 941-945.

（39）Yu, C.; Ganapathy, S.; de Klerk, N. J. J.; Roslon, I.; van Eck, E. R. H.; Kentgens, A. P. M.; Wagemaker, M., *J. Am. Chem. Soc.* **2016,** *138* (35), 11192-11201.

（40）Ganapathy, S.; Yu, C.; van Eck, E. R. H.; Wagemaker, M., *ACS Energy Lett.* **2019,** *4* (5), 1092-1097.

（41）Kim, S.; Kim, S. K.; Sun, P. C.; Oh, N.; Braun, P. V., *Nano Lett.* **2017,** *17* (11), 6893-6899.

（42）Lu, Y.; Tu, Z.; Archer, L. A., *Nat. Mater.* **2014,** *13* (10), 961-969.

（43）Mizushima, K.; Jones, P. C.; Wiseman, P. J.; Goodenough, J. B., *Mater. Res. Bull.* **1980,** *15* (6), 783-789.

（44）Yu, C.; Ganapathy, S.; Eck, E.; Wang, H.; Basak, S.; Li, Z.; Wagemaker, M., *Nat. Commun.* **2017,** *8* (1), 1086.

（45）Wang, B.; Zhao, Y.; Banis, M. N.; Sun, Q.; Adair, K. R.; Li, R.; Sham, T. K.; Sun, X., *ACS Appl. Mater. Interfaces* **2018,** *10* (2), 1654-1661.

（46）Segall, M. D.; Lindan, P. J. D.; Probert, M. J.; Pickard, C. J.; Hasnip, P. J.; Clark, S. J.; Payne, M. C., *J. Phys.: Condens. Matter* **2002,** *14* (11), 2717-2744.

（47）Clark, S. J.; Segall, M. D.; Pickard, C. J.; Hasnip, P. J.; Probert, M. J.; Refson, K.; Payne, M. C., *Z. Kristallogr.* **2005,** *220* (5-6), 567-570.

5.7 Supporting information

Table S5.1 Cystallographic data of LPSI-20Sn and corresponding refined parameters

Compound	**$Li_{6.24}P_{0.823}Sn_{0.177}S_{4.58}I_{0.9}$**
Space Group	F-43m
a, Å	10.21760
b, Å	10.21760
c, Å	10.21760
α=β=γ, °	90
V, Å^3	1066.7108
2θ interval, °	10 - 90
Rwp,%	2.83
Rp, %	1.81
X Ray Radiation	Cu kα (λ1 = 1.5406 Å, λ2 = 1.5444 Å)

Table S5.2 Rietveld analysis results for the XRD pattern of $Li_{6.24}P_{0.823}Sn_{0.177}S_{4.58}I_{0.9}$

Atom	x	y	z	OCC.	U	Site	Sym.
S1	0.25000	0.25000	0.75000	0.860	0.033	4d	-43m
S2	0.11643	-0.11643	0.61643	0.930	0.032	16e	3m
I1	0.0000	0.0000	1.0000	0.900	0.036	4a	-43m
P1	0.0000	0.0000	0.5000	0.823	0.013	4b	-43m
Sn1	0.0000	0.0000	0.5000	0.177	0.015	4b	-43m
Li1	0.2900	0.0250	0.7100	0.380	0.049	48h	m
Li2	0.2500	0.0200	0.7500	0.285	0.013	24g	2mm

Table S5.3 Atomic coordinates, occupation factor and isotropic displacement parameters of Li_6PS_5I obtained from database (space group F-43m, ICSD No. 04-018-1431), a = b = c = 10.145 Å, $\alpha = \beta = \gamma = 90°$

Atom	x	y	z	OCC.	U	Site	Sym.
S1	0.25000	0.25000	0.75000	1.000	0.016	4d	-43m
S2	0.11643	-0.11643	0.61643	1.000	0.019	16e	3m
I1	0.0000	0.0000	1.0000	1.000	0.030	4a	-43m
P1	0.0000	0.0000	0.5000	1.000	0.0130	4b	-43m
Li1	0.2900	0.0250	0.7100	0.370	0.0390	48h	m
Li2	0.2500	0.0200	0.7500	0.260	0.0500	24g	2mm

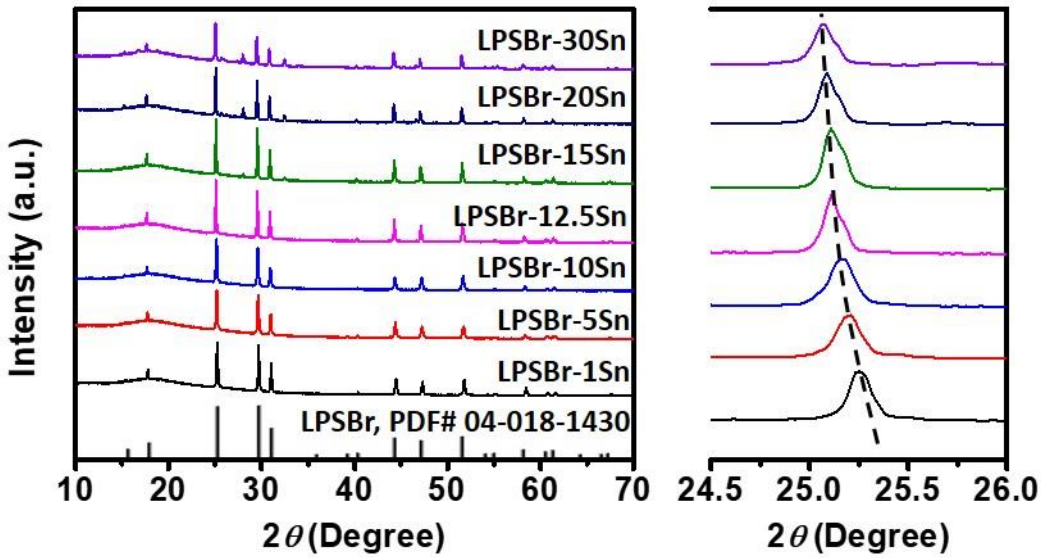

Figure S5.1 XRD patterns of the prepared LPSBr-xSn sulfide-based electrolytes (x = 1, 5, 10, 12.5, 15, 20, 30) and the magnified region in the range: 24.5º < 2θ < 26º.

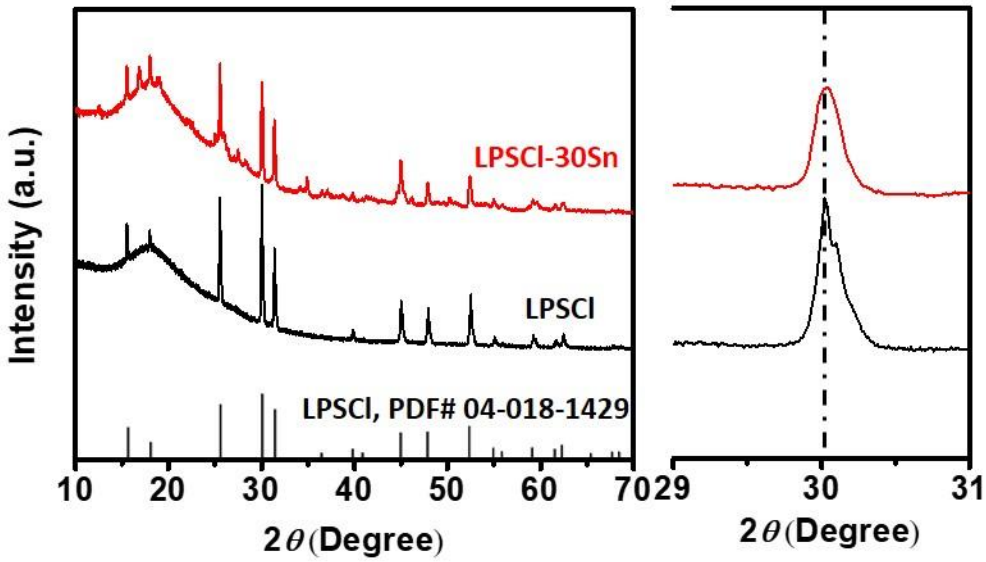

Figure S5.2 XRD patterns of the prepared LPSCl and LPSCl-30Sn sulfide-based electrolytes and the magnified region in the range: 29º < 2θ < 31º.

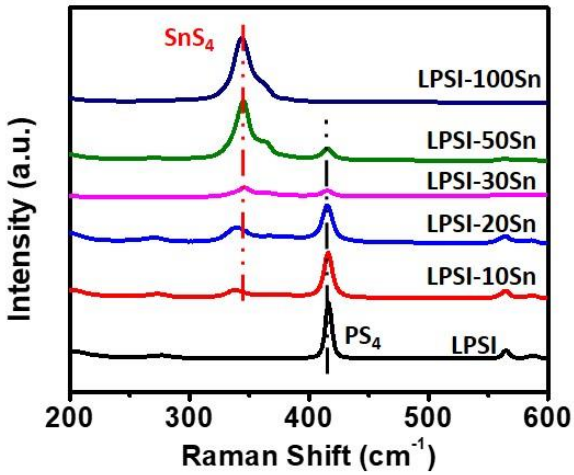

Figure S5.3 Raman spectra of the prepared LPSI-xSn sulfide-based electrolytes (x = 0, 10, 20, 30, 50, 100).

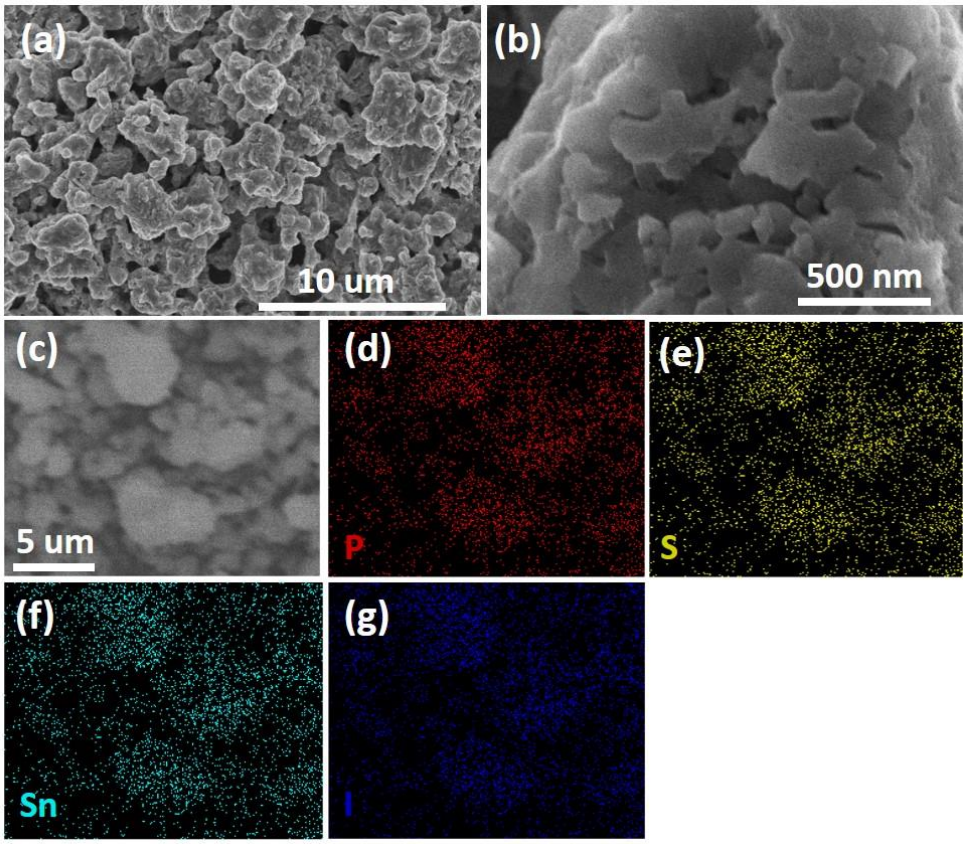

Figure S5.4 SEM images and the EDX mapping of P, S, Sn, and I elements in the LPSI-20Sn electrolyte.

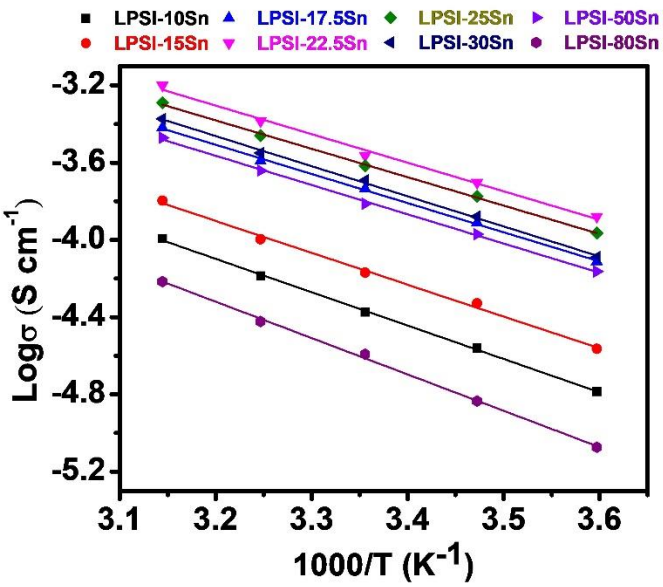

Figure S5.5 Arrhenius plots of the LPSI-xSn electrolyte (x = 10, 15, 17.5, 20, 22.5, 25, 30, 50, and 80).

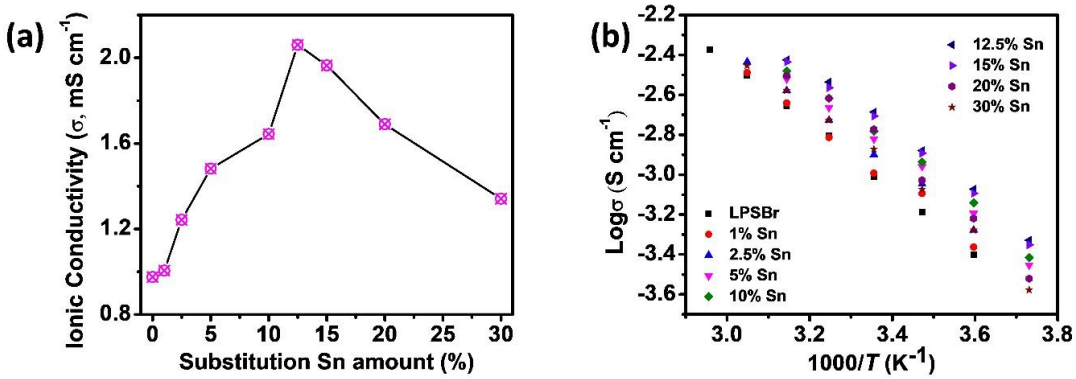

Figure S5.6 (a) Change trend of the room temperature (RT, 25 ^{o}C) ionic conductivity of LPSBr-xSn sulfide-based electrolytes; (b) Arrhenius plots of the LPSBr-xSn electrolyte (x = 1, 5, 10, 12.5, 15, 20, 30).

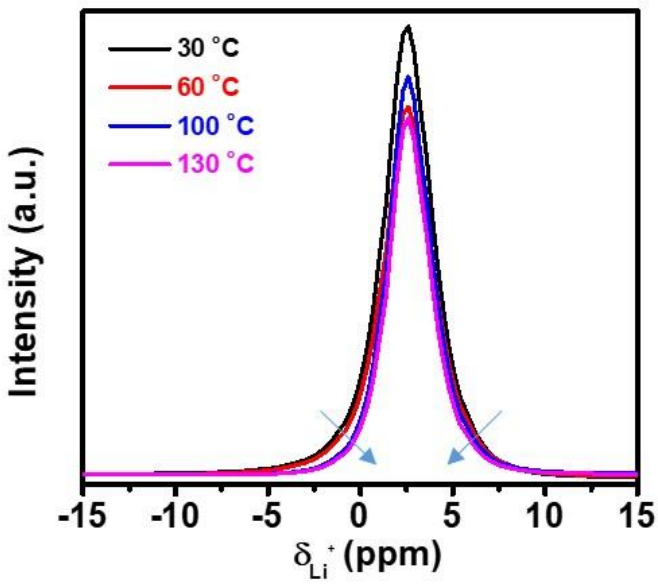

Figure S5.7 Motional narrowing curves of the static ^{7}Li NMR resonance of LPSI-20Sn at various temperatures.

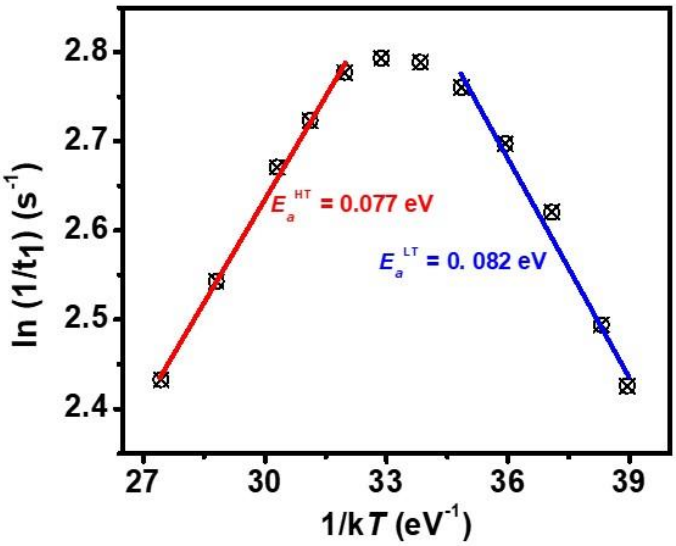

Figure S5.8 Arrhenius plots of the ^{7}Li spin−lattice relaxation (SLR) NMR rates measured in the laboratory (R1) frame for LPSI electrolytes.

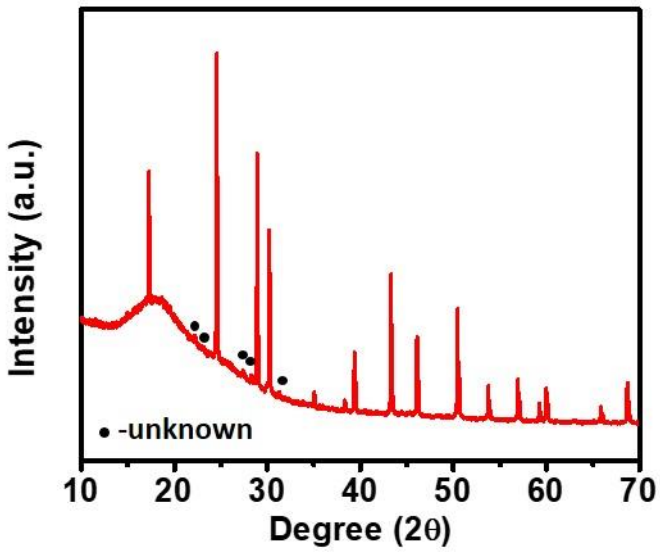

Figure S5.9 The magnified XRD pattern of the LPSI-20Sn electrolyte after exposing to 10% humidity overnight.

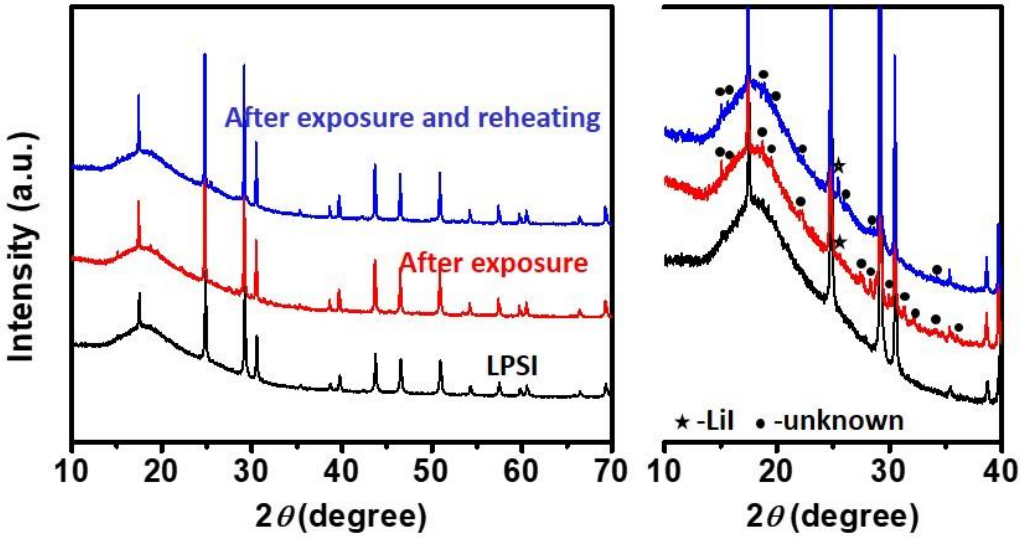

Figure S5.10 XRD patterns of the LPSI electrolyte before and after exposure to air with 10% humidity, as well as after reheating process. Many impurities can be observed when zooming out.

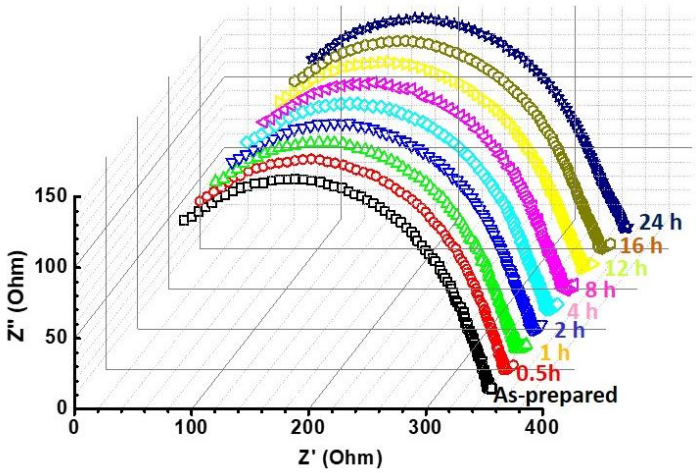

Figure S5.11 Time-resolved EIS of the Li//LPSI-20Sn//Li symmetric cell.

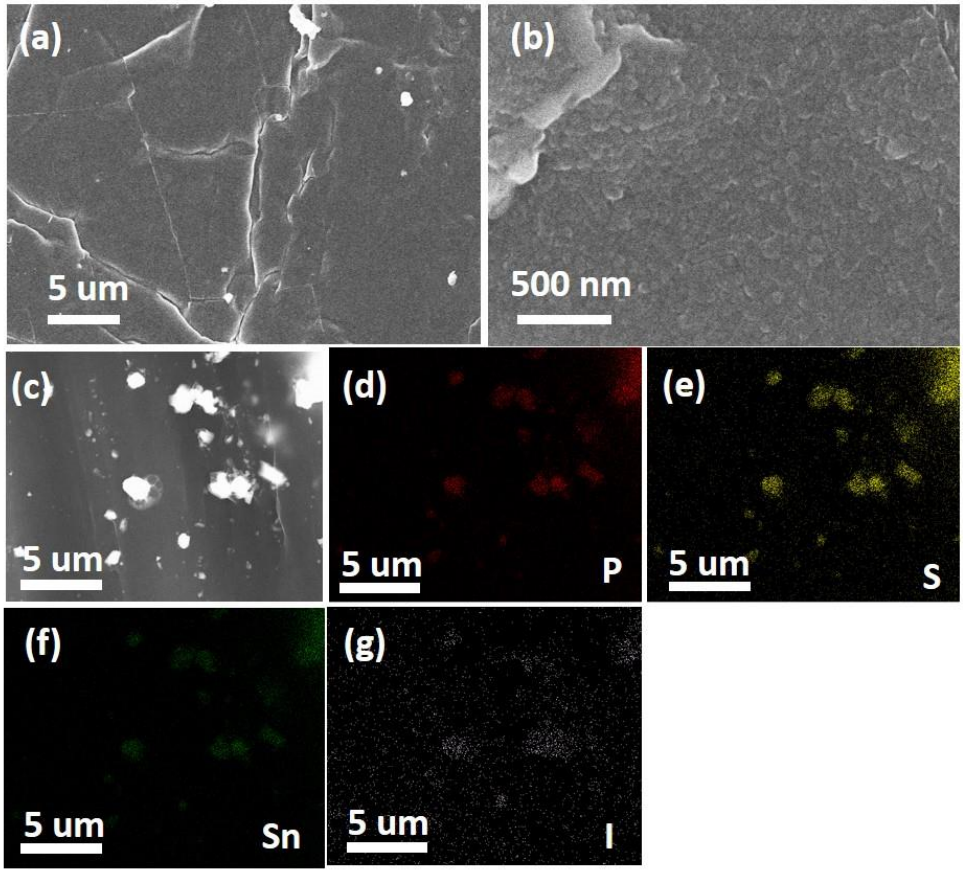

Figure S5.12 (a-b) SEM images of Li surface after ~60 h cycling in the Li//LPSI-20Sn//Li symmetric cell. (c) A selected EDX mapping area, and corresponding element mapping: (d)-P, (e)-S, (f)-Sn and (g)-I.

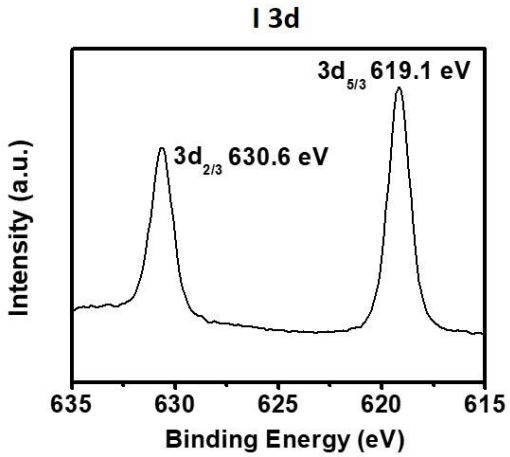

Figure S5.13 A XPS spectrum of I 3d at the Li metal surface after Li plating/stripping.

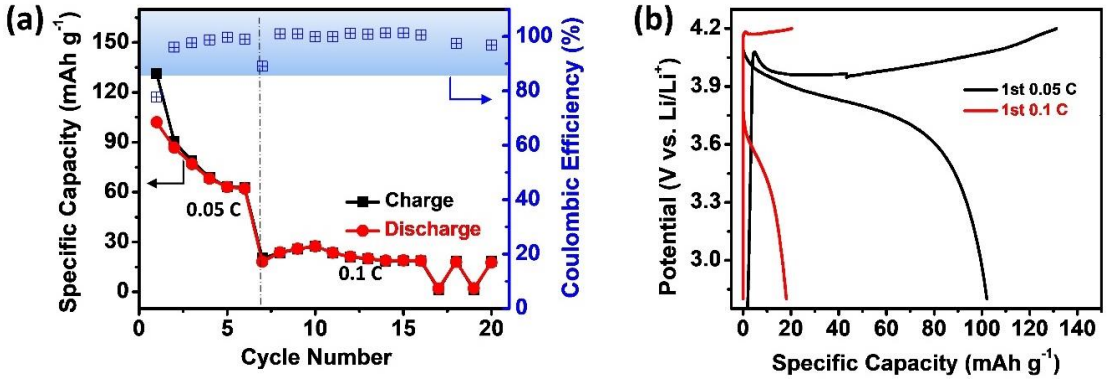

Figure S5.14 (a) Cycling stability and (b) characteristic charge-discharge profiles of the fabricated ASSLMBs: Li//LGPS//LCO@LNO//LGPS at RT.

Table S5.4 Summary of the solid-state sulfide electrolyte-based Li-Li symmetric cells performance

Cell configuration	*Plating current density, mA cm^{-2}*	*Plating specific capacity, mAh cm^{-2}*	*Number of cycle*	*Test temperature*	*Reference*
Li//LPSI-20Sn//Li	**0.1**	**0.1**	**350**	**RT**	**This work**
	1.26	**1**	**125**	**RT**	**This work**
Li/LiF//LPS//LiF/Li	0.5	0.1	100	RT	[1]
Li/LiI//LPS//LiI/Li	0.5	0.1	60	RT	[1]
Li//LPS30I//Li	0.3	0.3	100	RT	[2]
	0.6	0.6	100	60 °C	
	1.5	1.5	100	100 °C	
Li/Cu film//Li3PS4//Li/Cu film	1.3	6.5	5	100 °C	[3]
Li//Li7P2S8I//Li	0.2	0.2	800	RT	[4]
Li|LiFSI@LPS|Li	0.3	0.6	90	RT	[5]

Table S5.5 Summary of the sulfide electrolyte-based all-solid-state Li metal batteries performance (LCO cathode)

Battery configuration (anode/electrolyte/ cathode)	*Cycling stability (current density/ cycle number/ capacity retention)*	*Rate capability (current density/ capacity)*	*1st CE*	*Active material loading*	*Test T*	*Reference*
Li/LPSI-20Sn//LGPS//LCO @LNO//LGPS	**0.1 C/ 50 cycles/ 88.5 % (1 C corresponds to 1.3 mA cm^{-2})**	**0.05 C/ 123.7 mAh g^{-1} 1 C/ 93.8 mAh g^{-1}**	**91 %**	**8.92 mg/cm^2**	**RT**	**This work**
Li@LiF/$Li_7P_3S_{11}$(HFE)/LCO	0.1 mA cm^{-2}/ 100 cycles/ 81.4%	0.1 mA cm^{-2}/ 117.8 mAh g^{-1} 1 mA cm^{-2}/ 59.2 mAh g^{-1}	NA (~80%)	3.6 mg cm^{-2}	RT	[1]

Li//LPS-30LiI/LCO@LNO	0.2 C/ 40 cycles/ 82%	NA (0.2 C/ 120 mAh g^{-1})	NA	10 mg cm^{-2}	RT	[2]
Li//LiFSI@LPS//LCO	0.3 mA cm^{-2}/ 50 cycles/ 90%	NA (0.3 mA cm^{-2}/ 120 mAh g^{-1})	65 %	~7 mg cm^{-2}	RT	[5]
Li@alucone//LSnPS//LCO	0.1 C/ 150 cycles/ 50%	NA (0.1 C/ 120 mAh g^{-1})	75 %	~8 mg cm^{-2}	55 °C	[6]
Li@LiH_2PO_4//LGPS//LCO@LNO	0.1 C/ 50 cycles/ 91.9%	0.1 C/ 131.1 mAh g^{-1} 1 C/ 44.5 mAh g^{-1}	85.9%	~5.5 mg cm^{-2}	RT	[7]

References for the supporting information of Chapter 5

[1] R. Xu, F. Han, X. Ji, X. Fan, J. Tu, C. Wang, *Nano Energy* **2018**, 53, 958.

[2] F. D. Han, J. Yue, X. Zhu, C. S. Wang, *Adv. Energy Mater.* **2018**, 8, 1703644.

[3] A. Kato, M. Suyama, C. Hotehama, H. Kowada, A. Sakuda, A. Hayashi, M. Tatsumisago, *J. Electrochem. Soc.* **2018**, 165, A1950.

[4] E. Rangasamy, Z. C. Liu, M. Gobet, K. Pilar, G. Sahu, W. Zhou, H. Wu, S. Greenbaum, C. D. Liang, *J. Am. Chem. Soc.* **2015**, 137, 1384.

[5] X. L. Fan, X. Ji, F. D. Han, J. Yue, J. Chen, L. Chen, T. Deng, J. J. Jiang, C. S. Wang, *Sci. Adv.* **2018**, 4.

[6] C. Wang, Y. Zhao, Q. Sun, X. Li, Y. Liu, J. Liang, X. Li, X. Lin, R. Li, K. R. Adair, L. Zhang, R. Yang, S. Lu, X. Sun, *Nano Energy* **2018**, 53, 168.

[7] Z. H. Zhang, S. J. Chen, J. Yang, J. Y. Wang, L. L. Yao, X. Y. Yao, P. Cui, X. X. Xu, *ACS Appl. Mater. Interfaces* **2018**, 10, 2556.

Chapter 6

6 Sn-substituted glass-ceramic sulfide solid-state electrolytes

Comparing with the fluorinated sulfide (chapter 4), the Sn-substituted sulfide (chapter 5) performed better because of its versatile improvements in the performance. However, the effect of Sn substitution in sulfides was not fully explored by only focusing on the argyrodite LPSI system. In chapter 6, the 'three-in-one' effect of Sn substitution in the sulfide prototype electrolyte: Li_3PS_4 was studied systematically. To be specific, a new glass-ceramic $Li_{3.2}P_{0.8}Sn_{0.2}S_4$ (gc-$Li_{3.2}P_{0.8}Sn_{0.2}S_4$) SSE is synthesized to satisfy all requirements (high ionic conductivity, air stability, and Li metal stability), enabling high-performance ASSLMBs at room temperature (RT). Compared with the conventional Li_3PS_4 glass-ceramics, the present gc-$Li_{3.2}P_{0.8}Sn_{0.2}S_4$ SSE with 12 % amorphous content has an enlarged unit cell and a high Li^+ ion concentration, which leads to is a 6.2-times higher ionic conductivity (1.21×10^{-3} S cm^{-1} at RT) after a simple cold sintering process. The (P/Sn)S_4 tetrahedron inside the gc-$Li_{3.2}P_{0.8}Sn_{0.2}S_4$ SSE is verified to show a strong resistance toward reaction with H_2O in 5%-humidity air, demonstrating excellent air-stability. Moreover, the gc-$Li_{3.2}P_{0.8}Sn_{0.2}S_4$ SSE triggers the formation of Li-Sn alloys at the Li/SSE interface, serving as an essential component to stabilize the interface and deliver good electrochemical performance in both symmetric and full cells. The discovery of this gc-$Li_{3.2}P_{0.8}Sn_{0.2}S_4$ superionic conductor enriches the choice of advanced SSEs and accelerates the commercialization of ASSLMBs.

*One version of this chapter has been published in Advanced Materials 2021, 33 (8), 2006577.

6.1 Introduction

All-solid-state Lithium metal batteries (ASSLMBs) have been regarded as ideal energy storage devices because of their potential to maximize energy density and improve safety.[1-3] As a key part of ASSLMBs, the development of solid-state electrolytes (SSEs) has drawn increasing attention.[4-5] Among the various types of SSEs, the inorganic glass-ceramic SSE is one of the most promising categories.[6-7] Apart from the advantages of high ionic conductivity and superior mechanical properties in comparison to organic polymer-based SSEs, the glass-ceramic SSEs also show minimal grain boundary resistance and good contact with electrode materials compared to other inorganic ceramic SSEs.[8-9]

Sulfide-based glass-ceramic SSEs have received great attention due to their relatively low glass transition temperature (T_g, lower than 300 ^oC).[6, 10] The metastable Li-ion conductors (e.g., β-Li_3PS_4 and $Li_7P_3S_{11}$) can be precipitated from glass precursors and stabilized in a glass matrix at room temperature (RT).[11-13] Therefore, sulfide-based glass-ceramic SSEs are able to possess high ionic conductivities that are comparable to the well-known crystallized Li Argyrodites or thio-phosphate SSEs.[6, 14] However, sulfide-based glass-ceramic SSEs suffer from poor air-stability and Li metal incompatibility,[15] due to the facts that (1) Sulfide-based SSEs are constructed from P-centered polyhedral units and are extremely hygroscopic because of the intimate affinity between P and O from the moisture. Moreover, the S ligands tend to combine with H and generate toxic H_2S gas.[16] It is noted that Li_3PS_4-based sulfide SSEs shows relatively better resistance towards moisture among the various Li_2S-P_2S_5 electrolyte systems.[16] (2) Sulfide-based SSEs are prone to (electro)chemical reduction from the Li metal anode.[17] There is also a possibility that uneven Li deposition occurs at the Li/sulfide interface, leading to the formation of Li dendrites which may penetrate the soft electrolyte layer and cause short-circuits.[18] Therefore, it is rarely reported that a sulfide electrolyte can be used directly (without interlayers) facing Li metal to construct a workable ASSLMB.[6, 19]

To increase the air-stability of sulfide-based SSEs, crystallized Li_2SnS_3 and Li_4SnS_4 SSEs were developed.[20-21] Based on the hard and soft acids and bases (HSAB) theory, the Sn prefers to bond with S rather than interact with O when exposed to air. However, the limited

ionic conductivity (~10^{-5} S cm^{-1}) at RT hinders their applications.[21-22] Although Arsenic (As)-substituted Li_4SnS_4 SSEs can increase the ionic conductivity to 10^{-3} S cm^{-1} at RT, the hyper toxic As-based compounds prevent their commercialization.[22] Very recently, fractional substitution of P with Sn, Sb, or Zn in the crystallized sulfide SSEs have been reported to improve the air-stability,[23-26] but either insufficient ionic conductivity or poor compatibility with Li metal has impeded them to be used as a single-layer electrolyte for applications. To improve the Li metal compatibility, in addition to the additional and complicated interfacial modification (i.e., pre-treatment of Li metal and utilization of interlayers),[27-30] synthesizing sulfide SSEs with introducing halide elements has been verified as a more effective strategy that can increase the exchange current density and reduce the manufacturing cost.[31-32] Despite the progress, it is still very difficult to overcome the challenges of using the modified SSEs as a monolayer to fabricate practical ASSLMBs, which requires good ionic conductivity (> 10^{-3} S cm^{-1}), air-stability, as well as Li metal compatibility in an integrated manner.[2-3]

Herein, via selective Sn-substitution in the P sites of one classic glass-ceramic β-Li_3PS_4 (gc-Li_3PS_4), a new glass-ceramic $Li_{3.2}P_{0.8}Sn_{0.2}S_4$ (gc-$Li_{3.2}P_{0.8}Sn_{0.2}S_4$) SSE is obtained that can satisfy all the requirements to enable high-performance ASSLMBs. Our gc-$Li_{3.2}P_{0.8}Sn_{0.2}S_4$ SSEs possess an enlarged lattice and higher Li^+ ion concentration compared with gc-Li_3PS_4, offering a 6.2-fold increase in ionic conductivity (1.21×10^{-3} S cm^{-1}) at RT. ^{31}P magic-angle spinning (MAS) solid-state nuclear magnetic resonance (SS-NMR) spectroscopy was used, for the first time, to estimate the amount of amorphous material in the glass-ceramic SSEs. Benefiting from the strong affinity of Sn toward S, the new electrolyte shows excellent air-stability, which paves the way for large-scale processing in conventional dry rooms. Moreover, the incorporated Sn in the electrolyte is found to be capable of forming a Li-Sn alloy at the interface between the electrolyte and Li metal anode. This interface can enable smooth Li deposition and provides highly reversible cycling in all cell formats.

6.2 Experimental Section

6.2.1 Preparation of materials

Synthesis of gc-$Li_{3.2}P_{0.8}Sn_{0.2}S_4$ SSEs: All raw materials were purchased and used directly. Li_2S (Alfa Aesar, 99.9%), P_2S_5 (Sigma Aldrich, > 99 %), and SnS_2 (American Elements, 99.999 %) were weighed in a ratio of 8: 2: 1 (total 1 g) and sealed in a zirconia ball milling pot. The total mass of zirconia ball is ~ 40 g. Low-speed ball milling (150 rpm for 2 h) was firstly conducted to mix raw materials. A high-speed of 550 rpm for 20 h was carried out to prepare the glass electrolytes (g-$Li_{3.2}P_{0.8}Sn_{0.2}S_4$). The ball milling processes were conducted under an Ar gas atmosphere through use of a planetary ball milling apparatus. Subsequently, the ball-milled product was pressed into pellets, and sealed in quartz tubes for heat treatment. The annealing was conducted at 260 ^oC for 5 h in a muffle furnace, which was subsquently cooled down to room temperature. The rate of temperature increase was 5 ^oC/ min. A similar process was used to preprepare other gc-$Li_{3+x}P_{1-x}Sn_xS_4$ SSEs, where x is equal to 0.05, 0.1, 0.15, 0.175, 0.25, 0.3, and 0.4. All weighing and pressing work was completed in an Ar-filled glove box (O_2 < 0.1 ppm, H_2O < 0.1 ppm).

Synthesis of gc-Li_3PS_4 SSEs: Li_2S and P_2S_5 were used as the starting materials. They were weighed in a molar ratio of 3: 1 (totally 1 g) and sealed in a zirconia ball milling pot with ~ 40 g of milling balls. The same two-step ball milling method as described above was used to obtain glass-type Li_3PS_4 SSEs. Pellets of g-Li_3PS_4 was sealed in the quartz tube for the post annealing. The heating condition was adjusted to 220 ^oC for 5 h. The heating rate was also 5 ^oC/ min and natural cooling was used to obtain gc-Li_3PS_4 SSEs.

Synthesis of Li_4SnS_4 SSEs: Li_2S and SnS_2 were used as the starting materials. They were weighed in a molar ratio of 2: 1 (totally 1 g) and sealed in a zirconia ball milling pot with ~ 40 g of milling balls. A ball milling condition of 150 rpm/ 2 h was used to obtain the well-mixed precursors. The obtained mixture was then pressed to pellets, which were sealed in the quartz tube for post annealing (650 °C/ 24 h). To ensure the reaction proceeded to completion, a slow heating rate (18 °C/h) and cooling rate (4 °C/h) were applied to obtain the crystallized Li_4SnS_4 SSEs.

Preparation of LCO/LIC cathode composites: Li_3InCl_6 (LIC) SSEs were obtained according to the previously reported method (*Energy Environ. Sci.* **2019,** 12, 2665-2671). Due to the good cathode compatibility between LIC and LCO, commercial LCO (Sigma Aldrich, 99.8%) powders were used directly. LCO and LIC were mixed in a mass ratio of 7:3 by a roll mixer.

6.2.2 Ionic conductivity measurements

Ionic conductivity of the prepared electrolytes were determined by measuring electrochemical impedance spectroscopy (EIS) of the corresponding cells at the variable temperature (-5~55 ^{o}C, every 10 ^{o}C). The test cell was fabricated as follows: ~100 mg of the electrolytes were pressed (~300 MPa) into a pellet (diameter 1 cm, thickness ~0.7 mm). Then, two pieces of indium (In) foil serving as the current collector were pressed on both sides of the pellet in a model cell. The EIS was collected on a multichannel potentiostat 3/Z (German VMP3). The applied frequency range is 1 Hz ~ 7 MHz and the voltage amplitude is 20 mV.

6.2.3 Cell assembly and electrochemical measurements

Li-Li symmetric cells: Typically, 80 mg of the electrolyte (gc-$Li_{3.2}P_{0.8}Sn_{0.2}S_4$ or gc-Li_3PS_4 SSEs) was pressed by ~300 MPa in a PTFE mold to form a pellet. Two pieces of Li metal (China Energy Lithium Co. LTD) were placed onto both sides of the electrolyte pellet and then pressed with ~120 MPa for 3 minutes. Li plating/stripping experiments were carried out on LAND battery testing stations (CT-2001A, Wuhan Rambo Testing Equipment Co., Ltd.). The current density and cutoff capacity were set at 0.1 mA cm^{-2} and 0.1 mAh cm^{-2}.

Li-LCO/LIC ASSLMBs: The full cells consist of a three-layer structure. Typically, 80 mg of the electrolyte (gc-$Li_{3.2}P_{0.8}Sn_{0.2}S_4$ or gc-Li_3PS_4 SSEs) was pressed with ~300 MPa to form a solid electrolyte layer (10 mm diameter). 10 mg of LCO/LIC powder was uniformly spread onto the surface of the one side of electrolyte layer and pressed with ~360 MPa for 5 minutes. Finally, a Li metal foil was placed on the other side of the electrolyte layer and pressed by ~120 MPa for 3 minutes. The three-layer pellet cell was sandwiched between two stainless-steel rods as current collectors and sealed in the model cell. Galvanostatic charge-discharge was conducted on the LAND battery test system. The voltage window was set as 2.8~4.2 V (vs. Li/Li^+), and various constant current densities were applied to evaluate the cycling stability and the rate performance. All cell fabrication processes were conducted in an Ar-filled glove box (O_2 < 0.1 ppm, H_2O < 0.1 ppm).

6.2.4 Air stability measurements

The stability toward air with various humidity was evaluated as follows: Powder-like electrolytes were placed in an airtight chamber (35 cm× 40 cm× 35 cm) with humidity and gas control. After exposing the electrolyte to the moist air in this chamber overnight, XRD,

XANES, and EIS measurements were carried out to examine the air-stability for the 5%-humidity-exposure sample.

6.2.5 Characterization methods

Lab X-ray diffraction (XRD) measurements were performed on Bruker AXS D8 Advance with Cu Kα radiation (λ = 1.5406 Å). Kapton tape was used to cover the sample holder to prevent from the air exposure. Low-speed-scan XRD pattern of gc-$Li_{3.2}P_{0.8}Sn_{0.2}S_4$ electrolyte was obtained by scanning at the speed of 5 s $step^{-1}$ from 10 to 90° (2θ, one step corresponds to 0.02°). XRD Rietveld refinement was performed by using Topas3 software. SEM images and element mappings were obtained by using a Hitachi S-4800 field-emission scanning electron microscope (FE-SEM, acceleration voltage 5 kV) equipped with energy dispersive spectroscopy (EDS). Raman spectra were measured with a HORIBA Scientific LabRAM HR Raman spectrometer operated under laser beam at 532 nm. Powder-like electrolytes were sealed and sandwiched in two pieces of transparent glasses for the Raman test. Differential scanning calorimeter (DSC) analysis of the glass state electrolytes were performed with a TGA-DSC combined instrument (TA SDT Q600) using N_2 as the gas flow and a heating rate of 5 °C min^{-1}. X-ray photoelectron spectroscopy (XPS) spectra were obtain by using Krotos AXIS Ultra Spectrometer system using a monochromatic Al Kα source (25 mA, 15 kV).

^{119}Sn and ^{31}P MAS NMR measurements were conducted on a Varian/Chemagnetics Infinity Plus 400 WB NMR spectrometer equipped with an Oxford AS400 wide-bore magnet (Bo = 9.4 T). The samples were packed in 4.0 mm zirconia MAS rotors in an Ar-filled glovebox. Teflon tape pieces were used to seal the top of the rotors to avoid direct contact with the air. The spinning speeds were fixed at 14 kHz and 12 kHz for ^{119}Sn and ^{31}P, respectively. One pulse sequence was used to acquire all the spectra. The ^{119}Sn MAS NMR spectra were obtained at 148.9 MHz, using 45° excitation pulse of 1.40 μs and a relaxation delay of 8 s. The ^{31}P MAS NMR spectra were obtained at 161.7 MHz, using 45° excitation pulse of 1.13 μs and a relaxation delay of 15 s. The ^{119}Sn and ^{31}P NMR spectra were referenced with respect to $SnMe_4$ (δ_{iso} = 0.0 ppm) and 85% H_3PO_4 (δ_{iso} = 0.0 ppm) respectively by setting the ^{119}Sn peak of tetracyclohexyl tin to -97.5 ppm and ^{31}P peak of ammonium dihydrogen phosphate to +0.81 ppm.

^{7}Li SS-NMR measurements were carried out on the same NMR facility with a Varian stationary-sample HX 5.0 mm probe. The ^{7}Li Larmor frequency was 155.248 MHz. The π/2 and π pulse length were determined to be 2.3 and 4.5 μs, respectively. Chemical shifts were referenced with respect to a 1.0 M LiCl solution. The electrolyte sample was sealed in custom-made Teflon tubes (ϕ = 4.7 mm) in an argon-filled glovebox. The ^{7}Li spin-lattice relaxation times (T_1) at different temperatures (range: 25 ^{o}C ~ 190 ^{o}C) were determined using an inversion-recovery NMR experiment. The experimental data was fit to a 3-parameter inversion-recovery equation using the Chemagnetics Spinsight NMR software package.

Synchrotron-based characterizations were carried out at the Canadian Light Source (CLS). X-ray diffraction patterns of the samples were collected at the VESPERS beamline (07B2-1, 6 – 30 keV). The diffraction wavelength is 1.1227 Å. Profex and ALBULA softwares were used to process the data. X-ray absorption near edge structure (XANES) spectra were collected on the SXRMB beamline (06B1-1, 1.7 ~ 10 keV) using a Si(111) monochromator. XANES were recorded in the fluorescence mode using a Si solid-state detector and the data was processed with Athena software.

The finite element method (FEM) was used to emulate the distribution of Li^{+} flux at the interface. The physical model was a rectangle cell (thickness 0.8 μm × width 1.5 μm), consisting of Li-Sn alloys (d = 100 nm) and matrix (Li_2S + Li_3P). The bias voltage was set as 0.1 mV, and ground potential was applied. The model follows the charge conservation equation:

$$\nabla \cdot \left(\sigma_i \nabla \varphi \right) = 0$$

σ is the conductivity of species i (i = Li-Sn alloys, Matrix): at room temperature, σ (Li-Sn alloy) = 10^{-3} S cm^{-1} (*J. Electrochem. Soc.* **1987**, 134, 12, 3098; *J. Power Sources* **2010**, 195, 24, 7904-7929); σ (Li_2S) = 10^{-8} S cm^{-1} (*Chem. Lett.* **2015**, 44, 12, 1664-1666); σ (Li_3P) = 10^{-4} S cm^{-1} (*Solid State Ionics* **1989**, 34, 1-2, 97-102; *Angew.Chem. Int. Ed.* **2020**, 59, 2318-2322);

φ is the electrical potential (0.1 mV);

The effective conductivity of the matrix follows the *Bruggeman* correction:

$$\sigma_M = \frac{\varepsilon_a + \varepsilon_b}{\varepsilon_a / \left(\sigma_a \varepsilon_a^{1.5}\right) + \varepsilon_b / \left(\sigma_b \varepsilon_b^{1.5}\right)}$$

ε is the molar fraction of Li_2S and Li_3P in the matrix. The mole ratio of the interfacial products is 0.2/ 4/ 0.8 (Li-Sn alloys/ Li_2S/ Li_3P) according to the law of conservation of mass.

6.3 Results and discussion

The gc-$Li_{3.2}P_{0.8}Sn_{0.2}S_4$ SSEs were prepared via a two-step solid-state reaction method. Ball-milling was firstly used to make the stoichiometric precursor fully amorphous. Subsequently, the glass-state precursor was converted to a glass-ceramic state after a specific annealing process (see the **Experimental Section** for details). Synchrotron-based X-ray diffraction (SXRD) patterns of the electrolytes at different stages of synthesis are shown in **Figure 6.1a**. The featureless patterns of the electrolytes obtained after the first step indicate the success of amorphization for the precursors, namely glass-state $Li_{3.2}P_{0.8}Sn_{0.2}S_4$ (g-$Li_{3.2}P_{0.8}Sn_{0.2}S_4$). Differential scanning calorimeter (DSC) analysis of the g-$Li_{3.2}P_{0.8}Sn_{0.2}S_4$ revealed that ~259 ^oC is the T_g of the $Li_{3.2}P_{0.8}Sn_{0.2}S_4$ phase, which is higher than that of β-Li_3PS_4 (**Figure S6.1**, Supporting Information). After annealing g-$Li_{3.2}P_{0.8}Sn_{0.2}S_4$ at 260 ^oC for 4 hours, the gc-$Li_{3.2}P_{0.8}Sn_{0.2}S_4$ SSE was obtained. The characteristic diffraction peaks of gc-$Li_{3.2}P_{0.8}Sn_{0.2}S_4$ SSE are nearly identical to those of the gc-Li_3PS_4 SSEs, belonging to the metastable β-phase (PDF Card No. 04-010-1784). Nevertheless, upon close observation of the SXRD patterns (**Figure S6.2**), there is a low-angle shift occurring in the gc-$Li_{3.2}P_{0.8}Sn_{0.2}S_4$ sample, suggesting an expansion of the crystal structure after incorporating Sn (R_{Sn4+}: 0.55 Å > R_{P5+}: 0.17 Å). The 2D diffraction patterns of g-$Li_{3.2}P_{0.8}Sn_{0.2}S_4$ and gc-$Li_{3.2}P_{0.8}Sn_{0.2}S_4$ SSEs were recorded on the detector as displayed in **Figure 6.1b** and **c**, respectively. The distinct diffraction rings for the gc-$Li_{3.2}P_{0.8}Sn_{0.2}S_4$ SSE suggest the crystallinity is improved significantly after annealing. Raman measurements confirm that the incorporated Sn can partially replace P and bonds with S in the gc-$Li_{3.2}P_{0.8}Sn_{0.2}S_4$ SSEs. As shown in **Figure 6.1d**, the featured peaks at 345.4 and 419.6 cm^{-1} in the gc-$Li_{3.2}P_{0.8}Sn_{0.2}S_4$ sample can be ascribed to the stretching vibrations of Sn-S and P-S in forms of SnS_4 and PS_4 tetrahedrons, respectively.[33-34] X-ray absorption near edge spectroscopies (XANES) of P and S K-edges proves that the incorporated Sn

affect the fine structure of P and S atoms in the tetrahedra (**Figure S6.3**). Furthermore, scanning electron microscope (SEM) imaging combined with energy dispersive spectroscopy (EDS) elemental mapping indicates that P, S, and Sn are homogeneously dispersed in the sub-micro and irregular gc-$Li_{3.2}P_{0.8}Sn_{0.2}S_4$ particles (**Figure S6.4**). The conformal distribution of Sn reflects that Sn is incorporated into the gc-$Li_{3.2}P_{0.8}Sn_{0.2}S_4$ rather than being present as part of a physical mixture.

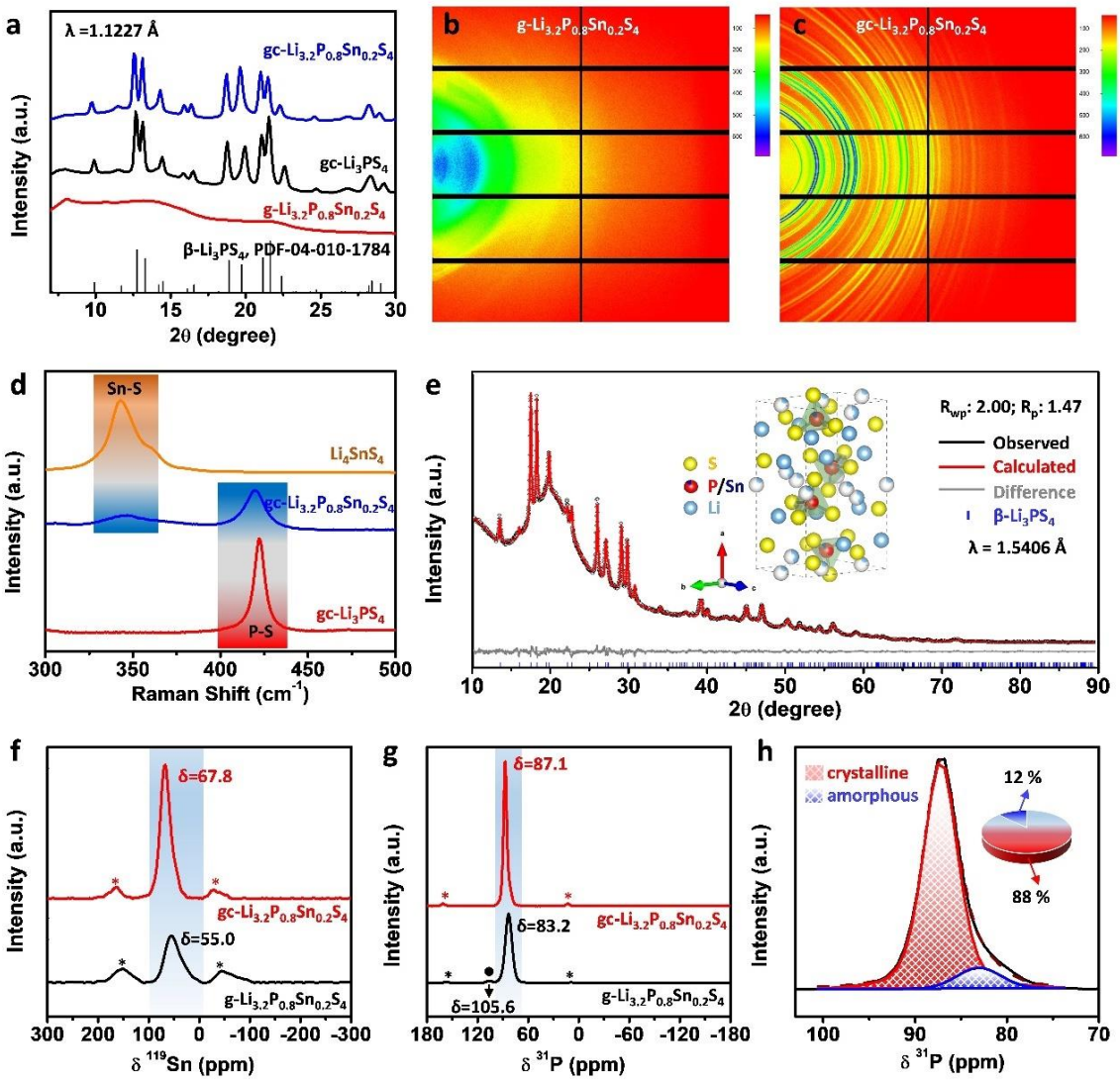

Figure 6.1 Structural analysis of gc-$Li_{3.2}P_{0.8}Sn_{0.2}S_4$ SSEs. (a) SXRD patterns of gc-$Li_{3.2}P_{0.8}Sn_{0.2}S_4$ SSEs compared with gc-$Li_{3.2}P_{0.8}Sn_{0.2}S_4$ and gc-Li_3PS_4 SSEs; 2D diffraction patterns from (b) g-$Li_{3.2}P_{0.8}Sn_{0.2}S_4$ and (c) gc-$Li_{3.2}P_{0.8}Sn_{0.2}S_4$ SSEs, which were recorded on a Pilatus 1M detector at the VESPERS beamline; (d) Raman spectra of gc-

$Li_{3.2}P_{0.8}Sn_{0.2}S_4$ SSEs compared with gc-Li_3PS_4 and crystallized Li_4SnS_4 SSEs; (e) Rietveld refinement patterns for gc-$Li_{3.2}P_{0.8}Sn_{0.2}S_4$ SSEs with an inset image of the unit cell. (f) ^{119}Sn and (g) ^{31}P MAS NMR spectra of gc-$Li_{3.2}P_{0.8}Sn_{0.2}S_4$ (red) and g-$Li_{3.2}P_{0.8}Sn_{0.2}S_4$ (black) SSEs. (h) Deconvolution of the ^{31}P MAS NMR spectrum of gc-$Li_{3.2}P_{0.8}Sn_{0.2}S_4$ SSEs. Spinning sidebands are marked with asterisks.

Rietveld refinement of the low speed-scan XRD (Bruker) pattern of gc-$Li_{3.2}P_{0.8}Sn_{0.2}S_4$ reveals the crystal information of the $Li_{3.2}P_{0.8}Sn_{0.2}S_4$ phase (**Figure 6.1e**). This composition is the only observed crystalline phase, which is analogous to the β-Li_3PS_4, belonging to the orthorhombic space group. The unit cell parameters of the Li-rich $Li_{3.2}P_{0.8}Sn_{0.2}S_4$ (a = 13.159 Å, b = 8.025 Å, c = 6.135 Å) are consistently larger than those of β-Li_3PS_4 (a = 13.066 Å, b = 8.015 Å, c = 6.101 Å) (**Table S6.1** and **Table S6.2**). This result quantifies the influence of Sn incorporation on the crystallographic structure, and further elucidates the reason for the low-angle shift of the diffraction peaks. The Rietveld analysis also suggests that the incorporated Sn atoms share the 4c site with P atoms and present an occupation ratio of 17 %, which is very close to the designed substitution content of 20 % (**Table S6.3**). The inserted schematic diagram in **Figure 6.1e** shows the crystal structure of $Li_{3.2}P_{0.8}Sn_{0.2}S_4$, which is mainly composed of Li cations and (P/Sn)S_4 anions. The Sn-substituted P atom (P/Sn) is located in the coordination center to bond with surrounding S atoms to form tetrahedral (P/Sn)S_4 anions. The isolated (P/Sn)S_4 tetrahedra are distributed in layers perpendicular to the a-axis kept apart by the LiS_6 octahedrons and LiS_4 tetrahedra (Li-S bonding is omitted to facilitate the observation of the incorporated Sn).

^{119}Sn and ^{31}P MAS NMR measurements were further carried out to obtain detailed structural and compositional information for the g-$Li_{3.2}P_{0.8}Sn_{0.2}S_4$ and gc-$Li_{3.2}P_{0.8}Sn_{0.2}S_4$ SSEs. ^{119}Sn and ^{31}P MAS spectra of both the glass and glass-ceramic samples exhibit a single resonance. However, the ^{119}Sn and ^{31}P peaks in the glass-ceramic sample are sharper and more intense compared to those of the glass sample, suggesting significantly enhanced crystallinity with more ordered Sn and P local structures.[35] As displayed in **Figure 6.1f**, ^{119}Sn resonance signals appear at 55.0 and 67.8 ppm for the glass and glass-ceramic samples, respectively. These chemical shift values are in the range of reported values for SnS_4 tetrahedra in various Tin sulfides.[21, 36] The confirmed tetrahedral geometry around Sn

is consistent with the above Raman analysis for the gc-$Li_{3.2}P_{0.8}Sn_{0.2}S_4$ SSEs. ^{31}P MAS spectrum of the g-$Li_{3.2}P_{0.8}Sn_{0.2}S_4$ SSEs (**Figure 6.1g**) exhibits two signals: a very weak peak at 105.6 ppm and a strong peak at 83.2 ppm. The former is assigned to P_2S_6 units and the later to PS_4 tetrahedra, which agrees well with previously reported results in the glass Li_3PS_4.[35] Upon annealing, the small peak due to P_2S_6 units disappeared completely in the spectrum of the gc-$Li_{3.2}P_{0.8}Sn_{0.2}S_4$ SSEs, while the characteristic peak of PS_4 tetrahedra moved to a higher chemical shift (87.1 ppm) and becomes more prominent. A careful inspection of the ^{31}P MAS spectrum of the glass-ceramic sample reveals that the 87.1 ppm peak has a weak shoulder appearing on the low-frequency side of the main peak. The deconvoluted spectrum shown in **Figure 6.1h** illustrates that the weak shoulder represents a signal positioned at 83.2 ppm coinciding with the amorphous peak in the glass sample. Therefore, the 83.2 and 87.1 ppm resonances in the deconvoluted spectrum are assigned to the amorphous and crystalline components, respectively. On the basis of the peak area of each signal derived from spectral integration, the amorphous content in the glass-ceramic sample is estimated at 12 %. To the best of our knowledge, this is the first time that the amorphous and crystalline contents are estimated in glass-ceramic SSEs.

The structural and compositional analysis confirms that the lower-valence Sn (IV) partially replaces P (V) to form a new gc-$Li_{3.2}P_{0.8}Sn_{0.2}S_4$ SSE. The quantification of the amorphous and crystallized parts in the glass-ceramic SSE is performed as well. The compensatory Li^+ ion concentration and enlarged unit cell embedded in the amorphous matrix are achieved by the Sn substitution, which are favorable towards increasing the Li^+ transport and ionic conductivity. More importantly, the Sn-S bond is capable of improving air-stability. In addition, it is expected that a Li-Sn alloy will form at the Li/gc-$Li_{3.2}P_{0.8}Sn_{0.2}S_4$ interface, which can regulate the uniform Li deposition and enable high-performance ASSLMBs at RT.

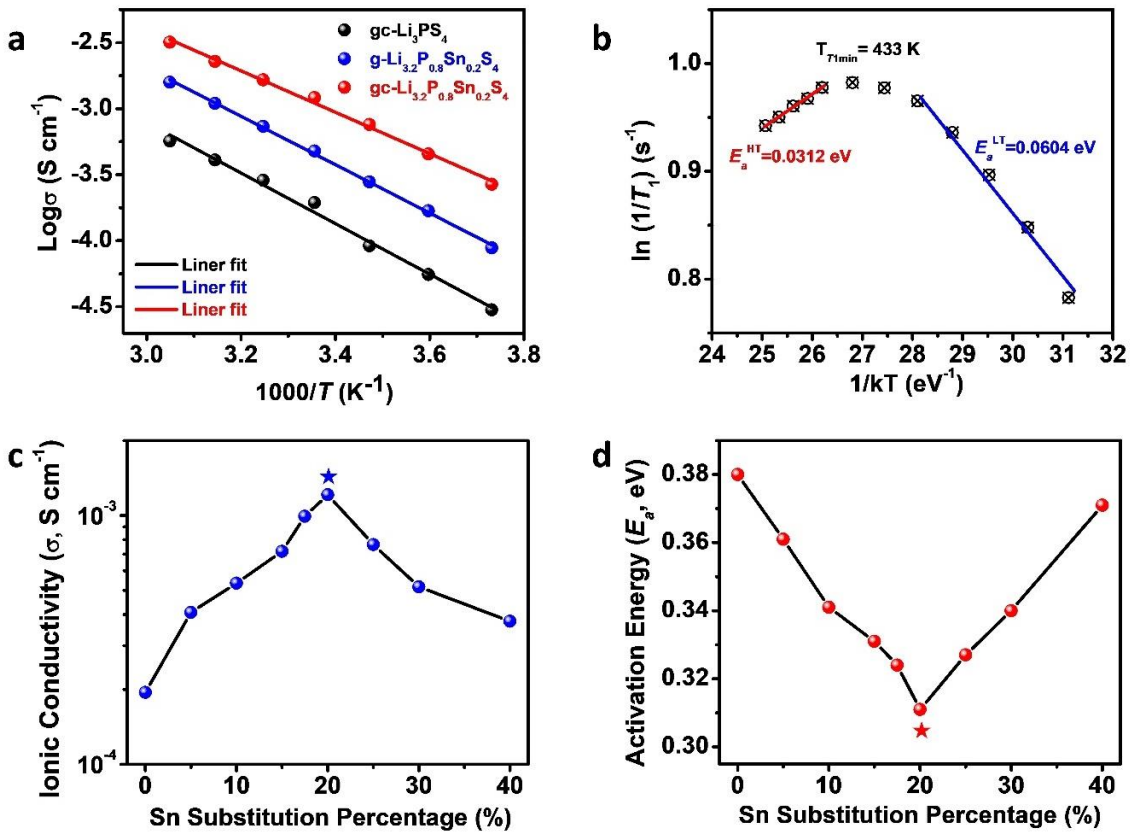

Figure 6.2 Li^+ ion dynamics in gc-$Li_{3.2}P_{0.8}Sn_{0.2}S_4$ SSEs. (a) Arrhenius plots of gc-$Li_{3.2}P_{0.8}Sn_{0.2}S_4$, g-$Li_{3.2}P_{0.8}Sn_{0.2}S_4$, and gc-$Li_3PS_4$ SSEs derived from the EIS measurements in a range of -5 to 55 ^oC; (b) Temperature-dependent ^7Li SLR rates measured in the laboratory frame for gc-$Li_{3.2}P_{0.8}Sn_{0.2}S_4$ SSEs; Ionic conductivities (c) and activation energies (d) of gc-$Li_{3+x}P_{1-x}Sn_xS_4$ (x = 0.05, 0.1, 0.15, 0.175, 0.25, 0.3, and 0.4) SSEs.

Electrochemical impedance spectroscopy (EIS) measurements were carried out to derive the Arrhenius plot of the prepared gc-$Li_{3.2}P_{0.8}Sn_{0.2}S_4$ SSEs. As shown in **Figure 6.2a**, the ionic conductivity (σ) of gc-$Li_{3.2}P_{0.8}Sn_{0.2}S_4$ reaches 1.21×10^{-3} S cm^{-1} at 25 ^oC, showing a 6.2-times increase for gc-Li_3PS_4 (1.94×10^{-4} S cm^{-1}) SSEs, and a 2.5-times increase for g-$Li_{3.2}P_{0.8}Sn_{0.2}S_4$ (4.79×10^{-4} S cm^{-1}). The σ of gc-$Li_{3.2}P_{0.8}Sn_{0.2}S_4$ is among the highest in all reported SSEs based on the ionic-conductive phase of β-Li_3PS_4, and is comparable to the well crystallized Li Argyrodites (Li_6PS_5Cl and Li_6PS_5Br).[6] And considering the ultralow electronic conductivity (2.83×10^{-9} S cm^{-1}) measured by chronoamperometry (CA) method (**Figure S6.5**), our gc-$Li_{3.2}P_{0.8}Sn_{0.2}S_4$ SSEs can be expected to be used directly as a single

electrolyte layer for ASSLMBs. The activation energy (E_a) of prepared SSEs is deduced from the slop of the Arrhenius plots. It is found that the incorporation of Sn effectively reduces the obstacles and promotes Li^+ ion transport. Even in the glass state of g-$Li_{3.2}P_{0.8}Sn_{0.2}S_4$, the derived E_a is only 0.363 eV, which is lower than that of gc-Li_3PS_4 (0.381 eV), and the E_a of the partially crystallized gc-$Li_{3.2}P_{0.8}Sn_{0.2}S_4$ is further decreased to 0.311 eV. To further analyze the Li^+ ion dynamics of the gc-$Li_{3.2}P_{0.8}Sn_{0.2}S_4$ SSEs, ^{7}Li SS-NMR experiments were conducted. ^{7}Li spin–lattice relaxation (SLR) rates ($1/T_1$) were measured as a function of temperatures (T). As shown in **Figure 6.2b**, the ln ($1/T_1$) vs. T plot show a maximum at the temperature of 433 K (i.e., T_{T1min} = 433 K) for gc-$Li_{3.2}P_{0.8}Sn_{0.2}S_4$ SSEs. The jump rate of Li^+ ions in both the high-temperature and low-temperature regimes fulfill the Arrhenius equation, which correspond to the Li^+ ion transport in long-range and short-range, respectively.[37] In this way, the activation energy for long-range (E_a^{HT}) and short-range (E_a^{LT}) transport can be deduced from the slops at 0.0312 and 0.0604 eV, respectively. It is not unreasonable that the E_a measured via ^{7}Li SS-NMR is lower than that derived from the EIS measurement, because the NMR results truly reflect the intrinsic Li^+ ion dynamics without being influenced by effects such as grain boundaries.[38] For gc-Li_3PS_4 SSEs, the maximum of ln ($1/T_1$) occurs at 453 K (**Figure S6.6**). The improved turnover temperature (compared to 433 K for gc-$Li_{3.2}P_{0.8}Sn_{0.2}S_4$) suggests that Li^+ ion hoping becomes more difficult in the gc-Li_3PS_4 SSEs without Sn incorporation.[37-38] This is further reflected by the higher activation energy (E_a^{LT}) of 0.158 eV for the gc-Li_3PS_4 SSEs.

Both EIS and NMR results confirm that the new gc-$Li_{3.2}P_{0.8}Sn_{0.2}S_4$ SSEs possess a favorable structure for Li^+ ion transport. Partial replacement of P with Sn expands the crystal cell and improves the Li^+ ion concentration, which dominate the main causes of the significantly improved Li^+ ion transport capability. Moreover, the unique glass-ceramic structure can maximize the σ of the metastable β-phase superionic conductor ($Li_{3.2}P_{0.8}Sn_{0.2}S_4$) at RT. In addition, we have also investigated the influence of Sn content on the σ and E_a by preparing a series of gc-$Li_{3+x}P_{1-x}Sn_xS_4$ SSEs, where x is equal to 0.05, 0.1, 0015, 0.175, 0.25, 0.3, and 0.4. The trends of the σ and E_a evolution along with the Sn percentage are displayed in **Figure 6.2c** and **d**, respectively. 20% (x = 0.2) was found to be the optimized ratio, where the σ is the highest and E_a is the lowest comparing to other

compositions. When x < 0.2, although the expanded crystal cell and increased Li^+ ion concentration do lead to an improved σ and reduced E_a, the improvement is not sufficient. Nevertheless, the σ appears to drop and the E_a increases when x > 0.2. This might be related to the lattice tolerance of the β-phase crystal structure, which also appeared in other sulfide SSEs built based on the PS_4^{3-} blocks.[23-24] In other words, once the incorporated percentage of Sn reaches a maximum while maintaining the orthorhombic phase, any further increase in the ratio may cause the collapse/distortion of this target phase or the generation of impurities.[39]

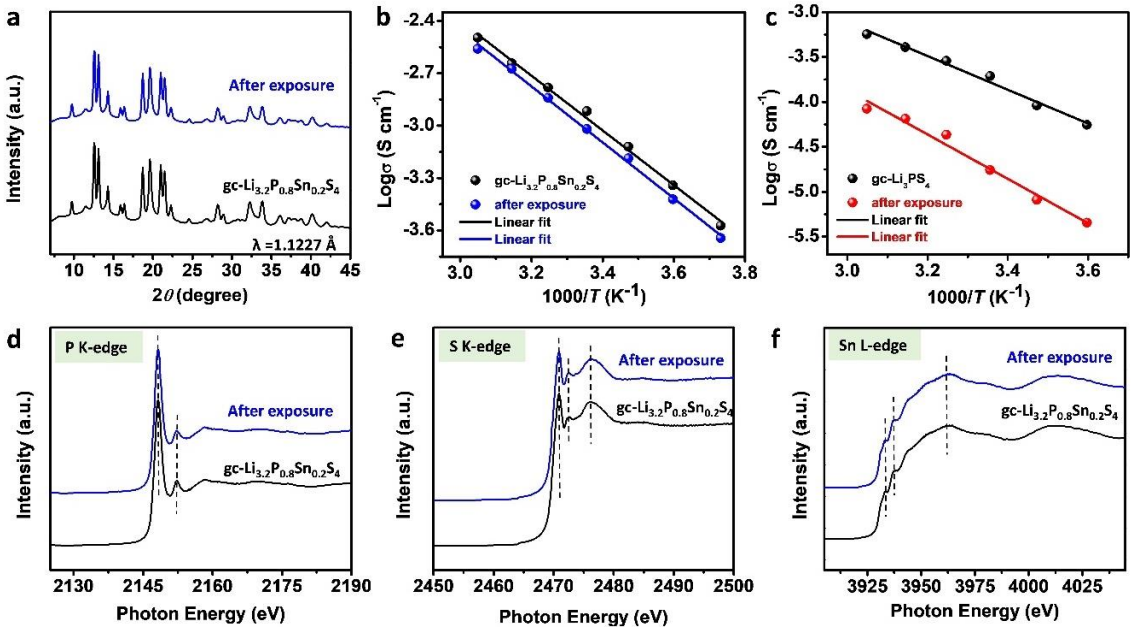

Figure 6.3 Characterization of the air-stability of the gc-$Li_{3.2}P_{0.8}Sn_{0.2}S_4$ SSEs. (a) Synchrotron-based XRD patterns of the gc-$Li_{3.2}P_{0.8}Sn_{0.2}S_4$ SSEs before and after exposure to air with 5% humidity; Arrhenius plots of the gc-$Li_{3.2}P_{0.8}Sn_{0.2}S_4$ SSEs (b) and gc-Li_3PS_4 SSEs (c) before and after exposure to air with 5% humidity; XANES of P K-edge (d), S-K-edge (e), and Sn L_3-edge (f) of the gc-$Li_{3.2}P_{0.8}Sn_{0.2}S_4$ SSEs before and after exposure to air with 5% humidity.

To examine whether the gc-$Li_{3.2}P_{0.8}Sn_{0.2}S_4$ SSEs can satisfy the processing requirements of dry room manufacturing for practical applications, we studied its resistance toward air with 5% humidity. After exposing the gc-$Li_{3.2}P_{0.8}Sn_{0.2}S_4$ SSEs to air with 5% humidity overnight, it was found that the crystal structure maintains unchanged (**Figure 6.3a**). EIS

measurements for the 5% humidity air-exposed gc-$Li_{3.2}P_{0.8}Sn_{0.2}S_4$ SSEs show negligible changes of σ (1.03×10^{-3} S cm^{-1} at RT) and E_a (0.320 eV), as displayed in **Figure 6.3b**. For comparison, the same exposure experiment was conducted on the gc-Li_3PS_4 SSEs. Relative intensity changes of the characteristic diffraction peaks and formation of impure phases (**Figure S6.7**) suggest that structural evolution and damage have occurred to the gc-Li_3PS_4 SSEs after exposure to air with 5% humidity overnight. Accordingly, a significant decline of σ (2.53×10^{-5} S cm^{-1} at RT) and increase of E_a (0.456 eV) appear for the 5% humidity air-exposed gc-Li_3PS_4 SSEs (**Figure 6.3c**). Furthermore, as shown in **Figure S6.8**, we tried exposing our gc-$Li_{3.2}P_{0.8}Sn_{0.2}S_4$ SSEs to the air with other humidity values (1-3%, 10%, and 20%) and found that 5% humidity is the upper limit if an ionic conductivity of 10^{-3} S cm^{-1} is considered as an essential indicator for battery applications.

XANES analysis was further conducted to confirm the structure stability of gc-$Li_{3.2}P_{0.8}Sn_{0.2}S_4$ SSEs after exposure to the air with 5% humidity. As displayed in **Figure 6.3d** to **f**, the featured peaks and spectral shapes of the P K-edge, S K-edge, and Sn L_3-edge are consistent with those in the pristine gc-$Li_{3.2}P_{0.8}Sn_{0.2}S_4$ SSEs, and are in agreement with previously reported features.[40-41] While decreased peak (whiteline) intensity and peak-energy-position shift of both P K-edge and S K-edge can be observed in the gc-Li_3PS_4 SSEs after exposure to the same ambient environment, illustrating the structural decomposition due to the exposure (**Figure S6.9**). We ascribe the good air-stability of gc-$Li_{3.2}P_{0.8}Sn_{0.2}S_4$ SSEs to the strong binding energy of Sn-S, which is difficult to break via reaction with H_2O in the moist air. This leads to a stabilized $(P/Sn)S_4$ tetrahedron, as well as keeping the glass part steady when exposed to 5% humidity air. Therefore, our gc-$Li_{3.2}P_{0.8}Sn_{0.2}S_4$ SSEs have the potential to be used in the dry room for large-scale processing.

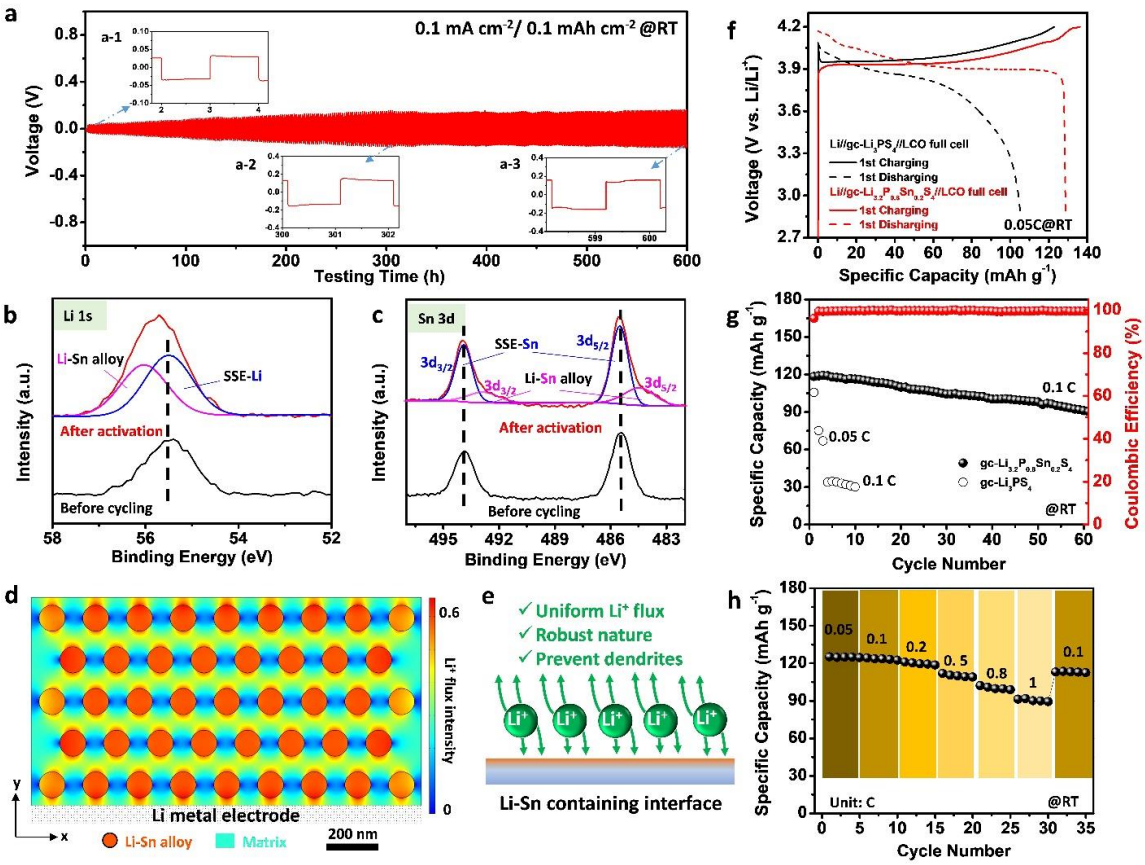

Figure 6.4 (a) Polarization curve of the Li//gc-$Li_{3.2}P_{0.8}Sn_{0.2}S_4$//Li symmetric cell tested at 0.1 mA cm^{-2}/0.1 mAh cm^{-2} and RT; (a-1, 2, and 3) Magnified regions of the polarization curves in (a); (b) Li 1s and (c) Sn 3d XPS spectra of the interfacial compositions between Li and gc-$Li_{3.2}P_{0.8}Sn_{0.2}S_4$ SSEs compared to the pristine $Li_{3.2}P_{0.8}Sn_{0.2}S_4$ SSEs before cycling; (d) Simulation results of Li^+ flux distribution at the interface formulated by the finite element method; (e) Schematic diagram of the working mechanism of the gc-$Li_{3.2}P_{0.8}Sn_{0.2}S_4$ derived Li anode interface enabling high-performance ASSLMBs; (f) Charging and discharging curves of the Li//gc-$Li_{3.2}P_{0.8}Sn_{0.2}S_4$//LCO full cell compared to the Li//gc-Li_3PS_4//LCO full cell; (g) Cycling stability of Li//gc-$Li_{3.2}P_{0.8}Sn_{0.2}S_4$//LCO at 0.1 C and RT; (h) Rate capability of Li//gc-$Li_{3.2}P_{0.8}Sn_{0.2}S_4$//LCO at RT.

Symmetric cells of Li//gc-$Li_{3.2}P_{0.8}Sn_{0.2}S_4$//Li were assembled to evaluate the Li metal compatibility. As shown in **Figure 6.4a**, the symmetric cell presents a long cycle with stable Li plating/stripping for over 600 h at a current density of 0.1 mA cm^{-2} and a cutoff capacity of 0.1 mAh cm^{-2}, prolonging the lifetime by 4 times compared to the Li//gc-

Li_3PS_4//Li symmetric cell (**Figure S6.10**). Close observations of the polarization curves (**Figure 6.4a-1**, **2** and **3**) suggest that the Li//gc-$Li_{3.2}P_{0.8}Sn_{0.2}S_4$//Li cell experienced an activation process in the initial 300 hours. The overpotential increases from ~25 mV to ~150 mV in this period, which corresponds to the formation of a stabilized Li/gc-$Li_{3.2}P_{0.8}Sn_{0.2}S_4$ interface. The nearly unchanged overpotential after 300 h proves that the in-situ formation of the interface is self-terminating due to the deficiency of electron/electron providers, and this stabilized interface can support a smooth Li plating/stripping process subsequently. The cycling time-resolved EIS plots for the symmetric cell are displayed correspondingly in **Figure S6.11**. The change of the impedance of the in-situ formed Li/gc-$Li_{3.2}P_{0.8}Sn_{0.2}S_4$ interface agrees well with the evolution of overpotential as discussed above. SEM images of the Li metal surface after cycling against gc-$Li_{3.2}P_{0.8}Sn_{0.2}S_4$ for 300 h are presented in **Figure S6.12**. It is found that the surface is very smooth, consisting of nanosized domains. X-ray photoelectron spectroscopy (XPS) was used to analyze the chemical composition of the activated Li/gc-$Li_{3.2}P_{0.8}Sn_{0.2}S_4$ interface. XPS spectra of Li 1s and Sn 3d at the SSE pellet surface are displayed in **Figure 6.4b** and **c**, respectively. The peak at 55.5 eV is assigned to the Li (+1) in the gc-$Li_{3.2}P_{0.8}Sn_{0.2}S_4$ SSEs. A new Li 1s peak located at 56.1 eV can be observed after the activation process. Accordingly, we can observe Sn in a reduced state in the Sn 3d spectrum. The main peaks assigned to the electrolyte are located at 493.9 and 485.5 eV corresponding to the $3d_{3/2}$ and $3d_{5/2}$, respectively. One additional pair of 3d peaks is seen to emerge at 492.9 and 484.5 eV, indicating some reduction of Sn.[42-43] The generation of the new peaks in Li 1s and Sn 3d regions suggest the formation of Li-Sn alloys during the activation process.[42]

Indeed, Li-Sn alloy has been used as a functional interlayer to improve the interfacial property between Li metal and organic liquid or Garnet-type electrolytes,[42-45] but it is rarely reported as an effective component to mitigate the thermodynamically unstable interface between Li metal and sulfide SSEs. It was generally believed that the electronically conductive Li-Sn alloy would boost the detrimental side reactions , thus reducing cycling performance.[46] However, we propose that Li-Sn alloys can still regulate the Li deposition at the interface of Li/sulfide SSEs, once a balance between the undesired effect of electronic conductivity and the positive Li plating/stripping nucleation derived from Li-Sn

alloys is achieved. Incorporating Sn in gc-$Li_{3.2}P_{0.8}Sn_{0.2}S_4$ SSEs rather than direct application as an interlayer is demonstrated as an excellent example to achieve this balance due to the in-situ formation of the electronically conductive Li-Sn alloy as well as insulating Li_2S and Li_3P interfacial products (**Figure S6.13**) with a homogenous distribution.[47] SEM with EDS analysis (**Figure S6.14**) for the cycled Li/SSE interface verifies the uniform dispersion of nanosized Li-Sn alloys and other insulating interfacial species.[42] We further developed a numerical simulation with the finite element method (FEM) to emulate the distribution of Li^+ flux at the interface. As shown in **Figure 6.4d**, in the physical model consisting of well-dispersed Li-Sn alloys and matrix (Li_2S and Li_3P), the intensity of Li^+ flux at the sites of Li-Sn alloys is obviously higher than that in the matrix. The high-intensity sites of Li^+ flux centered with Li-Sn alloys are distributed homogenously and connected with each other, constructing a high-speed transport network to keep the uniformity of Li^+ flux through the entire interface and towards the Li metal electrode. The values of Li^+ flux along the diagonal of the rectangular model are recorded against x and y axes (**Figure S6.15**), which are considered representative to witness the high Li^+ flux around Li-Sn alloys comparing to the poor Li^+ flux through the matrix. So far, we can reveal the working mechanism of the Li-Sn alloy-containing interface for the sulfide-based ASSLMBs as schematically shown in **Figure 6.4e**. The Li-Sn alloy and other insulating compounds (Li_3P and Li_2S) constitute a smooth Li anode interface. The uniformly embedded nanoscale Li-Sn alloy is beneficial to provide uniform Li^+ flux and regulate stable Li plating/stripping (preventing Li dendrites),[44-45] while the insulating interfacial products can effectively prevent further parasitic side reactions (robust nature).

Full cells were assembled to investigate the application potential of gc-$Li_{3.2}P_{0.8}Sn_{0.2}S_4$ SSEs. As shown in the schematic diagram of the full-cell configuration (**Figure S6.16**), the gc-$Li_{3.2}P_{0.8}Sn_{0.2}S_4$ SSE is employed as the electrolyte layer to separate Li metal anode and $LiCoO_2/Li_3InCl_6$ (LCO/LIC) cathode. The LCO loading reaches 8.9 mg cm^{-2}. LCO/LIC cathode composites are used due to the highly stable cathode interface.[48] The Li//gc-$Li_{3.2}P_{0.8}Sn_{0.2}S_4$//LCO full cell possesses excellent charging/discharging behavior at a current density of 0.05 C (1 C corresponds to 140 mA g^{-1}), as demonstrated in **Figure 6.4f**. In contrast, the full cell using gc-Li_3PS_4 as the electrolyte layer (Li//gc-Li_3PS_4//LCO) shows a large polarization and poor reversibility, which is an integrative reflection of the

low σ and the unstable Li/gc-Li_3PS_4 interface. The ASSLMBs (Li//gc-$Li_{3.2}P_{0.8}Sn_{0.2}S_4$//LCO) exhibit good durability at 0.1 C (**Figure 6.4g**). Specifically, the initial Coulombic efficiency reaches 96.18%, and the average value is 99.8 % for the following 60 cycles. A reversible specific capacity of 118.4 mAh g^{-1} is achieved for the first cycle, and maintains 91.1 mAh g^{-1} after 60 cycles, showing a retention of 77 %. Comparatively, the full battery using gc-Li_3PS_4 as the electrolyte layer shows a fast capacity decay at 0.05 C and a limited reversible capacity of ~30 mAh g^{-1} at 0.1 C. The rate performance of the Li//gc-$Li_{3.2}P_{0.8}Sn_{0.2}S_4$//LCO full cell was examined by elevating the discharging current densities, while keeping the charging current at 0.05 C to ensure complete delithiation of the cathode materials. As shown in **Figure 6.4h**, the reversible capacity is 124.7 mAh g^{-1} at the initial current density of 0.05 C. Along with the current density is increased, although the polarization becomes gradually increased (**Figure S6.17**), a capacity retention of 91.0 mAh g^{-1} can still be achieved under a high rate of 1 C. Afterwards, the capacity recovers to 113.0 mAh g^{-1} when the current rate is reverted to 0.1 C. Compared to other reported results, the cell performance using gc-$Li_{3.2}P_{0.8}Sn_{0.2}S_4$ SSE is among the best without any interlayer protection or Li metal modifications (**Table S6.4**).

6.4 Conclusion

In summary, an advanced glass-ceramic sulfide-based SSE (gc-$Li_{3.2}P_{0.8}Sn_{0.2}S_4$) has been developed to satisfy all the requirements for the development of practical ASSLMBs. **Table S6.5** summarizes the basic physicochemical properties of gc-$Li_{3.2}P_{0.8}Sn_{0.2}S_4$ SSEs compared with other representative sulfide-based SSEs. The ionic conductivity can reach as high as 1.21×10^{-3} S cm^{-1} at RT, which is one of the highest values among all the reported SSEs based on orthorhombic β-Li_3PS_4. Selective Sn (IV) substitution for P (V) is verified to enlarge the unit cell and induce increased Li^+ ion concentration to enhance the ionic conductivity. The amorphous content is estimated at 12 % via analysis of the ^{31}P MAS NMR spectrum of gc-$Li_{3.2}P_{0.8}Sn_{0.2}S_4$ SSEs. Excellent air-stability in a conventional dry-room level atmosphere (5% air humidity) is also obtained via the construction of strong Sn-S bonds and stabilized $(P/Sn)S_4$ tetrahedrons in the gc-$Li_{3.2}P_{0.8}Sn_{0.2}S_4$ SSEs. In addition, Sn substitution triggers the formation of Li-Sn alloys at the anode interface. It is verified by the FEM-based numerical simulation that interfacial Li-Sn alloys can regulate stable Li

plating/stripping, thus leading to improved Li metal compatibility. As a final result, the gc-$Li_{3.2}P_{0.8}Sn_{0.2}S_4$ SSE can be employed as a single electrolyte layer to enable ASSLMBs with excellent electrochemical performance, presenting great opportunity for industrial application.

6.5 Acknowledgments

This research was supported by the Natural Sciences and Engineering Research Council of Canada (NSERC), the Canada Research Chair Program (CRC), the Canada Foundation for Innovation (CFI), Ontario Research Foundation (ORF), China Automotive Battery Research Institute Co., Ltd., Glabat Solid-State Battery Inc., and the University of Western Ontario (UWO). The synchrotron research was performed at the Canadian Light Source, which is supported by the Canada Foundation for Innovation (CFI), the Natural Sciences and Engineering Research Council (NSERC), the National Research Council (NRC), the Canadian Institutes of Health Research (CIHR), the Government of Saskatchewan, and the University of Saskatchewan. The authors gratefully acknowledge Dr. Mathew Willans for his kind help on the test and analysis of NMR at J.B. Stothers NMR facility in the University of Western Ontario.

6.6 References

（1）Albertus, P.; Babinec, S.; Litzelman, S.; Newman, A., *Nat. Energy* **2018,** *3* (1), 16-21.

（2）Zhao, Q.; Stalin, S.; Zhao, C.-Z.; Archer, L. A., *Nat. Rev. Mater.* **2020,** *5* (3), 229-252.

（3）Cui, G., *Matter* **2020,** *2* (4), 805-815.

（4）Zhao, W.; Yi, J.; He, P.; Zhou, H., *Electrochem. Energy Rev.* **2019,** *2* (4), 574-605.

（5）Chen, R.; Li, Q.; Yu, X.; Chen, L.; Li, H., *Chem. Rev.* **2019,** *120* (14), 6820–6877.

（6）Zhang, Q.; Cao, D.; Ma, Y.; Natan, A.; Aurora, P.; Zhu, H., *Adv. Mater.* **2019,** *31*, 1901131.

（7）Lee, H.; Oh, P.; Kim, J.; Cha, H.; Chae, S.; Lee, S.; Cho, J., *Adv. Mater.* **2019,** *31* (29), 1900376.

（8）Hayashi, A.; Noi, K.; Sakuda, A.; Tatsumisago, M., *Nat. Commun.* **2012,** *3*, 856.

（9）Hayashi, A.; Tatsumisago, M., *Electron. Mater. Lett.* **2012,** *8* (2), 199-207.

（10）Zhang, Z.; Shao, Y.; Lotsch, B.; Hu, Y.-S.; Li, H.; Janek, J.; Nazar, L. F.; Nan, C.-W.; Maier, J.; Armand, M.; Chen, L., *Energy Environ. Sci.* **2018,** *11* (8), 1945-1976.

（11）Homma, K.; Yonemura, M.; Kobayashi, T.; Nagao, M.; Hirayama, M.; Kanno, R., *Solid State Ionics* **2011,** *182* (1), 53-58.

（12）Tsukasaki, H.; Mori, S.; Morimoto, H.; Hayashi, A.; Tatsumisago, M., *Sci. Rep.* **2017,** *7* (1), 4142.

（13）Mizuno, F.; Hayashi, A.; Tadanaga, K.; Tatsumisago, M., *Adv. Mater.* **2005,** *17* (7), 918-921.

（14）Seino, Y.; Ota, T.; Takada, K.; Hayashi, A.; Tatsumisago, M., *Energy Environ. Sci.* **2014,** *7* (2), 627-631.

（15）Xiao, Y.; Wang, Y.; Bo, S.-H.; Kim, J. C.; Miara, L. J.; Ceder, G., *Nat. Rev. Mater.* **2019,** *5* (2), 105-126.

（16）Muramatsu, H.; Hayashi, A.; Ohtomo, T.; Hama, S.; Tatsumisago, M., *Solid State Ionics* **2011,** *182* (1), 116-119.

（17）Zhu, Y.; He, X.; Mo, Y., *ACS Appl. Mater. Interfaces* **2015,** *7* (42), 23685-23693.

（18）Nagao, M.; Hayashi, A.; Tatsumisago, M.; Kanetsuku, T.; Tsuda, T.; Kuwabata, S., *Phys. Chem. Chem. Phys.* **2013,** *15* (42), 18600-18606.

（19）Zhang, Y.; Zuo, T.-T.; Popovic, J.; Lim, K.; Yin, Y.-X.; Maier, J.; Guo, Y.-G., *Mater. Today* **2020,** *33*, 56-74.

（20）Brant, J. A.; Massi, D. M.; Holzwarth, N. A. W.; MacNeil, J. H.; Douvalis, A. P.; Bakas, T.; Martin, S. W.; Gross, M. D.; Aitken, J. A., *Chem. Mater.* **2014,** *27* (1), 189-196.

（21）Kaib, T.; Haddadpour, S.; Kapitein, M.; Bron, P.; Schröder, C.; Eckert, H.; Roling, B.; Dehnen, S., *Chem. Mater.* **2012,** *24* (11), 2211-2219.

（22）Sahu, G.; Lin, Z.; Li, J.; Liu, Z.; Dudney, N.; Liang, C., *Energy Environ. Sci.* **2014,** *7* (3), 1053-1058.

（23）Zhao, F. P.; Liang, J. W.; Yu, C.; Sun, Q.; Li, X. N.; Adair, K.; Wang, C. H.; Zhao, Y.; Zhang, S. M.; Li, W. H.; Deng, S. X.; Li, R. Y.; Huang, Y. N.; Huang, H.; Zhang, L.; Zhao, S. Q.; Lu, S. G.; Sun, X. L., *Adv. Energy Mater.* **2020,** *10* (9), 1903422.

（24）Liang, J.; Chen, N.; Li, X.; Li, X.; Adair, K. R.; Li, J.; Wang, C.; Yu, C.; Norouzi Banis, M.; Zhang, L.; Zhao, S.; Lu, S.; Huang, H.; Li, R.; Huang, Y.; Sun, X., *Chem. Mater.* **2020,** *32* (6), 2664-2672.

（25）Liu, G. Z.; Xie, D. J.; Wang, X. L.; Yao, X. Y.; Chen, S. J.; Xiao, R. J.; Li, H.; Xu, X. X., *Energy Storage Mater.* **2019,** *17*, 266-274.

（26）Kwak, H.; Park, K. H.; Han, D.; Nam, K.-W.; Kim, H.; Jung, Y. S., *J. Power Sources* **2020,** *446*, 227338.

（27）Gao, Y.; Wang, D. W.; Li, Y. G. C.; Yu, Z. X.; Mallouk, T. E.; Wang, D. H., *Angew. Chem. Int. Ed.* **2018,** *57* (41), 13608-13612.

（28）Wang, C.; Zhao, Y.; Sun, Q.; Li, X.; Liu, Y.; Liang, J.; Li, X.; Lin, X.; Li, R.; Adair, K. R.; Zhang, L.; Yang, R.; Lu, S.; Sun, X., *Nano Energy* **2018,** *53*, 168-174.

（29）Xu, R.; Han, F.; Ji, X.; Fan, X.; Tu, J.; Wang, C., *Nano Energy* **2018,** *53*, 958-966.

（30）Fan, X.; Ji, X.; Han, F.; Yue, J.; Chen, J.; Chen, L.; Deng, T.; Jiang, J.; Wang, C., *Sci. Adv.* **2018,** *4* (12), 12.

（31）Zhao, F.; Sun, Q.; Yu, C.; Zhang, S.; Adair, K.; Wang, S.; Liu, Y.; Zhao, Y.; Liang, J.; Wang, C.; Li, X.; Li, X.; Xia, W.; Li, R.; Huang, H.; Zhang, L.; Zhao, S.; Lu, S.; Sun, X., *ACS Energy Lett.* **2020,** *5* (4), 1035-1043.

（32）Han, F.; Yue, J.; Zhu, X.; Wang, C., *Adv. Energy Mater.* **2018,** *8* (18), 1703644.

（33）Kanazawa, K.; Yubuchi, S.; Hotehama, C.; Otoyama, M.; Shimono, S.; Ishibashi, H.; Kubota, Y.; Sakuda, A.; Hayashi, A.; Tatsumisago, M., *Inorg. Chem.* **2018,** *57* (16), 9925-9930.

（34）Yubuchi, S.; Teragawa, S.; Aso, K.; Tadanaga, K.; Hayashi, A.; Tatsumisago, M., *J. Power Sources* **2015,** *293*, 941-945.

（35）Stoffler, H.; Zinkevich, T.; Yavuz, M.; Hansen, A. L.; Knapp, M.; Bednarcik, J.; Randau, S.; Richter, F. H.; Janek, J.; Ehrenberg, H.; Indris, S., *J. Phys. Chem. C* **2019,** *123* (16), 10280-10290.

（36）Mundus, C.; Taillades, G.; Pradel, A.; Ribes, M., *Solid State Nucl. Magn. Reson.* **1996,** *7* (2), 141-146.

（37）Yu, C.; Li, Y.; Willans, M.; Zhao, Y.; Adair, K. R.; Zhao, F. P.; Li, W. H.; Deng, S. X.; Liang, J. W.; Banis, M. N.; Li, R. Y.; Huang, H.; Zhang, L.; Yang, R.; Lu, S. G.; Huang, Y. N.; Sun, X. L., *Nano Energy* **2020,** *69*, 104396.

（38）Ganapathy, S.; Yu, C.; van Eck, E. R. H.; Wagemaker, M., *ACS Energy Lett.* **2019,** *4* (5), 1092-1097.

（39）Travis, W.; Glover, E. N. K.; Bronstein, H.; Scanlon, D. O.; Palgrave, R. G., *Chem. Sci.* **2016,** *7* (7), 4548-4556.

（40）Hakari, T.; Deguchi, M.; Mitsuhara, K.; Ohta, T.; Saita, K.; Orikasa, Y.; Uchimoto, Y.; Kowada, Y.; Hayashi, A.; Tatsumisago, M., *Chem. Mater.* **2017,** *29* (11), 4768-4774.

（41）Zheng, X. L.; De Luna, P.; de Arquer, F. P. G.; Zhang, B.; Becknell, N.; Ross, M. B.; Li, Y. F.; Banis, M. N.; Li, Y. Z.; Liu, M.; Voznyy, O.; Dinh, C. T.; Zhuang, T. T.; Stadler, P.; Cui, Y.; Du, X. W.; Yang, P. D.; Sargent, E. H., *Joule* **2017,** *1* (4), 794-805.

（42）Wan, M. T.; Kang, S. J.; Wang, L.; Lee, H. W.; Zheng, G. W.; Cui, Y.; Sun, Y. M., *Nat. Commun.* **2020,** *11* (1), 829.

（43）Shi, K.; Wan, Z.; Yang, L.; Zhang, Y.; Huang, Y.; Su, S.; Xia, H.; Jiang, K.; Shen, L.; Hu, Y.; Zhang, S.; Yu, J.; Ren, F.; He, Y. B.; Kang, F., *Angew. Chem. Int. Ed.* **2020,** *132* (29), 11882-11886.

（44）Tu, Z. Y.; Choudhury, S.; Zachman, M. J.; Wei, S. Y.; Zhang, K. H.; Kourkoutis, L. F.; Archer, L. A., *Nat. Energy* **2018,** *3* (4), 310-316.

（45）He, M.; Cui, Z.; Chen, C.; Li, Y.; Guo, X., *J. Mater. Chem. A* **2018,** *6* (24), 11463-11470.

（46）Wenzel, S.; Leichtweiss, T.; Krüger, D.; Sann, J.; Janek, J., *Solid State Ionics* **2015,** *278*, 98-105.

（47）Kato, A.; Kowada, H.; Deguchi, M.; Hotehama, C.; Hayashi, A.; Tatsumisago, M., *Solid State Ionics* **2018,** *322*, 1-4.

（48）Li, X.; Liang, J.; Luo, J.; Norouzi Banis, M.; Wang, C.; Li, W.; Deng, S.; Yu, C.; Zhao, F.; Hu, Y.; Sham, T.-K.; Zhang, L.; Zhao, S.; Lu, S.; Huang, H.; Li, R.; Adair, K. R.; Sun, X., *Energy Environ. Sci.* **2019,** *12* (9), 2665-2671.

6.7 Supporting Information

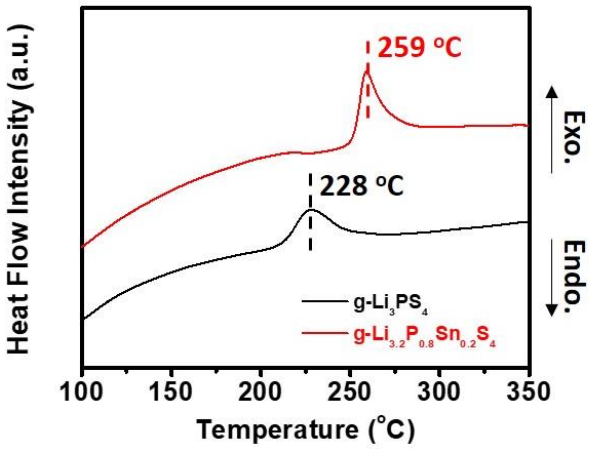

Figure S6.1 Comparison of DSC results of g-$Li_{3.2}P_{0.8}Sn_{0.2}S_4$ and g-Li_3PS_4 SSEs.

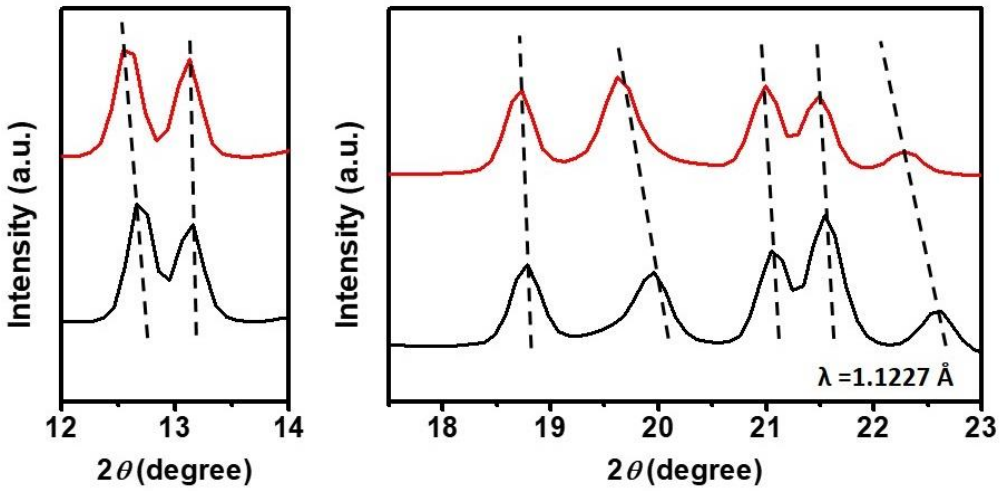

Figure S6.2 Magnified regions of the synchrotron-based XRD patters of g-$Li_{3.2}P_{0.8}Sn_{0.2}S_4$ (red) and g-Li_3PS_4 (black) SSEs.

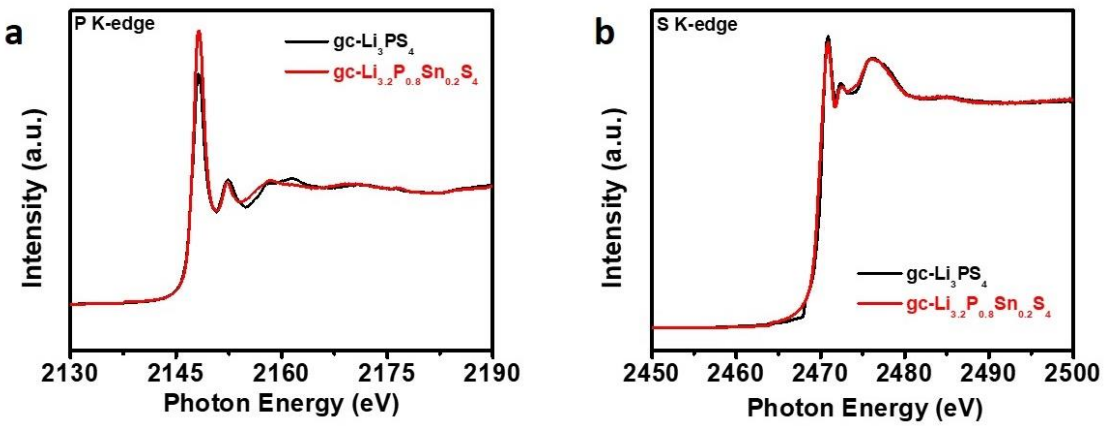

Figure S6.3 XANES of P K-edge (a) and S-K-edge (b) in gc-Li_3PS_4 and gc-$Li_{3.2}P_{0.8}Sn_{0.2}S_4$ SSEs.

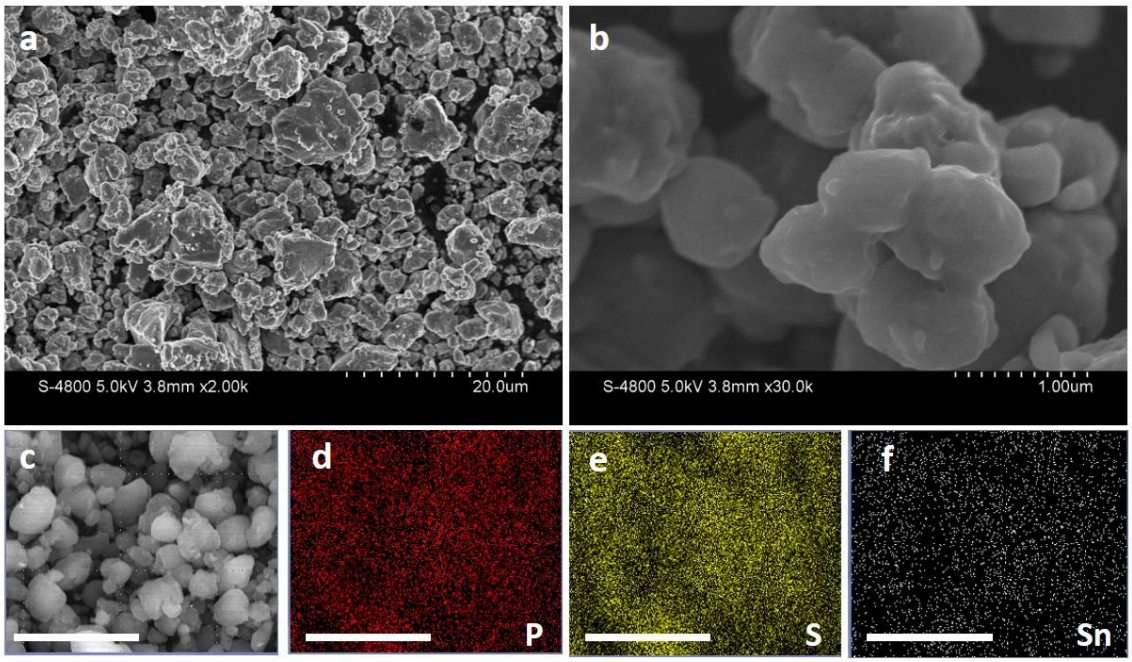

Figure S6.4 (a and b) SEM images of gc-$Li_{3.2}P_{0.8}Sn_{0.2}S_4$ SSEs with different scale bars; (e-f) EDX mapping of P, S, and Sn in the selected area (c), scale bar: 8 μm.

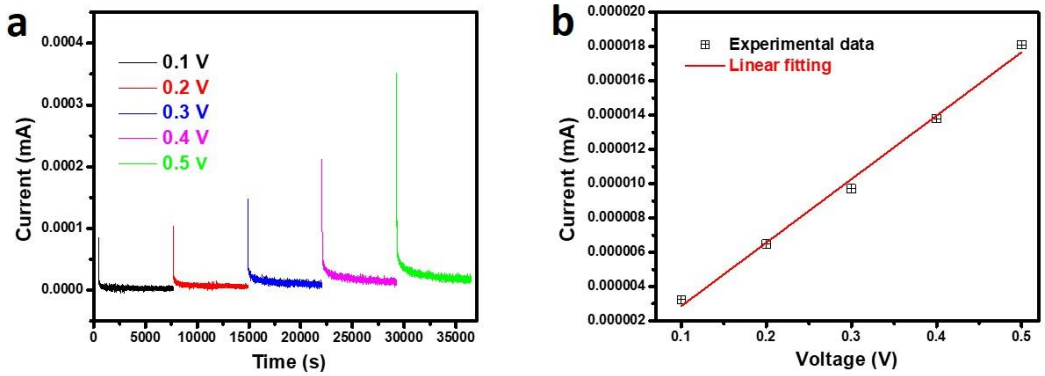

Figure S6.5 (a) DC polarization curves of Carbon//gc-$Li_{3.2}P_{0.8}Sn_{0.2}S_4$//Carbon symmetric cell at different voltages; (b) Stable current response as a function of applied voltage. The electronic conductivity can be derived from the slop of the linear fitting.

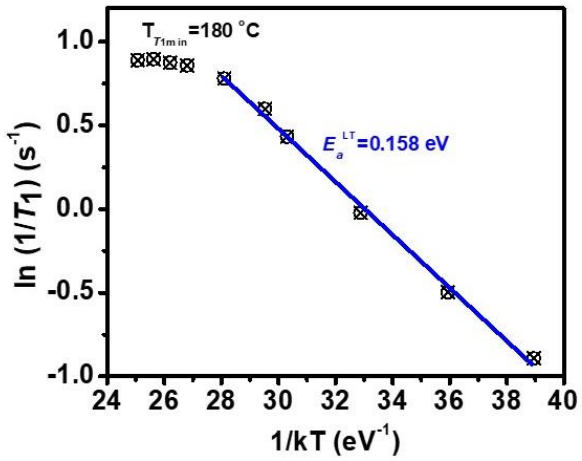

Figure S6.6 Temperature-dependent ^{7}Li SLR rates measured in the laboratory frame for gc-Li_3PS_4 SSEs.

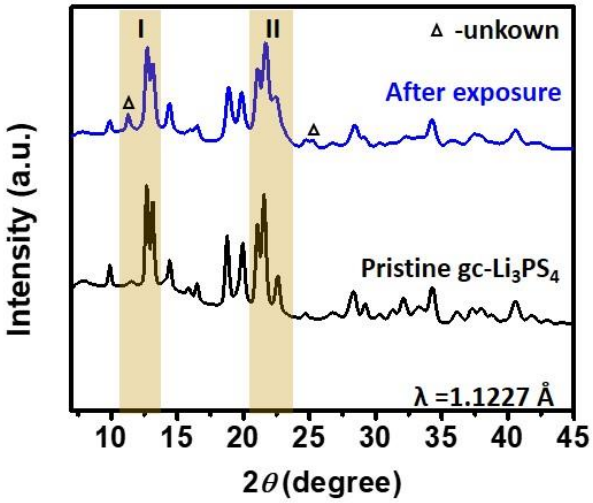

Figure S6.7 Synchrotron-based XRD patterns of the gc-Li_3PS_4 SSEs before and after exposure to dry air and air with 5% humidity.

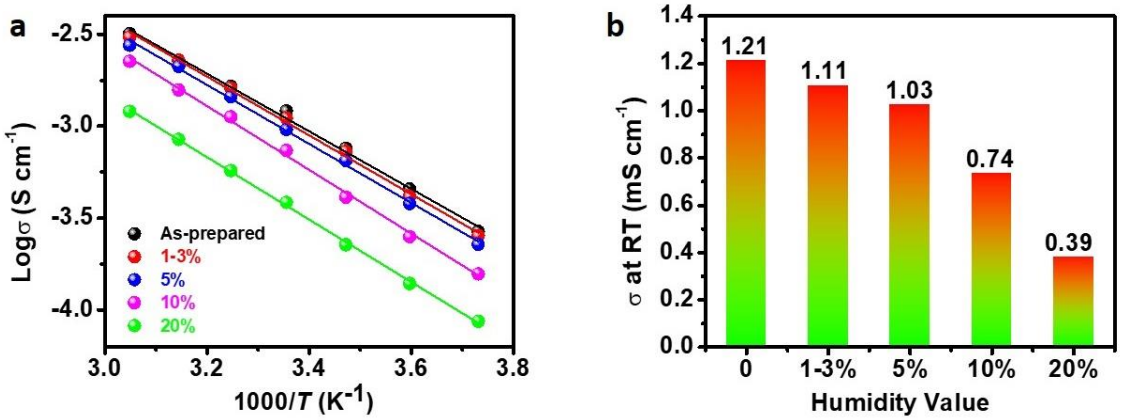

Figure S6.8 (a) Arrhenius plots of gc-$Li_{3.2}P_{0.8}Sn_{0.2}S_4$ SSEs before (as-prepared) and after exposing to air with various humidity values. (b) Room-temperature (RT) ionic conductivity (σ) of gc-$Li_{3.2}P_{0.8}Sn_{0.2}S_4$ SSEs that experienced exposure to air with various humidity.

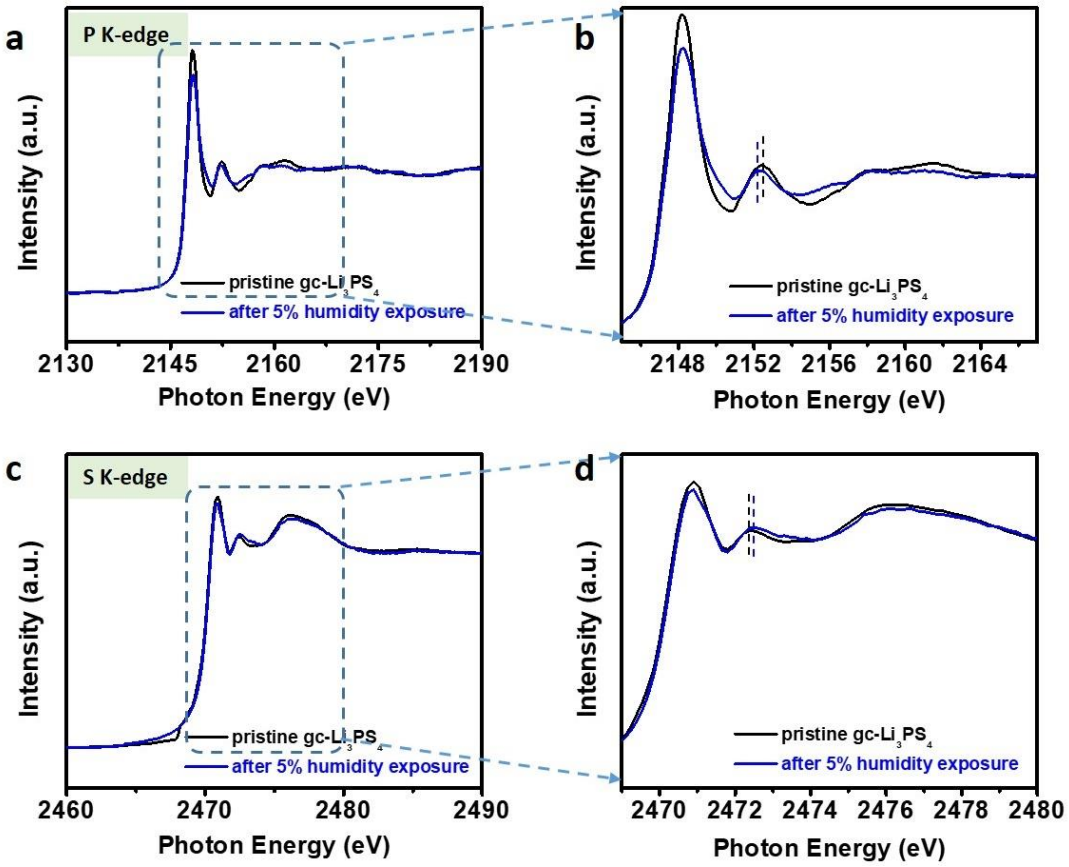

Figure S6.9 XANES of P K-edge (a), S-K-edge (c) of the gc-Li_3PS_4 SSEs before and after exposure to air with 5 % humidity; (b and d) The corresponding magnified regions.

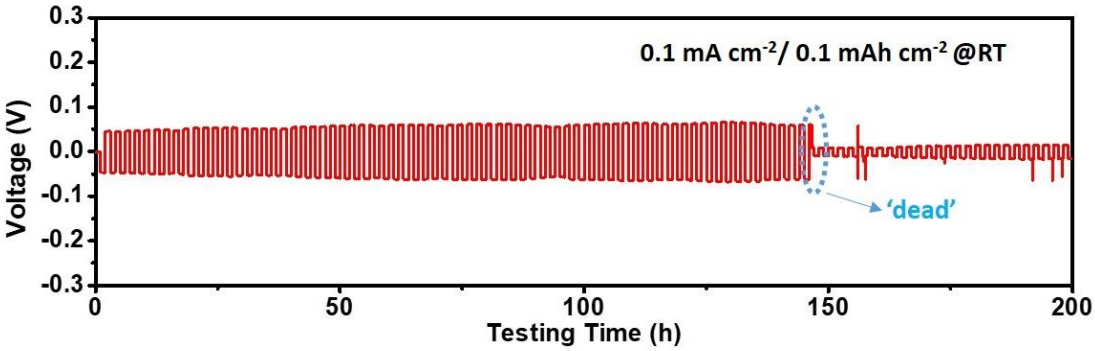

Figure S6.10 Polarization curve of the Li//gc-$Li_{3.2}P_{0.8}Sn_{0.2}S_4$//Li symmetric cell tested at 0.1 mA cm^{-2}/0.1 mAh cm^{-2} at RT.

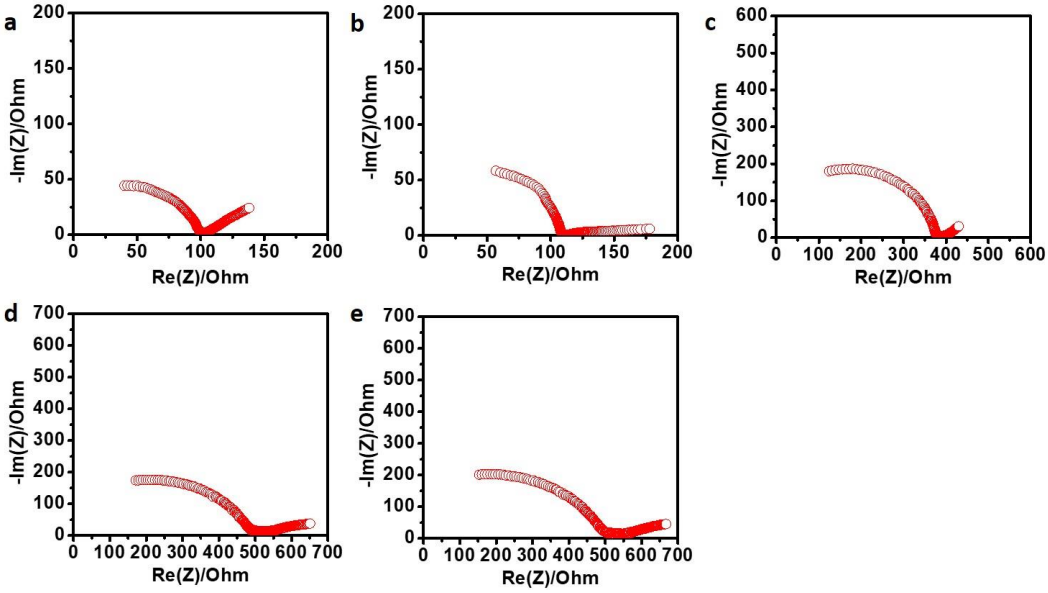

Figure S6.11 EIS plots of the Li//gc-$Li_{3.2}P_{0.8}Sn_{0.2}S_4$//Li symmetric cell after cycling at 0.1 mA cm^{-2}/0.1 mAh cm^{-2} and RT in various stages: (a) 0 h; (b) 4 h; (c) 150 h; (d) 300 h; (e) 500 h.

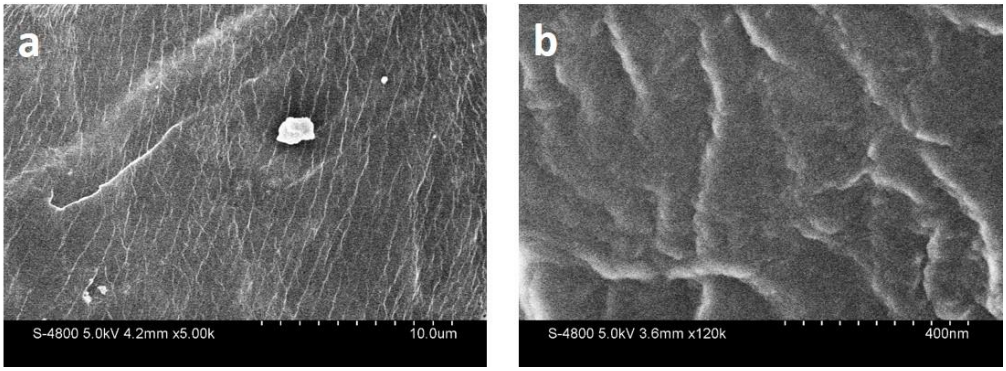

Figure S6.12 SEM images of the Li metal surface after cycling in symmetric cells at 0.1 mA cm^{-2}/0.1 mAh cm^{-2} and RT for 300 h (stabilized interface and overpotential).

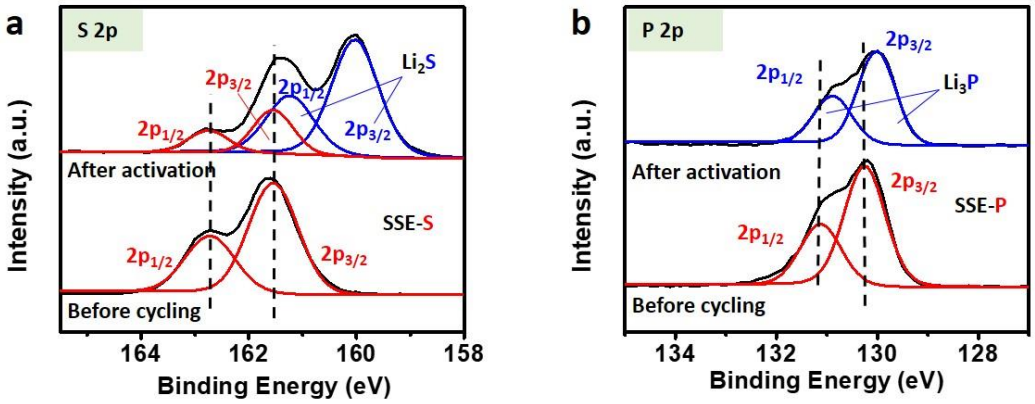

Figure S6.13 XPS spectra of (a) S 2p, and (b) P 2p at the interface of between Li and gc-$Li_{3.2}P_{0.8}Sn_{0.2}S_4$ SSEs, compared with those in the pristine $Li_{3.2}P_{0.8}Sn_{0.2}S_4$ SSEs.

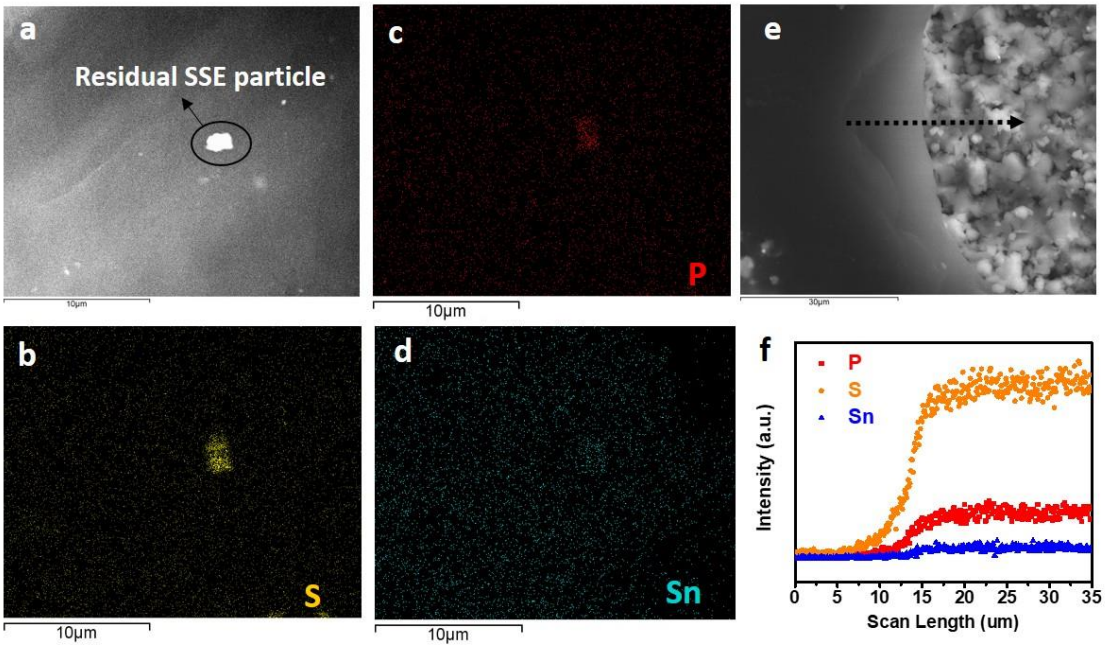

Figure S6.14 SEM with EDS analysis of the Li metal surface (a-d) and its cross section (e and f) after cycling for 300 h in the Li//gc-$Li_{3.2}P_{0.8}Sn_{0.2}S_4$//Li symmetric cell (0.1 mA cm^{-2}/0.1 mAh cm^{-2}): (a) the image of mapping area; (b-d) elemental mapping of S, P, and Sn; (e) a cross-section image of the Li/gc-$Li_{3.2}P_{0.8}Sn_{0.2}S_4$ interface after the cycling; (f) spectrum evolution obtained by a EDS linescan across the interface in (e) following the black arrow.

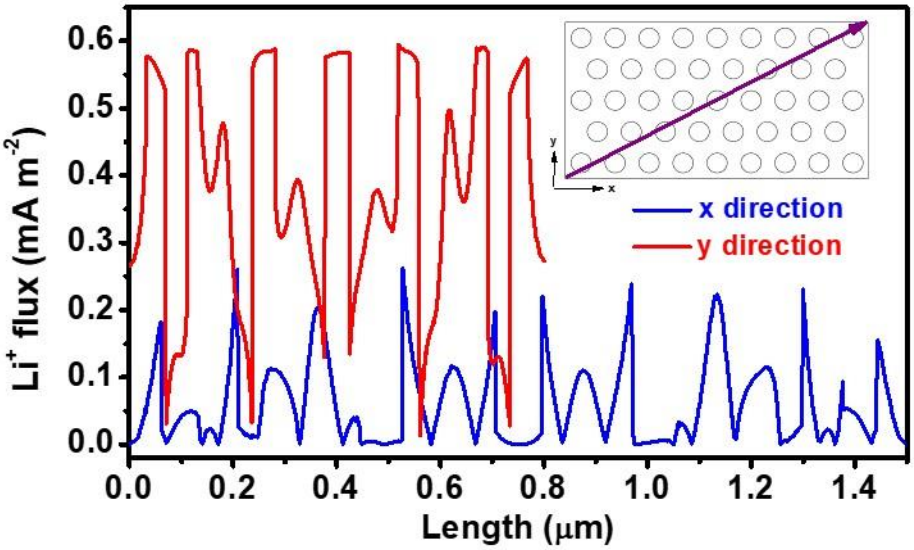

Figure S6.15 Extracted line graphs of Li^+ flux along the diagonal of the physical model (1.5 um × 0.8 um) against x and y axes. The schematic diagram is inserted.

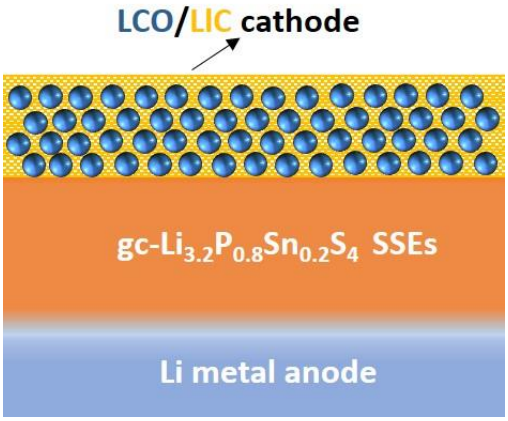

Figure S6.16 Schematic diagram of the Li//gc-$Li_{3.2}P_{0.8}Sn_{0.2}S_4$//LCO full cell.

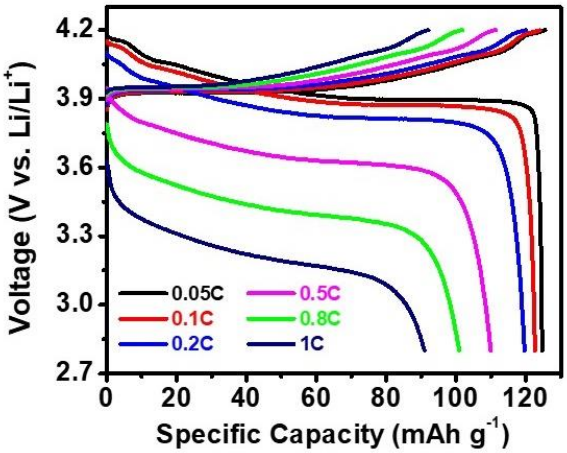

Figure S6.17 Charging and discharging curves of the Li//gc-$Li_{3.2}P_{0.8}Sn_{0.2}S_4$//LCO full cell at various current densities.

Table S6.1 Crystallographic data of $Li_{3.2}P_{0.8}Sn_{0.2}S_4$ and corresponding refinement parameters

Compound	**$Li_{3.2}P_{0.8}Sn_{0.2}S_4$**
Space Group	Pnma-Orthorhombic
a, Å	13.159
b, Å	8.025
c, Å	6.135
V, Å³	647.885
2θ interval, °	10 - 90

Rwp,%	2.00
Rp, %	1.47
X Ray Radiation	Cu kα (λ1 = 1.5406 Å, λ2 = 1.5444 Å)

Table S6.2 Crystallographic data of β-Li_3PS_4 obtained from the database (ICSD 04-010-1784)

Compound	**β-Li_3PS_4**
Space Group	Pnma-Orthorhombic
a, Å	13.066
b, Å	8.015
c, Å	6.101
V, $Å^3$	638.92
2θ interval, °	10 - 90
X Ray Radiation	Cu kα (λ1 = 1.5406 Å, λ2 = 1.5444 Å)

Table S6.3 Rietveld analysis results for the XRD pattern of $Li_{3.2}P_{0.8}Sn_{0.2}S_4$

Atom	x	y	z	OCC.	Site	Sym.
S1	0.93713	0.25000	0.25896	1	4c	m
S2	0.15628	0.02871	0.27567	1	8d	1
P3	0.08336	0.25000	0.18826	0.83	4c	m
Sn1	0.08336	0.25000	0.18826	0.17	4c	m
Li4	0.09905	0.25000	0.50223	1	4c	m
Li5	0.32182	0.02472	0.38891	0.9042	8d	1
Li6	0.00000	0.00000	0.50000	0.1691	4b	-1
S7	0.09715	0.25000	0.81306	0.81306	4c	m

Table S6.4 Summary of the sulfide electrolyte-based all-solid-state Li metal batteries' performance (LCO cathode)

Battery configuration (anode/electrolyte/ cathode)	**Cycle life (current density/ cycle number)**	**Rate capability (current density/ capacity)**	**1st CE**	**Active material loading**	**Reference**
Li//gc-$Li_{3.2}P_{0.8}Sn_{0.2}S_4$//LCO	0.1 C/ 60 cycles (1 C corresponds to 1.3 mA cm^{-2})	0.05 C / 124.7 mAh g^{-1} 1 C/ 91.0 mAh g^{-1}	96.2%	8.92 mg cm^{-2}	This work
Li//Li3N-LiF//Li3PS4//LCO (interlayer)	0.3 mA cm^{-2}/ 50 cycles	NA (0.3 mA cm^{-2}/ 101.3 mAh g^{-1})	78.6%	NA (~7.76 mg cm^{-2})	*Adv. Mater.* **2020**, doi.org/10.1002/adma.202002741
Li//pellet-sintered Li_6PS_5Cl//LCO/LNO (extra treatment)	0.35 mA cm^{-2}/ 100 cycles	0.1 C / 126 mAh g^{-1} 1 C/ 101 mAh g^{-1}	82.2%	NA (~3.12 mg cm^{-2})	*Nano Lett.* **2020**, 20, 6660
Li@$LPSCl_{0.3}F_{0.7}$// Li_6PS_5Cl//LCO@LNO (extra treatment)	0.1 C/ 50 cycles	0.05 C / 115 mAh g^{-1} 1 C/ 85.7 mAh g^{-1}	89%	8.92 mg cm^{-2}	*ACS Energy Lett.* **2020**, 5, 1035-1043

Li/LPSI-20Sn//$Li_{10}GeP_2S_{12}$//LCO@LNO (interlayer)	0.1 C/ 50 cycles	0.05 C/ 123.7 mAh g^{-1} 1 C/ 93.8 mAh g^{-1}	91%	8.92 mg cm^{-2}	*Adv. Energy Mater.* **2020**, 10 1903422
Li// $Li_{3.06}P_{0.98}Zn_{0.02}S_{3.98}O_{0.02}$// $Li_{10}GeP_2S_{12}$//LCO /LNO (interlayer)	0.1 C/ 100 cycles	NA (0.1 C/139.1 mAh g^{-1})	NA (~83%)	NA	Energy Storage Mater. **2019**, 17, 266
Li//LI_3PS_4-30LiI/LCO@LNO	0.2 C/ 40 cycles	NA (0.2 C/ 120 mAh g^{-1})	NA	10 mg cm^{-2}	*Adv. Energy Mater.* **2018**, 8, 1703644
Li//LiFSI@Li_3PS_4/ /LCO (extra treatment)	0.3 mA cm^{-2}/ 50 cycles	NA (0.3 mA cm^{-2}/ 120 mAh g^{-1})	65%	~7 mg cm^{-2}	*Sci. Adv.* **2018**, 4, eaau9245
Li@LiF/$Li_7P_3S_{11}$(HFE)/LCO (interlayer)	0.1 mA cm^{-2}/ 100 cycles	0.1 mA cm^{-2}/ 117.8 mAh g^{-1} 1 mA cm^{-2}/ 59.2 mAh g^{-1}	NA (~80%)	3.6 mg cm^{-2}	*Nano Energy* **2018**, 53, 958
Li@LiH_2PO_4//$Li_{10}GeP_2S_{12}$//LCO@LNO (interlayer)	0.1 C/ 50 cycles	0.1 C/ 131.1 mAh g^{-1} 1 C/ 44.5 mAh g^{-1}	85.9%	~5.5 mg cm^{-2}	*ACS Appl. Mater. Interfaces* **2018**, 10, 2556

Table S6.5 Physicochemical properties of gc-$Li_{3.2}P_{0.8}Sn_{0.2}S_4$ SSEs compared with other representative sulfide SSEs

Name of SSE	**Ionic conductivity (RT, S cm^{-1})**	**Electronic conductivity (RT, S cm^{-1})**	**Air stability**	**Interface with Li metal**	**Reference**
gc-$Li_{3.2}P_{0.8}Sn_{0.2}S_4$	1.21×10^{-3}	2.89×10^{-9}	Good	Good	This work
$Li_{10}GeP_2S_{12}$	12×10^{-3}	9×10^{-9}	Bad	Bad	Nat. Mater. **2011**, 10, 682; *Chem. Mater*. **2016**, 28, 7, 2400; *Adv. Energy Mater.* **2016**, 6, 1501590
gc-Li_3PS_4	1.6×10^{-4}	2.2×10^{-9}	Bad	Bad	*J. Phys. Chem. C* **2019**, 123, 10280; *Nat. Energy* **2019**, 4, 187; *ACS Appl. Mater. Interfaces* **2015**, 7, 23685
$Li_7P_3S_{11}$	3.2×10^{-3}	10^{-11}~10^{-10}	Bad	Bad	*Adv. Mater.* **2005**, 17, 918; *Solid State Ionics* **2019**, 343, 115073; *ACS Appl. Mater. Interfaces* **2015**, 7, 23685
Li_6PS_5Cl	3.1×10^{-3}	6.81×10^{-9}	Bad	Bad	*ACS Energy Lett.* **2020**, 5, 1035; *ACS Appl. Mater. Interfaces* **2015**, 7, 23685
Li_6PS_5Br	~1×10^{-3}	4.4×10^{-9}	Bad	Bad	*ACS Energy Lett.* **2019**, 4, 265; *J. Mater. Chem. A* **2018**, 6, 645

Li_3PS_4-LiI	5×10^{-4} ~ 1.8×10^{-3}	NA	NA	Good	*Adv. Energy Mater.* **2018**, 8, 1703644; *Adv. Energy Mater.* **2018**, 8, 1703644; *ACS Appl. Mater. Interfaces* **2015**, 7, 23685
Li_4SnS_4	7×10^{-5}	NA	Good	NA	*Chem. Mater.* **2012**, 24, 2211
Li_2SnS_3	1.5×10^{-5}	NA	Good	NA	*Chem. Mater.* **2015**, 27, 189

Chapter 7

7 Advanced cathode interface manipulated by atomic layer deposition

Through fluorinating Li_6PS_5Cl sulfide electrolytes (chapter 4), the Li metal interface stability can be improved. In the cases of using Sn substitution, sulfide SSEs (Li_6PS_5I, Li_3PS_4) have been verified to perform 'three-in-one' effect (chapter 5 and chapter 6). In this chapter, we move from synthesis and anode interface to the interface modification for cathode. A favorable Zr-based cathode interface is elaborately manipulated by the atomic layer deposition (ALD) for sulfide-based ASSLIBs. Flexile control over the Li sub-cycle during the preparation process is demonstrated to be crucial for achieving a robust cathode interface with a desirable Li^+ ionic conductivity. The ASSLIBs equipped with this functional interface exhibit excellent cycling stability and rate capability at room temperature (RT). Various electrochemical and spectroscopic characterizations reveal that the ionic conductive interface can significantly limit side reactions and induce a low polarization of the (de)intercalation toward cathode materials. The interfacial manipulation regarding ionic conductivity and structure realized by ALD provides a new strategy to achieve high-performance ASSLIBs.

*One version of this chapter has been published in *Energy Storage Materials* 2020, 33, 139-146

7.1 Introduction

Sulfide electrolyte-based all-solid-state Li-ion batteries (ASSLIBs) have attracted significant interest due to their intrinsic safety and high-energy-density compared to the conventional Li-ion batteries (LIBs) using organic liquid electrolytes.[1-3] However, issues associated with the interfacial compatibility between sulfide-electrolytes and the anode/cathode have inhibited their commercialization.[4-6] Utilizations of Li alloys (Li-In, Li-Al, Li-Sn, etc) or chemically/electrochemically pretreated Li metal anodes can effectively alleviate the anode interfacial problems.[7-9] In contrast, limited strategies have been demonstrated to stabilize the cathode interface in sulfide electrolyte-based ASSLIBs. The thermodynamic incompatibility of the cathode/sulfide electrolytes results in unfavorable side reactions and hampered Li^+ ion conductivity.[10-12] Development of functional coating layers on cathode particles is the most commonly used method to improve the stability of the cathode/sulfide electrolytes interface.[13-14]

The Zirconium (Zr)-based coating layer (ZrO_x or $LiZrO_x$) is one of the most promising cathode coating materials for ASSLIBs.[10, 13] Both simulation and experimental results have shown that improved electrochemical performance can be achieved by coating the Zr-based interface layers on cathode materials.[10, 15-17] Very recently, Samsung employed one Li_2O-ZrO_2 coating to endow a pouch cell-type sulfide electrolyte-based ASSLIB with an impressive cycling performance of 1000 cycles at 60 ºC.[16] Compared with the common-used $LiNO_x$ or $LiTaO_x$ coating layers for sulfide-based ASSLIBs.[10, 13] the Zr-based coating is predicted to improve the rate performance, because the derived Zr-based interface is capable of optimizing the electrical band structure to achieve an appropriate electronic conductivity.[18] In addition, the Zr-based rock-salt structure layer coated on the Li and Mn-rich (LMR) cathodes was also proved to suppress the deleterious phase transformation of the cathode materials in the liquid electrolyte-based Li-ion batteries.[19] Last but not least, the Zr element is much more abundant in the earth's crust compared with Nb or Ta, which can leading to a lower fabrication cost for practical applications.[20]

Li-containing coatings are important to provide required interfacial ionic conductivity (σ) for sulfide-based ASSLIBs.[13] By revisiting the reported Li-containing Zr-based coating

($LiZrO_x$), it is found that most of these coatings were developed via wet chemical approaches, and high temperature (HT, ≥ 650 ^oC) post-annealing was commonly employed to remove the organic solvent and achieve crystallized coatings.[15-16, 21-27] Nevertheless, the involved high-temperature process was reported to have the potential to cause degradation or phase change of the cathode materials, particularly for the interface-sensitive solid-state systems.[13] It is noted that Samsung's Li_2O-ZrO_2 cathode coating is among few wet chemical methods that employ low-temperature (LT) processes (350 or 300 ^oC),[15-16] but contributes to one of the best electrochemical performance in the field of ASSLIBs [11]. The obtained amorphous Li-containing Zr-based coating from LT process was verified to possess a sufficient σ and intact morphology to realize the excellent performance.[13, 16, 27] Therefore, development of LT or solvent-free routes is necessary to avoid the negative effects brought about by the HT process.

Atomic layer deposition (ALD) is an advanced film fabricating technique, capable of tuning the interface property with atomic-level thickness control at relatively low temperature (< 400 ^oC).[28] Compared with the conventional wet chemical method, the ALD method can not only show the ability of developing Li-containing transition metal oxides coating with uniform and conformal features, but also completely avoid the negative effects of using solvents and HT processes.[29] ALD-$LiNbO_x$[30-31] and ALD-$LiPO_x$[32] have been reported as effective cathode coatings to improve the interfacial compatibility between cathode materials and $Li_{10}GeP_2S_{12}$ (LGPS) sulfide electrolytes. However, the detailed Li^+ ion conducing effect derived from the ALD process on the electrochemical performance of sulfide-based ASSLIBs is still unknown, but undoubtedly plays a very important role.

Herein, for the first time, we choose Zr as the transition metal and develop a new lithium zirconium oxide (LZO) in alleviating the incompatible interface between $LiCoO_2$ (LCO) cathodes and Li_6PS_5Cl (LPSCl) sulfide electrolytes. The Zr-based film with and without Li incorporation obtained by ALD (abbreviated as ALD-LZO and ALD-ZrO_x, respectively) shows significant differences on the structure of the film, as well as the electrochemical performance of the ASSLIBs. The tunable σ of LZO layer manipulated by the preparation process is crucial for the delivered performance of the ASSLIBs.

Furthermore, the working mechanism of ALD-LZO coating to guarantee the interfacial stability is disclosed via multiple advanced chemical/electrochemical characterizations.

7.2 Experimental section

7.2.1 Synthesis of ALD-LZO and ALD-ZrO_x Films

N-doped carbon nanotubes (CNTs, prepared by previously reported chemical vapor deposition method),[33] $LiCoO_2$ (LCO, Sigma Aldrich, 99.8%), and glass slides were used as the substrates for established purposes. Tetrakis(dimethylamido) zirconium (IV) (TDMAZ, STREM CHEMICALS, INC. 99%), lithium tert-butoxide (LiO^tBu, STREM CHEMICALS, INC. > 98%), and deionized H_2O were used as the precursors. TDMAZ and LiO^tBu were kept at 75 ^oC and 170 ^oC respectively with heating jackets to provide vapor, while H_2O was kept at room temperature to provide vapor. For the ALD-LZO preparation, two separated sub-cycles (LiO_x and ZrO_x) are required as shown in **Figure S7.1** in the supplementary material. One single LiO_x sub-cycle process: (1) a 1 s pulse of LiO^tBu; (2) a 2 s extended exposure of LiO^tBu to the substrate; (3) purging of residual LiO^tBu with 12 s; (4) a 1.0 s pulse of H_2O; (5) a 1.0 s extended exposure of water vapor to the substrate; (6) a 20 s purge of residual H_2O. One single ZrO_x sub-cycle process: (1) a 1 s pulse of TDMAZ; (2) a 2 s extended exposure of TDMAZ to the substrate; (3) purging of residual TDMAZ with 12 s; (4) a 1.0 s pulse of H_2O; (5) a 1.0 s extended exposure of H_2O vapor to the substrate; (6) a 18 s purge of residual H_2O. One full cycle of ALD-LZO process includes one LiO_x sub-cycle and 4 ZrO_x sub-cycles. The deposition temperature was optimized as 270 °C based on the obtained ionic conductivity (230 ^oC and 300 ^oC were both tried). N_2 was used as the carrier gas and the ALD reactor was sustained at a high vacuum of 0.2 Torr with a continuously working pump. Just performing the sub-cycle of ZrO_x to prepare ALD-ZrO_x films on designate substrates.

7.2.2 Synthesis of Li_6PS_5Cl (LPSCl) SSEs

Li_2S (Alfa Aesar, 99.9%), P_2S_5 (Sigma Aldrich, >99%), and LiCl (Sigma Aldrich, 99.9 %, anhydrous) or LiCl (Sigma Aldrich, > 99.98 %, anhydrous) were used as the starting materials. As the previously reported solid-state reaction method,[34] stoichiometric starting materials were weighted and sealed in a zirconia ball-milling pot with a weight ratio of 1:40 (starting materials: zirconia balls) in an Ar-filled glovebox (H_2O < 0.1ppm, O_2 < 0.1

ppm). The mixture was mechanically milled by using a planetary ball milling apparatus at 510 rpm for 13 h. Then, the ball-milled product was pressed into pellets, sealed in quartz tubes for annealing (550 ^{o}C for 8 h) in a muffle furnace. The rate of temperature increasing was fixed at 20 ^{o}C/ min. After completing the annealing, the sample naturally cooled down to room temperature (RT). X-ray diffraction (XRD) and electrochemical impedance spectroscopy (EIS) measurements (**Figure S7.2**) suggest the high quality of the prepared Li_6PS_5Cl electrolyte.

7.2.3 Preparation of the LZO@LCO/LPSCl Cathode Composite

LZO@LCO powder and LPSCl electrolytes were mixed with a mass ratio of 7:3 using a roll mixer. No conductive carbon was added due to the intrinsic electronic conductive property of the LCO materials. Similar process was employed to prepare ZrO_x@LCO/LPSCl cathode composites.

7.2.4 Ionic Conductivity Measurements

According to the previously published method [35], firstly, 1000c ALD-LZO films prepared by 230, 270, and 300 ^{o}C respectively were deposited on the glass slides with Au patterns. Then, the ionic conductivity of prepared the ALD-LZO film was measured by the EIS and corresponding simulation method. This was completed on a multichannel potentiostation 3/Z (German VMP3). The applied frequency range is 0.1 Hz ~ 7 MHz and the amplitude is 20 mV. To obtain the Arrhenius plot, variable-temperature EIS was measured from 25 ^{o}C to 65 ^{o}C with an interval of 10 ^{o}C. The ionic conductivity (σ) of our ALD-LZO films was calculated by the equation: $\sigma = d/(R \cdot A)$, where the R is resistance measured by EIS, d and A are the thickness and the area of the deposited ALD-LZO film, respectively.

7.2.5 Assembly and Electrochemical Measurements of ASSLIBs

ASSLIBs were fabricated using LPSCl as the electrolyte, LZO@LCO/LPSCl as the cathode composite, and In foil as the anode. Typically, 80 mg of the LPSCl electrolyte was pressed under ~300 MPa to form a solid LPSCl layer (10 mm of diameter). 10 mg of LZO@LCO/LPSCl composite powder were uniformly spread onto the surface of the other side of LPSCl layer and pressed under ~360 MPa for 5 minutes. Finally, In foil was placed on the other side of the LPSCl pellet and pressed by ~120 MPa for 3 minutes. The three-layered pellet cell was sandwiched between two stainless-steel rods as current collectors and sealed in the model cell. All cell fabrication processes were performed in an Ar-filled

glove box. The loading mass of active material is ~8.92 mg/cm^2 in the ASSLIBs. Galvanostatic charge-discharge was conducted on the LAND battery test system. The voltage window was set as 1.9~3.6 V (vs. In^+/In), and various constant charging/discharging current densities were applied to evaluate the cycling stability and the rate capability. The galvanostatic intermittent titration technique (GITT) measurements were carried out using LAND battery test station. The transient discharge voltage profiles were recorded by applying a discharge current density of 0.01 C for 5 min followed by a 2h relaxation until the discharge voltage reaches 1.9 V. Cyclic voltammograms (CV) were performed on a VMP3 working station by applying a scan rate of 0.1 mV/s in a voltage range of 1.9 ~ 3.6 V. EIS measurements for ASSLIBs at the specific discharge/charge states were completed on the VMP3 station with an amplitude of 20 mV and frequencies ranging from 0.1 H to 7 MHz.

7.2.6 Characterization Methods

X-ray diffraction (XRD) measurements were performed on Bruker AXS D8 Advance with Cu Kα radiation (λ = 1.5406 Å). Scanning electron microscope (SEM) images were obtained by using a Hitachi S-4800 field-emission scanning electron microscope (FE-SEM, acceleration voltage 5 kV). Transmission electron microscope (TEM) images were obtained using a JEOL 2010F field emission TEM (acceleration voltage 200 kV), which is equipped with energy dispersive spectroscopy (EDS) for elemental mapping. X-ray photoelectron spectroscopy (XPS) spectra were obtain by using Krotos AXIS Ultra Spectrometer system using a monochromatic Al Kα source (25 mA, 15 kV). X-ray absorption near edge structure (XANES) spectra of Zr L-edge and K-edge were collected on the Soft X-ray Microcharacterization beamline (SXRMB, 1700 ~ 10000 eV) and Hard X-ray MicroAnalysis (HXMA, 5000 ~ 40000 eV) beamlines respectively at the Canadian Light Source (CLS). The energy scanning steps for collecting spectra were set as 0.2 eV on SXRMB and 0.5 eV on HXMA, respectively. SXRMB and HXMA data was processed with Athena software. Scanning transmission X-ray microscopy (STXM) was carried out on the Soft X-ray Spectromicroscopy (SM, 130 ~ 2700 eV) beamline at CLS. STXM data was analyzed using the aXis2000 software.

7.3 Results and Discussion

7.3.1 Effects of the introduced Li sub-cycle for obtained ALD-LZO films

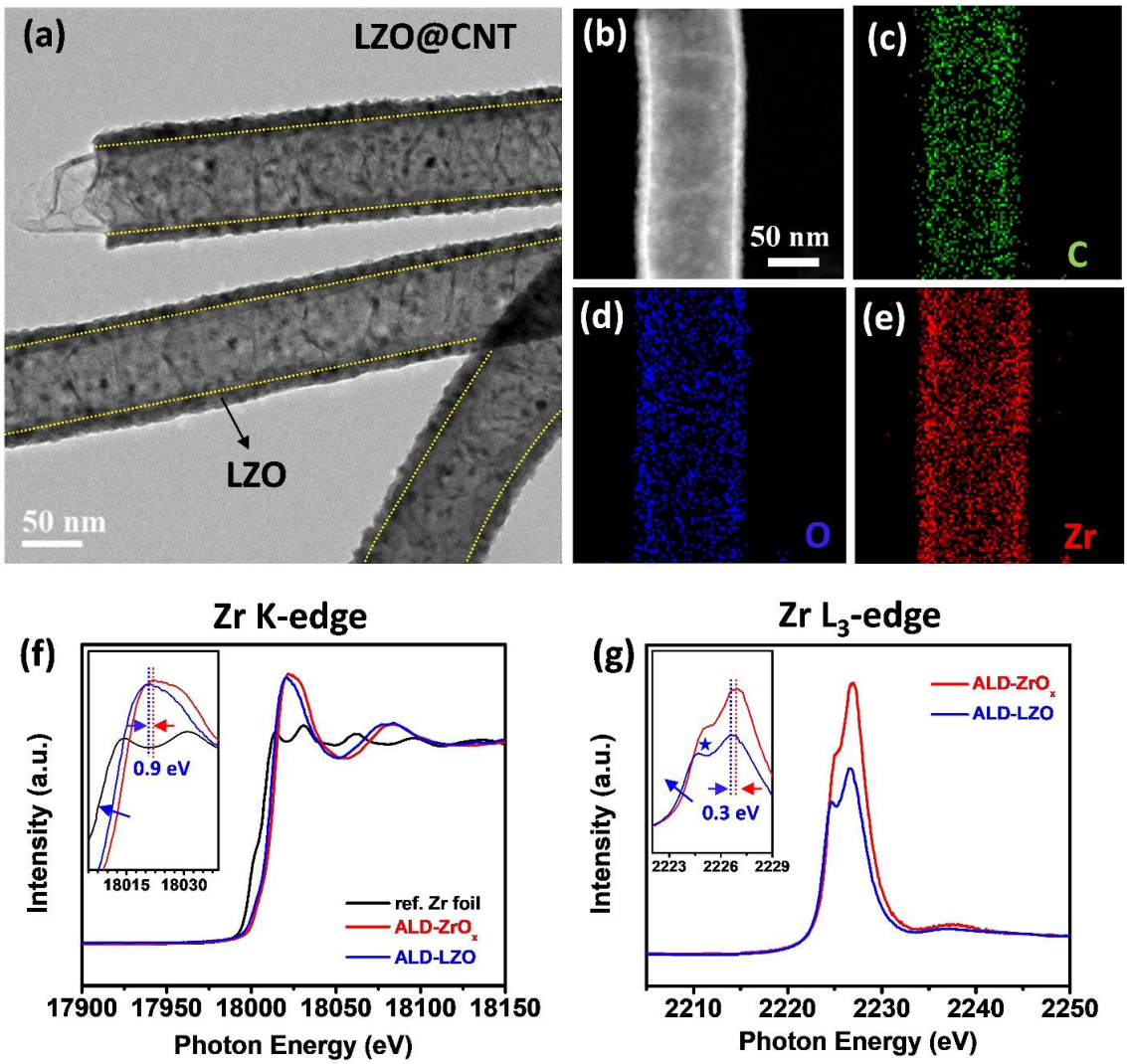

Figure 7.1 Characterizations of the prepared ALD-LZO film on CNTs. (a) a TEM image of the deposited LZO films on CNTs (LZO@CNT); (b) a STEM image of the LZO@CNT material; (c-e) EDX mapping of the C, O, and Zr elements on the LZO@CNT; (f and g) comparison of the XANES of Zr K-edge and L_3-edge spectra between the ALD deposited ZrO_x and LZO films.

The preparation of ALD films follows a layer-by-layer deposition process. Inspired by the previously published ALD processes by our group,[35-36] we choose solid-state organic

metal-based compounds: TDMAZ and LiO^{t}Bu as the Zr and Li precursors, respectively. H_2O is chosen as the oxidant for the sub-cycles. One single layer (one cycle) of Li containing LZO film can be obtained by alternatively introducing LiO^{t}Bu, H_2O, TDMAZ, and H_2O onto the substrate placed in the ALD chamber. The growth rate of the ALD-LZO film at a chamber temperature of 270 ^oC is 0.234 nm/cycle, which is determined by measuring the thickness of the deposited ALD-LZO films with various cycles on Si wafers (**Figure S7.3**). 50-cycles (50c) ALD-LZO film are deposited on the carbon nanotube (CNT) substrate (marked as LZO@CNT) for studying the structure of the ALD-LZO film. TEM measurements are carried out to witness an intact LZO coating layer decorates walls of the CNT (**Figure 7.1a**). The elemental mapping under the STEM (scanning transmission electron microscope) mode indicates that C, O, and Zr elements are homogeneously dispersed with spatial resolution in the LZO@CNT composite (**Figure 7.1b-e**). High-energy XPS measurements are used to observe the Li 1s spectrum as shown in **Figure S7.4a**, indicating Li is successfully introduced in the deposited LZO film. The Zr 3d spectrum of LZO film in **Figure S7.4b** shows typical 3d splitting peaks (184.2 and 181.8 eV for $3d_{5/2}$ and $3d_{3/2}$, respectively) of the Zr element, which agrees well with the LZO-related materials prepared by wet chemical methods.[37-38] XRD measurements cannot witness additional diffraction peaks for the LZO@CNT composites (**Figure S7.5**), indicating the amorphous nature of the deposited LZO films, which agrees well with the previously reported ALD coatings developed at low temperature (< 300 ^oC) [29]. To investigate the influence of introducing Li on the electronic structure of Zr in the ALD films (LZO and ZrO_x), XANES of Zr K-edge and L-edge were collected. Zr K-edge spectra of ALD-LZO and ALD-ZrO_x show distinct spectral features associated with oxidized zirconia species compared to that of the Zr foil reference sample (**Figure 7.1f**). The whiteline peak is seen to undergo a ~0.9 eV shift to a lower energy for the LZO compared with the ZrO_x, suggesting that the incorporated Li can interact with the Zr local environment as previously reported in other Li containing ternary oxides.[35, 39] A similar red-shift of photon energy is also reflected in the Zr L_3-edge spectra as shown in **Figure 7.1g**. The intensity of a small broad speak at ~2224.7 eV increases after Li incorporation, indicating electropositive Li^+ slightly lower the chemical state of Zr, and the polymerization degree of Zr-O polyhedrons in the LZO structure is reduced [39]. These

morphology and structure characterizations suggest that the simple addition of the sub-cycle with Li incorporating can successfully prepared ALD-LZO film. The distortion of the Zr environment induced by Li incorporation, as well as the disordered Zr-O polyhedron are expected to benefit the Li^+ ion migration in the LZO structure. ALD-LZO films of 1000 cycles are deposited onto the patterned glass slide for the electrochemical impedance spectroscopy (EIS) measurements. Nyquist plots under varied test temperatures and the derived Arrhenius plots are displayed in **Figure S7.6**. The ALD chamber temperature is optimized to be 270 ^{o}C for a decent ionic conductivity of 6.7×10^{-5} mS/cm at room temperature (RT) with an activation energy (E_a) of 0.39 eV. The Li^+ transport ability (especially the E_a) of LZO has overtaken other Li containing ternary oxides prepared by ALD methods,[40] and can be comparable to the most popular LNO coating for sulfide electrolyte-based ASSLIBs.[41]

7.3.2 ALD-LZO Coating on LCO Cathode Materials

The high-quality ALD-LZO films (deposition temperature at 270 ^{o}C, 25c) are deposited on LCO particles (marked as LZO@LCO) to evaluate this functional coating layer in ASSLIBs. First of all, the morphology and structure of LZO@LCO composites are investigated to confirm the core-shell features. The TEM image (**Figure 7.2a**) indicates the thin layer of LZO film with thickness of ~5 nm is continuous and acts as the outermost shell. The spatial distribution of Co, O, and Zr elements in the area of **Figure 7.2b** is revealed by the STEM-elemental mapping (**Figure 7.2c-e**). The signal intensity of Co element in the edge region is obviously weaker than that in the center, while the signal indication of Zr is consistent in the whole area. This illustrates the LZO film is conformally coated on the LCO particle. High-resolution TEM (**Figure 7.2f**) on a local area further verifies the LZO layer is coated on the well crystallized LCO particle. The clear and intact crystal lattice of the (003) plane of internal LCO core confirms that the low temperature deposition temperature (270 ^{o}C) has little side effect on the structure of LCO cathode materials. The XPS spectrum of Zr 3d in the LZO@LCO composite is presented in **Figure S7.7**. Splitting positions (184.3 and 181.9 eV for $3d_{5/2}$ and $3d_{3/2}$, respectively) of the Zr 3d spectrum are consistent with that shown in the LZO@CNT composite, suggesting the success of LZO coating on LCO particles. This obtained amorphous LZO coating avoids

the formation of island structure of the crystallized coating,[27] and benefits to generate an intact protection layer. In addition, the verified high ionic conductivity of this interfacial LZO coating can boost the required electrochemical reactions.

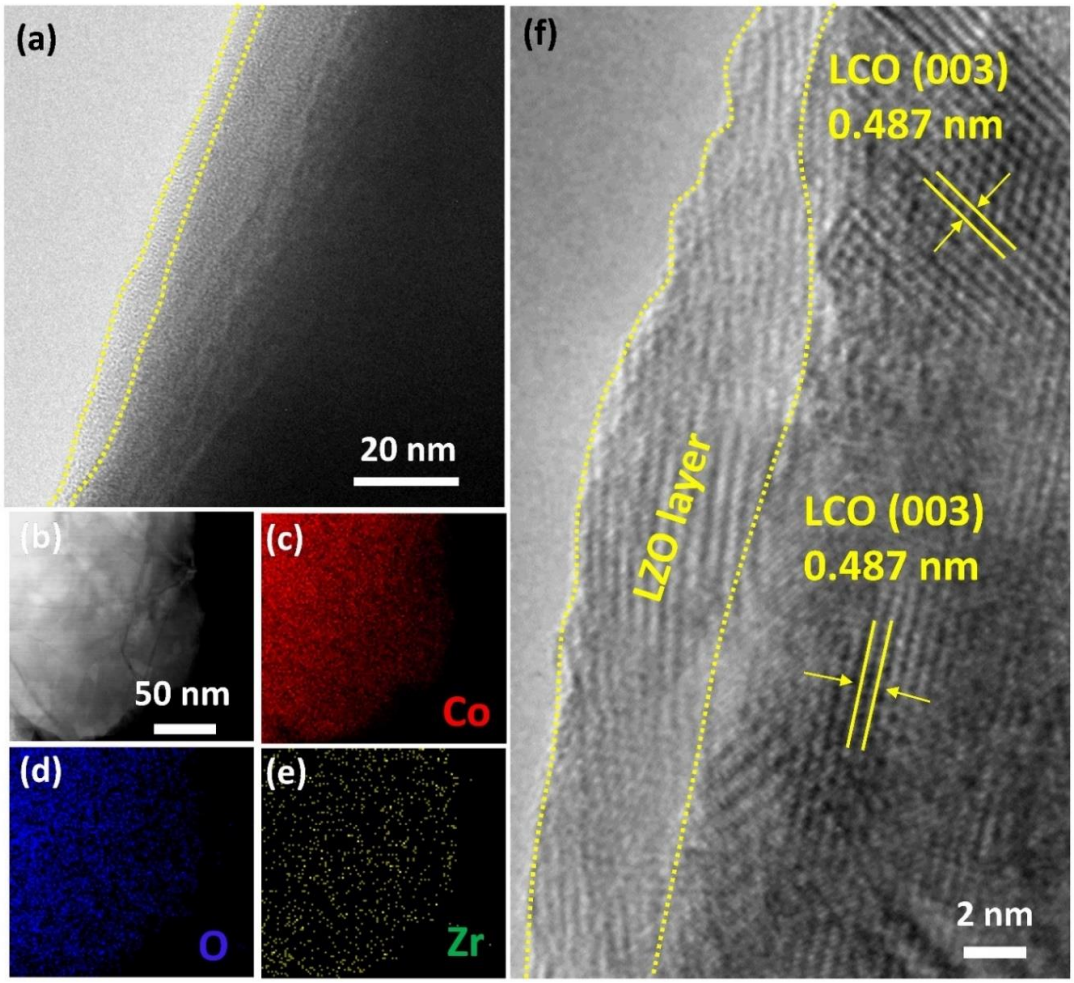

Figure 7.2 TEM characterizations of the 25 cycles of ALD-LZO deposited on the LCO particles (LZO@LCO). (a) a TEM image of the LZO@LCO composites; (b) a STEM image of the LZO@LCO composites; (c-e) EDX mapping of the Co, O, and Zr elements on the LZO@LCO composites; (f) a HRTEM image of LZO@LCO composites.

7.3.3 Excellent Electrochemical Performance of ASSLIBs

The LZO@LCO cathode composite is combined with Argyrodite Li_6PS_5Cl (LPSCl) sulfide SSEs and In anode to construct full batteries (In//LPSCl//LZO@LCO/LPSCl). The ALD-LZO coating layer is expected not only to provide sufficient Li^+ ion flux at the cathode

interface, but also to prevent the side reactions, which is illustrated in **Figure 7.3a**. First-cycle charge and discharge curves at a current density of 0.025 C (1 C= 140 mA/g_{LCO}) are displayed in **Figure 7.3b**. In the marked area of the charging curves, a slope exists in the first charging (1stC) curve of the In//LPSCl//LCO/LPSCl full battery without LZO coating, which is attributed to the space charge layer derived from the incompatible interface between oxide cathode materials and sulfide electrolytes [42]. However, this slope vanishes for the In//LPSCl//LZO@LCO/LPSCl full battery with LZO coating, which means the LZO coating layer can flatten the charge distribution and promote a stable LCO/LPSCl interface. As a result, the specific capacity of LCO cathode materials after coating LZO is 134.3 mAh/g with a high first-cycle coulombic efficiency of 89.0%. By contrast, the LCO cathode without LZO coating just exhibits a reversible specific capacity of 84.1 mAh/g and a much lower first-cycle coulombic efficiency of 63.8%. Cyclic voltammetry (CV) measurements verify that a large polarization occurs in the positive (charging) and negative (discharging) scan if LZO protection layer is not coated on the LCO cathode (**Figure 7.3c**). The rate capability of the In//LPSCl//LZO@LCO/LPSCl full battery is studied in detail. As displayed in **Figure 7.3d**, the reversible specific capacity at 0.05 C is 121.8 mAh/g, and gradually declines to 115.4, 104.6, 95.6, and 87.8 mAh/g when the current density increases to 0.1, 0.2, 0.5, and 0.8 C, respectively. Even at a high current density of 1 C, the specific capacity of 79.1 mAh/g can be retained. Importantly, the specific capacity is able to recover to 92.3 mAh/g when the current density reduces to 0.1 C. In sharp contrast, the bare LCO cathode exhibits poor lithiation kinetics when the current density elevates to 0.5 C, because very limited reversible capacity (~25 mAh/g) is obtained at this current. The rate capability based on ALD-LZO coating has overtaken that performed with the most popular LNO coating.[31] We ascribe this enhancement to the good electrical band structure derived by the Zr-containing interface.[18]

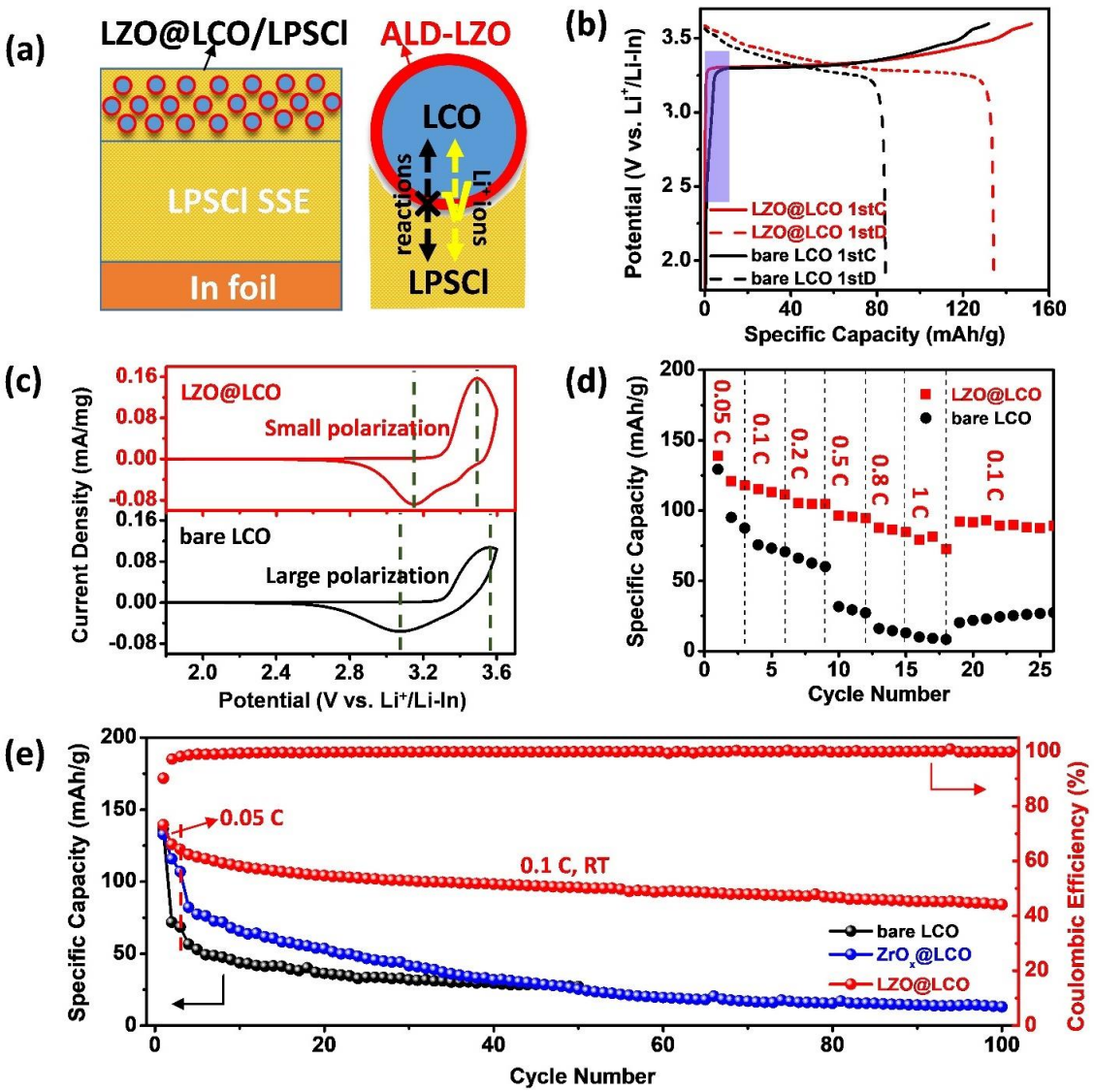

Figure 7.3 (a) A schematic diagram of the In//LPSCl//LZO@LCO/LPSCl all-solid-state battery and the proposed mechanism; (b) charge and discharge curves (0.025 C); (c) the first-cycle CV results at a scan rate of 0.1 mV/s; (d) rate capability and (e) long-term cycling stability of all-solid-state batteries with bare LCO, ZrO_x@LCO, and LZO@LCO cathodes. All electrochemical performances were obtained at room temperature (RT).

Long-term cycling stability of the In//LPSCl//LZO@LCO/LPSCl full battery is reflected in **Figure 7.3e**. After the initial three charging and discharging cycles at low current density of 0.05 C, the charged specific capacity of the full battery reaches 117.2 mAh/g at a current density of 0.1 C, and maintains 84.1 mAh/g (72 % retention) after 100 cycles. Without

LZO coating, the initial reversible capacity is 56.7 mAh/g, and drop to only 27.2 mAh/g at the 50th cycle. Obviously, the good performance via LZO coating layers cannot be achieved equivalently with ALD-ZrO_x coating (100c). The poor cycling stability and limited reversible specific capacity of ZrO_x@LCO cathode demonstrate the significance of introducing Li in the coating layer. The Li containing coating layer cannot only prevent the side reactions, but also provide essential support for the Li^+ ion migration at the interface of cathode/sulfide SSEs. In addition, we coated LCO particles with different layer numbers of LZO films to optimize the thickness of the ALD-LZO protection layer. Compared with 10c and 50c LZO coating layers, 25c LZO exhibits the optimal thickness (~5 nm) which shows the best cycling stability in In//LPSCl//LZO@LCO/LPSCl full batteries (**Figure S7.8**). A thinner LZO coating layer (**Figure S7.9a**) cannot ensure an intact protection layer on the LCO particle, while too thick of a LZO coating layers (**Figure S7.9c**) would hinder the Li^+ ion transfer through the interface. It is noted that the cycling stability of our ASSLIBs with the protection of ALD-LZO coating on LCO cathode has also surpassed previously reported result with LNO coating.[31, 43-44] We further correlate the effect of the interfacial ionic conductivity to the battery performance by examining the LZO film deposited on LCO cathodes at 230 ^oC and 300 ^oC. The result suggests that LZO obtained via 230 ^oC with lower ionic conductivity compared with those gained at 270 ^oC or 300 ^oC, delivering a lower specific capacity, faster capacity decay rate, as well as lower coulombic efficiency (**Figure S7.10**). In addition, the LZO film obtained at 300 ^oC on LCO particles is inferior to that obtained via 270 ^oC. This is ascribed to the larger growth rate of the LZO layer at higher deposition temperature. The resulting thicker LZO layer (**Figure S7.11**) is undesirable for the effective Li^+ ion transport at the interface between LCO cathodes and LPSCl SSEs.

7.3.4 Understanding the Mechanism of the ALD-LZO derived cathode interface

Various electrochemical and chemical structure characterizations were utilized to understand the functional mechanism of ALD-LZO coating layers on LCO cathode. Galvanostatic intermittent titration technique (GITT) was employed to track the polarization of full batteries. Transient discharging voltage profiles and the derived polarization curves are displayed in **Figure 7.4a**. In the spontaneous discharging process,

LZO@LCO cathode shows lower polarization than bare LCO. Especially after delivering a specific capacity of 50 mAh/g, the LZO coating layer can significantly prolong the discharge process of LCO cathode with a much smaller polarization. This means ALD-LZO induces a favorable interface between LCO cathode and LPSCl electrolytes, which can effectively reduce the interfacial polarization. EIS measurements were performed for the full batteries after the first charging process. **Figure 7.4b** shows the Nyquist plots with the corresponding equivalent circuits. The similar R_{SE} value (~22 Ω) imply a similar bulk resistance of the LPSCl layer in the two full batteries using bare LCO and LZO@LCO based cathode materials.[45] The LPSCl/In anode interface impedance can be described as R_{LF} (low-frequency region). A similar R_{LF} value (~120 Ω) helps to rule out any anode influence when analyzing the cathode part. The semi-circles at the middle-frequency and high-frequency represent the impedances of cathode composite layer/LPSCl layer interface (R_{MF}) and cathode materials/LPSCl interface in the cathode composite (R_{HF}), respectively.[45-47] After coating LCO with ALD-LZO films, these two values reduce significantly upon battery cycling, which is related to the inhibition of side reactions and fast Li^+ ions mobility at the cathode/LPSCl interface with LZO coating.

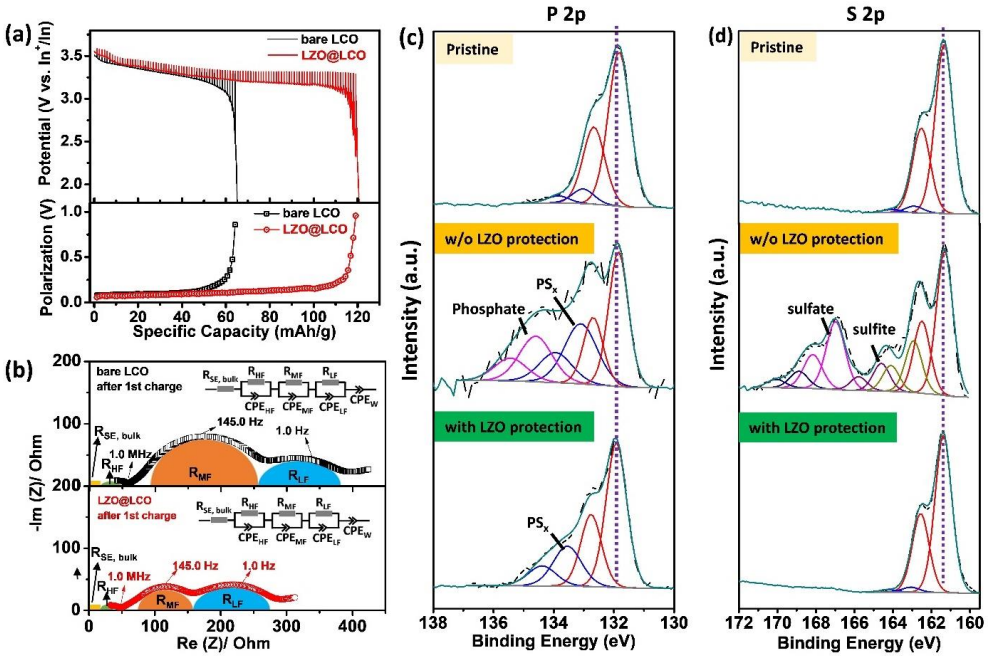

Figure 7.4 (a) Comparisons of the transient discharge voltage profiles and their corresponding polarization plots obtained by GITT, and (b) EIS analysis results for

In//LPSCl//LZO@LCO/LPSCl and In//LPSCl//LCO/LPSCl full batteries; (c and d) XPS spectra of the P 2p and S 2p before and after battery cycling with and w/o LZO protections on the LCO cathode particles.

XPS analysis were conducted on the cycled cathode composite with and without (w/o) LZO protection. P 2p and S 2p spectra present in **Figure 7.4c** and **Figure 7.4d**, respectively. P in the LPSCl can be oxidized to phosphorus polysulfides (PS_x) and phosphate upon electrochemically reacting with bare LCO cathode materials.[48-49] Similarly, S is oxidized to high-valence sulfites and sulfates without LZO protection.[49-50] These findings are in accordance with previously reported results, which are due to the incompatibility of the sulfide/LCO interface and the instability of LPSCl SSEs at voltages higher than 2.8 V.[48-50] In contrast, the electrochemically instable LCO/LPSCl interface can be alleviated by coating LCO with ALD-LZO. Although some PS_x species resulting from the decomposition of LPSCl at high voltage still exists in the cathode composite (with LZO protection) after cycling, the detrimental side reactions is prevented significantly and the S spectrum is maintained well. In addition, the XPS of Zr 3d spectrum (**Figure S7.12**) in the cycled cathode composite remains unchanged, indicating the ALD-LZO coating layer is robust and can withstand repeat Li^+ ion transfer through the LZO@LCO/LPSCl interface.

Due to the limited emission energy of XPS, no difference can be observed on the Co 2p spectra of the cycled LCO cathode with or without LZO coating (**Figure S7.13**). However, we can observe two kinds of distinct spectra of Co L-edge through synchrotron-based STXM. On the absorption edge (780 eV), micro-sized single LCO particles without and with LZO coating can be imaged as shown in **Figure 7.5a** and **Figure 7.5c**, respectively. The spectra of Co $L_{3,2}$ edge (**Figure 7.5b**) extracted from the marked areas in **Figure 7.5a** show that a broad peak (peak I) always exists, indicating the Co^{3+} in the LCO cathode was reduced when in contact with LPSCl directly after cycling [51-52]. The reduction reaction of Co^{3+} can be eliminated by the LZO protection. As shown in **Figure 7.5d**, the spectra corresponding to the marked positions remain consistent compared with the spectrum of Co $L_{3,2}$ edge in pristine LCO.

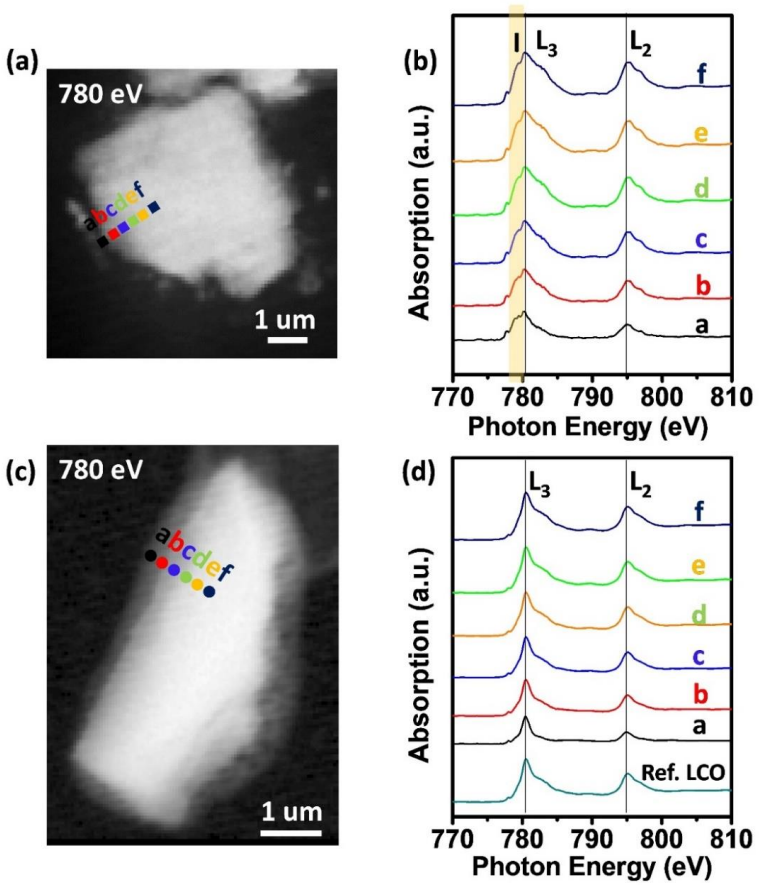

Figure 7.5 STXM optical density images of single LCO particle after 50 cycles of charging and discharging with bare LCO cathode (a) and LZO@LCO cathode (c), respectively. (b) XANES of Co $L_{3,2}$ edge of the marked areas in (a). (d) XANES of Co $L_{3,2}$ edge of the marked areas in (c).

7.4 Conclusion

In summary, ALD is utilized to rationally design Li-containing Zr-based cathode coating for sulfide-based ASSLIBs. Structural characterizations (including synchrotron-XANES) confirm the success of incorporating Li in the LZO film by an additional Li-related sub-cycle process, which affects the local electronic structure of the Zr metal centers. The presented Zr-Li interaction manipulated by the ALD deposition temperature (270 ^{o}C) is demonstrated to be favorable for a desirable ionic conductivity of 6.7×10^{-5} mS/cm at room temperature. ALD-LZO films coated on LCO cathode materials can significantly improve the RT performance for full batteries. A specific capacity of 117.2 mAh/g is achieved at

the current density of 0.1 C, and the capacity retention stands at 72% after 100 cycles. More importantly, the specific capacity reaches 79.1 mAh/g at 1 C. The effective interfacial manipulation provides essential Li^+ ion flux at the LCO/LPSCl interface, which can reduce the polarization of the electrochemical reactions. Moreover, various spectroscopic characterizations (XPS and synchrotron-STXM) reveal that the detrimental side reactions between LCO and LPSCl are significantly reduced with the LZO derived cathode interface. The flexible design of functional cathode interface realized by ALD paves the way to achieve advanced sulfide-based ASSLIBs.

7.5 Acknowledgments

This research was supported by the Natural Sciences and Engineering Research Council of Canada (NSERC), the Canada Research Chair Program (CRC), the Canada Foundation for Innovation (CFI), Ontario Research Foundation (ORF), China Automotive Battery Research Institute Co., Ltd., Glabat Solid-State Battery Inc. and Western University. The synchrotron research described in this work was performed at the Canadian Light Source, which is supported by the Canada Foundation for Innovation (CFI), the Natural Sciences and Engineering Research Council (NSERC), the Canadian Institutes of Health Research (CIHR), and the Government of Saskatchewan.

7.6 References

（1）Kato, Y.; Hori, S.; Saito, T.; Suzuki, K.; Hirayama, M.; Mitsui, A.; Yonemura, M.; Iba, H.; Kanno, R., *Nat. Energy* **2016,** *1* (4), 16030.

（2）Manthiram, A.; Yu, X.; Wang, S., *Nat. Rev. Mater.* **2017,** *2* (4), 16103.

（3）Ding, Y.; Cano, Z. P.; Yu, A.; Lu, J.; Chen, Z., *Electrochem. Energy Rev.* **2019,** *2* (1), 1-28.

（4）Xiao, Y.; Wang, Y.; Bo, S.-H.; Kim, J. C.; Miara, L. J.; Ceder, G., *Nat. Rev. Mater.* **2020,** *5*, 105–126.

（5）Zhang, Q.; Cao, D.; Ma, Y.; Natan, A.; Aurora, P.; Zhu, H., *Adv. Mater.* **2019,** *31* (44), 1901131.

（6）Zhao, F.; Liang, J.; Yu, C.; Sun, Q.; Li, X.; Adair, K.; Wang, C.; Zhao, Y.; Zhang, S.; Li, W.; Deng, S.; Li, R.; Huang, Y.; Huang, H.; Zhang, L.; Zhao, S.; Lu, S.; Sun, X., *Adv. Energy Mater.* **2020,** *10* (9), 1903422.

（7）Kanno, R.; Murayama, M.; Inada, T.; Kobayashi, T.; Sakamoto, K.; Sonoyama, N.; Yamada, A.; Kondo, S., *Electrochem. Solid-State Lett.* **2004,** *7* (12), A455-A458.

（8）Li, X. N.; Liang, J. W.; Li, X.; Wang, C. H.; Luo, J.; Li, R. Y.; Sun, X. L., *Energy Environ. Sci.* **2018,** *11* (10), 2828-2832.

（9）Takada, K.; Aotani, N.; Iwamoto, K.; Kondo, S., *Solid State Ionics* **1996,** *86-8*, 877-882.

（10）Xiao, Y. H.; Miara, L. J.; Wang, Y.; Ceder, G., *Joule* **2019,** *3* (5), 1252-1275.

（11）Chen, R.; Li, Q.; Yu, X.; Chen, L.; Li, H., *Chem. Rev.* **2019**, doi: 10.1021/acs.chemrev.9b00268.

（12）Wang, C. H.; Adair, K. R.; Liang, J. W.; Li, X. N.; Sun, Y. P.; Li, X.; Wang, J. W.; Sun, Q.; Zhao, F. P.; Lin, X. T.; Li, R. Y.; Huang, H.; Zhang, L.; Yang, R.; Lu, S. G.; Sun, X. L., *Adv. Funct. Mater.* **2019,** *29* (26), 1900392.

（13）Culver, S. P.; Koerver, R.; Zeier, W. G.; Janek, J., *Adv. Energy Mater.* **2019,** *9* (24), 1900626.

（14）Du, M.; Liao, K.; Lu, Q.; Shao, Z., *Energy Environ. Sci.* **2019,** *12* (6), 1780-1804.

（15）Ito, S.; Fujiki, S.; Yamada, T.; Aihara, Y.; Park, Y.; Kim, T. Y.; Baek, S. W.; Lee, J. M.; Doo, S.; Machida, N., *J. Power Sources* **2014,** *248*, 943-950.

（16）Lee, Y. G.; Fujiki, S.; Jung, C.; Suzuki, N.; Yashiro, N.; Omoda, R.; Ko, D. S.; Shiratsuchi, T.; Sugimoto, T.; Ryu, S.; Ku, J. H.; Watanabe, T.; Park, Y.; Aihara, Y.; Im, D.; Han, I. T., *Nat. Energy* **2020,** *5* (4), 299-308.

（17）Machida, N.; Kashiwagi, J.; Naito, M.; Shigematsu, T., *Solid State Ionics* **2012,** *225*, 354-358.

（18）Li, X. F.; Liu, J.; Meng, X. B.; Tang, Y. J.; Banis, M. N.; Yang, J. L.; Hu, Y. H.; Li, R. Y.; Cai, M.; Sun, X. L., *J. Power Sources* **2014,** *247*, 57-69.

（19）Li, X.; Zhang, K. J.; Mitlin, D.; Yang, Z. Z.; Wang, M. S.; Tang, Y.; Jiang, F.; Du, Y. G.; Zheng, J. M., *Chem. Mater.* **2018,** *30* (8), 2566-2573.

（20）Jiang, Z.; Xie, H.; Wang, S.; Song, X.; Yao, X.; Wang, H., *Adv. Energy Mater.* **2018,** *8* (27), 1801433.

（21）Zhang, J. C.; Li, Z. Y.; Gao, R.; Hu, Z. B.; Liu, X. F., *J. Phys. Chem. C* **2015,** *119* (35), 20350-20356.

（22）Ni, J.; Zhou, H.; Chen, J.; Zhang, X., *Electrochim. Acta* **2008,** *53* (7), 3075-3083.

（23）Song, B.; Li, W.; Oh, S. M.; Manthiram, A., *ACS Appl. Mater. Interfaces* **2017,** *9* (11), 9718-9725.

（24）Zheng, J. C.; Yang, Z.; Wang, P. B.; Tang, L. B.; An, C. S.; He, Z. J., *ACS Appl. Mater. Interfaces* **2018,** *10* (37), 31324-31329.

（25）Zhang, J. C.; Zhang, H.; Gao, R.; Li, Z. Y.; Hu, Z. B.; Liu, X. F., *Phys. Chem. Chem. Phys.* **2016,** *18* (19), 13322-13331.

（26）Wang, C.; Chen, L.; Zhang, H.; Yang, Y.; Wang, F.; Yin, F.; Yang, G., *Electrochim. Acta* **2014,** *119*, 236-242.

（27）Lim, Y. J.; Lee, S. M.; Lim, H.; Moon, B.; Han, K. S.; Kim, J. H.; Song, J. H.; Yu, J. S.; Cho, W.; Park, M. S., *Electrochim. Acta* **2018,** *282*, 311-316.

（28）George, S. M., *Chem. Rev.* **2010,** *110* (1), 111-131.

（29）Zhao, Y.; Zheng, K.; Sun, X. L., *Joule* **2018,** *2* (12), 2583-2604.

（30）Li, X.; Ren, Z. H.; Banis, M. N.; Deng, S. X.; Zhao, Y.; Sun, Q.; Wang, C. H.; Yang, X. F.; Li, W. H.; Liang, J. W.; Li, X. N.; Sun, Y. P.; Adair, K.; Li, R. Y.; Hu, Y. F.; Sham, T. K.; Huang, H.; Zhang, L.; Lu, S. G.; Luo, J.; Sun, X. L., *ACS Energy Lett.* **2019,** *4* (10), 2480-2488.

（31）Wang, C. H.; Li, X.; Zhao, Y.; Banis, M. N.; Liang, J. W.; Li, X. N.; Sun, Y. P.; Adair, K. R.; Sun, Q.; Liu, Y. L.; Zhao, F. P.; Deng, S. X.; Lin, X. T.; Li, R. Y.; Hu, Y. F.; Sham, T. K.; Huang, H.; Zhang, L.; Yang, R.; Lu, S. G.; Sun, X. L., *Small Methods* **2019,** *3* (10), 1900261.

（32）Deng, S.; Li, X.; Ren, Z.; Li, W.; Luo, J.; Liang, J.; Liang, J.; Banis, M. N.; Li, M.; Zhao, Y.; Li, X.; Wang, C.; Sun, Y.; Sun, Q.; Li, R.; Hu, Y.; Huang, H.; Zhang, L.; Lu, S.; Luo, J.; Sun, X., *Energy Storage Mater.* **2020,** *27*, 117-123.

（33）Yadegari, H.; Banis, M. N.; Xiao, B. W.; Sun, Q.; Li, X.; Lushington, A.; Li, R. Y.; Sham, T. K.; Cui, X. Y.; Sun, X. L., *Chem. Mater.* **2015,** *27* (8), 3040-3047.

（34）Yu, C.; Li, Y.; Willans, M.; Zhao, Y.; Adair, K. R.; Zhao, F. P.; Li, W. H.; Deng, S. X.; Liang, J. W.; Banis, M. N.; Li, R. Y.; Huang, H.; Zhang, L.; Yang, R.; Lu, S. G.; Huang, Y. N.; Sun, X. L., *Nano Energy* **2020,** *69*, 104396.

（35）Wang, S.; Zhang, Y.; Zhang, X.; Liu, T.; Lin, Y. H.; Shen, Y.; Li, L.; Nan, C. W., *ACS Appl. Mater. Interfaces* **2018**, 10 (49), 42279–42285

（36）Liu, J.; Meng, X.; Banis, M. N.; Cai, M.; Li, R.; Sun, X., *J. Phys. Chem. C* **2012,** *116* (27), 14656-14664.

（37）Wang, W. L.; Yin, Z. L.; Wang, J. P.; Wang, Z. X.; Li, X. H.; Guo, H. J., *J. Alloys Compd.* **2015,** *651*, 737-743.

（38）Wang, D.; Li, X. H.; Wang, Z. X.; Guo, H. J.; Huang, Z. J.; Kong, L. K.; Ru, J. J., *J. Alloys Compd.* **2015,** *647*, 612-619.

（39）Wang, B.; Liu, J.; Norouzi Banis, M.; Sun, Q.; Zhao, Y.; Li, R.; Sham, T. K.; Sun, X., *ACS Appl. Mater. Interfaces* **2017,** *9* (37), 31786-31793.

（40）Kazyak, E.; Chen, K.-H.; Davis, A. L.; Yu, S.; Sanchez, A. J.; Lasso, J.; Bielinski, A. R.; Thompson, T.; Sakamoto, J.; Siegel, D. J.; Dasgupta, N. P., *J. Mater. Chem. A* **2018,** *6* (40), 19425-19437.

（41）Glass, A. M.; Nassau, K.; Negran, T. J., *J. Appl. Phys.* **1978,** *49* (9), 4808-4811.

（42）Haruyama, J.; Sodeyama, K.; Han, L. Y.; Takada, K.; Tateyama, Y., *Chem. Mater.* **2014,** *26* (14), 4248-4255.

（43）Ohta, N.; Takada, K.; Sakaguchi, I.; Zhang, L. Q.; Ma, R. Z.; Fukuda, K.; Osada, M.; Sasaki, T., *Electrochem. Commun.* **2007,** *9* (7), 1486-1490.

（44）Kamaya, N.; Homma, K.; Yamakawa, Y.; Hirayama, M.; Kanno, R.; Yonemura, M.; Kamiyama, T.; Kato, Y.; Hama, S.; Kawamoto, K.; Mitsui, A., *Nat. Mater.* **2011,** *10* (9), 682-686.

（45）Ohta, N.; Takada, K.; Zhang, L. Q.; Ma, R. Z.; Osada, M.; Sasaki, T., *Adv. Mater.* **2006,** *18* (17), 2226-2229.

（46）Kim, A. Y.; Strauss, F.; Bartsch, T.; Teo, J. H.; Hatsukade, T.; Mazilkin, A.; Janek, J.; Hartmann, P.; Brezesinski, T., *Chem. Mater.* **2019,** *31* (23), 9664-9672.

（47）Okada, K.; Machida, N.; Naito, M.; Shigematsu, T.; Ito, S.; Fujiki, S.; Nakano, M.; Aihara, Y., *Solid State Ionics* **2014,** *255*, 120-127.

（48）Auvergniot, J.; Cassel, A.; Ledeuil, J. B.; Viallet, V.; Seznec, V.; Dedryvere, R., *Chem. Mater.* **2017,** *29* (9), 3883-3890.

（49）Banerjee, A.; Tang, H. M.; Wang, X. F.; Cheng, J. H.; Nguyen, H.; Zhang, M. H.; Tang, D. H. S.; Wynn, T. A.; Wu, E. A.; Doux, J. M.; Wu, T. P.; Ma, L.; Sterbinsky, G. E.; D'Souza, M. S.; Ong, S. P.; Meng, Y. S., *ACS Appl. Mater. Interfaces* **2019,** *11* (46), 43138-43145.

（50）Auvergniot, J.; Cassel, A.; Foix, D.; Viallet, V.; Seznec, V.; Dedryvere, R., *Solid State Ionics* **2017,** *300*, 78-85.

（51）Ishii, H.; Nakanishi, K.; Watanabe, I.; Ohta, T.; Kojima, K., *e-J. Surf. Sci. Nanotechnol.* **2011,** *9*, 416-421.

（52）Wang, Z. Y.; Lee, J. Z.; Xin, H. L. L.; Han, L. L.; Grillon, N.; Guy-Bouyssou, D.; Bouyssou, E.; Proust, M.; Meng, Y. S., *J. Power Sources* **2016,** *324*, 342-348.

7.7 Supporting information

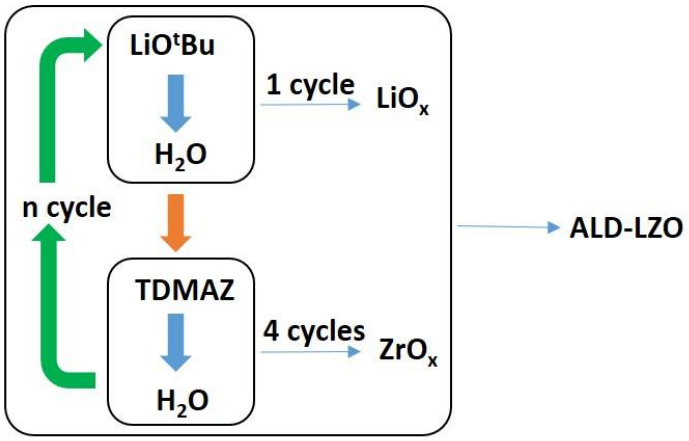

Figure S7.1 Schematic diagram of the ALD pulse route to prepare LZO coating layers on designated substrates.

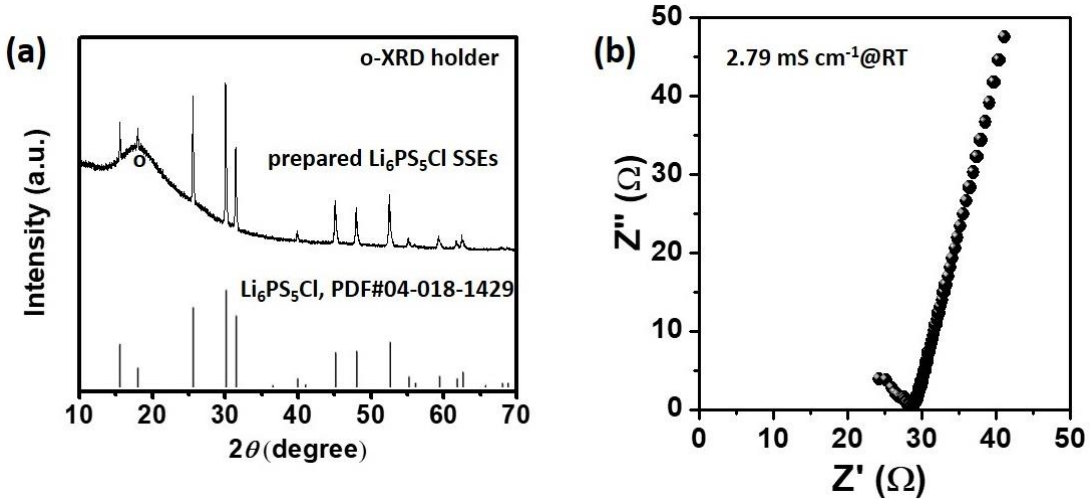

Figure S7.2 (a) XRD pattern of prepared Li6PS5Cl SSEs and (b) EIS curve measured at room temperature (RT).

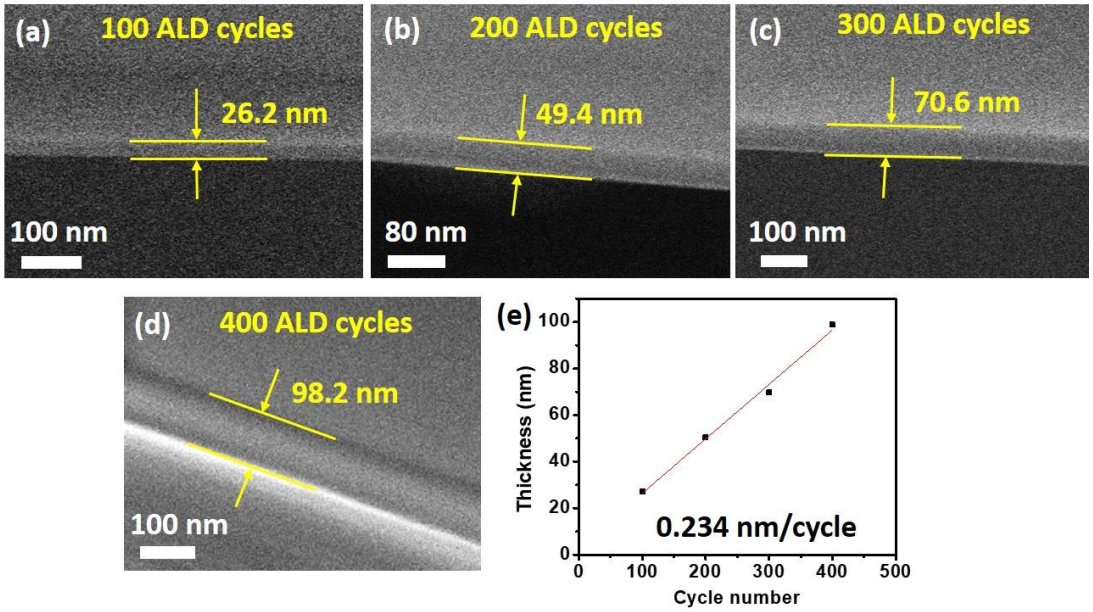

Figure S7.3 Scanning electron microscope (SEM) images of the cross-section of Si wafers that were deposited by various ALD cycles of LZO films: (a) 100 cycles, (b) 200 cycles, (c) 300 cycles, and (d) 400 cycles; (e) growth rate of the developed ALD-LZO films, deposition temperature 270 ^{o}C.

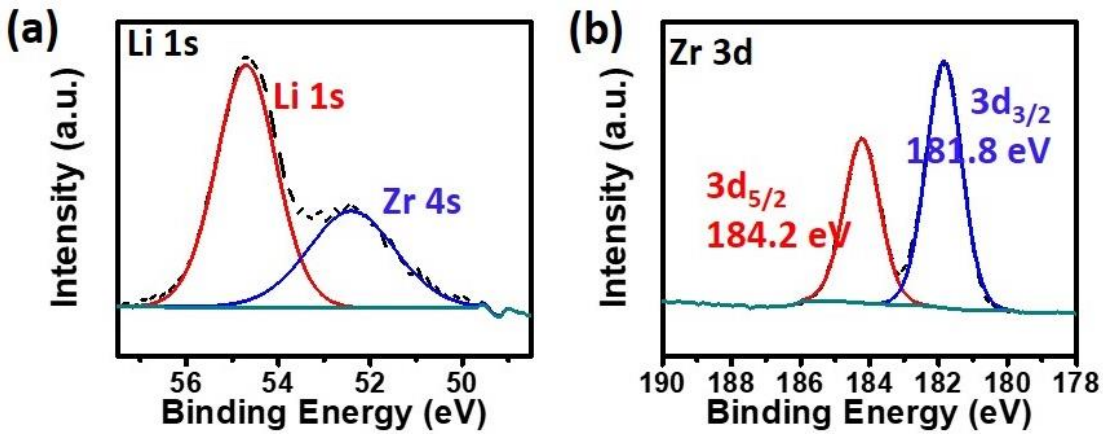

Figure S7.4 XPS spectra of (a) Li 1s and (b) Zr 3d in the LZO@CNT composites.

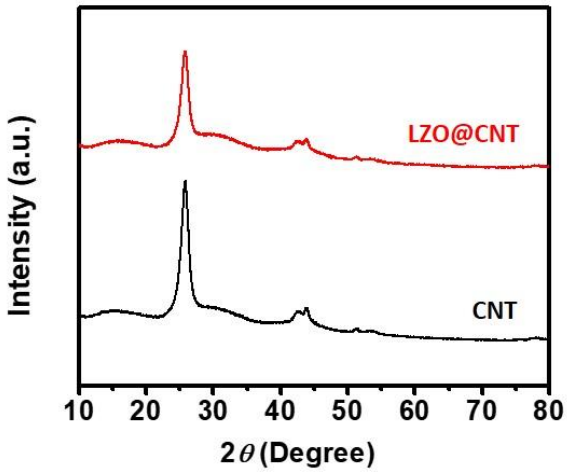

Figure S7.5 XRD patterns of the CNT and LZO@CNT suggest the amorphous feature of the deposited LZO films.

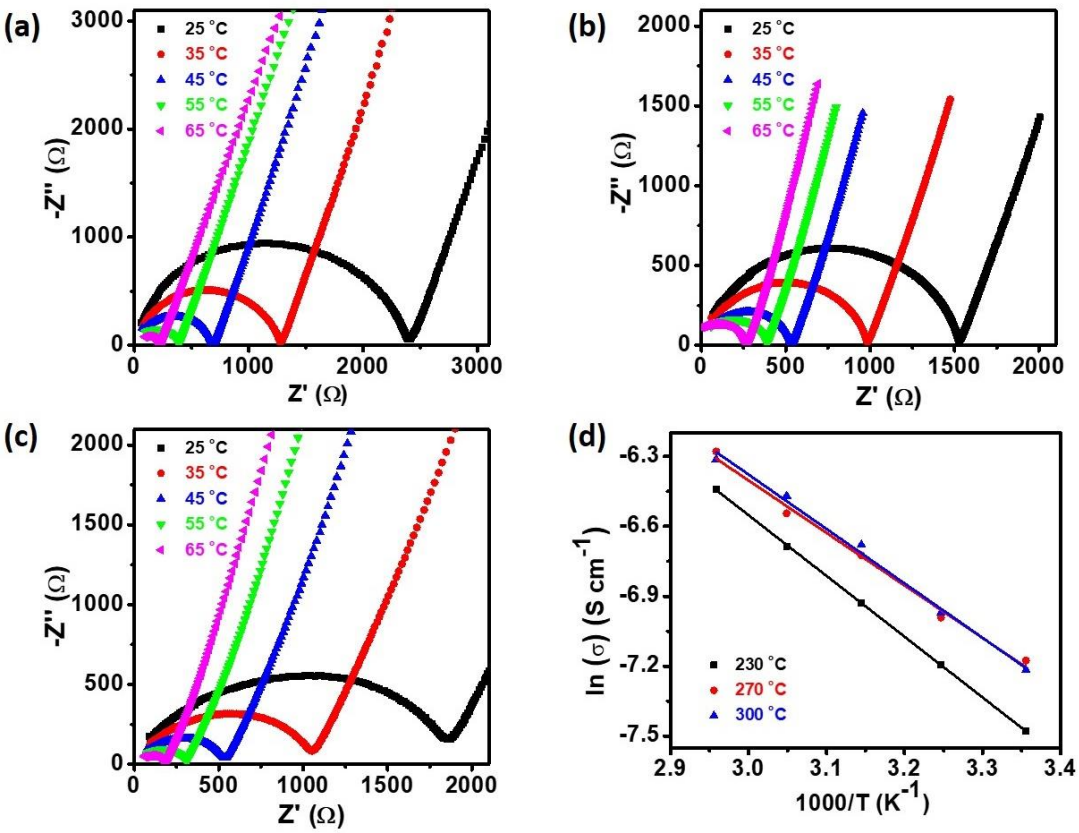

Figure S7.6 (a-c) Impedance plot of ALD-LZO films (1000c) that deposited on the patterned glass slide substrate by deposition temperature of 230, 270, and 300 ºC; (d) Arrhenius plots of the ALD-LZO film derived from the EIS results. (Scattered points are measured values and solid lines are fitted results.)

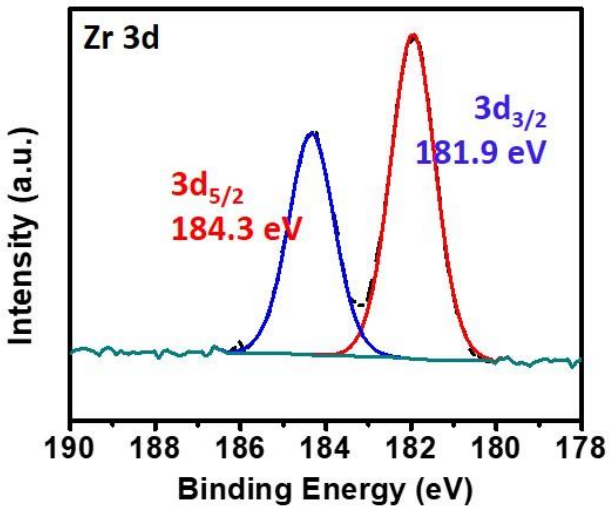

Figure S7.7 XPS spectra of Zr 3d and O1s in the ZrO_x@LCO composites.

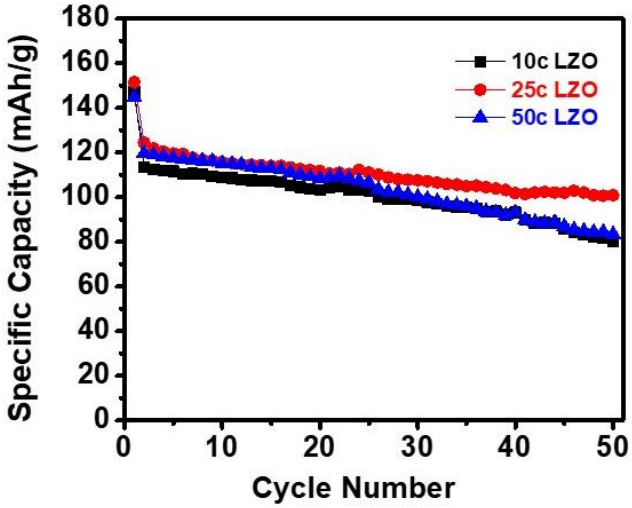

Figure S7.8 Cycling stability (charging capacity) of the In//LPSCl//LZO@LCO/LPSCl all-solid-state batteries employing various ALD cycles at the deposition temperature of 270 ^{o}C.

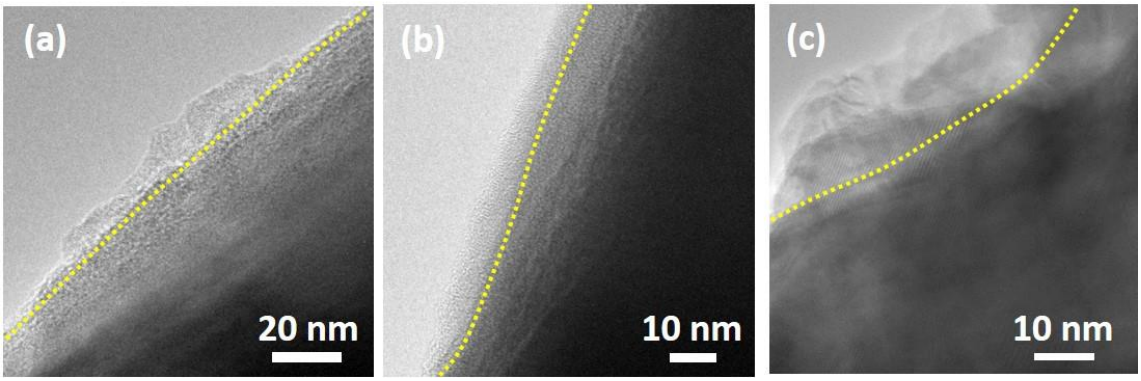

Figure S7.9 TEM images of the ALD-LZO films that are deposited on LCO particles with various ALD cycles: (a) 10c, (b) 25c, and (c) 50c at the same deposition temperature of 270 ^{o}C.

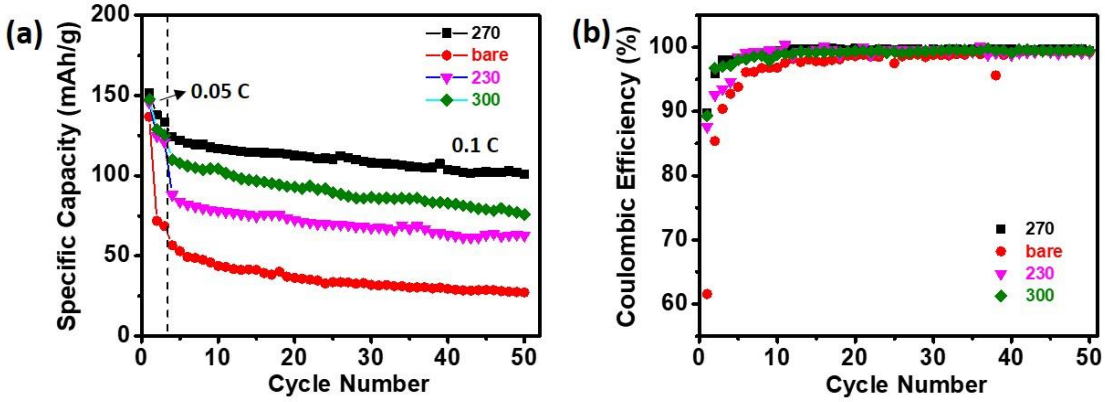

Figure S7.10 (a) Cycling stability of the In//LPSCl//LZO@LCO/LPSCl all-solid-state batteries employing various ALD-LZO deposition temperature (230, 270, and 300 ^{o}C) for 25 cycles; (b) the corresponding Coulombic efficiency.

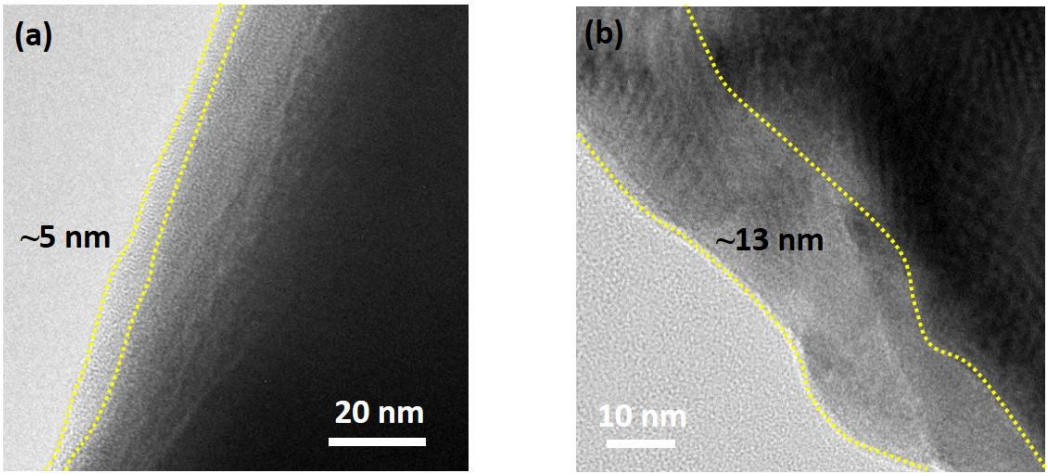

Figure S7.11 TEM images of 25c ALD-LZO films that are deposited on LCO particles with the deposition temperature of (a) 270 ^{o}C and (b) 300 ^{o}C.

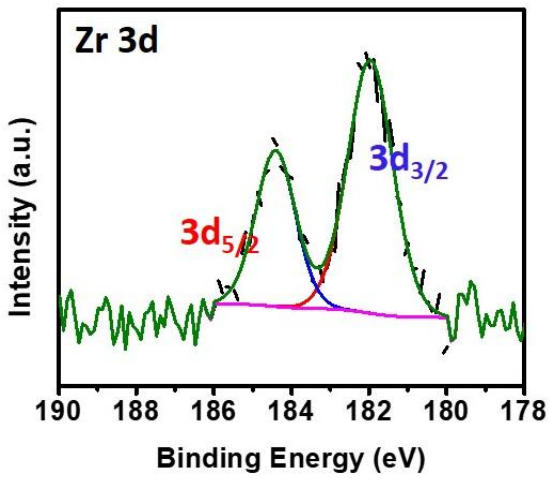

Figure S7.12 XPS spectra of Zr 3d in the LZO@LCO composites after cycling.

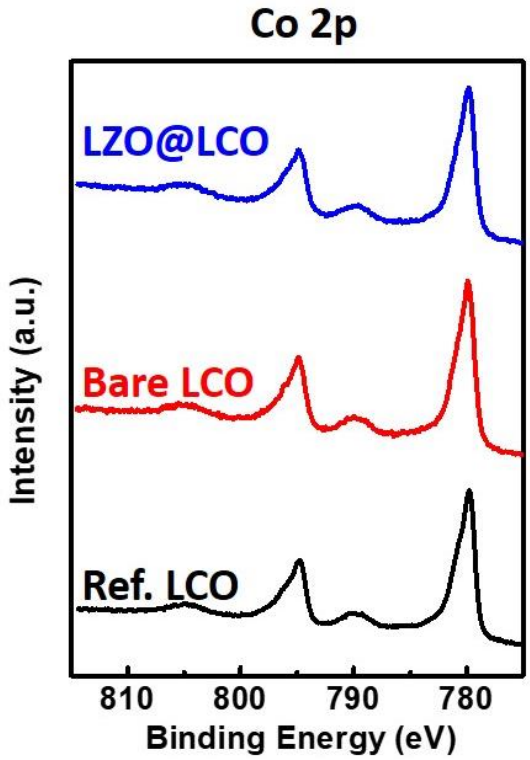

Figure S7.13 XPS spectra of Co 2p in the cathode composites with and w/o LZO coatings after battery cycling.

Chapter 8

8 Conclusions and Perspectives

This chapter summarize conclusions and contributions of this thesis. Additionally, personal statement and suggestions for future work are presented.

8.1 Conclusions

ASSLBs are regarded as the next-generation LIBs for electric vehicles (EVs) because of the advantages of high safety and energy density. However, the development of practical ASSLBs is hindered by lacking the high-performance SSEs, which can determine the electrochemical performance of ASSLBs. Generally, a qualified SSE should be a combination of two essential properties: high ionic conductivity and high electrode compatibility. In this thesis, sulfide-based SSEs are chosen as the study objects, synthesis and interface engineering and understanding are deeply preformed. The critical issues of developing sulfide-based ASSLBs are conspicuous. Although the ionic conductivity of some LGPS-type and Argyrodite-type vibrants can be up to 10^{-2} S cm^{-1} at RT, the electrode (anode and cathode) incompatibility and air instability are difficult to be overcome for practical applications. With respect to these challenges existing in sulfide SSEs and the related electrode interfaces, several strategies have been developed to address the specific problems as follows:

(1) Improving the Li metal/sulfide interface by fluorinating sulfide SSEs

Taking the popular Argyrodite Li_6LP_5Cl sulfide-based electrolytes as the example, F is incorporated in the system for the first time. It is verified that the fluorinated $LPSCl_{0.3}F_{0.7}$ electrolyte exhibits an outstanding stability towards Li metal during Li plating/stripping. In the Li//$LPSCl_{0.3}F_{0.7}$//Li symmetric cell, a stable Li plating/stripping for over 1000 hours can be achieved at the current density of 1.27 mA cm^{-2} and capacity of 1 mAh cm^{-2}. Even under a rarely reported current density of 6.37 mA cm^{-2} and capacity of 5 mAh cm^{-2}, the Li//$LPSCl_{0.3}F_{0.7}$//Li symmetric cell can still display a stable Li plating/stripping for over 250 hours. Furthermore, the excellent Li metal interface is applicable to realize high performance in Li@$LPSCl_{0.3}F_{0.7}$//LPSCl//LCO@LNO/LPSCl full batteries. The superior in-situ formed interface between Li metal and $LPSCl_{0.3}F_{0.7}$ is demonstrated to be endowed with highly dense and sheet-like surface morphology, as well as high concentration of LiF compounds. Overall, the fluorinated sulfide SSE can induce the formation of an ultra-stable Li metal interface and is expected to make significant steps towards the development of high-performance ASSLMBs.

(2) Enhancing air stability together with improved ionic conductivity and Li-metal compatibility by Sn substitution

Based on the hard and soft acids and bases (HSAB) theory, soft-acid Sn (+4) partially replace the hard-acid P (V) in two kinds of sulfide SSEs: Argyrodite Li_6PS_5I (LPSI) and glass-ceramic (gc) Li_3PS_4. The formed Sn-substituted PS_4 tetrahedra in both systems can stabilize the structure of modified sulfide SSEs. The mass and ionic conductivity of LPSI-20Sn (20% substitution) exhibit negligible changes after O_2 and 10%-humidity exposure (with reheating process), respectively. While in the Sn-substituted gc-Li_3PS_4, the improvement of air stability is much more effective, where gc-$Li_{3.2}P_{0.8}Sn_{0.2}S_4$ SSEs can withstand the exposure of air with 5% humidity (dry-room level atmosphere) for overnight.

In addition, the low-valence element substitution can induce a larger cell volume and increased Li^+ solubility, which endows the optimized LPSI-20Sn electrolyte with two orders of magnitudes higher (125 times) ionic conductivity (3.5×10^{-4} S cm^{-1}) compared with LPSI electrolyte (2.8×10^{-6} S cm^{-1}). Benefiting from the I-based chemistry in stabilizing the Li metal anode interface against sulfide electrolytes, Li-Li symmetric cells using LPSI-20Sn as the electrolyte can exhibit outstanding plating and stripping for over 200 hours at a high current density (1.26 mA cm^{-2}) and cut-off capacity (1 mAh cm^{-2}) in the Li//LPSI-20Sn//Li symmetric cell. LPSI-20Sn electrolyte was further employed as the Li-metal interlayer in ASSLMBs to provide a stabilized Li metal anode interface for achieving excellent cycling stability and rate capability.

20% of Sn substitution can also make the gc-$Li_{3.2}P_{0.8}Sn_{0.2}S_4$ SSEs possess high ionic conductivity of 1.21×10^{-3} S cm^{-1} which is 6 times higher than that of gc-Li_3PS_4 and is among the highest value in the reported sulfide SSEs based on orthorhombic β-Li_3PS_4. Sn substitution in this system was also verified to trigger the formation of Li-Sn alloys at the Li anode interface. It is verified by the FEM-based numerical simulation that interfacial Li-Sn alloys can regulate stable Li plating/stripping, thus leading to improved Li metal compatibility. As a final result, the gc-$Li_{3.2}P_{0.8}Sn_{0.2}S_4$ SSE can be employed as a single electrolyte layer to enable ASSLMBs with excellent electrochemical performance. Overall,

the versatile Sn substitution presents a great opportunity for industrial application of sulfide SSEs.

(3) Constructing favourable cathode/sulfide interface via ALD coating

ALD is utilized to rationally design Li-containing Zr-based cathode coating for sulfide-based ASSLBs. Structural characterizations (including synchrotron-XANES) confirm the success of incorporating Li in the LZO film by an additional Li-related sub-cycle process, which affects the local electronic structure of the Zr metal centers. The presented Zr-Li interaction manipulated by the ALD deposition temperature (270 ^{o}C) is demonstrated to be favorable for a desirable ionic conductivity of 6.7×10^{-5} mS/cm at room temperature. ALD-LZO films coated on LCO cathode materials can significantly improve the RT performance for full batteries. A specific capacity of 117.2 mAh/g is achieved at the current density of 0.1 C, and the capacity retention stands at 72% after 100 cycles. More importantly, the specific capacity reaches 79.1 mAh/g at 1 C. The effective interfacial manipulation provides essential Li^{+} ion flux at the LCO/LPSCl interface, which can reduce the polarization of the electrochemical reactions. Moreover, various spectroscopic characterizations (XPS and synchrotron-STXM) reveal that the detrimental side reactions between LCO and LPSCl are significantly reduced with the LZO derived cathode interface. The flexible design of functional cathode interface realized by ALD paves the way to achieve advanced sulfide-based ASSLIBs.

8.2 Contributions to this field

(1) Generally, the unstable sulfide/Li metal interface is viewed as one of main challenges in developing sulfide-based ASSLMBs. In this thesis, I have demonstrated fluorination and Sn doping strategies can effectively improve the interface stability between Li metal interface with various modified sulfide-based SSEs. The functional interface (LiF-rich, LiI-rich, or Li-Sn containing) derived from the element introduction have been proved to stabilize the Li metal interface with sulfides. These results have been reported for the first time, which can encourage more research to solve the problematic Li/sulfide interface from the point of electrolyte synthesis.

(2) Poor air-stability of common sulfide-based SSEs consisting of PS_4 coordination is another big challenge to commercialize sulfide SSEs for ASSLBs. In this thesis, replacing P (V) with Sn (IV) partially has been verified effective to improve the air stability of *Argyrodite*-type and β-Li_3PS_4 sulfide SSEs. The mechanism is based on the hard and soft acids and bases (HSAB) theory. In addition, benefiting from the enlarged unit cell caused by the aliovalent element substitution, the ionic conductivity of the modified sulfides shows significantly improved. Together with the obtained good Li metal compatibility, Sn-substituted Li_6PS_5I and Li_3PS_4 glass-ceramic SSEs have become promising SSEs that can directly contact with Li metal for sulfide-based ASSLMBs.

(3) Incompatibility between sulfide SSEs and oxide cathode materials is also one of the main obstacles to realize high-performance sulfide ASSLBs. In the thesis, advanced film fabrication technique of ALD has been used to design a new cathode coating materials (LZO) to improve the cathode interface stability. The ALD process is carefully controlled to tune the composition of the LZO coating, thus obtaining highly conductive and insulating interlayer to improve the interfacial stability between *Argyrodite* Li_6PS_5Cl SSEs and LCO cathode materials. This method provides a new coating choice in this field to alleviate the cathode interface problem.

8.3 Perspectives

Considerable progresses have been achieved in this thesis to develop high-performance ASSLBs, but there are still a lot of future work attracting our concerns. The perspectives of developing sulfide SSEs and ASSLBs using inorganic SSEs are presented as follows.

For sulfide SSEs and sulfide-based ASSLBs, the interface issues at both anode and cathode sides will become one of the hottest topics on the condition that ionic conductivity of sulfide SSEs is not the primary factor. In addition, development of air-stable sulfide SSEs in the dry-room operating condition is important to realize the commercialization of sulfides for practical applications.

(1) At the anode side, **first**, the mechanism of Li dendrites growth should be systematically studied. The influence factors would include the surface morphology of SSE pellets and

the used Li metal, the applied pressure during battery assembly and working, the electronic conductivity, and the physical properties of SSE pellets (e.g., grain boundary, particle size, tap density, porosity, etc). **Second**, the interfacial reactivity between Li metal SSEs should be reduced. This mostly relies on the in-situ formed interface possessing a high ionic conductivity while with a limited electronic conductivity. In the way, the high-quality passivation layer would prevent the endless interfacial reactions, and promote the Li-ion exchange at the interface. **Third**, the 'anode-free' concept should be transplanted to the sulfide-based ASSLBs. In the design of anode-free ASSLBs, all the shuttering Li ions as the energy carrier comes from the Li-rich cathode materials. Therefore, high reversibility (or high CE) of Li plating/stripping towards the current collector at anode side is essentially required, which brings new interface issue between the current collector (or anode substrate) and sulfide SSEs. The ideal collector or substrate facing the sulfide directly should perform (electro)chemical internes towards sulfides and compact contact with the SSE layer.

(2) At the cathode side, **first**, the coating methods other than wet-chemistry methods should be developed. For example, using PLD-based approaches have also been shown to be very effective and lossless, and ALD-based methods will likely have a stronger presence because of the diversity of available precursors deposited on the cathode materials. **Second**, highly ion-conducting coating materials should be vigorously developed. Currently, the highest ionic conductivity of coating layer is limited at 10^{-6} S cm^{-1} level at RT, which is still falling behind the SSEs. Therefore a large bottleneck needs to be overcome for Li^{+} ions transferring trough the cathode interface. There is no doubt that the efficiency of interfacial ion transport will be increased if highly ion-conducting coating layer is applied. **Third**, other than LCO cathode materials, many popular cathode materials (e.g., NCA, NMC, LNMO, and other high-voltage cathode) developed well in the LE-based LIBs are in urgent to be explored for the sulfide-based ASSLBs. These new cathode interface requires much deeper research compared with the benchmark-type LCO materials, since the interface problems would become much more complicated, due to the difference between polycrystals and single crystals, the cracking issues of NMC materials, the volume change and elusory phase transformation during (dis)charging, and so on.

(3) For the synthesis of air-stable sulfide SSEs, the element substitution of Sn has been demonstrated to improve the air stability of sulfide SSEs to some extent, but the ionic conductivity still shows decreased with long-term exposure in the moist air. Therefore, more strategies to improve the air stability are highly encouraged. For example, combining with air-stable oxide SSEs might be a feasible method to extend the expiration of sulfide SSEs without sacrificing high ionic conductivity. In addition, coating sulfide SSEs with nanosized hydrophobic layer would be a good choice, which can not only prevent the contact with air, but also not affect the Li^+ transport seriously.

For ASSLBs using other emerging inorganic SSEs, the discovery of superionic halide-based SSEs would encounter outbursts in the near future, showing a catch-up trend towards the superionic sulfide SSEs. Additionally, fluoride SSEs, showing the widest electrochemical window should be well exploited, which plays an essential role to realize ultrahigh-voltage ASSLBs. Last but not least, the fatal disadvantage of metal-containing halide SSEs, namely the Li-metal compatibility should be addressed.

(1) For exploiting new superionic halide-based conductors, it is urgent to improve the ionic conductivity of halide-based SSE up to 10^{-2} S cm^{-1} at room temperature, which would fulfill the purpose of using ASSLBs in wide temperature ranges, for example, at ultralow-temperature conditions. As the development of halide SSEs is in the renaissance stage, the structural information of the newly developed halide superionic conductors with improved synthesis approaches (e.g., high-energy ball milling, co-melting) should be compared well with those reported initially. The underlying mechanism of the re-gained high ionic conductivity should be well understood.

(2) To realize high-voltage ASSLBs, development of fluoride SSEs is believed extremely attractive. According to theoretical calculation, fluoride SSEs show ultrahigh oxidation limit over 6 V, which can match with any reported high-voltage cathode materials. However, the ionic conductivity of fluoride SSEs is as low as 10^{-6} S cm^{-1} at RT. This is ascribed to the strong electronegativity of F, which limits the Li^+ hoping among the active lattice sites.

(3) To develop Li-metal compatible halide SSEs, non-metal (NM) centered halide SSEs (Li-NM-X) should be developed as the emphasis. For example, B (+3) and Si (+4) are encouraged to serve as the center atom to construct stable polyhedral with halogens and Li ions. Although there might be side reactions at the interface using Li-NM-X SSEs and Li metal anode, the insufficient electronic conductivity of the interphase would prevent the endless interfacial reactions.

(4) Advanced characterizations, like X-ray synchrotron radiation, Neutron, solid-state NMR should be well developed to study the interface problem, structure information and ionic transport mechanism of new SSEs and ASSLBs.

Appendices

Appendix A: Permission from American Chemical Society (ACS) for Published Article on *ACS Energy Letters*

Copyright Clearance Center | RightsLink®

Home | Help | Email Support | Feipeng Zhao

ACS Publications
Most Trusted. Most Cited. Most Read.

Ultrastable Anode Interface Achieved by Fluorinating Electrolytes for All-Solid-State Li Metal Batteries

Author: Feipeng Zhao, Qian Sun, Chuang Yu, et al
Publication: ACS Energy Letters
Publisher: American Chemical Society
Date: Apr 1, 2020

Copyright © 2020, American Chemical Society

PERMISSION/LICENSE IS GRANTED FOR YOUR ORDER AT NO CHARGE

This type of permission/license, instead of the standard Terms & Conditions, is sent to you because no fee is being charged for your order. Please note the following:

- Permission is granted for your request in both print and electronic formats, and translations.
- If figures and/or tables were requested, they may be adapted or used in part.
- Please print this page for your records and send a copy of it to your publisher/graduate school.
- Appropriate credit for the requested material should be given as follows: "Reprinted (adapted) with permission from (COMPLETE REFERENCE CITATION). Copyright (YEAR) American Chemical Society." Insert appropriate information in place of the capitalized words.
- One-time permission is granted only for the use specified in your request. No additional uses are granted (such as derivative works or other editions). For any other uses, please submit a new request.

BACK | CLOSE WINDOW

Published paper: **Zhao, F.**; Sun, Q.; Yu, C.; Zhang, S.; Adair, K.; Wang, S.; Liu, Y.; Zhao, Y.; Liang, J.; Wang, C., Ultrastable anode interface achieved by fluorinating electrolytes for all-solid-state Li metal batteries. *ACS Energy Letters* **2020**, *5*, 1035-1043.

Appendix B: Permission from John Wiley and Sons for Published Article on *Advanced Energy Materials*

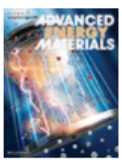

A Versatile Sn-Substituted Argyrodite Sulfide Electrolyte for All-Solid-State Li Metal Batteries

Author: Feipeng Zhao, Jianwen Liang, Chuang Yu, et al
Publication: Advanced Energy Materials
Publisher: John Wiley and Sons
Date: Jan 30, 2020

© 2020 WILEY-VCH Verlag GmbH & Co. KGaA, Weinheim

Order Completed

Thank you for your order.

This Agreement between Sir Feipeng Zhao ("You") and John Wiley and Sons ("John Wiley and Sons") consists of your license details and the terms and conditions provided by John Wiley and Sons and Copyright Clearance Center.

Your confirmation email will contain your order number for future reference.

Printable Details

License Number	5052570851506
License date	Apr 19, 2021

Licensed Content

Licensed Content Publisher	John Wiley and Sons
Licensed Content Publication	Advanced Energy Materials
Licensed Content Title	A Versatile Sn-Substituted Argyrodite Sulfide Electrolyte for All-Solid-State Li Metal Batteries
Licensed Content Author	Feipeng Zhao, Jianwen Liang, Chuang Yu, et al
Licensed Content Date	Jan 30, 2020
Licensed Content Volume	10
Licensed Content Issue	9
Licensed Content Pages	10

Order Details

Type of use	Dissertation/Thesis
Requestor type	Author of this Wiley article
Format	Print and electronic
Portion	Full article
Will you be translating?	No

About Your Work

Title	Development of advanced electrolytes and interfaces for high-performance all-solid-state lithium batteries
Institution name	Western University
Expected presentation date	Aug 2021

Additional Data

Requestor Location

Requestor Location	Sir Feipeng Zhao 1151 Richmond St London, ON N6A 3K7 Canada Attn: Sir Feipeng Zhao

Tax Details

Publisher Tax ID	EU826007151

Published paper: **Zhao, F.**; Liang, J.; Yu, C.; Sun, Q.; Li, X.; Adair, K.; Wang, C.; Zhao, Y.; Zhang, S.; Li, W., A Versatile Sn-Substituted Argyrodite Sulfide Electrolyte for All-Solid-State Li Metal Batteries. *Advanced Energy Materials* **2020**, 1903422.

Appendix C: Permission from John Wiley and Sons for Published Article on *Advanced Materials*

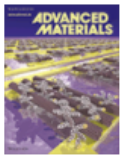

An Air-Stable and Li-Metal-Compatible Glass-Ceramic Electrolyte enabling High-Performance All-Solid-State Li Metal Batteries

Author: Feipeng Zhao, Sandamini H. Alahakoon, Keegan Adair, et al
Publication: Advanced Materials
Publisher: John Wiley and Sons
Date: Jan 20, 2021

Order Completed

Thank you for your order.

This Agreement between Sir Feipeng Zhao ("You") and John Wiley and Sons ("John Wiley and Sons") consists of your license details and the terms and conditions provided by John Wiley and Sons and Copyright Clearance Center.

Your confirmation email will contain your order number for future reference.

Printable Details

License Number	5052570774912
License date	Apr 19, 2021

Licensed Content

Licensed Content Publisher	John Wiley and Sons
Licensed Content Publication	Advanced Materials
Licensed Content Title	An Air-Stable and Li-Metal-Compatible Glass-Ceramic Electrolyte enabling High-Performance All-Solid-State Li Metal Batteries
Licensed Content Author	Feipeng Zhao, Sandamini H. Alahakoon, Keegan Adair, et al
Licensed Content Date	Jan 20, 2021
Licensed Content Volume	33
Licensed Content Issue	8
Licensed Content Pages	9

Order Details

Type of use	Dissertation/Thesis
Requestor type	Author of this Wiley article
Format	Print and electronic
Portion	Full article
Will you be translating?	No

About Your Work

Title	Development of advanced electrolytes and interfaces for high-performance all-solid-state lithium batteries
Institution name	Western University
Expected presentation date	Aug 2021

Additional Data

Requestor Location

Requestor Location	Sir Feipeng Zhao 1151 Richmond St London, ON N6A 3K7 Canada Attn: Sir Feipeng Zhao

Tax Details

Publisher Tax ID	EU826007151

Published paper: **Zhao, F.**; Alahakoon, S. H.; Adair, K.; Zhang, S.; Xia, W.; Li, W.; Yu, C.; Feng, R.; Hu, Y.; Liang, J., An Air-Stable and Li-Metal-Compatible Glass-Ceramic Electrolyte enabling High-Performance All-Solid-State Li Metal Batteries. *Advanced Materials* **2021**, *33*, 2006577.

Appendix D: Permission from Elsevier for Published Article on *Energy Storage Materials*

Copyright Clearance Center | RightsLink®

Home | Help | Email Support | Feipeng Zhao

ELSEVIER

Tuning bifunctional interface for advanced sulfide-based all-solid-state batteries

Author:
Feipeng Zhao,Yang Zhao,Jian Wang,Qian Sun,Keegan Adair,Shumin Zhang,Jing Luo,Junjie Li,Weihan Li,Yipeng Sun,Xiaona Li,Jianwen Liang,Changhong Wang,Ruying Li,Huan Huang,Li Zhang,Shangqian Zhao,Shigang Lu,Xueliang Sun

Publication: Energy Storage Materials

Publisher: Elsevier

Date: December 2020

© 2020 Elsevier B.V. All rights reserved.

Journal Author Rights

Please note that, as the author of this Elsevier article, you retain the right to include it in a thesis or dissertation, provided it is not published commercially. Permission is not required, but please ensure that you reference the journal as the original source. For more information on this and on your other retained rights, please visit: https://www.elsevier.com/about/our-business/policies/copyright#Author-rights

BACK | CLOSE WINDOW

© 2021 Copyright - All Rights Reserved | Copyright Clearance Center, Inc. | Privacy statement | Terms and Conditions
Comments? We would like to hear from you. E-mail us at customercare@copyright.com

Published paper: **Zhao, F.**; Zhao, Y.; Wang, J.; Sun, Q.; Adair, K.; Zhang, S.; Luo, J.; Li, J.; Li, W.; Sun, Y., Tuning bifunctional interface for advanced sulfide-based all-solid-state batteries. *Energy Storage Materials* **2020**, *33*, 139-146.

Appendix E: Permission from Elsevier for Published Article on *Nano Energy*

Copyright Clearance Center | RightsLink®

Home | Help | Email Support | Feipeng Zhao

Recent development of lithium argyrodite solid-state electrolytes for solid-state batteries: Synthesis, structure, stability and dynamics

Author: Chuang Yu,Feipeng Zhao,Jing Luo,Long Zhang,Xueliang Sun

Publication: Nano Energy

Publisher: Elsevier

Date: May 2021

© 2021 Elsevier Ltd. All rights reserved.

ELSEVIER

Journal Author Rights

Please note that, as the author of this Elsevier article, you retain the right to include it in a thesis or dissertation, provided it is not published commercially. Permission is not required, but please ensure that you reference the journal as the original source. For more information on this and on your other retained rights, please visit: https://www.elsevier.com/about/our-business/policies/copyright#Author-rights

BACK | CLOSE WINDOW

© 2021 Copyright - All Rights Reserved | Copyright Clearance Center, Inc. | Privacy statement | Terms and Conditions

Comments? We would like to hear from you. E-mail us at customercare@copyright.com

Published paper: Yu, C.#; **Zhao, F.#**; Luo, J.#; Zhang, L.; Sun, X., Recent Development of Lithium Argyrodite Solid-State Electrolytes for Solid-State Batteries: Synthesis, Structure, Stability and Dynamics. *Nano Energy* **2021**, 83, 105858. (co-first author)

Curriculum Vitae

Name:	Feipeng Zhao
Post-secondary Education and Degrees:	Soochow University Suzhou, Jiangsu, China 2010-2014 B.A. Soochow University Suzhou, Jiangsu, China 2014-2017 M.A. The University of Western Ontario London, Ontario, Canada 2017-2021 Ph.D.
Honours and Awards:	Ontario Trillium Scholarship 2017-2021 National Scholarship for Graduate Students of China 2016
Related Work Experience	Research Assistant The University of Western Ontario 2017-2021

Publications:

(A) Peer-reviewed journal papers based on this Thesis (First Author and co-first author)

(1) **Zhao, F.**, Zhang, S., Reid, J., Liang, J., Alahakoon, S.H., Li, W., Huang, Y., Sun, X. New superionic conductors: tantalum-centered halides. To be submitted, **2021**.

(2) **Zhao, F.**; Alahakoon, S. H.; Adair, K.; Zhang, S.; Xia, W.; Li, W.; Yu, C.; Feng, R.; Hu, Y.; Liang, J., An Air-Stable and Li-Metal-Compatible Glass-Ceramic Electrolyte enabling High-Performance All-Solid-State Li Metal Batteries. *Advanced Materials* **2021**, *33*, 2006577.

(3) **Zhao, F.**; Zhao, Y.; Wang, J.; Sun, Q.; Adair, K.; Zhang, S.; Luo, J.; Li, J.; Li, W.; Sun, Y., Tuning bifunctional interface for advanced sulfide-based all-solid-state batteries. *Energy Storage Materials* **2020**, *33*, 139-146.

(4) **Zhao, F.**; Sun, Q.; Yu, C.; Zhang, S.; Adair, K.; Wang, S.; Liu, Y.; Zhao, Y.; Liang, J.; Wang, C., Ultrastable anode interface achieved by fluorinating electrolytes for all-solid-state Li metal batteries. *ACS Energy Letters* **2020**, *5*, 1035-1043.

(5) **Zhao, F.**; Liang, J.; Yu, C.; Sun, Q.; Li, X.; Adair, K.; Wang, C.; Zhao, Y.; Zhang, S.; Li, W., A Versatile Sn-Substituted Argyrodite Sulfide Electrolyte for All-Solid-State Li Metal Batteries. *Advanced Energy Materials* **2020**, 1903422.

(6) Zhang, S.#; **Zhao, F.#;** Wang, S.#; Liang, J.; Wang, J.; Wang, C.; Zhang, H.; Adair, K.; Li, W.; Li, M.; Duan, H.; Zhang, Y.; Li, R.; Huang, H.; Zhang, L.; Zhao, S.; Lu, S.; Sham, T.K.; Mo, Y.; Sun, X., Advanced Ultrahigh-Voltage All-Solid-State Li-Ion Batteries Enabled by A Dual-Halogen CathodeSolid Electrolyte, submitted to Advance Energy Materials, **2021**, DOI: 10.1002/aenm.202100836. (co-first author)

(7) Yu, C.#; **Zhao, F.#**; Luo, J.#; Zhang, L.; Sun, X., Recent Development of Lithium Argyrodite Solid-State Electrolytes for Solid-State Batteries: Synthesis, Structure, Stability and Dynamics. *Nano Energy* **2021**, 83, 105858. (co-first author)

(8) Li, W.#; Wang, Z. #; **Zhao, F.#**; Li, M.; Gao, X.; Zhao, Y.; Wang, J.; Zhou, J.; Hu, Y.; Xiao, Q., Phosphorene Degradation: Visualization and Quantification of Nanoscale Phase Evolution by Scanning Transmission X-ray Microscopy. *Chemistry of Materials* **2020**, 32, 3, 1272–1280. (co-first author)

(B) Peer-reviewed journal papers related to this Thesis (Co-author)

(9) Li, M.; Li, W.; Hu, Y.; Yakovenko, A.; Ren, Y.; Luo, J.; Holden, W.; Shakouri, M.; Xiao, J.; Gao, X.; **Zhao, F.**; Sun, X.; et al. New insights into the high-performance black phosphorus anode for lithium-ion batteries. *Advanced Materials*, **2021**, DOI: 10.1002/adma.202101259.

(10) Zhao, Y.; Zhang, L.; Liu, J.; Adair, K.; Zhao, F.; Sun, Y.; Wu, T.; Bi, X.; Amine, K.; Lu, J., Atomic/molecular layer deposition for energy storage and conversion. *Chem Soc Rev* **2021**.

(11) Yu, R.; Banis, M. N.; Wang, C.; Wu, B.; Huang, Y.; Cao, S.; Li, J.; Jamil, S.; Lin, X.; Zhao, F., Tailoring bulk Li+ ion diffusion kinetics and surface lattice oxygen activity for high-performance lithium-rich manganese-based layered oxides. *Energy Storage Materials* **2021**, *37*, 509-520.

(12) Wang, S.; Feng, S.; Liang, J.; Su, Q.; Zhao, F.; Song, H.; Zheng, M.; Sun, Q.; Song, Z.; Jia, X., Insight into MoS2–MoN Heterostructure to Accelerate Polysulfide Conversion toward High-Energy-Density Lithium–Sulfur Batteries. *Advanced Energy Materials* **2021**, 2003314.

(13) Zhao, C.; Liang, J.; Li, X.; Holmes, N.; Wang, C.; Wang, J.; Zhao, F.; Li, S.; Sun, Q.; Yang, X., Halide-based solid-state electrolyte as an interfacial modifier for high performance solid-state Li–O2 batteries. *Nano Energy* **2020**, *75*, 105036.

(14) Zhang, S.; Zhao, Y.; Zhao, F.; Zhang, L.; Wang, C.; Li, X.; Liang, J.; Li, W.; Sun, Q.; Yu, C., Gradiently Sodiated Alucone as an Interfacial Stabilizing Strategy for Solid-State Na Metal Batteries. *Advanced Functional Materials* **2020**, *30*, 2001118.

(15) Yu, C.; Li, Y.; Willans, M.; Zhao, Y.; Adair, K. R.; Zhao, F.; Li, W.; Deng, S.; Liang, J.; Banis, M. N., Superionic conductivity in lithium argyrodite solid-state electrolyte by controlled Cl-doping. *Nano Energy* **2020**, *69*, 104396.

(16) Yu, C.; Li, Y.; Li, W.; Adair, K. R.; Zhao, F.; Willans, M.; Liang, J.; Zhao, Y.; Wang, C.; Deng, S., Enabling ultrafast ionic conductivity in Br-based lithium argyrodite electrolytes for solid-state batteries with different anodes. *Energy Storage Materials* **2020**, *30*, 238-249.

(17) Yu, C.; Li, Y.; Adair, K. R.; Li, W.; Goubitz, K.; Zhao, Y.; Willans, M. J.; Thijs, M. A.; Wang, C.; Zhao, F., Tuning ionic conductivity and electrode compatibility of Li3YBr6 for high-performance all solid-state Li batteries. *Nano Energy* **2020**, *77*, 105097.

(18) Yang, X.; Gao, X.; Mukherjee, S.; Doyle-Davis, K.; Fu, J.; Li, W.; Sun, Q.; Zhao, F.; Jiang, M.; Hu, Y., Phase Evolution of a Prenucleator for Fast Li Nucleation in All-Solid-State Lithium Batteries. *Advanced Energy Materials* **2020**, *10*, 2001191.

(19) Wang, C.; Liang, J.; Jiang, M.; Li, X.; Mukherjee, S.; Adair, K.; Zheng, M.; Zhao, Y.; Zhao, F.; Zhang, S., Interface-assisted in-situ growth of halide electrolytes eliminating interfacial challenges of all-inorganic solid-state batteries. *Nano Energy* **2020**, *76*, 105015.

(20) Liang, J.; Sun, Y.; Zhao, Y.; Sun, Q.; Luo, J.; Zhao, F.; Lin, X.; Li, X.; Li, R.; Zhang, L., Engineering the conductive carbon/PEO interface to stabilize solid polymer electrolytes for all-solid-state high voltage LiCoO2 batteries. *Journal of Materials Chemistry A* **2020**, *8*, 2769-2776.

(21) Li, X.; Liang, J.; Yang, X.; Adair, K. R.; Wang, C.; Zhao, F.; Sun, X., Progress and perspectives on halide lithium conductors for all-solid-state lithium batteries. *Energy & Environmental Science* **2020**, *13*, 1429-1461.

(22) Li, X.; Liang, J.; Adair, K. R.; Li, J.; Li, W.; Zhao, F.; Hu, Y.; Sham, T.-K.; Zhang, L.; Zhao, S., Origin of Superionic Li3Y1–x In x Cl6 Halide Solid Electrolytes with High Humidity Tolerance. *Nano Letters* **2020**, *20*, 4384-4392.

(23) Zhao, Y.; Liang, J.; Sun, Q.; Goncharova, L. V.; Wang, J.; Wang, C.; Adair, K. R.; Li, X.; Zhao, F.; Sun, Y., In situ formation of highly controllable and stable Na 3 PS 4 as a protective layer for Na metal anode. *Journal of Materials Chemistry A* **2019**, *7*, 4119-4125.

(24) Zhao, Y.; Amirmaleki, M.; Sun, Q.; Zhao, C.; Codirenzi, A.; Goncharova, L. V.; Wang, C.; Adair, K.; Li, X.; Yang, X., Natural SEI-inspired dual-protective layers via atomic/molecular layer deposition for long-life metallic lithium anode. *Matter* **2019**, *1*, 1215-1231.

(25) Wang, S.; Liao, J.; Yang, X.; Liang, J.; Sun, Q.; Liang, J.; Zhao, F.; Koo, A.; Kong, F.; Yao, Y., Designing a highly efficient polysulfide conversion catalyst with paramontroseite for high-performance and long-life lithium-sulfur batteries. *Nano Energy* **2019**, *57*, 230-240.

(26) Wang, S.; Chen, H.; Liao, J.; Sun, Q.; Zhao, F.; Luo, J.; Lin, X.; Niu, X.; Wu, M.; Li, R., Efficient trapping and catalytic conversion of polysulfides by VS4 nanosites for Li–S batteries. *ACS Energy Letters* **2019**, *4*, 755-762.

(27) Wang, C.; Li, X.; Zhao, Y.; Banis, M. N.; Liang, J.; Li, X.; Sun, Y.; Adair, K. R.; Sun, Q.; Liu, Y., Manipulating interfacial nanostructure to achieve high-performance all-solid-state lithium-ion batteries. *Small Methods* **2019**, *3*, 1900261.

(28) Wang, C.; Adair, K. R.; Liang, J.; Li, X.; Sun, Y.; Li, X.; Wang, J.; Sun, Q.; Zhao, F.; Lin, X., Solid-state plastic crystal electrolytes: effective protection interlayers for sulfide-based all-solid-state lithium metal batteries. *Advanced Functional Materials* **2019**, *29*, 1900392.

(29) Li, X.; Liang, J.; Luo, J.; Banis, M. N.; Wang, C.; Li, W.; Deng, S.; Yu, C.; Zhao, F.; Hu, Y., Air-stable Li 3 InCl 6 electrolyte with high voltage compatibility for all-solid-state batteries. *Energy & Environmental Science* **2019**, *12*, 2665-2671.

(30) Kong, F.; Liu, S.; Li, J.; Du, L.; Banis, M. N.; Zhang, L.; Chen, G.; Doyle-Davis, K.; Liang, J.; Wang, S., Trimetallic Pt–Pd–Ni octahedral nanocages with subnanometer thick-wall towards high oxygen reduction reaction. *Nano Energy* **2019**, *64*, 103890.

(31) Zhao, Y.; Yang, X.; Sun, Q.; Gao, X.; Lin, X.; Wang, C.; Zhao, F.; Sun, Y.; Adair, K. R.; Li, R., Dendrite-free and minimum volume change Li metal anode achieved by three-dimensional artificial interlayers. *Energy Storage Materials* **2018**, *15*, 415-421.

(32) Wang, S.; Gong, F.; Yang, S.; Liao, J.; Wu, M.; Xu, Z.; Chen, C.; Yang, X.; Zhao, F.; Wang, B., Graphene Oxide-Template Controlled Cuboid-Shaped High-Capacity VS4 Nanoparticles as Anode for Sodium-Ion Batteries. *Advanced Functional Materials* **2018**, *28*, 1801806.

(C) Publications before joining UWO

(33) **Zhao, F.**; Shen, S.; Cheng, L.; Ma, L.; Zhou, J.; Ye, H.; Han, N.; Wu, T.; Li, Y.; Lu, J., Improved sodium-ion storage performance of ultrasmall iron selenide nanoparticles. *Nano Letters* **2017**, *17*, 4137-4142.

(34) **Zhao, F.**; Gong, Q.; Traynor, B.; Zhang, D.; Li, J.; Ye, H.; Chen, F.; Han, N.; Wang, Y.; Sun, X., Stabilizing nickel sulfide nanoparticles with an ultrathin carbon layer for improved cycling performance in sodium ion batteries. *Nano Research* **2016**, *9*, 3162-3170.

(35) **Zhao, F.**; Han, N.; Huang, W.; Li, J.; Ye, H.; Chen, F.; Li, Y., Nanostructured CuP 2/C composites as high-performance anode materials for sodium ion batteries. *Journal of Materials Chemistry A* **2015**, *3*, 21754-21759.

(36) **Zhao, F.**; Wang, Y.; Xu, X.; Liu, Y.; Song, R.; Lu, G.; Li, Y., Cobalt hexacyanoferrate nanoparticles as a high-rate and ultra-stable supercapacitor electrode material. *ACS Appl Mater Interfaces* **2014**, *6*, 11007-11012.

(37) Liu, Y.#; **Zhao#, F.#**; Li, J.; Li, Y.; McLeod, J. A.; Liu, L., Influence of crystal phase on TiO 2 nanowire anodes in sodium ion batteries. *Journal of Materials Chemistry A* **2017**, *5*, 20005-20013. (co-first author)

(38) Li, P.; Ma, L.; Wu, T.; Ye, H.; Zhou, J.; Zhao, F.; Han, N.; Wang, Y.; Wu, Y.; Li, Y., Chemical Immobilization and Conversion of Active Polysulfides Directly by Copper Current Collector: A New Approach to Enabling Stable Room-Temperature Li-S and Na-S Batteries. *Advanced Energy Materials* **2018**, *8*, 1800624.

(39) Zhou, J.; Wang, L.; Yang, M.; Wu, J.; Chen, F.; Huang, W.; Han, N.; Ye, H.; Zhao, F.; Li, Y., Hierarchical VS2 nanosheet assemblies: a universal host material for the reversible storage of alkali metal ions. *Adv Mater* **2017**, *29*, 1702061.

(40) Ye, H.; Wang, L.; Deng, S.; Zeng, X.; Nie, K.; Duchesne, P. N.; Wang, B.; Liu, S.; Zhou, J.; Zhao, F., Amorphous MoS3 Infiltrated with Carbon Nanotubes as an Advanced Anode Material of Sodium-Ion Batteries with Large Gravimetric, Areal, and Volumetric Capacities. *Advanced Energy Materials* **2017**, *7*, 1601602.

(41) Ye, H.; Ma, L.; Zhou, Y.; Wang, L.; Han, N.; Zhao, F.; Deng, J.; Wu, T.; Li, Y.; Lu, J., Amorphous MoS3 as the sulfur-equivalent cathode material for room-temperature Li–S and Na–S batteries. *Proceedings of the National Academy of Sciences* **2017**, *114*, 13091-13096.

(42) Wang, Y.; Zhou, J.; Wu, J.; Chen, F.; Li, P.; Han, N.; Huang, W.; Liu, Y.; Ye, H.; Zhao, F., Engineering SnS 2 nanosheet assemblies for enhanced electrochemical lithium and sodium ion storage. *Journal of Materials Chemistry A* **2017**, *5*, 25618-25624.

(43) Sun, N.; Wen, Z.; Zhao, F.; Yang, Y.; Shao, H.; Zhou, C.; Shen, Q.; Feng, K.; Peng, M.; Li, Y., All flexible electrospun papers based self-charging power system. *Nano Energy* **2017**, *38*, 210-217.

(44) Liu, Y.; Chen, F.; Ye, W.; Zeng, M.; Han, N.; Zhao, F.; Wang, X.; Li, Y., High-Performance Oxygen Reduction Electrocatalyst Derived from Polydopamine and Cobalt Supported on Carbon Nanotubes for Metal–Air Batteries. *Advanced Functional Materials* **2017**, *27*, 1606034.

(45) Huang, W.; Ma, X. Y.; Wang, H.; Feng, R.; Zhou, J.; Duchesne, P. N.; Zhang, P.; Chen, F.; Han, N.; Zhao, F., Promoting effect of Ni (OH) 2 on palladium nanocrystals leads to greatly improved operation durability for electrocatalytic ethanol oxidation in alkaline solution. *Adv Mater* **2017**, *29*, 1703057.

(46) Han, N.; Wang, Y.; Ma, L.; Wen, J.; Li, J.; Zheng, H.; Nie, K.; Wang, X.; Zhao, F.; Li, Y., Supported cobalt polyphthalocyanine for high-performance electrocatalytic CO2 reduction. *Chem* **2017**, *3*, 652-664.

(47) Chen, J.; Huang, Y.; Zhao, F.; Ye, H.; Wang, Y.; Zhou, J.; Liu, Y.; Li, Y., A hierarchical α-MoC 1− x hybrid nanostructure for lithium-ion storage. *Journal of Materials Chemistry A* **2017**, *5*, 8125-8132.

(48) Zeng, M.; Liu, Y.; Zhao, F.; Nie, K.; Han, N.; Wang, X.; Huang, W.; Song, X.; Zhong, J.; Li, Y., Metallic cobalt nanoparticles encapsulated in nitrogen-enriched graphene shells: its bifunctional electrocatalysis and application in zinc–air batteries. *Advanced Functional Materials* **2016**, *26*, 4397-4404.

(49) Ye, W.; Chen, F.; Zhao, F.; Han, N.; Li, Y., CuWO4 nanoflake array-based single-junction and heterojunction photoanodes for photoelectrochemical water oxidation. *ACS Appl Mater Interfaces* **2016**, *8*, 9211-9217.

(50) Ye, H.; Wang, Y.; Zhao, F.; Huang, W.; Han, N.; Zhou, J.; Zeng, M.; Li, Y., Iron-based sodium-ion full batteries. *Journal of Materials Chemistry A* **2016**, *4*, 1754-1761.

(51) Wang, X.; Wang, B.; Zhong, J.; Zhao, F.; Han, N.; Huang, W.; Zeng, M.; Fan, J.; Li, Y., Iron polyphthalocyanine sheathed multiwalled carbon nanotubes: A high-performance electrocatalyst for oxygen reduction reaction. *Nano Research* **2016**, *9*, 1497-1506.

(52) Liu, Y.; Wang, H.; Cheng, L.; Han, N.; Zhao, F.; Li, P.; Jin, C.; Li, Y., TiS2 nanoplates: a high-rate and stable electrode material for sodium ion batteries. *Nano Energy* **2016**, *20*, 168-175.

(53) Huang, Y.; Gong, Q.; Song, X.; Feng, K.; Nie, K.; Zhao, F.; Wang, Y.; Zeng, M.; Zhong, J.; Li, Y., Mo2C nanoparticles dispersed on hierarchical carbon microflowers for efficient electrocatalytic hydrogen evolution. *Acs Nano* **2016**, *10*, 11337-11343.

(54) Zhou, Y.; Wang, B.; Liu, C.; Han, N.; Xu, X.; Zhao, F.; Fan, J.; Li, Y., Polyanthraquinone-based nanostructured electrode material capable of high-performance pseudocapacitive energy storage in aprotic electrolyte. *Nano Energy* **2015**, *15*, 654-661.

(55) Huang, W.; Wang, H.; Zhou, J.; Wang, J.; Duchesne, P. N.; Muir, D.; Zhang, P.; Han, N.; Zhao, F.; Zeng, M., Highly active and durable methanol oxidation electrocatalyst based on the synergy of platinum–nickel hydroxide–graphene. *Nat Commun* **2015**, *6*, 1-8.

(56) Han, N.; Zhao, F.; Li, Y., Ultrathin nickel–iron layered double hydroxide nanosheets intercalated with molybdate anions for electrocatalytic water oxidation. *Journal of Materials Chemistry A* **2015**, *3*, 16348-16353.

(57) Shan, W.; Chen, L.; Chu, Y.; Zhao, F.; Liang, G.; Gu, A.; Yuan, L., Synthesis of a fully capped mesoporous silica and its hybrids with extremely low dielectric constant and loss. *Microporous and mesoporous materials* **2013**, *176*, 199-208.

(58) Mi, Y..; Liang, G.; Gu, A.; Zhao, F.; Yuan, L., Thermally conductive aluminum nitride–multiwalled carbon nanotube/cyanate ester composites with high flame retardancy and low dielectric loss. *Industrial & Engineering Chemistry Research* **2013**, *52*, 3342-3353.

(D) Conference presentation and abstract

(1) Zhao, F.; Zhang, S.; Sun, X., Advanced solid-state electrolytes and interfaces for high-performance all-solid-state lithium batteries, 2021 Virtual CAMBR Day of Western University, June 10, 2021. (Virtual Poster)

(2) Zhao, F.; Liang, J.; Sun, X., Sulfide-Based All-Solid-State Batteries: From Electrolyte Synthesis to Interface Design, ECS 237th Meeting Abstracts, 2020. (Abstract)

(3) Zhao, F.; Sun, X., Versatile Sn-Substituted Sulfide Electrolytes for High-Performance All-Solid-State Li-Metal Batteries, 2020 International Forum on Functional Materials of China, America and Canada. (Virtual Oral)

(4) Zhao, F.; Sun, X., Versatile Sn-Substituted Sulfide Electrolytes for High-Performance All-Solid-State Li-Metal Batteries, ECS Canadian Section 2020 Fall Symposium. (Virtual Oral)

(5) Zhao, F.; Sun, X., Versatile Sn-Substituted Sulfide Electrolytes for High-Performance All-Solid-State Li-Metal Batteries, 2020 Western University ECS Student Chapter Symposium. (Virtual Oral)

(6) Zhao, F.; Sun, X., Ultra-Stable Anode Interface Performed by Incorporating LiF in Li6PS5Cl-Based Sulfide Electrolytes, CSME-CFDSC Congress 2019, London, Canada, June 2-5. (Oral)